UNIVERSITY OF COPENHAGEN
FACULTY OF SCIENCE

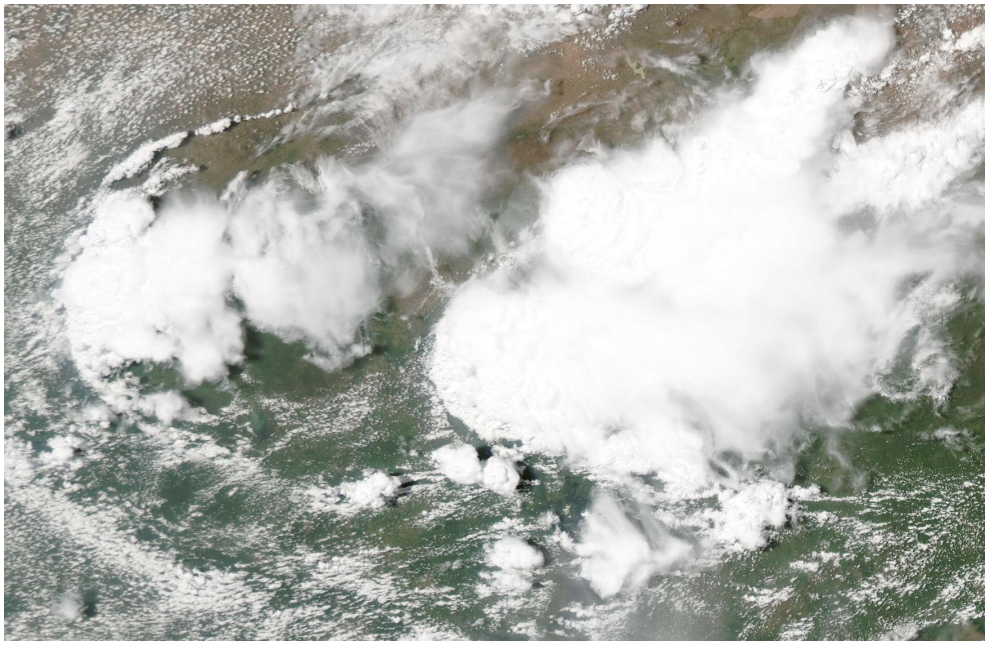

PhD thesis

Development of a Deep Learning Approach for the Segmentation of Convective Cold Pools in Satellite-Observable Data

Jannik Höller

Advisor: Jan O. Härter

Submitted: March 8, 2024

This thesis has been submitted to the PhD School of The Faculty of Science, University of Copenhagen

Abstract

Convective cold pools (CPs) result from convective downdrafts that are horizontally deflected when reaching Earth's surface. While spreading, CPs influence the distribution of low-level moisture and can trigger new convection by lifting warmer ambient air. Organizing convection, CPs are directly linked to extreme events such as mesoscale convective systems and thus crucial for the understanding of the underlying dynamics. Despite the socio-economic importance of such weather extremes, the role of CPs in convective organization is not yet sufficiently understood.

One of the main challenges is to accurately track dynamic CP gust fronts and link them to triggered convection. Although idealized models help us continuously disentangle the underlying mechanisms, they have so far been unable to capture the causal chains of CPs and lack observational benchmarks. Especially over tropical land, where CPs are ubiquitous, CP observations are mostly limited to event-based case studies due to the lack of relevant high-resolution data.

The goal of the present thesis is to (i) identify a detectable signature of CPs in geostationary satellite data, which is globally available with good spatio-temporal resolutions, and (ii) devise a corresponding approach for detecting CP regions.

In manuscript I, we address (i) by analyzing the space-borne signatures of 4218 CPs which we identified from almost 43 years of high-resolution near-surface data collected from twelve automatic weather stations spanning equatorial Africa. The identified CPs are accompanied by a mean decrease in satellite-derived brightness temperature of around 30 K. Moreover, in the majority of cases, CP gust fronts coincide with maximum brightness temperature decrease rates.

Modern deep learning methods can learn spatial patterns at various scales, making them well-suited to detect the identified CP signatures in satellite imagery and address (ii). However, their training requires substantial amounts of annotated ground truth data, which, for satellite data, can only be generated manually. To facilitate the generation of annotated data, we thus simulate cloud and rainfall fields based on different environmental conditions and automatically annotate the simulated scenes using a novel CP detection and tracking algorithm (CoolDeTA), presented in manuscript II. As CoolDeTA utilizes both thermodynamic and dynamic variables to detect and track CPs, the boundaries of the identified CPs align well with satellite-observable cloud signatures.

Using the annotated simulation scenes, we train convolutional neural networks for the segmentation of CPs in cloud and rainfall fields in manuscript III. Applied to an unknown test set, the trained neural networks achieve pixel accuracies of around 94% and successfully detect $\geq$ 83% of the CPs. In an additional case study, based on a simulation setup with realistic boundary

conditions for a day over West Africa, the developed method confirmed its promising performance, further demonstrating its potential with respect to real satellite data. In the future, our method may open for large-scale observational studies of mesoscale CP dynamics and convective organization.

Dansk Resumé

Konvektive cold pools (CPs) opstår fra konvektive nedstigninger, der horisontalt afbøjes, når de når Jordens overflade. Mens de spreder sig, påvirker CPs fordelingen af lavniveau-fugtighed og kan udløse ny konvektion ved at løfte varmere omgivende luft. Ved at organisere konvektionen er CPs direkte knyttet til ekstreme begivenheder såsom mesoskale konvektive systemer og er derfor afgørende for forståelsen af de underliggende dynamikker. På trods af den socioøkonomiske betydning af sådanne vejrudsving er rollen af CPs i konvektiv organisation endnu ikke tilstrækkeligt forstået.

En af de største udfordringer er at nøjagtigt spore dynamiske CP-gustfronte og forbinde dem til udløst konvektion. Selvom idealiserede modeller hjælper os med kontinuerligt at adskille de underliggende mekanismer, har de hidtil været ude af stand til at fange CPs årsagssammenhænge og mangler observationelle benchmarks. Især over tropiske områder, hvor CPs er udbredte, er CP-observationer primært begrænset til hændelsesbaserede casestudier på grund af manglen på relevant højopløsningsdata.

Målet med nærværende afhandling er at (i) identificere en påviselig signatur af CPs i geostationære satellitdata, som er globalt tilgængelige med gode rumlige og tidsmæssige opløsninger, og (ii) udvikle en tilsvarende tilgang til at detektere CP-regioner.

I manuskript I adresserer vi (i) ved at analysere de rumfartssignaturer af 4218 CPs, som vi identificerede fra næsten 43 års højopløselige nær-overfladedata indsamlet fra tolv automatisk vejrstationer spredt ud over Ækvatorialafrika. De identificerede CPs ledsages af et gennemsnitligt fald i satellitbaseret lysstyrke temperatur på ca. 30 K. Desuden falder CP-gustfronte i flertallet af tilfældene sammen med maksimale fald i lysstyrke temperatur.

Moderne deep learning-teknikker kan lære rumlige mønstre i forskellige skalaer, hvilket gør dem velegnede til at detektere de identificerede CP-signaturer i satellitbilleder og adressere (ii). Dog kræver deres træning betydelige mængder af annoterede ground truth-data, som for satellitdata kun kan genereres manuelt. For at lette genereringen af annoterede data simulerer vi derfor sky- og nedbørsfelter baseret på forskellige miljømæssige forhold og annoterer automatisk de simulerede scener ved hjælp af en ny CP-detektions- og sporing-algoritme (CoolDeTA), præsenteret i manuskript II. Da CoolDeTA udnytter både termodynamiske og dynamiske variabler til at detektere og spore CPs, stemmer grænserne for de identificerede CPs godt overens med satellit-observerbare sky-signaturer.

Ved at anvende de annoterede simulations-scener træner vi konvolutionelle neurale netværk til segmentering af CPs i sky- og regnmarkeder i manuskript III. Anvendt på et ukendt testsæt opnår de trænede neurale netværk pixelnøjagtigheder på ca. 94% og detekterer succesfuldt $\geq$ 83% af CPs. I et yderligere case-studie, baseret på en simulationsopsætning med realistiske grænsebetingelser for en dag over Vestafrika, bekræftede den udviklede metode sin lovende præstation og demonstrerede yderligere dens potentiale med hen-

syn til ægte satellitdata. I fremtiden kan vores metode åbne for storskala observationelle studier af mesoskale CP-dynamikker og konvektiv organisation.

Preface

This thesis represents the culmination of three years of dedicated research conducted between March 2021 and March 2024 at the Leibniz Centre for Tropical Marine Research in Bremen. Throughout this journey, I was enrolled at the PhD School of SCIENCE at the University of Copenhagen.

Doctoral candidate and author

Jannik Höller

Principal supervisor

Professor Jan Olaf Mirko Härter, PhD
Niels Bohr Institute
University of Copenhagen

Co-supervisor

Nicolas André Da Silva, PhD
Integrated Modeling Department
Leibniz Centre for Tropical Marine Research

Assessment committee

Associate Professor Peter Ditlevsen, PhD (Chair)
Niels Bohr Institute
University of Copenhagen

Raphaela Vogel, PhD
Meteorological Institute
University of Hamburg

Professor Andreas Fink, PhD
Institute for Meteorology and Climate Research
Karlsruhe Institute of Technology

The cover picture shows a true-color satellite scene of two cold pools traveling over tropical West Africa on May 9, 2022. The scene was captured by the Moderate Resolution Imaging Spectroradiometer aboard the Aqua satellite and obtained from the NASA Worldview website.

Acknowledgement

First and foremost, I would like to express my gratitude to my principal supervisor, **Jan Härter**. From the very beginning, you have ignited my passion for cold pools. I fondly remember our weekly "scientific walks" during the pandemic when normal office operations were not yet possible. Even afterwards, despite your busy schedule, you always made ample time to discuss both technical and personal matters with me thoroughly and extensively. With your extensive knowledge, curiosity, and positive attitude, you consistently managed to dispel any doubts and inspire me anew. I couldn't have asked for a better supervisor than you.

Furthermore, I would like to extend my gratitude to my co-supervisor, **Nicolas Da Silva**. You consistently made time for our weekly meetings and were always available when I needed your advice. Your knowledge, calm demeanor, and thoughtful approach seamlessly complemented Jan's supervision, offering me an additional valuable perspective.

I would also like to thank all colleagues and collaborators who have accompanied me on this journey, making it a unique experience that I will always cherish. A special thanks to **Romain Fiévet** and **Edward Engelbrecht** for conducting simulations, which were crucial for the success of this PhD project.

Additionally, I would like to thank all members of the assessment committee for dedicating their time to evaluate this thesis.

Lastly, I want to thank my family and friends for their unwavering support over the past three years, even if it meant enduring more discussions about cold pools and neural networks than they might have preferred.

List of Papers

The following manuscripts, authored by the candidate, have been included in this thesis:

Manuscript I

Hoeller, J., Haerter, J. O., & Da Silva, N. A. (2023). Characteristics of Station-Derived Convective Cold Pools Over Equatorial Africa. Authorea Preprints. https://essopenarchive.org/doi/full/10.22541/essoar.170067109.99041093. Accepted on March 1, 2024 for publication in Geophysical Research Letters.

Manuscript II

Hoeller, J., Fiévet, R., & Haerter, J. O. (2024). Detecting cold pool family trees in convection resolving simulations. Journal of Advances in Modeling Earth Systems, 16(1), e2023MS003682. https://doi.org/10.1029/2023MS003682.

Manuscript III

Hoeller, J., Fiévet, R., Engelbrecht, E., & Haerter, J. O. (2024). U-net segmentation for the detection of convective cold pools from cloud and rainfall fields. Journal of Geophysical Research: Atmospheres, 129(1), e2023JD040126. https://doi.org/10.1029/2023JD040126.

The following manuscript, co-authored by the candidate during the PhD project, has not been included in this thesis:

Bleischwitz, R., Hoeller, J., & Kriegl, M. (2023). Ship recycling — estimating future stocks and readiness for green steel transformation. Environmental Research Letters, 18(12), 124034. https://doi.org/10.1088/1748-9326/ad0a55.

Contents

List of Abbreviations

ANN Artificial Neural Network.

ASTER Advanced Spaceborne Thermal Emission and Reflection Radiometer.

CAPE Convective Available Potential Energy.

CIN Convective Inhibition.

CNN Convolutional Neural Network.

CoolDeTA Cold Pool Detection and Tracking Algorithm.

CP Convective Cold Pool.

EL Equilibrium Level.

EOS Earth Observing System.

ESA European Space Agency.

ETM+ Enhanced Thematic Mapper Plus.

EUMETSAT European Organisation for the Exploitation of Meteorological Satellites.

FCN Fully Convolutional Neural Network.

GEO Geostationary.

GOES Geostationary Operational Environmental Satellite.

HRV High-Resolution Visible.

IR Infrared.

LCL Lifting Condensation Level.

LFC Level of Free Convection.

MCS Mesoscale Convective System.

MJO Madden-Julian Oscillation.

ML Machine Learning.

MLP Multilayer Perceptron.

MODIS Moderate Resolution Imaging Spectroradiometer.

MSG Meteosat Second Generation.

MSI Multi-Spectral Imager.

MTG Meteosat Third Generation.

NASA National Aeronautics and Space Administration.

NOAA National Oceanic and Atmospheric Administration.

RF Random Forest.

SEVIRI Spinning Enhanced Visible and Infrared Imager.

SVM Support Vector Machine.

UTC Coordinated Universal Time.

VIIRS Visible Infrared Imaging Radiometer Suite.

Chapter 1

Introduction

High-impact weather events, such as extreme rainfall, are often associated with organized convective systems (Biagioli & Tompkins, 2023). Due to global warming, the frequency and intensity of these events have risen over recent decades (De Paola et al., 2014; Klein et al., 2021; H. Lee et al., 2023; Taylor et al., 2017, 2018) and are projected to continue increasing in the 21st century (Taylor et al., 2017). Despite the significant socio-economic consequences associated with such extreme events, the underlying dynamics, especially the mesoscale dynamics of thunderstorm outflows and their role in convective organization, are not yet fully understood.

Over the last decades, numerous studies, primarily relying on idealized simulations, have helped disentangle the involved mechanisms and have confirmed the importance of thunderstorm outflows — often referred to as "convective cold pools" (CPs) — in organizing and initiating convection (Böing, 2016; Droegemeier & Wilhelmson, 1985; Feng et al., 2015; Haerter et al., 2019; Jeevanjee & Romps, 2015; B. Meyer & Haerter, 2020; Moncrieff & Liu, 1999; Moseley et al., 2016; Schlemmer & Hohenegger, 2014; Tompkins, 2001; Weisman et al., 1988). However, even in idealized simulations, where all relevant diagnostic variables are available across the entire simulation domain at high-resolution, discerning the causal chains of convective events proves challenging. A fundamental challenge in establishing meaningful connections between convective events lies in accurately tracking CP gust fronts throughout multiple stages of their life cycle, despite their evolving characteristics. Furthermore, idealized simulation studies often lack observational benchmarks, primarily due to the limited availability of relevant high-resolution data. This lack of benchmark observations is particularly pronounced for tropical continents, although organized convective systems contribute substantially to the annual precipitation in these regions (Fink et al., 2006; Laurent et al., 1998; Maranan et al., 2018; Mathon & Laurent, 2001; Mathon et al., 2002) and play a significant role in natural disasters, such as intense flooding events (Atiah et al., 2023; De Paola et al., 2014).

Usually, the identification of CP gust fronts from observations involves screening near-surface time series of relevant meteorological variables (de Szoeke et al., 2017; Emmel et al., 2010; Kirsch et al., 2021; Kruse et al., 2022; Redl et al., 2015; Vogel et al., 2021; Zuidema et al., 2017) or manually inspecting radar images (Borque et al., 2020; Brandes, 1977; Engerer et al., 2008; Wakimoto, 1982). However, due to the limited availability of such data, particularly over tropical continents, neither of these approaches is suitable for global-scale investigations into continental CPs and their impact on convective organization. Currently, only satellite data offers the potential for such global-scale investigations.

Recent studies have highlighted the capability of satellite data for detecting CPs (Caton Harrison et al., 2021; Garg et al., 2020). Yet, the proposed methods rely on outflow signatures confined to arid regions (Caton Harrison et al., 2021) or oceans (Garg et al., 2020), making them inapplicable over tropical continents. To achieve global-scale detection of CPs over tropical continents, it is necessary to identify and utilize alternative space-borne signatures.

1.1 Objectives

As mentioned before, the mesoscale dynamics of CPs and their role in convective organization are not yet fully understood. To enhance our comprehension of the underlying mechanisms, new approaches for detecting and tracking CPs are required. Of particular importance are space-borne approaches applicable over tropical continents.

Accordingly, the first goal of the present thesis is to explore the space-borne patterns associated with CPs and identify a detectable signature. Due to their relatively high spatio-temporal resolution and independence from solar reflections, the present thesis focuses on brightness temperatures from geostationary satellites.

The second goal of this thesis is to devise an approach for detecting CPs in satellite-observable data, leveraging the identified signature. For a given scene, the desired output is a binary image where each pixel is either black if it belongs to a CP, or white if it does not, enabling the subsequent tracking of spatio-temporal relationships among convective events.

The subsequent chapters of this thesis are structured to provide an understanding of key elements pertinent to this PhD project. Chapter 2 delves into the fundamentals of atmospheric convection and convective organization, with a particular focus on the role of cold pools and their signatures in observational data. Chapter 3 presents an introduction to satellite observations in the context of earth observation. Chapter 4 offers an overview of image segmentation methods and their applications in earth observation, particularly in atmospheric science, with a special emphasis on artificial neural networks due to their significance for the present thesis. Chapter 5 is dedicated to the pre-

sentation of the manuscripts authored by the PhD candidate, showcasing the culmination of the research efforts. Finally, Chapter 6 encapsulates the conclusions drawn from the PhD project, featuring key findings, their discussion, and outlining future perspectives.

Chapter 2

Convection and Convective Organization

Most concepts addressed in this thesis, such as CPs, are linked with the broader topic of convection and its organization, which will be discussed in more detail in the following chapter. In this thesis, "convection" specifically refers to atmospheric convection, given its focus on atmospheric phenomena.

In atmospheric science, convection refers to the vertical movement of air caused by force imbalances (Markowski & Richardson, 2010). To highlight relevant forces, the vertical momentum equation for an inviscid fluid

$$\frac{dw}{dt} = -\frac{1}{\rho}\frac{\partial p}{\partial z} - g\,, \tag{2.1}$$

where w represents the vertical velocity component, ρ denotes air density, p is pressure and g is the gravitational acceleration, can be rewritten as (Markowski, 2007)

$$\frac{dw}{dt} = -\frac{1}{\rho}\frac{\partial p'}{\partial z} - B, \tag{2.2}$$

where primes indicate deviations from a hydrostatic reference state. The first term on the right hand side, $-\frac{1}{\rho}\frac{\partial p'}{\partial z}$, denotes the vertical perturbation pressure gradient force, while B represents the buoyancy force

$$B = -g\frac{\rho'}{\rho}\,. \tag{2.3}$$

A parcel of air less dense than its environment experiences a positive buoyancy force which gives rise to a vertical ascent unless it is compensated by other forces. Based on this vertical movement, convection drives the fluid toward a stable configuration in which it is neutrally stratified again (Stevens, 2005). This buoyancy-driven type of convection is sometimes referred to as "free convection," contrasting with vertical fluid flows driven by dynamic perturbation pressure gradients, known as "forced convection" (Markowski & Richardson, 2010).

2.1 Parcel Theory

A straightforward approach to assess the static stability of an observed stratification is the parcel theory. By assuming that the density of an imagined parcel without dimensions is unaffected by pressure perturbations, water vapor, and liquid water (Markowski & Richardson, 2010), Eq. 2.2 reduces to

$$\frac{dw}{dt} = B\,, \tag{2.4}$$

and Eq. 2.3 becomes

$$B = g\frac{T - \overline{T}}{\overline{T}}\,, \tag{2.5}$$

where T represents the air temperature of the parcel and $\overline{T}$ is the environmental air temperature.

To assess the static stability of an air layer in an observed atmospheric temperature profile, the associated rate at which the temperature decreases with altitude, known as the "lapse rate," can be compared against the lapse rate $\Gamma_p \equiv \partial_z T$ an air parcel would have if lifted adiabatically. For sub-saturated (dry) air, Γ_p equals the dry adiabatic lapse rate, Γ_d, given by (Markowski & Richardson, 2010)

$$\Gamma_d \equiv -\frac{\partial T}{\partial z} = \frac{g}{c_p} \approx 9.8\,\mathrm{K\ km^{-1}}\,, \tag{2.6}$$

where c_p is the specific heat at constant pressure. For saturated (moist) air, Γ_p equals the moist adiabatic lapse rate, Γ_m, which is smaller than Γ_d due to the latent heat associated with condensing water vapor. The level at which the air parcel becomes fully saturated, i.e., the level at which the parcel lapse rate changes from Γ_d to Γ_m, is referred to as the lifting condensation level (LCL). An observed environmental lapse rate, γ, can be considered stable with respect to infinitesimal vertical displacements if $\gamma < \Gamma_p$ and unstable if $\gamma > \Gamma_p$.

Apart from comparing the local environmental lapse rate γ to Γ_p, the stability of an observed atmospheric temperature profile can be assessed by determining the convective available potential energy (CAPE) and the convective inhibition (CIN) as

$$\mathrm{CAPE} = \int_{\mathrm{LFC}}^{\mathrm{EL}} B\,dz\,, \tag{2.7}$$

$$\mathrm{CIN} = -\int_{0}^{\mathrm{LFC}} B\,dz\,, \tag{2.8}$$

where LFC denotes the level of free convection, after which the parcel becomes buoyant and ascends vertically, and EL is the equilibrium level at which the parcel is no longer buoyant. While CAPE represents the potential energy that

is released and converted to kinetic energy during the ascent of the parcel from the LFC to the EL, CIN represents the work required to initially lift the parcel from the surface ($z = 0$) to the LFC (Markowski & Richardson, 2010). It can be shown (Markowski, 2007) that the maximum updraft velocity is linked to CAPE by

$$w_{max} = \sqrt{2\,\mathrm{CAPE}}\,. \tag{2.9}$$

Due to the assumptions involved, w_{max} can be considered an upper limit for free convection, sometimes referred to as the "thermodynamic speed limit" (Markowski, 2007). Large CAPE values $\gtrsim 2500\,\mathrm{J\ kg^{-1}}$ are often associated with severe storms (Markowski & Richardson, 2010).

Fig. 2.1 visualizes an example of a convective event observed in Niamey, Niger (magenta marker in Fig. 2.1a) on May 21, 2023. At 00:00 UTC, the sounding (Fig. 2.1b) featured a large CIN of $273\,\mathrm{J\ kg^{-1}}$ and the corresponding satellite-derived $10.8\,\mu$m brightness temperatures (Fig. 2.1c) confirm that mainly stratiform clouds were present, indicative of stable conditions. However, after sunrise, the 2-m air temperature increased due to solar radiation (Fig. 2.1g), completely eroding CIN by 12:00 UTC, with CAPE almost doubling to $2955\,\mathrm{J\ kg^{-1}}$. The corresponding satellite image reveals that by that time, most of the stratiform clouds have vanished, while the first convective cells started to develop (Fig. 2.1e). Then, after reaching its peak at around 15:00 UTC, the temperature decreased by approximately 8 °C between 16:00 UTC and 19:00 before stabilizing again (Fig. 2.1g). The relatively rapid cooling compared to the second half of the previous day is most likely associated with the evaporation of precipitation from the convective event (labeled "A" in Fig. 2.1f), which formed close to Niamey. Also the second, more rapid temperature drop of 7 °C observed between 03:00 UTC and 04:00 UTC on the subsequent night (Fig. 2.1g) can be attributed to a convective system, in this case, the one labeled "B" in Fig. 2.1f.

2.2 Convective Cold Pools

As observed for the example event presented in the previous section, convective events cool the air when portions of their precipitation evaporate in a sub-saturated sub-cloud layer. Similar to radiative heating, which induces buoyancy and initiates convective updrafts, this cooling process makes the air negatively buoyant. Coupled with the drag of the precipitation, the negative buoyancy causes the air to descend (Byers & Braham, 1949). Upon reaching Earth's surface, such a convective downdrafts is horizontally deflected. The resulting cold outflow is known as a cold dome (Byers & Braham, 1949) or a cold pool (Miller & Betts, 1977). Confusion with radiatively cooled pools of air can be avoided by adding a term such as "convective" or "precipitation-induced", i.e., convective cold pool (CP).

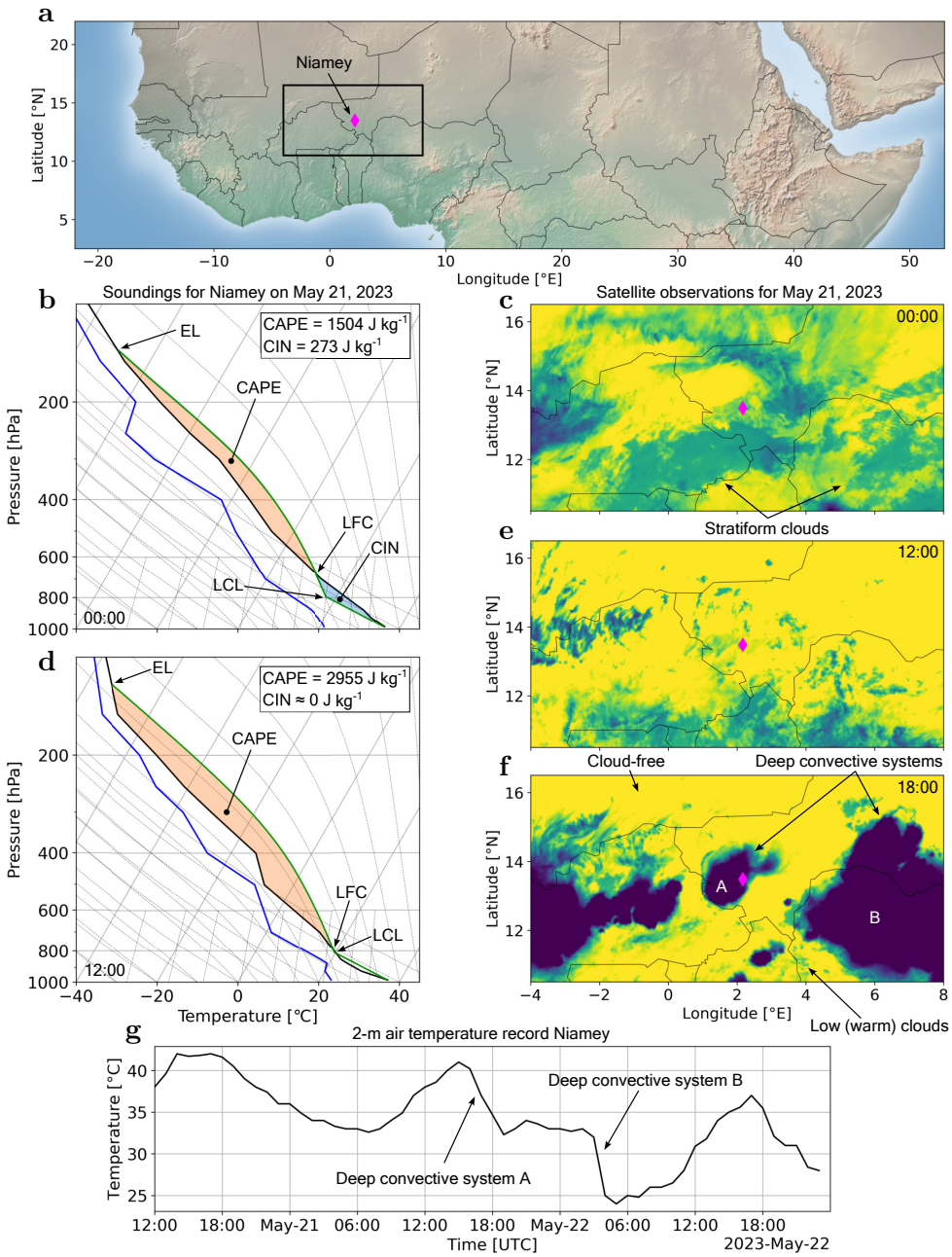

Figure 2.1: Convective event over Niamey, Niger. **a**, Map of Africa indicating the location of Niamey and the region of interest (black rectangle). **b**, Sounding from Niamey on May 21, 2023, at 00:00 UTC. Profiles for dewpoint temperature (blue), temperature (black), and temperature of adiabatic parcel ascent (green) are shown. CAPE and CIN values from NOAA (2024) are indicated in the upper right corner. Dewpoint temperature and temperature data from University of Wyoming (2024). **c**, Satellite-derived 10.8 μm brightness temperatures (see Section 3 for definition) for the region of interest on May 21, 2023, at 00:00 UTC; computed from Meteosat Second Generation 0° effective radiances, provided by EUMETSAT. **d**–**e**, analogous to (b) and (c) but for 12:00 UTC. **f**, analogous to (c) but for 18:00 UTC. **g**, Hourly 2-m air temperatures for Niamey from May 20 to May 22, 2023; data from Meteostat (2024).

Driven by horizontal pressure gradients, the cold outflow behaves as a density or gravity current and intrudes into the warmer ambient air (Charba, 1974; Goff, 1976; Mueller & Carbone, 1987; J. E. Simpson, 1969; Wakimoto, 1982) (Fig. 2.2). Similar to density currents, fully developed (mature) CPs feature a head, which can reach several kilometers in height, and a smaller body behind it (Charba, 1974; Mahoney, 1988). The CP head is associated with peak wind gusts (Charba, 1974) and followed by a turbulent wake (Shapiro et al., 1985) resulting from backward-propagating Kelvin-Helmholtz instabilities at its top (Mueller & Carbone, 1987). The leading edge of the CP is usually referred to as the gust front due to the strong wind gusts associated with it (Charba, 1974).

The collision of the gust front with ambient air causes a nonhydrostatic pressure rise ahead of it (Wakimoto, 1982), forcing the ambient air to ascend, often generating updrafts exceeding $6\,\mathrm{m\ s^{-1}}$ (Goff, 1976). In the formative stage, when the CP gust front is still close to the convective core of its parent thunderstorm, triggered updrafts can support the updraft fueling the parent system (Goff, 1976). As soon as the CP gust front has traveled away from the convective core, the triggered updraft is no longer coupled to the parent system but creates a secondary updraft. Depending on the properties of the CP as well as the environmental conditions, such an updraft can overcome an existing CIN and trigger new convection (Addis et al., 1984; Droegemeier & Wilhelmson, 1985; Shapiro et al., 1985). As the CP matures and loses momentum, the velocity of the triggered updraft tends to decrease (Goff, 1976). Upon dissipation of the parent system, the CP enters its final stage, where it is no longer supplied with cold air. For cylindrical CPs, Romps and Jeevanjee (2016) analytically derived that the maximum CP radius is relatively insensitive to its initial conditions, typically reaching around 14 times its initial radius, while its duration can vary over multiple orders of magnitude.

2.2.1 The Role of Cold Pools in Convective Organization

In general, self-organization is the result of local interactions between many elements, or constituents, of a complex system (Christensen & Moloney, 2005), transferring its state from disordered to ordered spontaneously. Self-organization can be observed in systems of various scientific disciplines and is often conceptually structured in terms of distinct "universality classes". Such concepts have been translated to studies of Earth's atmosphere (Peters & Neelin, 2006; Yano et al., 2012). With respect to the organization of convective clouds, self-organization, has been suggested to be involved in phenomena, such as the formation and intensification of mesoscale convective systems (MCSs) and tropical cyclones (Muller & Romps, 2018; Nolan et al., 2007; Parker, 2021; Parker et al., 2020), as well as the Madden-Julian Oscillation (MJO) (Arnold & Randall, 2015; Bretherton et al., 2005).

CPs are well-established triggers and organizers of convection (Addis et

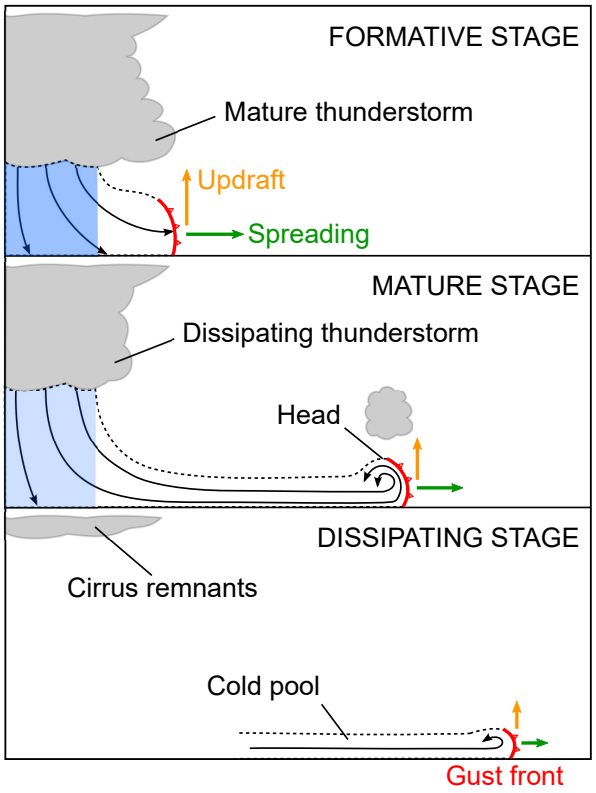

Figure 2.2: Schematic diagram illustrating the life cycle stages of a convective cold pool. Created based on figures from Charba (1974), Goff (1976), and Wakimoto (1982).

al., 1984; Byers & Braham, 1949; Feng et al., 2015; Goff, 1976; Haerter et al., 2020; Shapiro et al., 1985; Tompkins, 2001). While early research focused on mechanical lifting at the CP gust front as the primary triggering mechanism (dynamic effect; see previous section), Tompkins (2001) proposed that the high water vapor content at the CP gust front makes this region favorable for convection by eliminating CIN (thermodynamic effect). Since then, several studies have examined the contributions of the dynamic and the thermodynamic effect to initiating convection (Feng et al., 2015; Fuglestvedt & Haerter, 2020; Jeevanjee & Romps, 2015; Torri et al., 2015). Although neither effect appears dominant (Fuglestvedt & Haerter, 2020; Torri et al., 2015), mechanical lifting plays a crucial role in triggering boundary layer mass flux, necessary for convection initiation (Jeevanjee & Romps, 2015). However, buoyancy from the moist anomaly reduces CIN and assists in reaching the LFC (Torri et al., 2015). In this regard, Droegemeier and Wilhelmson (1985) demonstrated that CPs trigger more rapid and intense convection in regions with high low-level moisture content, while the convection remains shallow in drier regions.

Tompkins (2001) assumed that the high moisture content at the CP gust front primarily arises from evaporating precipitation. While rain evaporation does seem to contribute to the excess moisture at the CP gust front compared to its surroundings (Torri & Kuang, 2016), recent studies have emphasized the

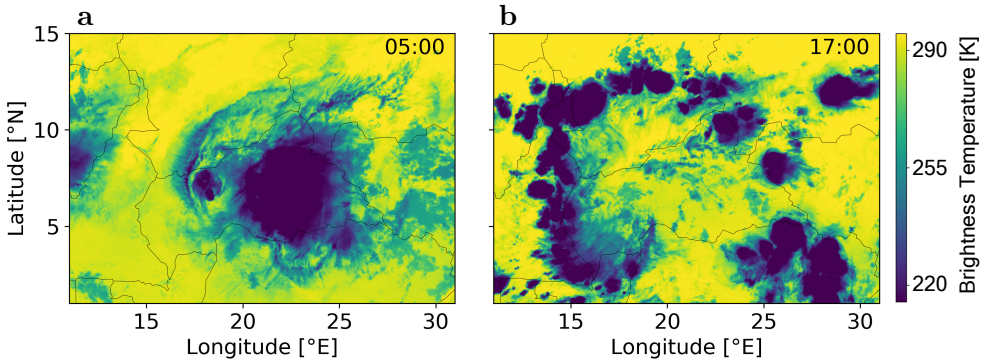

Figure 2.3: **a**, Satellite-derived 10.8 μm brightness temperatures (see Section 3 for definition) over tropical Africa on May 3, 2022, at 05:00 UTC; computed from Meteosat Second Generation 0° effective radiances, provided by EUMETSAT. The dark blue region in the center represents a large dissipating convective system. **b**, Similar to (a) but for 17:00 UTC. The large convective system has dissipated, and new convective cells have developed at its boundary, most likely due to the accumulated moisture.

roles of surface fluxes (Langhans & Romps, 2015; Torri & Kuang, 2016) and moisture advection (Chandra et al., 2018; Schlemmer & Hohenegger, 2016) in elevating moisture levels. Moisture advection, where CP gust fronts accumulate moisture as they spread, appears to be the most significant contributor over both ocean and land surfaces (Schlemmer & Hohenegger, 2016), particularly since deep convection typically develops in moist environments (Langhans & Romps, 2015). The resulting accumulation of moisture at CP boundaries extends from the surface throughout the boundary layer (Schlemmer & Hohenegger, 2014). New convection tends to predominantly develop in such regions of high low-level moisture or "moist patches" (Kurowski et al., 2018; Schlemmer & Hohenegger, 2014; Wilson & Schreiber, 1986) (Fig. 2.3).

The accumulation of moisture is particularly pronounced during CP collisions, where low-level moisture from a larger area is drawn into the convergence zone along the stationary collision line (Fuglestvedt & Haerter, 2020). In combination with enhanced updraft velocities (Feng et al., 2015; B. Meyer & Haerter, 2020) and reduced entrainment drying due to cloud clustering (Feng et al., 2015; Kurowski et al., 2018), colliding CPs trigger more and deeper convection compared to isolated CPs (Feng et al., 2015; Wilson & Schreiber, 1986). Due to mass continuity, triggered updrafts develop before the actual collision of the CP gust fronts and intensify until the collision occurs (Droegemeier & Wilhelmson, 1985; Wilson & Schreiber, 1986). For the southeastern United States, Purdom and Marcus (1981) found that 73% of approximately 10,000 observed afternoon thunderstorms developed from colliding CPs. Moreover, several cases of tornado formation along CP collision

lines have been documented (Holle & Maier, 1980; Weaver & Nelson, 1982; Wilson & Schreiber, 1986).

Simulations have demonstrated that artificially suppressing CPs can reduce or even suppress deep clouds and heavy rainfall (Böing et al., 2012; Khairoutdinov & Randall, 2006). By influencing the moisture distribution, including the size and anomaly of moist patches, and generating updrafts, CPs play a crucial role in transitioning from shallow to deep convection (Böing et al., 2012; Khairoutdinov & Randall, 2006; Kurowski et al., 2018; Schlemmer & Hohenegger, 2014). Additionally, CPs initiate a positive feedback loop: stronger CPs lead to deeper convection and heavier precipitation, subsequently generating more intense downdrafts and stronger CPs (Böing et al., 2012; Schlemmer & Hohenegger, 2014). Regarding the contribution of moist patches, Schlemmer and Hohenegger (2014) argued that the size of the moist patch, which reduces the entrainment of environmental air experienced by the updraft, appears more influential than the moisture anomaly itself.

2.2.2 Cold Pool Signatures in Observational Data

In near-surface time series, CP gust fronts are typically characterized by a rapid drop in temperature and increases in wind speed (Kruse et al., 2022). The drop in temperature is primarily influenced by evaporative cooling; however, Kirsch et al. (2021) demonstrated that the downward transport of upper-level air becomes increasingly significant when CPs are associated with larger drops in equivalent potential temperature. As CPs propagate, the temperature drop gradually dissipates due to turbulent mixing and surface fluxes (de Szoeke et al., 2017; Grant & van den Heever, 2016). Surface characteristics strongly influence these fluxes, with enhanced surface fluxes within CPs tending to reduce both CP propagation speed and the occurrence of large CPs (Gentine et al., 2016). Regarding the spatial temperature structure within the CP, recent observations from a dense station network in Germany indicate that the strongest temperature drop is typically measured at the CP center (Kirsch et al., 2023).

The increase in wind speed observed at CP gust fronts stems from the expansion of the CP, as discussed at the beginning of Section 2.2. Often, this increase is preceded by an abrupt change in wind direction (Engerer et al., 2008; Goff, 1976; Provod et al., 2016; Wakimoto, 1982). Due to complex flow patterns and local turbulence, the propagation speed of CPs may not always align with locally measured wind speeds at the gust front (Kruse et al., 2022; Rooney, 2018). Nevertheless, several studies have shown that the movement of CPs can be effectively described by equations governing the propagation speed of density currents when considering local temperature and wind observations (Charba, 1974; Kruse et al., 2022; Mueller & Carbone, 1987; Wakimoto, 1982). However, on a global scale — when considering spatial averages of a CP's

temperature and its radial expansion velocity — this relationship may not hold true (Kirsch et al., 2023).

While consistent signals in near-surface temperature and wind time series are observed across various observational studies, the strength of these signals varies significantly depending on the environmental conditions. Table 2.1 provides a summary of identified CP perturbations from selected observational studies, each based on over 150 CP events. In subtropical and tropical ocean regions, both the observed temperature drops and increases in wind speed tend to be weaker compared to those over land. Temperature drops over the ocean range from 1.2 to 1.8 K, contrasting with 2.9 to 3.3 K over the Netherlands and Northern Germany. The ocean-land difference in observed wind increases is somewhat smaller, with ranges of 1.5 to 3 m s^{-1} over the ocean and 3.6 to 4.4 m s^{-1} over land. However, especially CP properties over land exhibit substantial variability depending on the region and environmental conditions. For instance, the strongest CP events identified by Kirsch et al. (2021) showed near-surface temperature drops of up to $10.8K$ and wind speed increases of up to 11 m s^{-1}. Additionally, Engerer et al. (2008) observed mean temperature drops ranging between 5.4 K and 9.5 K, along with mean wind gusts of at least 15 m s^{-1} for 39 CP events in Oklahoma associated with MCSs. Daytime and early evening observations featured even greater mean temperature drops of 11 K. Moreover, in the Sahel region, specifically in Niamey, Niger, Provod et al. (2016) reported a mean temperature drop of 5.3 K based on 38 identified CP events.

The observed moisture signals over the ocean align with the description in Section 2.2.1, showing an increase in specific humidity at the CP gust front followed by a subsequent decrease in the CP interior (Table 2.1). Over land, however, there is greater variation. While Kirsch et al. (2021) report a median increase in specific humidity of 1 g kg^{-1}, Kruse et al. (2022) observe a decrease in water vapor concentration shortly after the temperature drop begins (no specific value reported). Even within the same location, Provod et al. (2016) notes substantial differences between CP moisture signals: pre-monsoon CPs were associated with persistent increases in specific humidity, while CPs during the monsoon and the subsequent retreat exhibited persistent decreases. Historical observations by Byers and Braham (1949) of 79 CPs over Florida and Ohio indicate an average drop in specific humidity of around 3.3 g kg^{-1}.

Fig.2.4 shows the near-surface time series derived from weather stations for three distinct CP events identified over equatorial Africa as part of this thesis (manuscript I, Section 5.1), accompanied by corresponding satellite-derived infrared (IR) observations. Each of these CP events was detected at two stations, referred to as station 1 and station 2, based on the gust front arrival times at each location. The two satellite images associated with each CP event depict snapshots closest to the station-derived gust front passage. The three examples highlight the diverse near-surface perturbations linked to

Author	Region	#CPs	ΔT [K]	Δu [m s^{-1}]	Δq [g kg^{-1}]
Chandra et al. (2018)	Eq. Indian Ocean	296	-1.5	2	0.25
				1.5	-1
Vogel et al. (2021)	Barbados	3889	-1.2	2.81	0.2
					-0.43
Wills et al. (2021)	Tropical Pacific	382	-1.8	3	0.17
					-0.16
Kirsch et al. (2021)	Northern Germany	489	-3.3	3.6	1
Kruse et al. (2022)	Netherlands	189	-2.9	4.4	n.a.

Table 2.1: Summary of selected observational cold pool (CP) studies with over 150 sampled CP events. The table includes columns for the author and region of each study, the number of CP events considered, as well as observed CP perturbations in near-surface temperature (ΔT), wind speed (Δu), and specific humidity (Δq). Perturbations are presented as mean values for Chandra et al. (2018) and Wills et al. (2021), and median values for all other studies. For Δq, when two values are provided, they represent the mean or median maximum (upper value) and minimum (lower value) Δq, accounting for moister CP gust fronts and drier CP interiors. Note that the two values provided by Chandra et al. (2018) for Δu denote mean perturbations of CPs observed at a research vessel (103 CPs; upper value) and at Gan Island (193 CPs; lower value).

CPs over land, influenced not only by varying environmental conditions but also by the temporal evolution of individual CP events.

Apart from near-surface temperature, wind speed and moisture, also the pressure signal associated with CPs exhibits several notable characteristics. Prior to the passage of the CP gust front, the surface pressure typically begins to rise due to the collision of the CP with ambient air (Charba, 1974; Engerer et al., 2008; Goff, 1976; Wakimoto, 1982). The onset of this pressure increase usually precedes the temperature drop associated with the CP by approximately 15 minutes (Engerer et al., 2008; Goff, 1976; Kirsch et al., 2021). Within the CP itself, there is a zone of high pressure known as the "meso-high" (Engerer et al., 2008). The magnitude of the pressure increase within the CP is primarily driven by the CP's temperature and depth, with colder and deeper CPs giving rise to larger pressure increases (Provod et al., 2016; Wakimoto, 1982). While most CPs are associated with a pressure rise, it is worth noting that some CPs can be linked to pressure decreases, for example due to mesolows (de Szoeke et al., 2017; Engerer et al., 2008; Zipser, 1977).

Weather stations provide localized information, necessitating dense networks like the one utilized by Kirsch et al. (2023) to obtain spatial insights into CPs. Consequently, many studies rely on data from ground-based radars or satellites to either confirm identified CPs or derive additional details (Borque

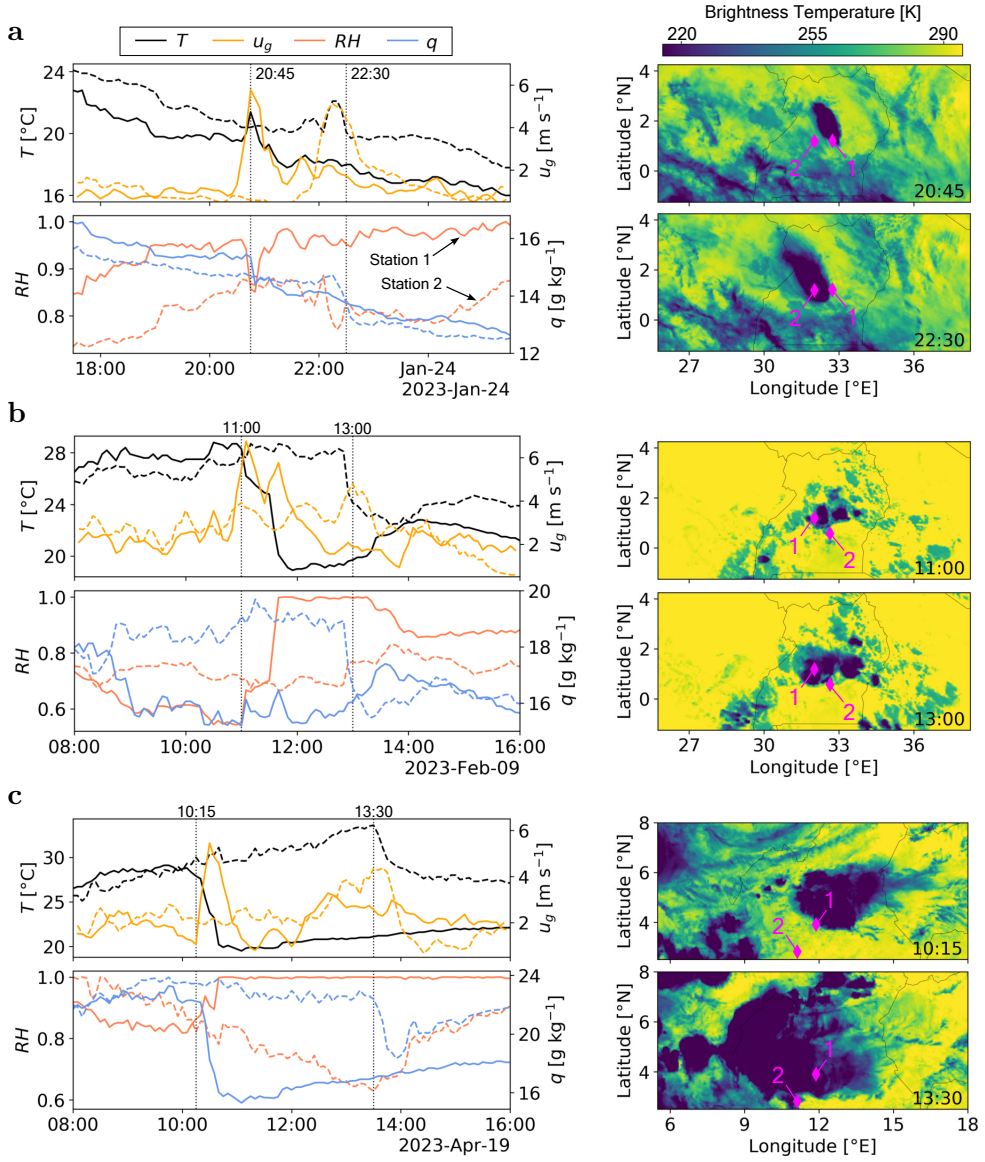

Figure 2.4: Examples of cold pool (CP) passages identified in the study associated with manuscript I (Hoeller et al., 2023). **a**, Time series of near-surface temperature (T), wind gust speed (u_g), relative humidity (RH), and specific humidity (q) recorded at two weather stations during a CP event in Uganda on January 23, 2023 (left panels), along with the two closest satellite snapshots to the station-derived CP passage (right panels); satellite scenes represent 10.8 μm brightness temperatures (see Section 3 for definition), computed from Meteosat Second Generation 0° effective radiances, provided by EUMETSAT; station locations are indicated in the satellite scenes by magenta markers; solid time series correspond to station 1, dashed time series to station 2. **b**, Similar to (a) but for a CP event on February 9, 2023. **c**, Similar to (a) but for a CP event observed in Cameroon on April 19, 2023.

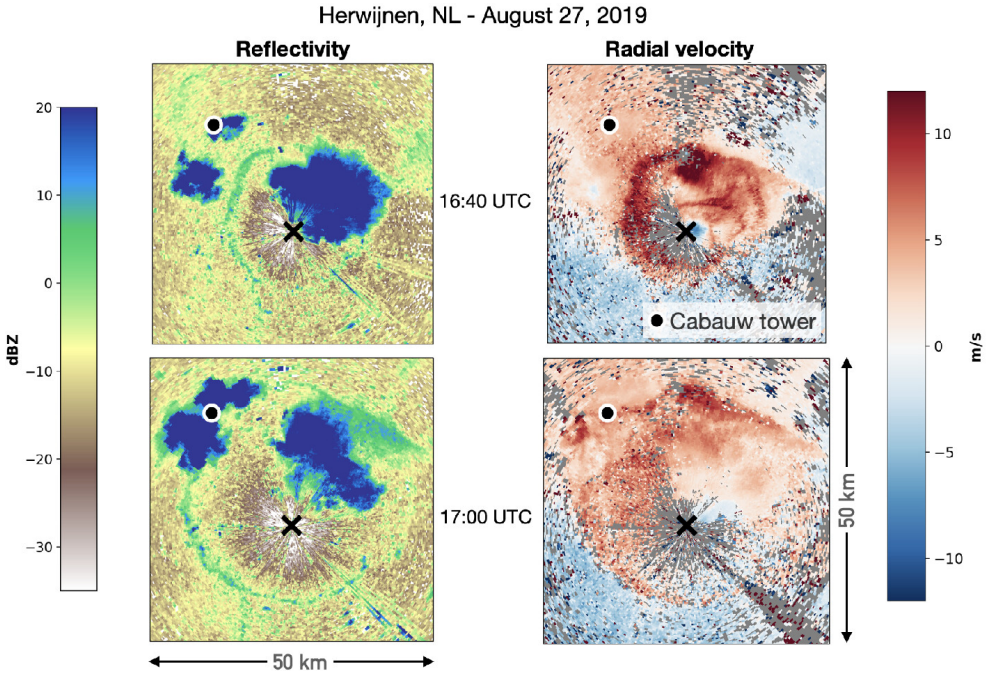

Figure 2.5: Radar observations of a convective cold pool over the Netherlands. Figure adapted from Kruse et al. (2022). Note: The middle panel depicting snapshots at 16:50 UTC has been omitted for simplicity.

et al., 2020; Engerer et al., 2008; Feng et al., 2015; Goff, 1976; Kirsch et al., 2023; Kruse et al., 2022; Provod et al., 2016; Redl et al., 2015; Vogel et al., 2021; Wakimoto, 1982; Wilson & Schreiber, 1986). Fig. 2.5 illustrates a radar-observed CP over the Netherlands. In radar imagery, CPs are often recognizable by the presence of radially spreading thin line echoes, indicative of raindrops, dust, and insects carried with the gust front (Kruse et al., 2022; Wakimoto, 1982), as well as echo-free regions resulting from drier boundary layer air within the CP (Feng et al., 2015).

A comparable CP signature is observable in satellite imagery, where CPs are occasionally accompanied by spreading low-level cloud arcs (Purdom & Marcus, 1981; Rauber et al., 2007; Shapiro et al., 1985; Vogel et al., 2021) (Fig.2.6). Such cloud patterns are linked to convective triggering at the CP gust front, as discussed in Section 2.2.1. At times, CP-associated cloud patterns become apparent only when analyzing a sequence of satellite images rather than a single snapshot, allowing for the utilization of dynamic information associated with the expanding gust front (Shapiro et al., 1985).

However, satellite imagery offers more than just visible cloud patterns. Caton Harrison et al. (2021) discerned CP gust fronts over the Sahara by identifying the dust they stir up, leveraging a combination of different IR

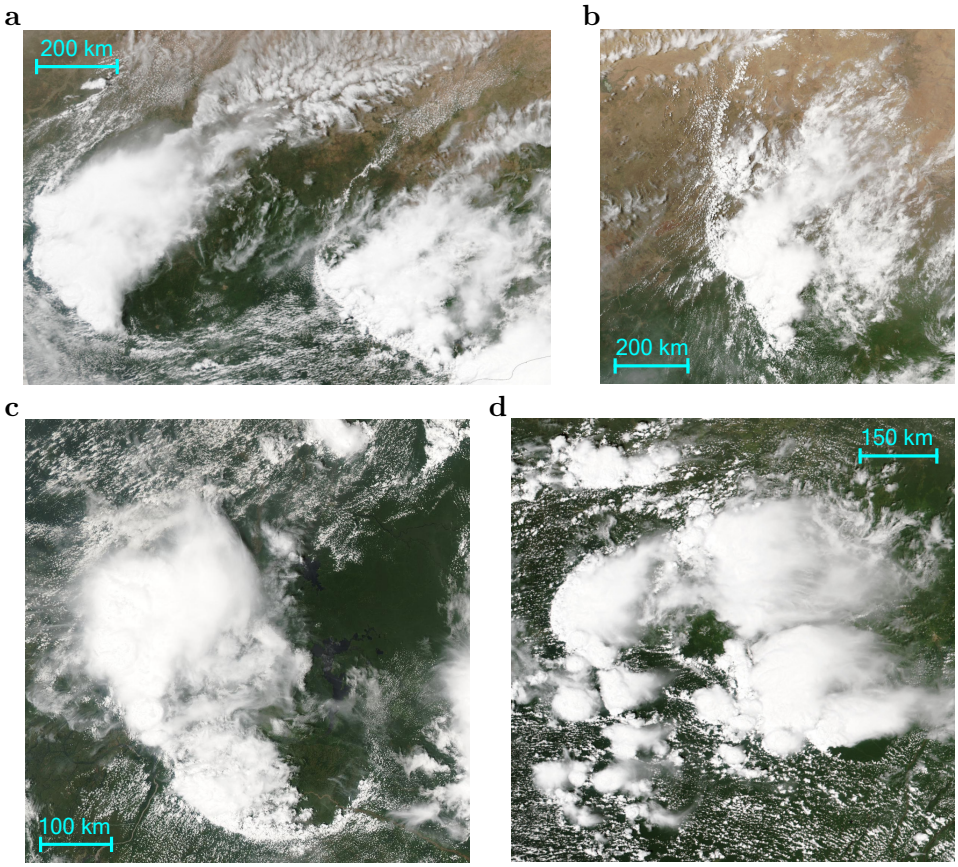

Figure 2.6: True-color satellite imagery depicting cold pools over tropical Africa. **a**, Scene from tropical West Africa, captured by the Visible Infrared Imaging Radiometer Suite (VIIRS) instrument aboard the NOAA-20 satellite on June 3, 2022. **b**, Scene from tropical West Africa, captured by the Moderate Resolution Imaging Spectroradiometer (MODIS) aboard the Aqua satellite on April 28, 2023. **c**, Scene from equatorial Africa, captured by the VIIRS instrument aboard the NOAA-20 satellite on February 6, 2023. **d**, Analogous to (c) but for October 30, 2023. All satellite scenes were retrieved from the NASA Worldview website.

satellite channels sensitive to dust. Meanwhile, Garg et al. (2020) introduced a novel technique to detect CPs using wind gradients derived from space-borne scatterometer wind fields. Yet, this approach is not applicable for CP observations over land, as scatterometers measure the wind field via wave patterns at ocean surfaces.

Chapter 3

Satellite-Based Earth Observation

Satellite observations play a crucial role in numerous earth observation applications, including the monitoring of weather patterns, climate, and environmental changes (Kansakar & Hossain, 2016). Given their potential for the global-scale detection of CPs, they hold significant importance in the context of this thesis. Therefore, this chapter provides a concise introduction to satellite-based earth observation, with a specific emphasis on the utilization of geostationary satellite observations in this thesis.

Most satellite observations used in the field of atmospheric science originate from (near) polar orbiting or geostationary (GEO) satellites. Polar orbiting satellites traverse the Earth from pole to pole, resulting in an inclination of approximately 90° between their orbiting plane and the equatorial plane. With an orbital period of approximately 100 minutes, they make multiple passes over the equator each day, gradually capturing images of the entire planet. Typically orbiting at altitudes of 700–800 km above the surface, polar satellites offer high spatial resolutions, $\sim \mathcal{O}(10\,\mathrm{m})$. Many of them are in sun-synchronous orbits, ensuring that they pass over a specific location at the same time each day to facilitate the monitoring of changes. Examples of (near) polar orbiting, sun-synchronous satellites include the Earth Observing System (EOS) satellites Aqua and Terra, operated by the National Aeronautics and Space Administration (NASA), as well as most of the Sentinel satellites from the Copernicus program of the European Space Agency (ESA).

GEO satellites, in contrast, orbit at an altitude of approximately 35,786 km above the surface to match the Earth's rotational period. This results in a fixed position relative to the Earth's surface, enabling the continuous monitoring of a designated area at relatively high temporal resolutions. Three significant geostationary satellite programs for global earth observation and weather monitoring are the Geostationary Operational Environmental Satellite (GOES) program, operated by the National Oceanic and Atmospheric

Administration (NOAA); the Himawari series, operated by the Japan Meteorological Agency; and the Meteosat program, managed by the European Organisation for the Exploitation of Meteorological Satellites (EUMETSAT). While the GOES satellites cover the Americas and large parts of the Atlantic and Pacific oceans, the Himawari series serves the Asia-Pacific region. The Meteosat satellites provide coverage of Europe, Africa, and the Indian Ocean. Currently, the Meteosat Second Generation (MSG) satellites are operational, but they will soon be replaced with the Meteosat Third Generation (MTG) satellites, which offer similar capabilities to the current GOES and Himawari satellites.

As detecting and tracking CPs requires continuous observations with sub-hourly resolutions (Section 2.2), the present thesis focuses on data from GEO satellites. However, to investigate the CP signature in the satellite data, ground-based observations are needed first to detect reference CPs based on known signatures. For this purpose, automatic weather stations in equatorial Africa were used (manuscript I, Section 5.1). Accordingly, the present thesis relies mainly on imagery captured by the MSG Spinning Enhanced Visible and Infrared Imager (SEVIRI) (Aminou, 2002), a passive sensor which measures the electromagnetic energy emitted or reflected by the observed scene. In total, SEVIRI offers 12 spectral channels spanning the visible, near-IR, and IR spectrum, with a temporal resolution of 15 minutes. The spatial resolution at the sub-satellite point is 3 km for all channels, except for one high-resolution visible (HRV) channel with a resolution of 1 km.

For applications such as cloud segmentation or rainfall estimation, combining satellite channels from both the visible and IR spectrum has proven beneficial (Ackerman et al., 1998; Ameur et al., 2004; Drönner et al., 2018; Kühnlein et al., 2014; Saunders & Kriebel, 1988). However, since visible channels measure reflected sunlight, such approaches work only for daytime applications and require different strategies for nighttime observations. For this reason, the present thesis focuses on IR observations which are independent of reflected sunlight.

For better interpretation, the IR radiances measured by satellites are typically converted into equivalent brightness temperatures. This is accomplished by applying the Planck function, which relates the radiance emitted by an object to its temperature, incorporating sensor-specific regression coefficients. MSG radiances can be converted to brightness temperatures using Equation 5.3 and the corresponding regression coefficients from Tables 7.2–7.5 provided by EUMETSAT (2012).

Chapter 4

Image Segmentation

Satellite images contain a wealth of information about the Earth's surface, atmosphere, and dynamic processes. Computer vision techniques, encompassing tasks such as classification, object detection, and image segmentation, serve as indispensable tools to extract meaningful insights from these vast data sets (Asokan & Anitha, 2019; Ferreira et al., 2020; Li et al., 2020). While classification involves assigning predefined labels to images, object detection identifies and locates specific objects within a scene. Segmentation goes a step further by partitioning an image into distinct regions (Guo et al., 2018).

To reveal the causal chains among convective events and investigate the role of CPs in convective organization, the approach for detecting CPs in space-borne data needs to partition the input images into regions. The desired output of the CP detection method developed as part of this thesis is thus a binary image where each pixel is either black if it belongs to a CP, or white if it does not. In image processing, this kind of task is commonly known as "semantic segmentation" (Guo et al., 2018). The following chapter presents an overview of commonly used image segmentation methods and their applications in earth observation, with a focus on atmospheric science.

4.1 Traditional Segmentation Approaches

Traditional image segmentation approaches can be broadly categorized into three groups, (1) thresholding or clustering, (2) region extraction, and (3) edge detection (Fu & Mui, 1981).

4.1.1 Thresholding and Clustering

Thresholding approaches partition images by establishing global or adaptive intensity or color thresholds. In the simplest scenario, binary segmentation can be achieved by setting pixels with values smaller than a threshold to 0 and those with values equal to or greater than the threshold to 1.

Clustering can be considered as a multidimensional extension of the thresholding concept (Fu & Mui, 1981). Based on feature similarity, the pixels are grouped into distinct clusters. A frequently used clustering method is the k-means algorithm (Lloyd, 1982), an unsupervised technique that divides a data set into k distinct clusters by assigning data points to the cluster with the nearest centroid and iteratively updating centroids based on the mean of the assigned points. Yet, despite its strength in grouping similar data points together, the k-means algorithm suffers from noise and outliers (Gan & Ng, 2017) and, similar to threshold-based approaches, struggles to segment non-linearly separable data (Baranwal & Salapaka, 2018).

An example for the application of thresholding and clustering in the field of earth observation, is the identification and classification of cloud pixels in satellite images. Saunders and Kriebel (1988) proposed threshold-based daytime and nighttime tests to identify pixel in polar orbiting satellite images from Western Europe and the North Atlantic as either cloud-free or cloud-filled. If the tests neither satisfied all conditions for cloud-free, nor for cloud-filled pixels, the pixel was considered partly cloudy. Similar tests have been employed to mask clouds in MODIS images from the Terra and Aqua satellites (Ackerman et al., 1998; Platnick et al., 2003). However, developing such tests requires expert knowledge, and the thresholds are usually tuned to specific scenarios, lacking generalizability beyond those cases. To overcome these shortcomings, Ameur et al. (2004) developed a method to segment clouds in Meteosat images using a k-means algorithm. To utilize spatial cloud patterns rather than absolute values for the segmentation, Ameur et al. (2004) applied the k-means algorithm to textural parameters which they calculated based on both visible and IR images.

Due to the simplicity and physical interpretation, thresholding and clustering approaches have also been used to identify simulated CPs or their associated rain patches (Drager & van den Heever, 2017; Feng et al., 2015; Fournier & Haerter, 2019; Gentine et al., 2016; Henneberg et al., 2020; Tompkins, 2001). For this purpose, the approaches usually rely on negative buoyancy anomalies or related quantities, since the air inside CPs is cooler and generally drier than the surrounding environmental air (Section 2.2.2). However, the absence of relevant high-resolution observational data restricts the application of thresholding- or clustering-based segmentation approaches for CPs to simulations. While Tompkins (2001) and Feng et al. (2015) used fixed buoyancy thresholds of $-0.005\,\mathrm{m^2 s^{-1}}$ and $-0.003\ \mathrm{m^2 s^{-1}}$ to segment CPs in simulations, Gentine et al. (2016) applied a k-means algorithm to the lowest model level virtual potential temperature field to classify each pixel as either CP or environment. Similarly, the k-means algorithm was utilized in manuscript II (Section 5.2) as a component of the CP detection and tracking algorithm (CoolDeTA) for simulation data, which was eventually employed to derive ground truth labels for supervised learning (manuscript III; Section 5.3). Rain patches associated with simulated CPs are typically segmented by applying

a rainfall intensity threshold of 1 mmh^{-1} in combination with a minimum rain patch area (Drager & van den Heever, 2017; Fournier & Haerter, 2019; Henneberg et al., 2020).

4.1.2 Region Extraction

Region-based segmentation approaches focus on grouping pixels into regions with shared properties and can be subdivided into region merging, region splitting, and a combination of both (Fu & Mui, 1981). Region merging initially treats individual pixels as separate regions. By iteratively merging neighboring regions with similar characteristics, the regions are expanded until cohesive regions are formed. Region splitting takes the opposite direction, starting with the entire image as one region. Based on certain criteria, this region is divided into smaller sub-regions. The process is repeated for each sub-region until the desired level of similarity is achieved. An early review of region growing approaches was presented by Zucker (1976).

A popular region-based approach is the watershed algorithm (Vincent & Soille, 1991), originally introduced in image processing by Digabel and Lantuéjoul (1978) and Lantuéjoul (1978). The watershed algorithm treats pixels as elevations and separates regions based on their topography in the resulting intensity landscape. The boundaries between different regions represent the watershed lines. They are typically determined by gradually flooding the topographic landscape from the points with the lowest elevation or minima (Vincent & Soille, 1991), or by modeling the process of raindrops falling onto the topographic landscape and following the steepest path down to the next valley or minimum (Bieniek & Moga, 2000; Kornilov & Safonov, 2018).

By applying the watershed algorithm to the result of a binary masking, it can also be used to further subdivide contiguous patches of ones. Similar to the approach by Gentine et al. (2016), CoolDeTA relies on the watershed algorithm to differentiate individual CP instances in cloud-resolving simulation output. In this case, the intensity landscape is calculated using near-surface fields of temperature, specific humidity, and vertical wind speed.

4.1.3 Edge Detection

Edge-based segmentation approaches identify distinct regions by detecting the boundaries between them. To detect these boundaries, they rely on intensity gradients, leveraging the fact that intensity changes in an image usually correspond to region boundaries (Yu et al., 2023). However, a significant drawback of edge-based segmentation approaches is their limited robustness, as gaps in detected edges due to noise or small intensity gradients can hinder the segmentation of enclosed regions (Fu & Mui, 1981; Yu et al., 2023).

4.2 Classical Machine Learning-Based Approaches

In contrast to most of the traditional segmentation techniques discussed so far, classical machine learning (ML) methods, such as support vector machines (SVMs) (Cortes & Vapnik, 1995) and random forests (RFs) (Breiman, 2001), can handle more complex relationships and have thus been suggested for many image processing tasks in remote sensing — for comprehensive reviews see Mountrakis et al. (2011) and Belgiu and Drăguţ (2016). Both SVMs and RFs are supervised learning techniques and require labeled data sets to learn how to map input features to target labels.

SVMs are designed to identify the optimal hyperplane that separates data points belonging to different classes in feature space (Cortes & Vapnik, 1995). The hyperplane is selected to maximize the margin, which represents the distance between the hyperplane and the closest data points, known as support vectors, from each class (Sehad et al., 2017).

RFs are ensembles of decision tree classifiers (Quinlan, 1986). Decision trees exhibit tree-like structures composed of nodes and branches. Whereas the internal nodes in a decision tree represent decisions based on specific feature values, the leaf nodes denote the predictions or classifications of the decision tree. The branches connect the nodes based on the decision outcomes at internal nodes. The final RF output is typically determined using a rule-based approach, e.g., by selecting the decision tree output with the highest number of occurrences among all decision trees (Rodriguez-Galiano et al., 2012). Considering an ensemble of decision trees, as opposed to an individual tree, has been shown to decrease the variance of the final output (Gislason et al., 2006) and increase the robustness with respect to noise (Rodriguez-Galiano et al., 2012).

With regard to cloud detection, Y. Lee et al. (2004) employed multicategory SVMs to classify pixels in simulated and observed MODIS images over an ocean surface as cloud-free, water cloud, or ice cloud. They found that SVMs offer advantages over the existing threshold-based MODIS cloud masking algorithms. Hollstein et al. (2016) compared decision tree classifiers with a classical Bayesian method, as well as other techniques such as RFs and SVMs for a similar task but with more classification categories using input Sentinel-2 Multi-Spectral Imager (MSI) scenes. They discovered that the classical Bayesian method, RFs and SVMs achieved comparably high skills, outperforming individual decision trees.

Kühnlein et al. (2014) and Sehad et al. (2017) developed similar pixel-based segmentation approaches to estimate rainfall from MSG SEVIRI imagery. Kühnlein et al. (2014) proposed a three-step process for the retrieval of rainfall rates, with each step associated with a different RF model. In the first two steps, the RF models served as binary classifiers to identify precipitating cloud areas and distinguish between convective and convective-stratiform cloud regions. In the final step, they evaluated rainfall rates using a regression

RF model. On the other hand, Sehad et al. (2017) estimated the 3-hourly and daily accumulated rainfall using two SVMs, one for daytime and one for nighttime estimations. To train and test the models, both Kühnlein et al. (2014) and Sehad et al. (2017) utilized ground-based radar observations. Sehad et al. (2017) further validated their results by comparing them with measurements from a rain gauge network.

Another prominent segmentation task in Earth observation is land cover monitoring (Rodriguez-Galiano et al., 2012). While Gislason et al. (2006) used a RF approach to differentiate between nine forest classes and water in a mountainous area in Colorado, United States, Rodriguez-Galiano et al. (2012) applied their RF model to observations from Granada, Spain, distinguishing 14 thematically different categories. As Hollstein et al. (2016), both Gislason et al. (2006) and Rodriguez-Galiano et al. (2012) found that their RF model outperforms an individual decision tree classifier. Kavzoglu and Colkesen (2009) trained SVMs for pixelwise land cover classification in Landsat Enhanced Thematic Mapper Plus (ETM+) and Terra Advanced Spaceborne Thermal Emission and Reflection Radiometer (ASTER) images recorded over a district in Turkey.

4.3 Artificial Neural Networks

In image segmentation, context information is often crucial for accurately classifying a pixel. For instance, when looking at an image snippet it is generally not possible to determine the object to which a pixel belongs without context information. Also segmentation tasks in Earth observation, such as the pixelwise classification of clouds, benefit from textural information (Giannakos & Feidas, 2013; Gu et al., 1989). Traditional segmentation approaches, as well as SVMs and RFs, can indirectly leverage textural information by providing calculated textural properties as input. However, the success in this scenario heavily relies on the selection of appropriate textural input features, and unexplored features will remain unutilized.

Artificial neural networks (ANNs) can capture context information and model complex nonlinear relationships. Inspired by the structure and functioning of the human brain (Rosenblatt, 1958), ANNs constitute a category of ML models organized into interconnected nodes across layers.

4.3.1 Multilayer Perceptrons

A common type of ANN is the multilayer perceptron (MLP). It comprises an input layer, at least one hidden layer, and an output layer (Fig. 4.1). MLPs are fully connected ANNs, implying that each node links to all nodes in the adjacent layers.

Forward propagation. During the forward propagation, inputs are passed through the neural network to generate the outputs. The input layer receives

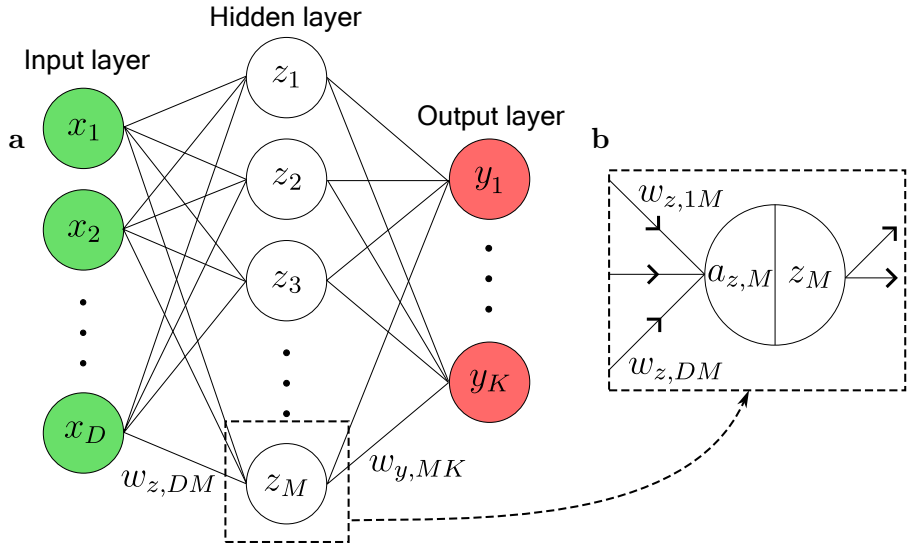

Figure 4.1: Architecture of a multilayer perceptron (MLP). **a**, MLP consisting of an input layer, a hidden layer, and an output layer. Nodes symbolize neurons; text inside nodes indicates each node's output signal. Each connection line is associated with a network weight. **b**, Schematic of the input and output signals of hidden layer node M. While the node input $a_{z,M}$ is computed as the weighted sum of the connected inputs $x_1, \ldots, x_D$, the node output z_M is derived based on an activation function $f(\cdot)$ as $z_M = f(a_{z,M})$.

the input variables $x_1, \ldots, x_D$ and forwards them to the connected nodes of the hidden layer. The connections between the nodes are associated with tunable weights, $w_{z,ij}$. While the subscript z indicates the connected layer, the subscripts i and j denote the indices of that link's start and end node (Fig. 4.1). The input $a_{z,j}$ to a hidden layer node j is computed as

$$a_{z,j} = \sum_{i=1}^{D} w_{z,ij} x_i \,, \tag{4.1}$$

where $i = 1, \ldots, D$ denotes the indices of the connected input layer nodes. The node inputs **a** are also referred to as "activations" (Bishop, 2006). To enable the network to learn nonlinear relationships, the activations are typically transformed with a nonlinear activation function $f(\cdot)$ before passing to the next layer. The corresponding output z_j of a hidden layer node j can thus be expressed as

$$z_j = f(a_{z,j}) \,. \tag{4.2}$$

Using the frequently applied logistic sigmoid function (Bishop, 2006) as acti-

vation function, z_j is computed as

$$z_j = \frac{1}{1 + e^{-a_{z,j}}} \,. \tag{4.3}$$

For networks with multiple hidden layers, the previous steps are repeated for each hidden layer. In this case, the hidden layer outputs $\mathbf{z}^l$ of a layer l are passed to the next layer $l + 1$, to compute the outputs $\mathbf{z}^{l+1}$.

In the final output layer, the activation $a_{y,k}$ of a node k is analogously calculated as

$$a_{y,k} = \sum_{j=1}^{M} w_{y,jk} z_j \,, \tag{4.4}$$

where $j = 1, \ldots, M$ denotes the indices of the connected hidden layer nodes. However, the final activation function might be adapted to produce the desired output for the given task (Bishop, 2006). For problems with multiple output classes, the logistic sigmoid function is generalized to the so called "softmax" function. For an output layer node k, the softmax function $h(\cdot)$ is written as

$$y_k = h(a_{y,k}) = \frac{e^{a_{y,k}}}{\sum_{n=1}^{K} e^{a_{y,n}}} \,, \tag{4.5}$$

where $n = 1, \ldots, K$ denotes the indices of the output layer nodes.

Combining all the steps, the computation of the output y_k of the sample MLP from Fig. 4.1 can be expressed as

$$y_k(\mathbf{x}, \mathbf{w}) = h\left(\sum_{j=1}^{M} w_{y,jk}\, f\left(\sum_{i=1}^{D} w_{z,ij} x_i\right)\right) \,. \tag{4.6}$$

Backpropagation. Typically, MLPs find application in supervised learning tasks, where the network weights are iteratively adjusted during training to minimize the discrepancy between predicted outputs and actual target values. For this purpose, the network outputs for a specific data sample are compared against the desired outputs, also referred to as the "ground truth." The associated error is then propagated backward from the output layer to the input layer to tune the network weights of each layer based on their contribution to the overall error. This process is commonly known as "backpropagation" (Bishop, 2006).

The total error associated with a network prediction can be expressed as

$$E = \sum_{k=1}^{K} E_k \,, \tag{4.7}$$

where $k = 1, \ldots, K$ denotes the indices of the output layer nodes. The underlying error function, which is applied to evaluate the outputs, depends on

the specific task. Common error functions include mean squared error for regression tasks and cross-entropy loss for classification problems.

Since the error function typically exhibits a highly nonlinear dependence on the weights (Bishop, 2006), a straightforward approach is to iteratively adjust the network weights by moving a small step in the direction of the negative gradient. In this case, the new weight $w^*_{l,jk}$ connecting nodes j and k in layer l can be obtained from the current weight $w_{l,jk}$ as

$$w^*_{l,jk} = w_{l,jk} - l_r \cdot \frac{\partial E}{\partial w_{l,jk}}\,, \tag{4.8}$$

where l_r is a parameter modulating the step size, known as the "learning rate".

The gradient of the total error E with respect to each weight can be calculated using the chain rule. For the weight $w_{y,MK}$ from the final layer of the sample network (Fig. 4.1), the corresponding computation can be expressed as

$$\frac{\partial E}{\partial w_{y,MK}} = \frac{\partial E}{\partial y_K}\frac{\partial y_K}{\partial a_{y,K}}\frac{\partial a_{y,K}}{\partial w_{y,MK}}\,, \tag{4.9}$$

illustrated by the green path in Fig. 4.2. Since $w_{y,MK}$ is only connected to the output y_K, it is solely influenced by the associated error component, E_K.

The weight $w_{z,DM}$ in the previous layer is calculated analogously by extending the chain rule based on the blue path in Fig. 4.2. Its computation can be expressed as

$$\frac{\partial E}{\partial w_{z,DM}} = \left(\sum_{k=1}^{K}\frac{\partial E}{\partial y_k}\frac{\partial y_k}{\partial a_{y,k}}\frac{\partial a_{y,k}}{\partial z_M}\right)\frac{\partial z_M}{\partial a_{z,M}}\frac{\partial a_{z,M}}{\partial w_{z,DM}}\,, \tag{4.10}$$

where $k = 1, \ldots, K$ denotes the indices of the output layer nodes influenced by weight $w_{z,DM}$. Due to its connection to both y_1 and y_K, its contributions to both E_1 and E_K are considered in the sum.

In modern ML frameworks such as PyTorch and TensorFlow, automatic differentiation methods automate the process of calculating gradients by applying the chain rule of calculus systematically and efficiently (Baydin et al., 2018; Paszke et al., 2017). For this purpose, intermediate values and activations are stored during the forward pass.

Due to their ability to leverage textural features and approximate highly nonlinear relationships, many approaches based on MLPs have been proposed for earth observation tasks such as the estimation of precipitation from satellite data (Capacci & Conway, 2005; Chen et al., 2019; Giannakos & Feidas, 2013; Grimes et al., 2003; Hsu et al., 1997; H. Meyer et al., 2017; Rivolta et al., 2006), outperforming traditional methods such as look-up tables (Capacci & Conway, 2005) and classical ML methods such as SVMs and RFs (H. Meyer et al., 2016). Moreover, Wood and Hartmann (2006) employed an MLP to classify the mesocale structure of approximately 20,000 MODIS scenes from

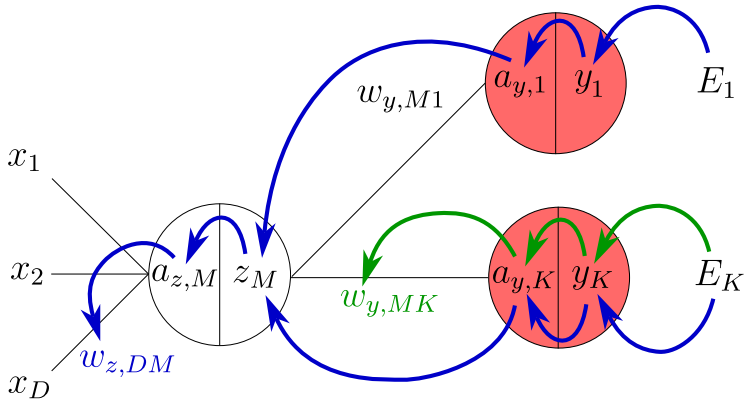

Figure 4.2: Error backpropagation paths for the adjustment of two sample weights, $w_{z,DM}$ (blue path) and $w_{y,MK}$ (green path), from different layers of the multilayer perceptron presented in Fig. 4.1.

two regions above the subtropical eastern Pacific using four spatial variability types. For the training and testing of the network, they manually labeled approximately 1,000 scenes based on visual inspection. Although they used their MLP for image classification rather than pixelwise classification or segmentation, their work demonstrates the potential of ANNs for studying the mesoscale organization of convection.

Due to enhanced computer performance and more efficient algorithms, MLPs in more recent publications, such as those suggested by Chen et al. (2019), have shown a trend towards deeper networks with more hidden layers and higher node numbers. This trend is driven by the understanding that deeper neural networks can generally model more complex relationships (Le Goff et al., 2017; Wang et al., 2018). However, the rapidly increasing computational cost of deepening the fully connected network architecture severely limits the depth of MLPs and has thereby fostered the advancement of other network architectures like convolutional neural networks (CNNs) (Fukushima, 1980; LeCun et al., 1989). While the term "deep learning" typically encompasses ANNs with two or more hidden layers (Nielsen, 2015), modern network architectures for deep ANNs used in image segmentation often comprise significantly more hidden layers (Badrinarayanan et al., 2017; Long et al., 2015; Noh et al., 2015; Ronneberger et al., 2015).

4.3.2 Convolutional Neural Networks

The architecture of CNNs (Fig. 4.3a) is designed to efficiently process grid-like data, such as images, and leverages the stronger correlation between nearby pixels compared to those further apart (Bishop, 2006). This is achieved through the concept of convolution, where a small convolution filter, also

referred to as a "kernel," is slid over the input to extract local features by computing the dot product between the filter weights and the values in the input region covered by the filter (Fig. 4.3b). The size of the step taken during this sliding movement is known as the stride. With a stride of one, the filter moves over each input pixel, transitioning from one pixel to the next. The filter weight sharing between neurons (LeCun et al., 1998) drastically reduces the number of parameters compared to fully connected networks. Furthermore, the weight sharing enables the network to learn translation-invariant representations, as features identified in one part of the image can be reused in other regions. To obtain a convolution result with the same dimensions as the input image, the latter can be extended by adding rows and columns of zeros at the image boundaries, referred to as "zero-padding" (Albawi et al., 2017). Similar to MLPs, each convolutional layer is followed by a nonlinear activation, resulting in abstracted feature maps which are passed to the next layer.

Further CNN components are pooling layers and fully connected layers. Pooling layers reduce the spatial dimensions of the generated feature maps by aggregating several feature map values. A common tiling size for the aggregation is 2x2, which downsamples the feature map dimensions by a factor of two. The retained value per tile is generally either the maximum value within the tile (max pooling) or the average value (average pooling). At the end of the CNN architecture, fully connected layers identical to MLPs allow the network to integrate high-level features learned by the convolutional and pooling layers and perform classification or regression tasks. For this purpose, the grid-like feature maps are flattened.

Like MLPs, CNNs are feed-forward networks, where input information flows through the network in a constant direction to generate the output (from left to right in Fig. 4.3a). Moreover, the use of backpropagation for network training is typically analogous to MLPs.

Another similarity to MLPs is that CNNs output classifications rather than segmentations. In this context, Liu et al. (2016) utilized a CNN architecture to detect extreme weather events, specifically tropical cyclones, atmospheric rivers, and weather fronts, in climate data, achieving detection accuracies ranging between 89% and 99%. Similarly, Cintineo et al. (2020) trained a CNN for the automated detection of intense convection in geostationary satellite images from GOES-16. They observed that the model successfully learned the significance of complex features such as strong brightness temperature gradients for identifying intense convection. Both these studies primarily focused on recognizing the presence of patterns corresponding to extreme events or intense convection within the input images (classification), rather than precisely locating them in the image (segmentation).

Using CNNs with a classical architecture, as depicted in Fig. 4.3, for image segmentation generally requires an approach with multiple classifications, each associated with a forward pass. While Pan et al. (2019) generated an output

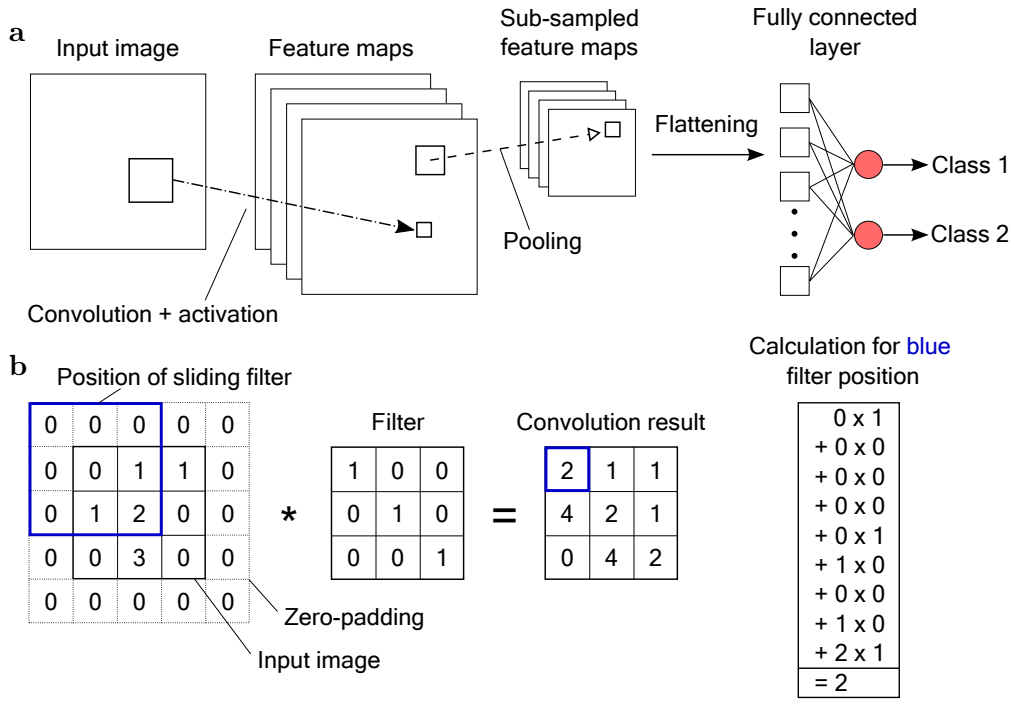

Figure 4.3: **a**, Architecture of a convolutional neural network consisting of a convolutional layer with nonlinear activation, a pooling layer, and a fully connected layer with two output classes. **b**, Visualization of the convolution process, here convolving a zero-padded 3x3 input image with a 3x3 filter and a stride of one.

for larger sub-regions rather than individual pixels to limit the computational cost, Maggiori et al. (2016) experimented with a patch-based prediction approach for pixelwise classification. During each forward pass, their CNN generated 256 outputs, representing the predicted pixels of a 16x16 patch. The final segmentation was derived by recombining the predicted patches. Comparing the final segmentation results to those of a fully convolutional neural network (FCN) where they replaced the fully connected layers with deconvolution-based upsampling, they found that the FCN network outperformed the patch-based approach in terms of accuracy and efficiency. Consistent with these findings, the classical CNN architecture is typically adapted for image segmentation tasks by integrating a decoder, which upsamples the downsampled feature maps back to the original image resolution (Section 4.3.3).

4.3.3 Encoder-Decoder Networks

The convolutional and pooling layers in CNNs progressively decrease the resolution of the input images to extract diverse features across different scales.

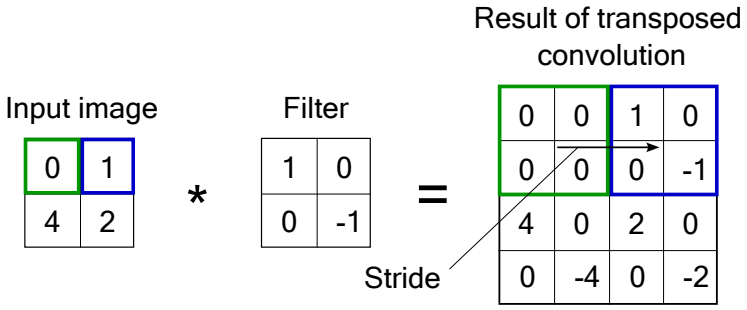

Figure 4.4: Visualization of the transposed convolution process, depicted here with a 2x2 input image, a 2x2 filter, and a stride of two. Each pixel in the input image is multiplied by all filter weights, and each of these multiplication results is then projected onto an output pixel. The stride determines the step size of the projection in the output as the filter slides from one input pixel to the next.

The resultant feature maps can be regarded as a transformed, more abstract representation of these features. Drawing an analogy to the field of information theory, the path responsible for downsampling in neural networks is commonly referred to as the "encoder".

Yet, semantic segmentation necessitates an output where each input pixel is assigned a specific class. For an end-to-end solution, it is thus required to upsample the encoded feature maps back to the original input resolution. Analogous to the encoder, this upsampling path is termed the "decoder". In recent years, the majority of deep learning models for image segmentation tasks have adopted an encoder-decoder structure (Minaee et al., 2021).

A common upsampling technique is transposed convolution, also known as deconvolution or fractionally strided convolution (Dumoulin & Visin, 2016). As regular convolution, it involves a convolutional filter which slides over the input to generate an output (Fig. 4.4). However, instead of aggregating information, transposed convolution expands the input based on the filter weights to produce a larger output. The output size can be controlled via the stride: the larger the stride, the larger the corresponding output. Unlike traditional upsampling techniques such as bilinear interpolation, where the upsampling operation is fixed, transposed convolution learns how to properly restore the decoded spatial information by optimizing the filter weights during training (Noh et al., 2015).

Skip connections, which directly link encoder and decoder layers, are another crucial component of encoder-decoder architectures. By integrating feature maps from the encoder into the decoder, skip connections allow the decoder to access high-resolution features, thereby enabling more precise segmentation (Long et al., 2015).

A popular example of an encoder-decoder architecture is U-Net (Ron-

neberger et al., 2015). It was introduced for biomedical image segmentation tasks and has been successfully applied to numerous segmentation problems (Siddique et al., 2021). In earth observation, U-Net or its variants have, for instance, been used for segmenting high-resolution aerial images (Diakogiannis et al., 2020; C. H. Simpson et al., 2023), landslide mapping (Meena et al., 2022; Prakash et al., 2020), and forest cover monitoring (Bragagnolo et al., 2021; John & Zhang, 2022).

With respect to atmospheric applications, Drönner et al. (2018) employed a neural network with U-Net architecture for segmenting clouds in multispectral satellite images captured by MSG SEVIRI over Europe. Comparing the results to an RF approach, they found that the U-Net outperformed the RF approach in accuracy, efficiency, and robustness. Building on the work of Wood and Hartmann (2006), Rasp et al. (2020) used a U-Net architecture to segment mesoscale organizational patterns of shallow convection in Terra and Aqua MODIS scenes from the trades. To reduce the time for the ground truth labeling, they utilized a crowdsourcing platform where 67 scientists labeled 10,000 satellite scenes by drawing rectangular boxes around detected organizational patterns. Despite the noise among the labels of different scientists and the rectangular-shaped regions of the target labels, the network learned the underlying shape of the organizational patterns. Moreover, the U-Net architecture has been proposed for precipitation nowcasting from radar data (Han et al., 2021) as well as the segmentation of atmospheric rivers in ERA5 reanalysis data (Galea et al., 2024).

Due to its strength in leveraging features of different scales for segmentation, the U-Net was also used as architecture for the approach developed in the present thesis for the segmentation of CPs from cloud and rainfall fields (manuscript III, Section 5.3).

Chapter 5

Contributions

The upcoming chapter introduces the manuscripts associated with the candidate's PhD project. Complete references for each manuscript are provided in the "List of Papers" at the beginning of this thesis. Furthermore, both the first and second manuscripts are supplemented with additional supporting information, located immediately after the main manuscript in Section 5.1 and Section 5.2, respectively.

5.1 Characteristics of Station-Derived Convective Cold Pools Over Equatorial Africa

The following manuscript presents a statistical analysis of 4218 CPs identified in near-surface time series data collected from twelve automatic weather stations across equatorial Africa. The CPs were detected using temperature and wind criteria similar to those employed by Kirsch et al. (2021) and Kruse et al. (2022) for CPs in Northern Germany and the Netherlands, and were automatically verified using satellite imagery. The primary objective was to investigate space-borne signatures of CPs, with a particular focus on infrared imagery obtained from geostationary satellites. For this purpose, we analyzed satellite-derived brightness temperature time series corresponding to the locations of weather stations around the time of the identified CP gust front passage. Additionally, the study addresses a critical research gap by presenting the first climatology of CPs observed over tropical continents.

Characteristics of Station-Derived Convective Cold Pools Over Equatorial Africa

Jannik Hoeller[1,2], **Jan O. Haerter**[1,2,3,4], **Nicolas Da Silva**[1]

[1]Integrated Modeling, Leibniz Centre for Tropical Marine Research, Fahrenheitstr. 6, 28359 Bremen, Germany
[2]Niels Bohr Institute, Copenhagen University, Blegdamsvej 17, 2100 Copenhagen, Denmark
[3]Physics and Earth Sciences, Constructor University Bremen, Campus Ring 1, 28759 Bremen, Germany
[4]Department of Physics and Astronomy, University of Potsdam, Karl-Liebknecht-Straße 32, 14476 Potsdam, Germany

Key Points:

- 4218 cold pools are identified across equatorial Africa based on temperature and wind criteria.
- The occurrence and intensity of the observed cold pools are related to low-level moisture conditions and the depth of convection.
- The identified cold pool gust fronts closely correlate with satellite-observed brightness temperature discontinuities.

Corresponding author: Jannik Hoeller, jannik.hoeller@leibniz-zmt.de

Abstract
Due to their potential role in organizing tropical mesoscale convective systems, a better understanding of cold pool (CP) dynamics in such regions is critical, particularly over land where the diurnal cycle further concentrates convective activity. Numerical models help disentangle the processes involved but often lack observational benchmarks. To close this gap, we analyze nearly 43 years of five-minute resolution near-surface timeseries, recorded from twelve automatic weather stations across equatorial Africa during 2019-2023. We identify 4218 CPs based on criteria for temperature and wind. The identified CP gust fronts, which exhibit respective median temperature and specific humidity decreases of $5.3\,K$ and $2.8\,g\,kg^{-1}$, closely correlate with satellite-observed brightness temperature discontinuities. Despite weak diurnal variation in precipitation, observed CP occurrence shows a pronounced diurnal cycle with an afternoon peak — a feature we attribute to low-level moisture conditions. Our findings can serve as observational benchmark to improve simulations of CP organization.

Plain Language Summary

Convective cold pools form when rain evaporates underneath thunderstorm clouds. The evaporation causes the air to cool and sink toward the ground, where it is deflected horizontally. Cold pools are thus associated with strong gusty winds, and over tropical land, they can be especially vigorous. Cold pools are also suggested to contribute to the organization of thunderstorm clouds into large clusters of rain-producing areas. The widespread, heavy rainfall can then cause flooding. To better predict such flooding in numerical weather models, having a precise observational basis for cold pool properties is essential — yet currently missing in equatorial Africa. We here provide such an observational benchmark by analyzing thousands of cold pools using timeseries of near-surface temperature, wind, humidity and precipitation. We additionally show that the cold pools can even be detected from satellite data when analyzing abrupt changes in cloud top temperature. Such satellite-based detection could open for cold pool studies across all tropical land areas — of great practical relevance to the prediction of thunderstorm clusters.

1 Introduction

Convective cold pools (CPs) are caused by the evaporation of rainfall beneath deep convective clouds (Zuidema et al., 2017). The resultant denser air volume spreads out laterally along the surface and can cause a so-called "gust front" (GF) along its edges (Charba, 1974). The GF features strong horizontal and vertical winds along with moisture and temperature anomalies which together can give rise to additional deep convective events, e.g., under collisions (Purdom, 1976; Feng et al., 2015). CPs are thus important agents in mediating interactions between deep convective cells and thus the self-organization of thunderstorm systems (Simpson, 1980; Tompkins, 2001b; Haerter et al., 2019; Jensen et al., 2021).

Recent idealized cloud-resolving and large-eddy simulations have provided new insight into CP structure and dynamics, such as on required mesh resolution (Fiévet et al., 2022), moisture rings (Langhans & Romps, 2015; Drager et al., 2020), or general interaction mechanisms (Tompkins, 2001a; Torri et al., 2015; Meyer & Haerter, 2020; Haerter et al., 2020), and triggered a range of simplified conceptual models (Böing, 2016; Haerter, 2019; Haerter et al., 2019; Nissen & Haerter, 2021; Niehues et al., 2022), which may help elucidate organizing mechanisms. New methods of CP detection in numerical studies have also been developed which help automatize the tracking of GFs and their interactions (Gentine et al., 2016; Torri & Kuang, 2019; Fournier & Haerter, 2019; Henneberg et al., 2020; Hoeller et al., 2023, 2024a).

Despite this progress in numerical and theoretical work, direct measurements of CPs are still limited to specific geographic regions, such as the tropical and sub-tropical ocean (Zipser, 1977; Zuidema et al., 2012; Vogel, 2017; Chandra et al., 2018; Vogel et al., 2021), mid-latitude continental regions in Central Europe (Kirsch et al., 2021; Kruse et al., 2022) or North America (Mueller & Carbone, 1987; Wakimoto, 1982; Engerer et al., 2008; Hitchcock et al., 2019; van den Heever et al., 2021), and — with a focus on dust storms — semi-arid tropical regions (Redl et al., 2015; Emmel et al., 2010; Caton Harrison et al., 2021).

Indeed, the importance of collecting information on CPs and precipitation in deep tropical regions has been pointed out (Adams et al., 2015) but systematic, climatological studies on CPs in such regions are still rare or lacking. This may partially be due to difficult environmental conditions which pose challenging demands on equipment and maintenance (Parker et al., 2008). Also the availability of funds may hinder systematic long-term campaigns in some regions. A notable exception is the trans-African hydrometeorological observatory (TAHMO) which offers a promising network of station measurements in many sub-Saharan African countries (van de Giesen et al., 2014). Using a range of stations from the TAHMO network, we here present a climatology of CP measurements for equatorial Africa and compare findings to previous work in other geographic regions.

2 Data

2.1 Station data

We utilize data from twelve ATMOS41 automatic weather stations (AWS) (Fig. 1), operated by TAHMO. The stations are situated in Cameroon, the Democratic Republic of Congo (DR Congo), Nigeria, and Uganda. To investigate the influence of regional climatic differences on CPs, we group stations according to their respective deployment countries in our analysis.

The AWS provide data at a five-minute temporal resolution. All stations are installed at an approximate height of two meters above the surface. We employ the station records of precipitation, atmospheric pressure, air temperature, relative humidity, and wind gust speed. ATMOS41 determines the latter by measuring instantaneous wind speed every ten seconds and outputting the maximum instantaneous wind speed value within any given five-minute interval. If an instantaneous wind speed is larger than eight times the running average of the previous ten instantaneous measurements, the measurement is rejected. While this method may prevent spurious spikes in the wind record under normal conditions, it can cause missing wind data in cases of large and sudden wind changes. Given the frequent occurrence of such strong wind variations associated with CP GFs, approximately 22% of all identified CPs have an incomplete wind record.

We analyze the data recorded by these AWSs from January 1, 2019, to September 30, 2023. As not all AWSs were operational throughout the entire period, we limit our analysis for each station to days with complete air temperature records. Additionally, we require the air temperature to be recorded for a minimum of ten consecutive minutes from the previous day and for the subsequent 120 minutes on the following day. The resulting number of analysis days per station is indicated in Fig. 1. In total, we analyzed 15602 days and thus nearly 43 years of station data.

Based on the station-measured variables, we additionally compute both mixing ratio, r and saturated mixing ratio, r_{sat} (see Text S1), and derive the specific humidity, $q \equiv r/(1+r)$ and the specific humidity deficit, $q_D \equiv q_{sat} - q = r_{sat}/(1+r_{sat}) - q$.

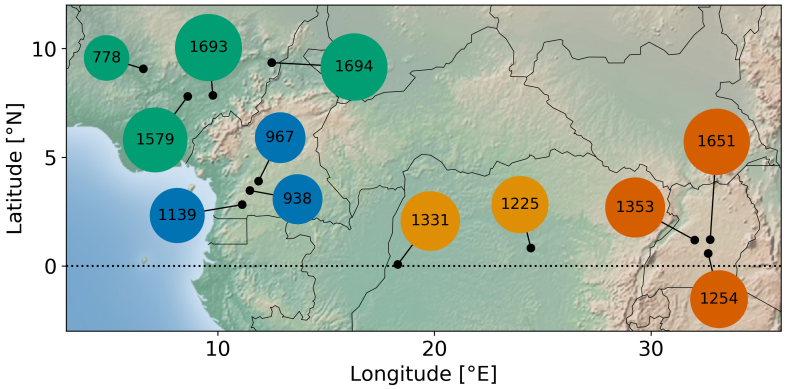

Figure 1: **Weather station data employed.** Map of equatorial Africa showing station locations (filled black circles). Numbers within colored circles and the size of the circle area represent available days of station data with a complete record of air temperature. Stations are grouped into four regions denoted by the colored circles: Cameroon (blue), Democratic Republic of Congo (yellow), Nigeria (green), Uganda (red).

2.2 Satellite data

Apart from the station data, we utilize infrared brightness temperature measurements which we derive from satellite-measured effective radiances. The radiances are extracted from Meteosat Second Generation (MSG) 0° products provided by the European Organisation for the Exploitation of Meteorological Satellites (EUMETSAT). The data has a baseline repeat cycle of 15 min and a spatial resolution of 3 km in the sub-satellite point. To convert the radiances to brightness temperatures we employ equation 5.3 and the corresponding regression coefficients of EUMETSAT (2012).

3 Methods

3.1 Cold Pool Detection Algorithm

(i) Temperature criterion. A potential CP event is detected at a given time t if three conditions apply: (1), similar to Kirsch et al. (2021) we require a substantial temperature decrease $\Delta T \leq -2\,K$, within the 20 min window from $t - 5\,min$ to $t + 15\,min$. Additionally, we require (2), the decrease of ΔT to be monotonic and (3), $T(t) - T(t - 5\,min) \leq -0.5\,K$.

While the chosen conditions minimize the risk of high false alarm rates due to typical diurnal temperature changes, some weak or dissipating CP GFs might be missed. Choosing a ΔT of $-1.5\,K$ as used by Kruse et al. (2022) leads to approximately 28% more identifications, marginally weakening CP-associated median temperature and specific humidity decreases by 11–12%, without impacting overall results.

(ii) Wind criterion. To confirm detected potential CP events, we adapt the wind criterion introduced by Kruse et al. (2022). For this purpose, we compute the wind gust speed anomaly for each time t as

$$\Delta u_g(t) \equiv u_g(t) - \overline{u}_g(t)\,, \tag{1}$$

where u_g is the wind gust speed (see Sec. 2.1) and $\overline{u}_g$ its centered 2-hour running mean, i.e., the mean value of the 25 wind gust speeds recorded during the the corresponding 2-hour window.

For a potential CP event at time t we identify the maximum wind gust speed anomaly, Δu_g^{max}, between $t - 20\,min$ and $t + 40\,min$. We retain it as potential CP event if

$$\Delta u_g^{max} \geq \overline{\Delta u}_g(t) + n_w\,\sigma_{\Delta u_g}(t)\,, \tag{2}$$

with $n_w = 3$, the centered 24-hour running mean of the wind gust speed anomaly, $\overline{\Delta u}_g$, and the corresponding 24-hour running standard deviation, $\sigma_{\Delta u_g}$. While higher n_w mainly increase the number of missed CPs, smaller n_w values give rise to more false positive detections. For instance, using $n_w = 2$ would yield 12% more identifications, with 2.5 times as many events that cannot be attributed to convective events in satellite data and, therefore, are rejected in step (iv).

As the potential CP onset is defined based on the temperature criterion, we also search for associated wind gusts in a $20\,min$ time window before this onset. We choose $20\,min$ rather than the $10\,min$ used by Kruse et al. (2022) since our temperature criterion involves a minimum decrease of $-0.5\,K$ within $5\,min$ to define the onset of potential CPs and might thus delay the onset in comparison to Kruse et al. (2022). The $40\,min$ time window after potential CP onset allows significant wind offsets while ensuring a temporal relation between ΔT and Δu_g^{max}. Halving both time windows would reduce CP identifications by about 7%, with negligible impact on overall results.

In case of missing wind gust speed anomalies between $t-20\,min$ and $t+40\,min$, we identify the maximum wind gust speed, u_g^{max} within this time window rather than Δu_g^{max} and retain the event as potential CP if

$$u_g^{max} \geq \overline{u}_g(t - 80\,min) + n_{miss}\,\sigma_{u_g}(t - 80\,min)\,, \tag{3}$$

with $n_{miss} = 2$, the centered 2-hour running mean, $\overline{u}_g$, and the corresponding standard deviation, σ_{u_g}. Approximately 25% of the detected CPs is identified based on Eq. 3 rather than Eq. 2. By evaluating $\overline{u}_g$ and σ_{u_g} $80\,min$ before potential CP onset, we keep again a $20\,min$ offset between the onset and the 2-hour time window of the reference values. Since portions of the wind record are missing, we choose n_{miss} conservatively. Yet, neither the number of identifications nor the results are sensitive to the selection of n_{miss}.

If no wind gust speed data has been recorded between $t-20\,min$ and $t+40\,min$, or if the reference values $\overline{u}_g(t-80\,min)$ and $\overline{u}_g(t-80\,min)$ could not be computed due to missing data, we consider the event as "no CP."

Differing from Kruse et al. (2022), we evaluate the wind criterion based on wind gust speed rather than wind speed. Since we work with station data with a temporal resolution of $5\,min$ in contrast to $1\,min$ in (Kruse et al., 2022), we find wind gust speed a better indicator for CP GFs than wind speed.

(iii) Duplicate detection check. Often, a CP fulfills the defined criteria (i) and (ii) not only at time t, but also at subsequent time steps. Depending on the evolution of temperature and wind gust speed behind the CP GF, time steps in which the criteria are met can even be separated from each other by time steps in which the criteria are not met. To avoid duplicate detection of a given CP, we drop detected events if at least one other event was detected within $20\,min$ before that particular event. Given the variety of environmental conditions under which we observe CPs at our station locations, we find this definition to be more permissive than the absolute $60\,min$ time window after detected temperature decreases, within which Kirsch et al. (2021) considers any detected decrease as part of the same event.

(iv) Space-borne verification. In some cases, especially during the Nigerian dry season, neither condition (i) nor (ii) may suffice to completely prevent false positive detec-

tions caused by strong diurnal temperature changes. Consequently, we validate each detected event using satellite-measured $10.8\,\mu m$ brightness temperatures, $BT_{10.8}$. We consider an event at time t as CP if the minimum $BT_{10.8}$ recorded between $t - 3\,h$ and t within a 2° radius around the station is less than $240\,K$.

The parameters of the verification ensure the presence of temporally related convective events in the vicinity of the potential CP event. Applying this verification to all detected events, 71 false positive detections are identified and dropped. Reducing the radius around the station from 2° to 1.5° would increase the number of rejected events to 85.

3.2 Determination of Cold Pool Anomalies

We analyze the effects of a detected CP with respect to different station-measured meteorological variables by considering a time window relative to CP onset, t_0, from $t_0-40\,min$ to $t_0+120\,min$. Within this time window, we evaluate the CP associated anomalies $y'(t) \equiv y(t) - y_{ref}$ for a meteorological variable y based on an unperturbed reference state y_{ref}, which we define as the temporal mean of instantaneous measurements in a time interval before CP onset. Since the onset is defined based on the temperature drop and thus could be different for other variables, we choose the time interval from $t_0-40\,min$ to $t_0-20\,min$ to keep a sufficient margin of $20\,min$ to the CP onset while preserving the required temporal proximity. To minimize any distortion of the reference state through the diurnal cycle, we deviate from this definition only for temperature anomalies and follow the approach of the refined temperature drop from Kruse et al. (2022) instead, i.e., we consider the maximum temperature of the two measurements in the $10\,min$ time window preceding the CP onset as unperturbed reference temperature.

Due to the coarser temporal resolution, we extend the time window in which we analyze the anomalies before CP onset to $60\,min$ for satellite-measured $10.8\,\mu m$ brightness temperatures, $BT_{10.8}$, and define the reference brightness temperature, $BT^{ref}_{10.8}$, as the mean of the three observations in the time interval from $t_0-60\,min$ to $t_0-30\,min$. As there might not be a brightness temperature observation at the station-derived CP onset, t_0, we define the closest satellite time step as $\hat{t}_0$ and measure the CP time relative to it. The brightness temperature anomalies, $BT'_{10.8}$, are then computed analogously to those for station-measured variables. Moreover, to further investigate the space-borne CP signature, we additionally determine the temporal change of $BT'_{10.8}$, as $\Delta BT'_{10.8}(t) = BT'_{10.8}(t) - BT'_{10.8}(t - 15\,min)$.

The overall impact of the described parameter choices on the observed anomalies is relatively weak. For instance, doubling the time interval for computing the unperturbed reference state from $20\,min$ to $40\,min$, while maintaining the $20\,min$ offset to CP onset, would result in a 1.4% enhancement in the median specific humidity drop. Similarly, calculating the unperturbed reference temperature based on the mean value of the four measurements before CP onset, instead of using the maximum of the previous two, would lead to a 1.3% reduction in the median temperature drop.

4 Results

4.1 Seasonal and Diurnal Cycle of Observed Cold Pools

First, we derive the seasonal and diurnal cycles of CPs in the different sub-regions (Fig. 1) and relate them with precipitation, convection depth and moisture conditions (Fig. 2). With about 0.3–0.6 CPs per day in the high seasons (Fig. 2a, Table S2), equatorial Africa boasts particular CP abundance compared to previous climatologies in other continental regions with about 0.1–0.3 CPs per day (Redl et al., 2015; Kirsch et al., 2021; Kruse et al., 2022). In every sub-region, the number of CPs peaks twice during the course

of the year with a first maximum between March and May and a second maximum between September and October. The bi-modality in the annual cycle of CPs largely corresponds to the latitudinal migration of the Inter-Tropical Convergence Zone (ITCZ) as reflected in the precipitation seasonal cycles (Fig. 2c). However, we note that precipitation may not explain all the features of the annual cycle of CPs and the differences between sub-regions. For instance, Nigeria presents a single precipitation peak in September whereas CP occurrence peaks in both May and September. There, the strong CP activity during May may be related to the combination of deeper convection (Fig. 2e) fed by high equivalent potential temperatures (θ_E; Fig. S1) and of higher low-level specific humidity deficit (q_D; Fig. 2g) boosting rain evaporation. We also note that Uganda receives the least precipitation among sub-regions while experiencing most frequent CPs during the year. We attribute the larger number of CPs in Uganda to generally drier conditions at low levels (Fig. 2g).

The diurnal cycle of CPs strongly peaks between 15 LT and 18 LT in all regions except Nigeria, where the peak is reached between 18 LT and 21 LT (Fig. 2b). The high CP activity during the afternoon can be directly related to the afternoon peak in (deep) convection, highlighted by maxima in precipitation (Fig. 2d) and lower brightness temperatures (Fig. 2f). Consistently with earlier studies (Zhang et al., 2016; Camberlin et al., 2018; Andrews et al., 2023), precipitation shows secondary nocturnal peaks in Uganda and Congo, and remains high during the night in Nigeria, whereas the proportion of CPs displays local minima during these hours. This mismatch between precipitation and CPs is likely to be related to both the decline of convection during the night (leading to weaker rainfall intensities and downdrafts) and to moister conditions at the surface (reducing rainfall evaporative cooling; Fig. 2h) which both inhibit CP formation (Zuidema et al., 2017).

4.2 Observed Cold Pool Characteristics

We further characterize equatorial African CPs by relating their temperature and moisture anomalies (defined in Sec. 3.2). On average, such CPs are accompanied by $5\,K$ drops in temperature — compared to $3\,K$ in Germany; Kirsch et al. (2021) — occurring within approximately 30 minutes, with little variability among sub-regions (Fig. 3a, Table S2). In distinction to Kirsch et al. (2021), the CPs we analyze here generally show decreases in specific humidity after CP passage (Fig. 3d). Interestingly, we find that the magnitude of this decrease is smaller for the elevated (Table S1) stations of Uganda ($-1\,g\,kg^{-1}$) characterized by less deep convection (Fig. 2e,f) and drier low-level environments (Fig. 2g,h) compared to the other sub-regions (about $-3\,g\,kg^{-1}$). Less deep convection is likely to be associated with lower (relative to the ground) convective downdrafts origins (Zuidema et al., 2017), importing less upper-level dry air to the surface. This may combine with enhanced rain evaporation due to drier environments, thus explaining the more modest reduction in specific humidity over Uganda. When considering the 25% driest (moistest) low-level pre-CP environments, we further evidence the large impact of moisture conditions, and thus of rain evaporation, on CP temperature and moisture anomalies in all sub-regions (Fig. 2b,c,e,f): CP anomalies typically are $3\,K$ cooler and $2\,g\,kg^{-1}$ moister in the driest pre-CP conditions than in the moistest pre-CP conditions. We note weak maxima in specific humidity occurring few minutes after CP onset — so-called moisture rings (Tompkins, 2001a; Langhans & Romps, 2015; Schlemmer & Hohenegger, 2016) — over Cameroon, Uganda and Congo for the driest pre-CP environments. Finally, the temporal evolution of q_D (Fig. 3g,h,i) reveals that, in the driest environments, rain evaporation may not be sufficient to saturate the low-level air — similar to Germany; Kirsch et al. (2021).

Addressing CP cloud characteristics, we find that 96% (Uganda) to 100% (Congo) of CP GFs are accompanied by shallow or deep convective clouds (Fig. S2a). More specifically, CPs are generally accompanied by a strong decrease in $BT_{10.8}$ (Fig. 4a), e.g., reach-

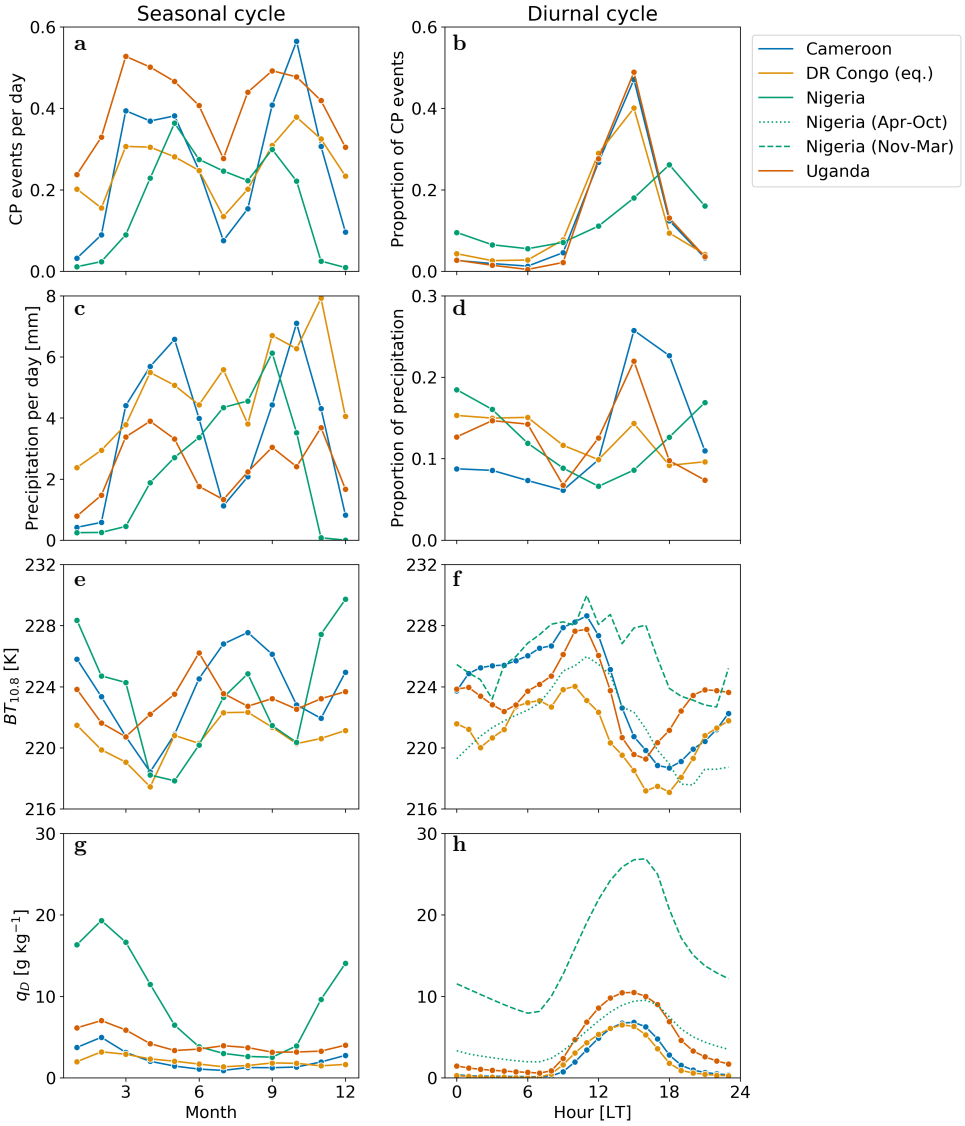

Figure 2: **Observed seasonal and diurnal cycles.** Line colors indicate distinct subregions (see legend). **a**, Mean number of daily cold pool (CP) events for each month. Lines interpolate linearly between markers to facilitate the interpretation; colors indicate different regions. The number of CP events is normalized based on the number of analyzed days per month and region. **b**, Proportion of CP events at different times of the day. Each marker represents the proportion of CP events observed within a given 3-hour time interval, starting with the interval [0,3) for the marker at 0 LT. **c**, Analogous to (a) but for precipitation. **d**, Analogous to (b) but for precipitation. **e**, Mean 10.8 μm brightness temperature, $BT_{10.8}$, of deep clouds ($BT_{10.8} \leq 240\,K$) for each month. **f**, Mean $BT_{10.8}$ of deep clouds at different times of the day. The two lines for Nigeria represent rainy (Apr–Oct, dotted) and dry months (Nov–Mar, dashed). **g**, Analogous to (e) but for mean specific humidity deficit, q_D. **h**, Analogous to (f) but for mean q_D.

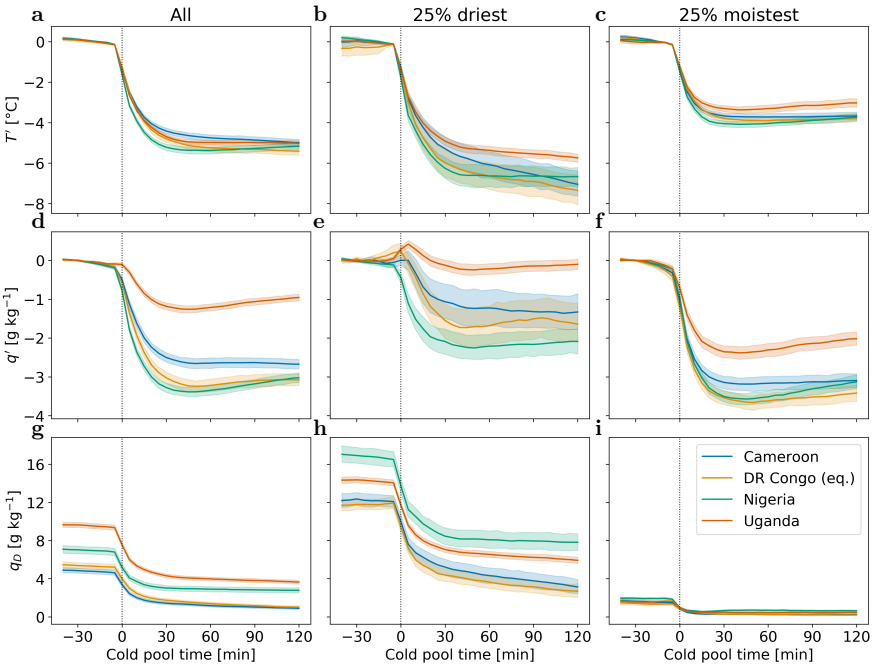

Figure 3: **Station-derived cold pool (CP) properties relative to CP onset, t_0.** **a**, Mean temperature anomalies, T', for different regions; shading indicates the 95% confidence interval. **b**, Analogous to (a) but for the 25% driest pre-CP environments of each region w.r.t. the reference specific humidity deficit, q_D^{ref}, prior to t_0. **c**, Analogous to (b) but for the 25% moistest pre-CP environments. **d**–**f**, Analogous to (a)–(c) but for mean specific humidity anomalies, q'. **g**–**i**, Analogous to (a)–(c) but for mean specific humidity deficits, q_D. Note that only timeseries of CPs, where t_0 is more than 120 minutes apart from other CP onsets, are included in the analysis.

ing $36\,K$ in Congo. The $BT_{10.8}$ minimum is typically achieved 30–45 minutes after CP onset. While this minimum is delayed w.r.t. the CP onset, we find a minimum of the time derivative of $BT'_{10.8}$ to be synchronized with CP onset in all sub-regions (Fig. 4b). This observation suggests that CPs in equatorial Africa, and potentially other regions, might be detectable from space-borne satellite data.

5 Summary and Discussion

The present study provides multi-year statistics of cold pool characteristics in equatorial Africa, based on five-minute near-surface weather data. Using detection methods similar to those in previous studies focused on mid-latitude continental regions, key findings include that temperature drops upon gust front passage often exceed $5\,K$ and specific humidities typically decrease by more than $3\,g\,kg^{-1}$. Weak moisture rings can only be identified in some of the sub-regions for the driest pre-cold pool environments — in agreement with Kruse et al. (2022) for data in the Netherlands where moisture rings were generally not detected.

Seasonally, the rate of cold pool occurrence roughly follows precipitation statistics. Diurnally, in contrast, cold pool occurrence sharply peaks during the drier late afternoon

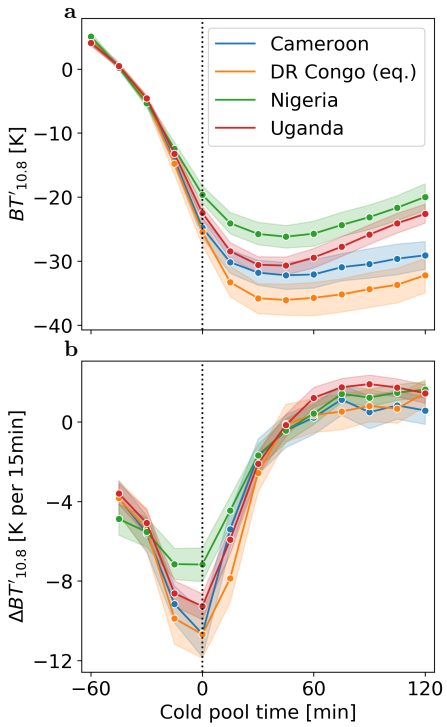

Figure 4: **Space-borne signatures of cold pools (CPs) relative to CP onset, $\hat{t}_0$.** **a**, Mean $10.8\mu m$ brightness temperature anomalies, $BT'_{10.8}$, of station-derived CPs for different regions; shading indicates the 95% confidence interval. **b**, Analogous to (a) but for the corresponding derivative $\Delta BT'_{10.8}$.

times, departing from the weak precipitation diurnal cycle. We suggest this may be due to the nocturnal boundary layer often being close to saturation, thus diminishing cold pool occurrence there. This finding may have important implications for thunderstorm organization through cold pool activity: the limited time window where cold pools actually occur during the day means that self-organization may be limited to relatively short periods of the day. One could speculate that it is the lack of cold pool activity that limits the duration of mesoscale convective systems, often less than 12 hours, rather than the precipitation itself — which is more spread out over the day. Yet, further investigations are needed to substantiate this claim, e.g., by using additional radiosonde data to explore the vertical coordinate Future studies should also analyze if deep convection is more scattered during nocturnal periods when fewer cold pools occur. Comparisons with oceanic cold pools and their organizational effects, which tend to be weaker (Zuidema et al., 2017), would be insightful.

Our cold pool detection algorithm can be adapted to other regions, provided that there are in-situ weather stations measuring surface wind and temperature with at least 5-min temporal resolution. However, in-situ weather stations meeting this requirement are still limited in the tropics, whereas cold pools are abundant. Encouragingly, our findings may have implications for satellite-based cold pool detection: we show that gust front passage clearly correlates with discontinuities in satellite-derived brightness temperature. We generally observe a significant decrease in brightness temperatures around the time

of the gust front passage, with maximum decrease rates at the station-derived cold pool onset. Our findings thus suggest that cold pools in equatorial Africa, and potentially other regions, could be directly detectable from geostationary satellite data on a continental scale. While significant decreases in brightness temperature alone are not a sufficient criterion for identifying cold pool gust fronts, the concurrence with spatiotemporal patterns like radially spreading cloud arcs and rapidly expanding deep convection (Text S2, Fig. S3) could aid neural networks, such as those developed by Hoeller et al. (2024a), in limiting the number of false positive detections. Even in cases where not all parts of a cold pool gust front exhibit brightness temperature drops (Fig. S2b), the presence of such spatiotemporal patterns may enable the neural networks to accurately track the gust front.

Open Research

Both the code for the cold pool gust front identification and the processed data sets are licensed under Creative Commons Attribution 4.0 International and were used in version 2.0 (Hoeller et al., 2024b). The raw data of the automatic weather stations was provided by TAHMO and is not publicly available. For more information about the data, please visit `https://tahmo.org/climate-data/`. Interested parties may contact info@tahmo.org for this data. The satellite-observed radiances were extracted from Meteosat Second Generation (MSG) 0° products (`https://navigator.eumetsat.int/product/EO:EUM:DAT:MSG:HRSEVIRI`), provided by EUMETSAT without a licence on an unrestricted basis. Figures were made with Matplotlib version 3.5.2 (Hunter, 2007; Caswell et al., 2022) and seaborn version 0.12.2 (Waskom, 2021).

Conflicts of Interest Statement

The authors have no conflicts of interest to declare.

Acknowledgments
The authors gratefully acknowledge funding by a grant from the VILLUM Foundation (grant number: 13168) and the European Research Council (ERC) under the European Union's Horizon 2020 research and innovation program (grant number: 771859) and the Novo Nordisk Foundation Interdisciplinary Synergy Program (grant no. NNF19OC0057374). This work used resources of the Deutsches Klimarechenzentrum (DKRZ), granted by its Scientific Steering Committee (WLA) under project ID bb1166. Additionally, the authors thank the Trans-African Hydro-Meteorological Observatory (TAHMO) for the provision of meteorological data. Interested parties may contact info@tahmo.org for these data.

References

Adams, D. K., Fernandes, R. M., Holub, K. L., Gutman, S. I., Barbosa, H. M., Machado, L. A., ... others (2015). The amazon dense gnss meteorological network: A new approach for examining water vapor and deep convection interactions in the tropics. *Bulletin of the American Meteorological Society*, *96*(12), 2151–2165.

Andrews, P. C., Cook, K. H., & Vizy, E. K. (2023). Mesoscale convective systems in the congo basin: seasonality, regionality, and diurnal cycles. *Climate Dynamics*, 1–22. doi: 10.1007/s00382-023-06903-7

Böing, S. J. (2016). An object-based model for convective cold pool dynamics. *Mathematics of Climate and Weather Forecasting*, *2*(1).

Camberlin, P., Gitau, W., Planchon, O., Dubreuil, V., Funatsu, B. M., & Philippon, N. (2018). Major role of water bodies on diurnal precipitation regimes in eastern africa. *International Journal of Climatology*, *38*(2), 613-629. Retrieved from `https://rmets.onlinelibrary.wiley.com/doi/abs/10.1002/joc.5197` doi: https://doi.org/10.1002/joc.5197

Caswell, T. A., Droettboom, M., Lee, A., de Andrade, E. S., Hoffmann, T., Klymak, J., ... Ivanov, P. (2022). *matplotlib/matplotlib: Release (version 3.5.2) [software]*. Zenodo. Retrieved from `https://doi.org/10.5281/zenodo.6513224` doi: 10.5281/zenodo.6513224

Caton Harrison, T., Washington, R., & Engelstaedter, S. (2021). Satellite-derived characteristics of saharan cold pool outflows during boreal summer. *Journal of Geophysical Research: Atmospheres*, *126*(3), e2020JD033387.

Chandra, A. S., Zuidema, P., Krueger, S., Kochanski, A., de Szoeke, S. P., & Zhang, J. (2018). Moisture distributions in tropical cold pools from equatorial indian

ocean observations and cloud-resolving simulations. *Journal of Geophysical Research: Atmospheres*, *123*(20), 11–445.

Charba, J. (1974). Application of gravity current model to analysis of squall-line gust front. *Monthly Weather Review*, *102*(2), 140–156.

Drager, A. J., Grant, L. D., & van den Heever, S. C. (2020). Cold pool responses to changes in soil moisture. *Journal of Advances in Modeling Earth Systems*, *12*(8), e2019MS001922.

Emmel, C., Knippertz, P., & Schulz, O. (2010). Climatology of convective density currents in the southern foothills of the atlas mountains. *Journal of Geophysical Research: Atmospheres*, *115*(D11).

Engerer, N. A., Stensrud, D. J., & Coniglio, M. C. (2008). Surface characteristics of observed cold pools. *Monthly Weather Review*, *136*(12), 4839–4849.

EUMETSAT. (2012). *The conversion from effective radiances to equivalent brightness temperatures (version 1).* Retrieved from `https://www-cdn.eumetsat.int/files/2020-04/pdf_effect_rad_to_brightness.pdf`

Feng, Z., Hagos, S., Rowe, A. K., Burleyson, C. D., Martini, M. N., & de Szoeke, S. P. (2015). Mechanisms of convective cloud organization by cold pools over tropical warm ocean during the amie/dynamo field campaign. *Journal of Advances in Modeling Earth Systems*, *7*(2), 357–381.

Fiévet, R., Meyer, B., & Haerter, J. O. (2022). On the sensitivity of convective cold pools to mesh resolution. *Earth and Space Science Open Archive*, 24. Retrieved from `https://doi.org/10.1002/essoar.10512297.1` doi: 10.1002/essoar.10512297.1

Fournier, M. B., & Haerter, J. O. (2019). Tracking the gust fronts of convective cold pools. *Journal of Geophysical Research: Atmospheres*, *124*(21), 11103–11117.

Gentine, P., Garelli, A., Park, S., Nie, J., Torri, G., & Kuang, Z. (2016). Role of surface heat fluxes underneath cold pools. *Geophys. Res. Lett.*, *43*, 874-883. doi: 10.1002/2015gl067262

Haerter, J. O. (2019). Convective self-aggregation as a cold pool-driven critical phenomenon. *Geophysical Research Letters*, *46*(7), 4017–4028. doi: https://doi.org/10.1029/2018GL081817

Haerter, J. O., Böing, S. J., Henneberg, O., & Nissen, S. B. (2019). Circling in on convective organization. *Geophysical Research Letters*, *46*(12), 7024–7034. doi: https://doi.org/10.1029/2019GL082092

Haerter, J. O., Meyer, B., & Nissen, S. B. (2020). Diurnal self-aggregation. *npj Climate and Atmospheric Science*, *3*. doi: 10.1038/s41612-020-00132-z

Henneberg, O., Meyer, B., & Haerter, J. O. (2020). Particle-based tracking of cold pool gust fronts. *J. Adv. Model. Earth Syst.*, *12*. doi: 10.1029/2019ms001910

Hitchcock, S. M., Schumacher, R. S., Herman, G. R., Coniglio, M. C., Parker, M. D., & Ziegler, C. L. (2019). Evolution of pre-and postconvective environmental profiles from mesoscale convective systems during pecan. *Monthly Weather Review*, *147*(7), 2329–2354.

Hoeller, J., Fiévet, R., Engelbrecht, E., & Haerter, J. O. (2024a). U-net segmentation for the detection of convective cold pools from cloud and rainfall fields. *Journal of Geophysical Research: Atmospheres*, *129*(1), e2023JD040126.

Hoeller, J., Fiévet, R., & Haerter, J. O. (2023). Detecting cold pool family trees in convection resolving simulations. *Authorea Preprints*.

Hoeller, J., Haerter, J. O., & Da Silva, N. (2024b). *Identification algorithm for cold pool gust fronts in weather station data from equatorial africa (version 2.0) [software].* Zenodo. Retrieved from `https://doi.org/10.5281/zenodo.10117788` doi: 10.5281/zenodo.10117788

Hunter, J. D. (2007). Matplotlib: A 2d graphics environment. *Computing in Science & Engineering*, *9*(3), 90–95. doi: 10.1109/MCSE.2007.55

Jensen, G. G., Fiévet, R., & Haerter, J. O. (2021). The diurnal path to persistent convective self-aggregation. *arXiv preprint arXiv:2104.01132*.

Kirsch, B., Ament, F., & Hohenegger, C. (2021). Convective cold pools in long-term boundary layer mast observations. *Monthly Weather Review*, *149*(3), 811–820.

Kruse, I. L., Haerter, J. O., & Meyer, B. (2022). Cold pools over the netherlands: A statistical study from tower and radar observations. *Quarterly Journal of the Royal Meteorological Society*, *148*(743), 711–726.

Langhans, W., & Romps, D. M. (2015). The origin of water vapor rings in tropical oceanic cold pools. *Geophysical Research Letters*, *42*(18), 7825–7834.

Meyer, B., & Haerter, J. O. (2020, 11). Mechanical forcing of convection by cold pools: Collisions and energy scaling. *J. Adv. Model. Earth Syst.*, *12*(11), n/a–n/a. Retrieved from `https://doi.org/10.1029/2020MS002281` doi: 10.1029/2020MS002281

Mueller, C. K., & Carbone, R. E. (1987). Dynamics of a thunderstorm outflow. *Journal of the Atmospheric sciences*, *44*(15), 1879–1898.

Niehues, J., Jensen, G. G., & Haerter, J. O. (2022). Self-organized quantization and oscillations on continuous fixed-energy sandpiles. *Physical Review E*, *105*(3), 034314.

Nissen, S. B., & Haerter, J. O. (2021). Circling in on convective self-aggregation. *Journal of Geophysical Research: Atmospheres*, *126*(20), e2021JD035331.

Parker, D. J., Fink, A., Janicot, S., Ngamini, J.-B., Douglas, M., Afiesimama, E., ... others (2008). The amma radiosonde program and its implications for the future of atmospheric monitoring over africa. *Bulletin of the American Meteorological Society*, *89*(7), 1015–1028.

Purdom, J. F. (1976). Some uses of high-resolution goes imagery in the mesoscale forecasting of convection and its behavior. *Monthly Weather Review*, *104*(12), 1474–1483.

Redl, R., Fink, A. H., & Knippertz, P. (2015). An objective detection method for convective cold pool events and its application to northern africa. *Monthly Weather Review*, *143*(12), 5055–5072.

Schlemmer, L., & Hohenegger, C. (2016). Modifications of the atmospheric moisture field as a result of cold-pool dynamics. *Quarterly Journal of the Royal Meteorological Society*, *142*, 30–42. doi: https://doi.org/10.1002/qj.2625

Simpson, J. (1980). Downdrafts as linkages in dynamic cumulus seeding effects. *Journal of Applied Meteorology*, *19*(4), 477–487.

Tompkins, A. M. (2001a). Organization of tropical convection in low vertical wind shears: The role of cold pools. *Journal of the Atmospheric Sciences*, *58*, 1650-1672. doi: 10.1175/1520-0469(2001)058<1650:ootcil>2.0.co;2

Tompkins, A. M. (2001b). Organization of tropical convection in low vertical wind shears: The role of water vapor. *Journal of the Atmospheric Sciences*, *58*(6), 529–545.

Torri, G., & Kuang, Z. (2019). On cold pool collisions in tropical boundary layers. *Geophys. Res. Lett.*, *46*, 399-407. doi: 10.1029/2018gl080501

Torri, G., Kuang, Z., & Tian, Y. (2015). Mechanisms for convection triggering by cold pools. *Geophysical Research Letters*, *42*(6), 1943–1950.

van de Giesen, N., Hut, R., & Selker, J. (2014). The trans-african hydro-meteorological observatory (tahmo). *Wiley Interdisciplinary Reviews: Water*, *1*(4), 341–348.

van den Heever, S. C., Grant, L. D., Freeman, S. W., Marinescu, P. J., Barnum, J., Bukowski, J., ... others (2021). The colorado state university convective cloud outflows and updrafts experiment (c 3 loud-ex). *Bulletin of the American Meteorological Society*, *102*(7), E1283–E1305.

Vogel, R. (2017). *The influence of precipitation and convective organization on the structure of the trades* (Unpublished doctoral dissertation). Universität Hamburg Hamburg, Retrieved from `https://pure.mpg.de/rest/items/item_2503092/component/file_2503091/content`.

Vogel, R., Konow, H., Schulz, H., & Zuidema, P. (2021). A climatology of trade-

wind cumulus cold pools and their link to mesoscale cloud organization. *Atmospheric Chemistry and Physics*, *21*(21), 16609–16630.

Wakimoto, R. M. (1982). The life cycle of thunderstorm gust fronts as viewed with doppler radar and rawinsonde data. *Monthly weather review*, *110*(8), 1060–1082.

Waskom, M. L. (2021). seaborn: statistical data visualization. *Journal of Open Source Software*, *6*(60), 3021. Retrieved from `https://doi.org/10.21105/joss.03021` doi: 10.21105/joss.03021

Zhang, G., Cook, K. H., & Vizy, E. K. (2016). The diurnal cycle of warm season rainfall over west africa. part i: Observational analysis. *Journal of Climate*, *29*(23), 8423 - 8437. doi: 10.1175/JCLI-D-15-0874.1

Zipser, E. (1977). Mesoscale and convective–scale downdrafts as distinct components of squall-line structure. *Monthly Weather Review*, *105*(12), 1568–1589.

Zuidema, P., Li, Z., Hill, R. J., Bariteau, L., Rilling, B., Fairall, C., ... Hare, J. (2012). On trade wind cumulus cold pools. *Journal of the Atmospheric Sciences*, *69*(1), 258–280.

Zuidema, P., Torri, G., Muller, C., & Chandra, A. (2017). A survey of precipitation-induced atmospheric cold pools over oceans and their interactions with the larger-scale environment. *Surveys in Geophysics*, 1–23.

References From the Supporting Information

Bolton, D. (1980). The computation of equivalent potential temperature. Monthly weather review , 108 (7), 1046–1053.

Wallace, J. M., & Hobbs, P. V. (2006). Atmospheric science: an introductory survey (Vol. 92). Elsevier.

Supporting Information for "Characteristics of Station-Derived Convective Cold Pools Over Equatorial Africa"

Jannik Hoeller[1,2], Jan O. Haerter[1,2,3,4], Nicolas Da Silva[1]

[1]Integrated Modeling, Leibniz Centre for Tropical Marine Research, Fahrenheitstr. 6, 28359 Bremen, Germany

[2]Niels Bohr Institute, Copenhagen University, Blegdamsvej 17, 2100 Copenhagen, Denmark

[3]Physics and Earth Sciences, Constructor University Bremen, Campus Ring 1, 28759 Bremen, Germany

[4]Department of Physics and Astronomy, University of Potsdam, Karl-Liebknecht-Straße 32, 14476 Potsdam, Germany

Contents of this file

1. Text S1 to S2
2. Tables S1 to S2
3. Figures S1 to S3

Introduction

Text S1 describes the computation employed for mixing ratio, saturated mixing ratio, equivalent potential temperature, and temperature at the lifting condensation level. Text S2 presents two contrasting examples of observed cold pools (CPs). Table S1 contains geographic information regarding the deployed automatic weather stations. Table S2

summarizes statistics on the 4218 CPs which we identified in five-minute near-surface data of twelve automatic weather stations in tropical Africa, recorded between January 1, 2019 and September 30, 2023. Fig. S1 shows the station-derived seasonal and diurnal cycle of near-surface equivalent potential temperature for different regions across equatorial Africa. Fig. S2 shows two probability distributions of satellite-derived properties of the identified CP gust fronts. Fig. S3 visualizes the two contrasting examples of observed CPs presented in Text S2.

As in the main article, the statistics in Table S2, as well as the data in Fig. S1 and Fig. S2, are grouped based on the stations' deployment countries to enable an investigation of regional differences. In addition to general information on CP occurrence, Table S2 contains data on the strength of station-observed near-surface CP anomalies, as well as satellite-observed brightness temperatures. We assess the overall strength of a an anomaly by its largest extreme value in the time window from $t_0 - 20\,min$ to $t_0 + 120\,min$. Only for temperature, T, based on which the CP onset was defined, we consider the time window from t_0 to $t_0 + 120\,min$ instead. For simplicity we refer to extreme values of anomalies as perturbations and denote them with a "δ". Whether the identified extreme values are maxima or minima depends on the variable and the detected CP: While we exclusively search for minima for T and equivalent potential temperature (θ_e), we look for maxima for wind gust speed (u_g), relative humidity (RH) and atmospheric pressure (p). For specific humidity, q, which may exhibit positive as well as negative perturbations, we search for both minima and maxima and consider the extreme value with the larger absolute value as perturbation. We define a maximum or minimum, respectively, as the

largest local maximum or minimum in the corresponding time window. An instantaneous measurement $y(t)$ at time t is a local maximum if $y(t - 5\,min) \leq y(t) > y(t + 5\,min)$ and analogously for a local minimum. If a certain anomaly record of an identified CP has missing values or does not have an extreme value, we do not assign a perturbation. With respect to satellite-observed brightness temperatures, we evaluate the minimum brightness temperature, $BT_{10.8}^{min}$ by determining the minimum $10.8\,\mu m$ brightness temperature in the time window from $\hat{t}_0 - 60\,min$ to $\hat{t}_0 + 120\,min$, i.e., the corresponding time window around the satellite-observed CP onset, $\hat{t}_0$, which we define in the main article.

Text S1.

Based on the station-measured variables, we compute the saturated vapor pressure of water, e_{sat}, using equation 10 of Bolton (1980). We then derive the saturated mixing ratio, r_{sat}, by plugging e_{sat} and the station-measured atmospheric pressure, p, into the following equation from chapter 3.5.1 of Wallace and Hobbs (2006):

$$r_{sat} = 0.622 \frac{e_{sat}}{p - e_{sat}}. \tag{1}$$

To compute the mixing ratio, r, we adapt equation 3.64 of Wallace and Hobbs (2006). For the computation of the temperature at the lifting condensation level, T_{LCL}, and the equivalent potential temperature, θ_E, we employ equation 22 and 43, respectively, of Bolton (1980).

Text S2.

The first CP (Fig. S3a) was detected in DR Congo at station TA00673 on November 28, 2021, at 13:40 UTC and associated with a mesoscale convective system, visible in the satellite-derived $10.8\,\mu m$ brightness temperature image at 13:45 UTC (Fig. S3b). The corresponding brightness temperature timeseries of all different wavelength channels (Fig. S3d) show a significant brightness temperature decrease at the station location around CP onset, with a maximum decrease rate coinciding with the onset. Between 12:30 and 14:45 UTC, the brightness temperature dropped by $85\,K$ in the $10.8\,\mu m$ channel and then slowly increased again. Concurrently, the station record (Fig. S3f) reveals a massive air temperature drop of $9.6\,K$ between 13:40 and 14:00 UTC, accompanied by increased wind gust speeds of up to $6.5\,m\,s^{-1}$. By 14:00 UTC, when the temperature had

stabilized, the air became fully saturated. Five minutes later, the rainfall intensity peaked at approximately $65\,mm\,h^{-1}$.

The second CP (Fig. S3; right column) was detected in Uganda at station TA00222 on July 2, 2021, at 12:05 UTC. During the time it was detected, the CP featured arc-shaped shallow convection at the gust front, distinctly separated from the parent convection by clear skies (Fig. S3c). The corresponding brightness temperature timeseries at the station (Fig. S3e) confirm the passage of low-level clouds precisely coinciding with the time of the station-derived CP onset. Around the CP onset, no rainfall was measured at the station (Fig. S3g). The observed wind gust speed increased approximately 5–10 minutes before the drop in air temperature and reached a peak value of $10\,m\,s^{-1}$ at CP onset.

References

Bolton, D. (1980). The computation of equivalent potential temperature. *Monthly weather review*, *108*(7), 1046–1053.

Wallace, J. M., & Hobbs, P. V. (2006). *Atmospheric science: an introductory survey* (Vol. 92). Elsevier.

Table S1. Geographic information regarding the deployed automatic weather stations.

Station code	Country	Latitude [°N]	Longitude [°E]	Elevation [m]
TA00220	Uganda	1.21	32.74	1047
TA00222	Uganda	1.19	32.02	1069
TA00224	Uganda	0.57	32.64	1168
TA00410	DR Congo	0.82	24.46	464
TA00459	Nigeria	9.07	6.57	198
TA00580	Nigeria	7.84	9.78	162
TA00581	Nigeria	9.35	12.50	220
TA00584	Nigeria	7.80	8.62	104
TA00673	DR Congo	0.07	18.31	311
TA00717	Cameroon	3.90	11.89	734
TA00728	Cameroon	2.82	11.13	581
TA00730	Cameroon	3.47	11.49	665

Table S2. Summary of observed cold pool (CP) statistics including the total number of CPs and CPs per day, along with median values of different CP properties; sub- and superscripts indicate the interquartile range.

	Cameroon	DR Congo (eq.)	Nigeria	Uganda	All
$\#CPs$	788	649	1028	1753	4218
$\#CPs/day$	0.26	0.25	0.18	0.41	0.27
δT	$-4.90^{+1.20}_{-1.70}$	$-5.50^{+1.60}_{-1.80}$	$-5.40^{+1.40}_{-2.00}$	$-5.30^{+1.50}_{-2.00}$	$-5.30^{+1.50}_{-1.90}$
δq	$-3.08^{+1.07}_{-1.13}$	$-3.73^{+1.04}_{-1.20}$	$-3.77^{+1.10}_{-1.08}$	$-1.92^{+1.29}_{-0.95}$	$-2.83^{+1.26}_{-1.26}$
δu_g	$2.85^{+1.28}_{-1.00}$	$2.85^{+1.43}_{-1.01}$	$4.53^{+1.91}_{-1.47}$	$3.18^{+1.25}_{-0.90}$	$3.24^{+1.37}_{-1.06}$
$\delta\theta_e$	$-15.94^{+4.25}_{-5.10}$	$-18.58^{+4.64}_{-6.32}$	$-18.54^{+5.09}_{-5.46}$	$-12.54^{+4.48}_{-4.58}$	$-15.56^{+4.84}_{-5.37}$
δRH	$0.15^{+0.07}_{-0.07}$	$0.16^{+0.07}_{-0.08}$	$0.14^{+0.08}_{-0.05}$	$0.21^{+0.08}_{-0.07}$	$0.17^{+0.07}_{-0.07}$
δp	$1.23^{+0.77}_{-0.67}$	$1.35^{+0.75}_{-0.77}$	$1.67^{+0.83}_{-0.68}$	$0.85^{+0.60}_{-0.45}$	$1.20^{+0.75}_{-0.65}$
$BT^{min}_{10.8}$	211^{+18}_{-12}	204^{+12}_{-8}	203^{+15}_{-7}	217^{+26}_{-12}	210^{+20}_{-11}

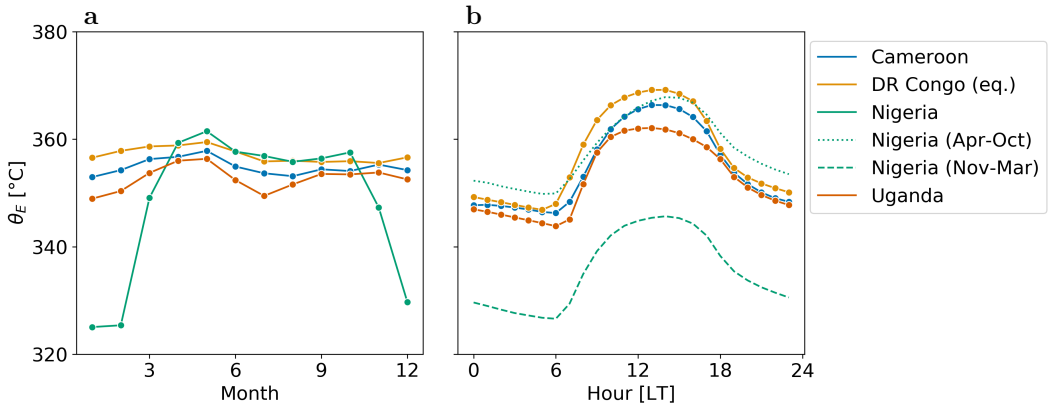

Figure S1. Station-derived seasonal and diurnal cycle of near-surface equivalent potential temperature, θ_E. **a**, Mean θ_E for each month. Lines interpolate linearly between markers to facilitate the interpretation; colors indicate different regions. **b**, Mean θ_E at different times of the day. Each marker represents the mean value for a given 3-hour time interval, starting with the interval [0,3) for the marker at 0 LT. Lines and colors analogous to (a). The two lines for Nigeria represent rainy months (Apr–Oct, dotted) and dry months (Nov–Mar, dashed).

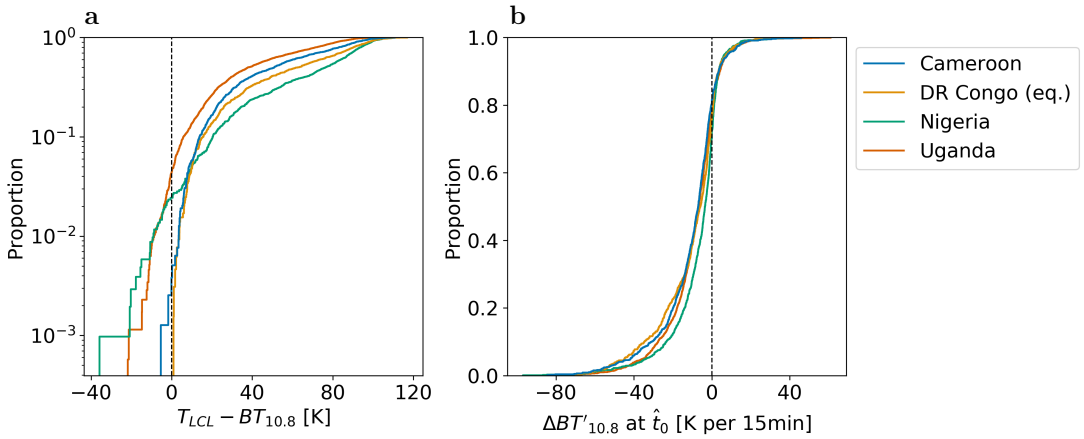

Figure S2. Probability distributions of satellite-derived cold pool (CP) properties. **a**, Distribution of the difference between the temperature at the lifting condensation level, T_{LCL}, and the corresponding 10.8 μm brightness temperature, $BT_{10.8}$ of identified CP gust fronts; to increase the robustness, the difference is calculated based on the mean values of the two measurements at the nearest satellite time steps around the station-derived CP onset, t_0. Values below zero represent gust fronts with clear skies. Colors indicate different regions. **b**, Distribution of the temporal change of 10.8 μm brightness temperature anomalies, $\Delta BT'_{10.8}$, at the satellite-observed CP onset, $\hat{t}_0$; colors analogous to (a).

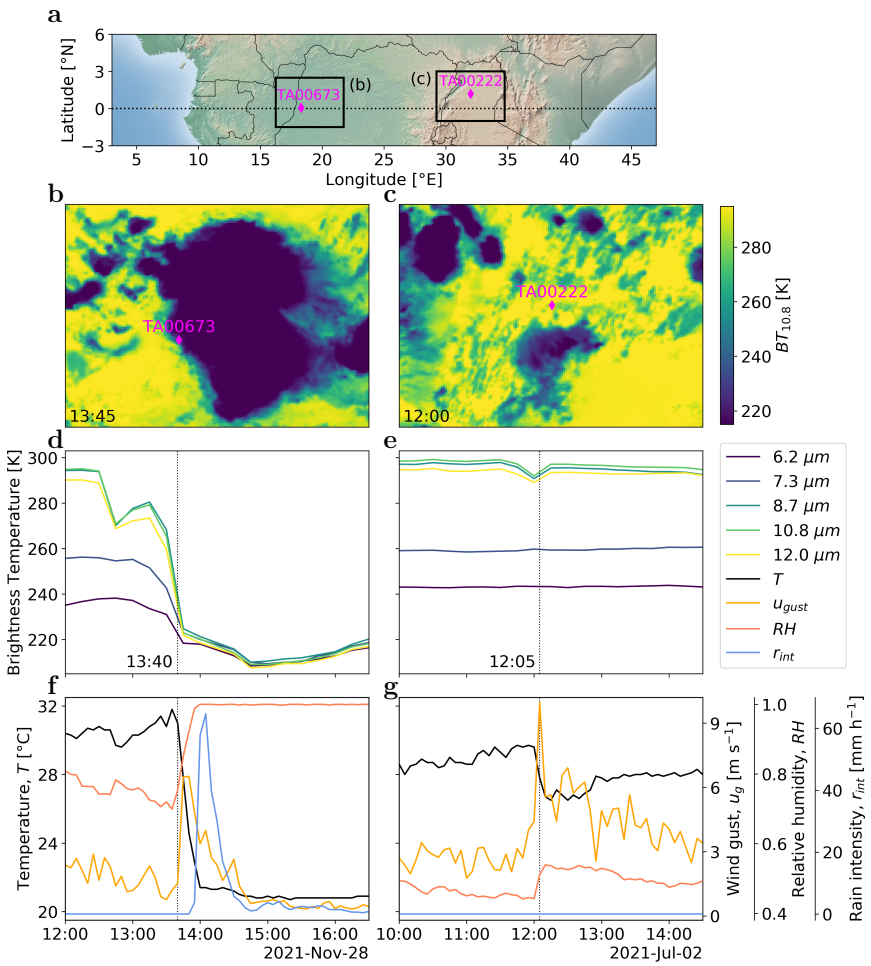

Figure S3. Cold pool (CP) case studies. **a**, Map displaying the locations of the stations utilized in the two case studies. Rectangles indicate the regions depicted in (b) and (c). **b**, Satellite-derived 10.8μm brightness temperatures, $BT_{10.8}$, in the vicinity of station TA00673 on November 28, 2021, at 13:45, close to a station-derived CP onset at 13:40. **c**, Analogous to (b) but for station TA00222 on July 2, 2021, at 12:00 and a CP onset at 12:05. **d**, Timeseries of satellite-derived brightness temperatures at station TA00673 during the CP event visualized in (b). **e**, Analogous to (d) but for the CP event at station TA00222 visualized in (c). **f-g**, Analogous to (d-e) but for different near-surface observations.

February 29, 2024, 6:51am

5.2 Detecting Cold Pool Family Trees in Convection Resolving Simulations

The following manuscript introduces a novel algorithm designed for the detection and tracking of CPs in cloud-resolving simulation data. Inspired by the physical process of CP formation, the algorithm identifies individual CPs based on labeled rainfall patches that have the potential to give rise to CPs under specific conditions. Each CP that forms inherits the same label as its parent rain patch. By tracking the causal relationships between CP events and the rain patches they trigger, the algorithm facilitates investigations into the role of CPs in convective organization. Moreover, as the algorithm incorporates both thermodynamic and dynamic variables, the boundaries of segmented CPs closely correspond to the locations of new convective initiation. As a result, the algorithm serves as a valuable tool for automatically generating ground truth data to train and test neural networks using simulated satellite observations, a capability utilized in manuscript III (Section 5.3).

Check for updates

JAMES | Journal of Advances in Modeling Earth Systems

RESEARCH ARTICLE
10.1029/2023MS003682

Detecting Cold Pool Family Trees in Convection Resolving Simulations

Jannik Hoeller[1,2], Romain Fiévet[2], and Jan O. Haerter[1,2,3,4]

[1]Integrated Modeling, Leibniz Centre for Tropical Marine Research, Bremen, Germany, [2]Niels Bohr Institute, Copenhagen University, Copenhagen, Denmark, [3]Physics and Earth Sciences, Constructor University Bremen, Bremen, Germany, [4]Department of Physics and Astronomy, University of Potsdam, Potsdam, Germany

Key Points:

- Our CoolDeTA algorithm reliably detects and tracks cold pools and their causal chains
- We propose a simple conceptual model which reproduces the cascade-like mesoscale cold pool dynamics identified by CoolDeTA
- CoolDeTA opens for new studies into the dynamics of convective self-organization through cold pools

Supporting Information:

Supporting Information may be found in the online version of this article.

Correspondence to:

J. Hoeller,
jannik.hoeller@leibniz-zmt.de

Citation:

Hoeller, J., Fiévet, R., & Haerter, J. O. (2024). Detecting cold pool family trees in convection resolving simulations. *Journal of Advances in Modeling Earth Systems*, *16*, e2023MS003682. https://doi.org/10.1029/2023MS003682

Received 22 FEB 2023
Accepted 16 DEC 2023

Abstract Recent observations and modeling increasingly reveal the key role of cold pools in organizing the convective cloud field. Several methods for detecting cold pools in simulations exist, but are usually based on buoyancy fields and fall short of reliably identifying the active gust front. The current cold pool (CP) detection and tracking algorithm (CoolDeTA), aims to identify cold pools and follow them in time, thereby distinguishing their active gust fronts and the "offspring" rain cells generated nearby. To accomplish these tasks, CoolDeTA utilizes a combination of thermodynamic and dynamical variables and examines the spatial and temporal relationships between cold pools and rain events. We demonstrate that CoolDeTA can reconstruct CP family trees. Using CoolDeTA we can contrast radiative convective equilibrium (RCE) and diurnal cycle CP dynamics, as well as cases with vertical wind shear and without. We show that the results obtained are consistent with a conceptual model where CP triggering of children rain cells follows a simple birth rate, proportional to a CP's gust front length. The proportionality factor depends on the ambient atmospheric stability and is lower for RCE, in line with marginal stability as traditionally ascribed to the moist adiabat. In the diurnal case, where ambient stability is lower, the birth rate thus becomes substantially higher, in line with periodic insolation forcing—resulting in essentially run-away mesoscale excitations generated by a single parent rain cell and its CP.

Plain Language Summary Cold pools are cooled air masses below thunderstorm clouds, produced when rain evaporates underneath such clouds. Cold pools are important, as they produce strong gusts and have been associated with clumping of rain cells, whereby heavy rainfall over relatively small areas could be generated—with implications for flooding. The current work describes a method that helps identify such cold pools in computer simulation data. In contrast to earlier methods, we here show that the interaction between a CP and its surroundings can be reconstructed by the method. We show that this identification works under a range of contexts, such as when horizontal wind is applied in the simulations or when the surface temperature is not constant—as might often be the case over a land surface. The identification reveals interesting dynamical effects, such as that in some cases, cold pools can kick-start a form of chain reaction, by which "rain cell children" of it give rise to additional cold pools that again produce children, and so forth. The dynamics revealed is in line with expectations of widespread, so-called mesoscale convective systems over land, whereas over an ocean surface the dynamics is much less explosive.

1. Introduction

Convectively-generated cold pools are dense air masses forming beneath precipitating thunderstorm clouds when a fraction of hydrometeors evaporates within the subcloud layer (Droegemeier & Wilhelmson, 1985; Simpson, 1980). Besides the higher density compared to their surroundings, cold pools manifest themselves by a divergent near-surface wind field and vortical structures along their "dynamical edges," that is, the demarcation between the cold pool (CP) and the ambient atmosphere. Many recent studies have considered the characteristics of cold pools (Drager & van den Heever, 2017; Fournier & Haerter, 2019; Gentine et al., 2016; Henneberg et al., 2020; Schlemmer & Hohenegger, 2016; Torri & Kuang, 2019), because they have been implicated in the spatio-temporal organization of the convective cloud field—thus impacting non-random organization of rainfall, with consequences for extreme events, such as flooding (Böing, 2016; Haerter et al., 2019; Jensen et al., 2021; Schlemmer & Hohenegger, 2016; Simpson, 1980; Tompkins, 2001b).

Observationally, measuring cold pools is difficult, as high-resolution spatio-temporal records of the subcloud boundary layer are required to track a given spreading CP. Field campaigns thus often remain restricted to a

© 2024 The Authors. Journal of Advances in Modeling Earth Systems published by Wiley Periodicals LLC on behalf of American Geophysical Union.
This is an open access article under the terms of the Creative Commons Attribution License, which permits use, distribution and reproduction in any medium, provided the original work is properly cited.

19422466, 2024, 1, Downloaded from https://agupubs.onlinelibrary.wiley.com/doi/10.1029/2023MS003682 by Cochrane Germany, Wiley Online Library on [28/02/2024]. See the Terms and Conditions (https://onlinelibrary.wiley.com/terms-and-conditions) on Wiley Online Library for rules of use; OA articles are governed by the applicable Creative Commons License

particular, often spatially confined area (Feng et al., 2015; Hohenegger et al., 2023), use point-like or lower-dimensional measurements (Engerer et al., 2008; Zuidema et al., 2017), or need to resort to indirect signals, such as cleared areas in radar imagery (de Szoeke et al., 2017) or combinations of point and radar measurements (Kruse et al., 2022). Yet, from existing observational studies, it is evident that CP interactions help structure the cloud field and qualify as a mechanism to induce thunderstorm precipitation cells (Moncrieff & Liu, 1999). Measurements of the ocean temperature after CP events also point to lowered sea surface temperatures after pronounced CP occurrences (Pei et al., 2018), thus possibly giving rise to locally anti-correlated rain activity.

Numerical approaches hardly suffer from a lack of data coverage. Yet, in the past, three-dimensional simulations at cloud-resolving $\mathcal{O}(100m)$ resolution have not been possible over domain sizes of several hundred kilometers and weeks, required for reaching steady state dynamics. In recent years, however, the required scales have become accessible, and numerical simulations aimed at improving our understanding of cold dynamics have become feasible. For instance, process-oriented computer simulations have helped appreciate the role of cold pools in organizing the thermal and momentum structure within the subcloud layer (Böing et al., 2012). Further, numerical studies have helped elucidate the role of surface heat fluxes, induced by cold pools as they move along (Torri & Kuang, 2016), a dynamics which might affect the formation of so-called moisture rings (Chandra et al., 2018). The partitioning of surface heat fluxes into latent and sensible contributions was found to be strongly dependent on soil moisture, a variable which conversely also affects the size and propagation speed of cold pools due to changes in boundary layer humidity and rain shaft areas (Drager et al., 2020; Gentine et al., 2016).

On the larger-scale level of simulated mesoscale organization, cold pools have been suggested as a possible cause for non-random distributions of rain cells in space (Haerter et al., 2019), which may arise when CP gust fronts collide to trigger new cells at the loci of collision (Böing, 2016; Moseley et al., 2016; Torri & Kuang, 2019). Cold pools were also found to affect the moisture distribution in the subcloud layer (Böing et al., 2012; Schlemmer & Hohenegger, 2016) and may thereby aid the transitioning from shallow to deep convection (Kurowski et al., 2018). Even the paradigmatic "convective self-aggregation" (CSA), a system-scale symmetry breaking, was found to be affected by CP activity (Haerter, 2019; Jeevanjee & Romps, 2013; Muller et al., 2022; Nissen & Haerter, 2021). In an effort to study more realistic configurations, recent numerical experiments employ temporally varying surface temperatures to investigate the impact of the diurnal cycle on correlated CP activity, especially regarding the formation of mesoscale convective systems (MCS) (Haerter et al., 2020; Jensen et al., 2021), stimulating conceptual models to help explain the complex processes involved (Niehues et al., 2021).

Interestingly, only few attempts have been made at parameterizing cold pools in larger-scale climate models (Grandpeix & Lafore, 2010; Rio et al., 2009; Rooney et al., 2021). This may be due to an incomplete understanding of the fundamental processes affecting CP interaction, dynamics, and thermodynamic modifications of the boundary layer, as well as the pre-moistening of the lower free troposphere. Process-focused studies that leave out parts of the components involved (Fiévet et al., 2023; Haerter & Schlemmer, 2018; Meyer & Haerter, 2020; Romps & Jeevanjee, 2016), may help improve parameterizations further.

Several recent works have brought forward methods to track cold pools, in particular their gust fronts, in numerical simulations (Drager & van den Heever, 2017; Fournier & Haerter, 2019; Henneberg et al., 2020; Hirt et al., 2020; Rochetin et al., 2021; Schlemmer & Hohenegger, 2016). Yet, the detection of cold pools in numerical simulations is far from trivial: (a) the area affected by rainfall, where the CP is fed by rain evaporation, is often not cleanly delimited and subject to setting a threshold value, for example, on the precipitation rate; (b) the CP density current, as a highly dynamic object, experiences turbulent mixing and heat exchange with the surface and ambient environment, and is subject to spontaneous symmetry breaking, such as under the formation of "lobe-and-cleft" instabilities—again feeding back on the dynamics (Härtel et al., 2000; Markowski & Richardson, 2010; Simpson, 1972; Wakimoto, 2001); (c) the larger-scale pattern of cold pools and the rain cells produced by their collisions, is highly complex, with families formed by CP-rain cell networks making for a challenging tracking problem.

The current work addresses these challenges by building an algorithm which identifies cold pools and their causal chains based on a combination of buoyancy and dynamical measures. We apply our algorithm to cloud resolving simulation data based on radiative convective equilibrium (RCE) and diurnal cycle setups with and without wind shear to examine the impact of the simulation setup on CP dynamics. Based on the identified causal chains of cold pools, we investigate how the total accumulated rainfall of a given CP relates to (a) its capacity to trigger new rain

19422466, 2024, 1, Downloaded from https://agupubs.onlinelibrary.wiley.com/doi/10.1029/2023MS003682 by Cochrane Germany, Wiley Online Library on [28/02/2024]. See the Terms and Conditions (https://onlinelibrary.wiley.com/terms-and-conditions) on Wiley Online Library for rules of use; OA articles are governed by the applicable Creative Commons License

cells and (b) the number of colliding cold pools which triggered its parent convection. Furthermore, we show examples of derived CP family trees and propose a simple conceptual model that replicates the observed cascade-like dynamics of cold pools within MCS.

2. Methods

2.1. Cloud Resolving Simulation Data

We employ the System for Atmospheric Modeling (SAM) (Khairoutdinov & Randall, 2006) to simulate the convective cloud field for a set of numerical experiments. The horizontal domain size is chosen to be square $L \times L$, with $L = 240$ km in all simulations, and the horizontal grid spacing Δh is chosen as $\Delta h = 200$ m throughout, thus yielding $N = 1{,}200$ grid boxes in each horizontal dimension. Cyclic boundary conditions are chosen in both horizontal dimensions. We found this horizontal mesh resolution a suitable compromise, where relatively large domain sizes can be simulated for several days, yet, key CP effects, such as the dynamic gust front, can be simulated at satisfactory detail (Bryan et al., 2003; Fiévet et al., 2023; Hirt et al., 2020; Meyer & Haerter, 2020; Straka et al., 1993). The mesh is discretized along the vertical direction z using 64 levels of increasing depth Δz, ranging from $\Delta z = 50$ m at the first level ($z = 25$ m) to 1,000 m at the domain's top boundary ($z = 26$ km). The model resolves a non-hydrostatic anelastic form of the Euler equations, and uses the liquid water static energy and the total precipitating/nonprecipitating water mixing ratios as prognostic variables. We use the embedded one-moment microphysics scheme (Khairoutdinov & Randall, 2003) along with a first-order turbulent subgrid scheme (Smagorinsky, 1963). The radiative fluxes are calculated using the National Center for Atmospheric Research Community Atmosphere Model version 3 (Collins et al., 2006).

The surface conditions are prescribed and taken as a (saturated) sea surface of a given, horizontally-homogeneous surface temperature T_s, that is, $T_s(x, y, t) = T_s(t)$. We distinguish two sensitivities:

1. To mimic a *diurnal cycle*, we allow $T_s(t)$ to vary sinusoidally as

$$T_s(t) = \overline{T}_s - \Delta T \cos(2\pi\, t/T). \tag{1}$$

   here, $\overline{T}_s = 298$ K and ΔT is either chosen as 0 K, which we term "rce," or as 2 and 4 K, respectively, termed "diu."
2. To simulate *large scale wind shear*, we additionally impose a height dependent wind tendency in the x-direction, with a piecewise linear profile given by

$$\begin{aligned} u_0(z < 1\,\text{km}) &= 0, \\ u_0(1\,\text{km} < z < 19\,\text{km}) &= \delta_u \left(\frac{z - 1\,\text{km}}{18\,\text{km}} \right), \\ u_0(z > 19\,\text{km}) &= \delta_u. \end{aligned} \tag{2}$$

The velocity field is nudged toward this profile using a typical linear-relaxation term in the momentum equation with a timescale of $\tau = 1$ day. This timescale is chosen to preserve the internal subdiurnal variability occurring through convective organization, such as through CP dynamics.

The above settings for ΔT and wind shear give rise to the six setups used in this paper, namely rce0K, diu2K, and diu4K, which can each have $\delta_u = 0$ or $\delta_u = 16$ m s^{-1}. For each setup we run the simulation for 7.5 days.

The integration time step, $\sim\mathcal{O}(s)$, varies accordingly with a maximum admissible Courant-Friedrichs-Lewy (CFL) number of 0.8. The simulation output frequency is of one every $\Delta t = 10$ min. Each Δt, the following instantaneous fields are output: surface rainfall intensity $I(x, y, t)$, near-surface specific humidity $q(x, y, t) = q(x, y, z = 25\text{ m}, t)$, virtual temperature $T_v(x, y, t) = T_v(x, y, z = 25\text{ m}, t)$, the horizontal wind vector $\mathbf{u} \equiv (u, v)$, with $u = u(x, y, z = 25\text{ m}, t)$ and $v = v(x, y, z = 25\text{ m}, t)$ as the lowest-level horizontal wind components in the x and y directions, and near-surface vertical wind speed $w = w(x, y, z = 25\text{ m}, t)$. For simplicity, we refer to Δt as the "time step" throughout the paper. The discrete time $t = t_n \equiv n\Delta t$, measured from the beginning of the simulation, is often denoted by the integer time step n. Similarly, we use integers $i \in \{1, \ldots, N\}$ and $j \in \{1, \ldots, N\}$ to

19422466, 2024, 1, Downloaded from https://agupubs.onlinelibrary.wiley.com/doi/10.1029/2023MS003682 by Cochrane Germany, Wiley Online Library on [28/02/2024]. See the Terms and Conditions (https://onlinelibrary.wiley.com/terms-and-conditions) on Wiley Online Library for rules of use; OA articles are governed by the applicable Creative Commons License

label the two discrete positions $x = x_i \equiv i\Delta h$ and $y = y_j \equiv j\Delta h$. Note that $x_i = x_{i+N}$ and $y_j = y_{j+N}$ in accordance with the cyclic boundary conditions. For a given 2D field Q we often use $Q(i, j, n)$ to refer to the numerical value of Q at horizontal position (x_i, y_j) and time t_n.

2.2. Cold Pool Detection and Tracking Procedure

The main goal of the proposed algorithm is to detect and track cold pools in data from numerical simulations, while observing and identifying the involved causal relations between cold pools and rain cells: On the one hand, cold pools require evaporating precipitation and are thus inevitably linked to particular rain cells. To accommodate this causal relation, rain cells are taken as the origin of cold pools in the proposed algorithm. Thus, a rain cell is a required condition for the identification of a CP. Each rain cell in the domain is assigned a unique rain identification number (ID). In case a rain cell generates a CP, the CP receives the same ID as the associated rain cell. On the other hand, CP gust fronts can trigger new rain cells, which might again generate new cold pools (Böing, 2016; Haerter et al., 2019; Tompkins, 2001a). Accordingly, the algorithm stores rain cells triggered at a CP gust front, as well as potential cold pools emerging from these rain cells, as children of that particular CP. In this manner, the algorithm not only detects and tracks cold pools, but also their relationships.

The proposed CP detection and tracking algorithm (CoolDeTA) consists of four main steps: (a) identification of rain patches (RPs), (b) segmentation of the domain into "potential CP" and "no CP" regions, (c) derivation of markers, and (d) labeling of cold pools. These steps are performed for every output time step of the respective simulation or simulation time window.

For notational convenience we introduce several definitions:

- The deviation of any given scalar quantity $Q(i, j, n)$ relative to its spatial mean is denoted as

$$Q'(i,j,n) = Q(i,j,n) - \overline{Q}(n), \tag{3}$$

  where $\overline{Q}(n)$ denotes the spatial mean at t_n.
- Occasionally, we require Q at a given time step t_n to be normalized to the range between zero and one. This is accomplished by the rescaling

$$\hat{Q}(i,j,n) = \frac{Q(i,j,n) - \min(Q(n))}{\max(Q(n)) - \min(Q(n))}, \tag{4}$$

  where $\min(Q(n))$ or $\max(Q(n))$ refer to the minimum and maximum of the two-dimensional field $Q(n)$ at time step t_n.
- For simpler notation we write the Kronecker delta symbol as $\delta(a, b)$, which equals unity for $a = b$ and zero otherwise.
- Two (spatial) indices (i, j) and (i', j') are considered contiguous, if $dist((i,j) - (i',j')) = 1$, where *dist* denotes the shortest distance operator, which ensures cyclic boundary conditions on the toroidal square lattice geometry.
- We use $p_r(i, j, n)$ and $p_{cp}(i, j, n)$ to indicate $N \times N$ integer fields for labeling RPs and CP patches at time step t_n. Analogously, we also define an auxiliary field $p_{seg}(i, j, n)$. For either, we define a superscript m as labeling the subset of indices (i, j, n) of p_r or p_{cp}, where the integer is equal to m, for example, $p_r^m \equiv \{(i,j,n) \in [1,N] \times [1,N] \times [1 \wedge p_r(i,j,n) = m]\}$.

(i) *Identifying RPs*. At any discrete time t_n a *RP* is defined as a spatially contiguous region in which the rain intensity $I(x_i, y_j, t_n) \geq I_0$. Generally, we employ $I_0 = 2$ mm hr^{-1}, which has been determined as critical rate for downdrafts penetrating into the subcloud layer (Barnes & Garstang, 1982). The algorithm assigns a unique ID to every RP identified by this procedure. In this way, $p_r(i, j, n)$ is populated at each time step t_n, where

$$p_r(i,j,n) = \begin{cases} 0 \text{ if } I(i,j,n) < I_0 \\ \text{otherwise: ID of respective rain patch.} \end{cases} \tag{5}$$

19422466, 2024, 1, Downloaded from https://agupubs.onlinelibrary.wiley.com/doi/10.1029/2023MS003682 by Cochrane Germany, Wiley Online Library on [28/02/2024]. See the Terms and Conditions (https://onlinelibrary.wiley.com/terms-and-conditions) on Wiley Online Library for rules of use; OA articles are governed by the applicable Creative Commons License

For robustness, a given RP, labeled m, at time step index n is only retained if its area $A(p_r,n,m) \equiv \Delta h^2 \sum_{i,j=1}^{N} \delta(p_r(i,j,n),m) \geq A_0$, where we use $A_0 = 2\ \mathrm{km}^2$ as a threshold. Otherwise, the corresponding values of p_r are set to zero.

(ii) *Segmentation*. At each time t_n, we use an indicator field

$$\mathcal{I}_{seg}(i,j,n) = \hat{s}'(i,j,n) + \left(1 - \hat{T}_v'(i,j,n)\right), \tag{6}$$

where $s'(i, j, n)$ are the horizontal wind speed fluctuations, computed as

$$s'(i,j,n) \equiv \sqrt{u'(i,j,n)^2 + v'(i,j,n)^2}. \tag{7}$$

$\mathcal{I}_{seg}(i,j,n)$ is a measure which we assume to be increased in areas where cold pools are present. Since cold pools are associated with fluctuating horizontal wind speeds but decreased virtual potential temperatures, $\hat{T}_v'(i,j,n)$ in Equation 6 is subtracted from unity, that is, relatively low T_v increases the probability of a CP. The two quantities are combined with equal weights to ensure equal importance is given to both thermodynamic and dynamical features. We choose perturbations rather than absolute quantities in Equation 6 to be able to apply the method to simulations with other boundary conditions, such as non-zero surface winds, and thus increase the method's scope of application.

A k-means algorithm (Pedregosa et al., 2011) now subdivides every grid cell (i, j) into two cluster groups, namely "potential CP" or "no CP" by minimizing the one-dimensional distance metric within both cluster groups. The result is a horizontal $N \times N$ binary segmentation $p_{bin}(i, j, n)$ with $p_{bin}(i, j, n) = 1$ for all "potential CP" grid cells and $p_{bin}(i, j, n) = 0$ for all "no CP" cells. As an example, Figure 1a shows the corresponding histogram of $\mathcal{I}_{seg}$ for diu4K at time step t_{471} representing a morning scene. The lower and upper cluster groups represent regions where cold pools are considered prohibited versus feasible. A "cold pool" grid cell must fall within the feasible cluster group. Yet, additional criteria below are required.

Spreading quickly beyond the boundaries of their RPs, fully developed cold pools should at least encompass the same area as their related RPs. Thus, we apply the minimum area A_0 criterion from (i) also to the identified "potential CP" regions. For this reason, spatially contiguous "potential CP" regions in $p_{bin}(i, j, n)$ are identified and labeled with a unique integer number. The result is, analogous to (i), a horizontal $N \times N$ integer field $p_{seg}(i, j, n)$ where a patch, labeled m, is only retained if its area $A(p_{seg},n,m) \equiv \Delta h^2 \sum_{i,j=1}^{N} \delta\left(p_{seg}(i,j,n),m\right) \geq A_0$.

(iii) *Deriving markers*. A marker could be defined as a center of mass (COM) of a given RP m at time t_n. We however found that the actual (dynamical) downdraft within this patch more precisely marks the CP center. A good choice for the downdraft field $\mathcal{I}_{Tw}(i,j,n)$ was found to be a combination of normalized temperature and vertical velocity, namely

$$\mathcal{I}_{Tw}(i,j,n) = \hat{T}(i,j,n) + \hat{w}(i,j,n), \tag{8}$$

so that for a given patch, labeled m,

$$\mathcal{I}_{mar}^{m}(i,j,n) = 1 - \hat{\mathcal{I}}_{Tw}^{m}(i,j,n), \tag{9}$$

which is large for locations of minimal temperature and vertical velocity. The corresponding COM, $\left(C_x^m, C_y^m\right)$, follows as

$$C_x^m = \frac{\sum_{i,j=1}^{N} x_i \mathcal{I}_{mar}^{m}(i,j,n)}{\sum_{i,j=1}^{N} \mathcal{I}_{mar}^{m}(i,j,n)}, \tag{10}$$

19422466, 2024, 1, Downloaded from https://agupubs.onlinelibrary.wiley.com/doi/10.1029/2023MS003682 by Cochrane Germany, Wiley Online Library on [28/02/2024]. See the Terms and Conditions (https://onlinelibrary.wiley.com/terms-and-conditions) on Wiley Online Library for rules of use; OA articles are governed by the applicable Creative Commons License

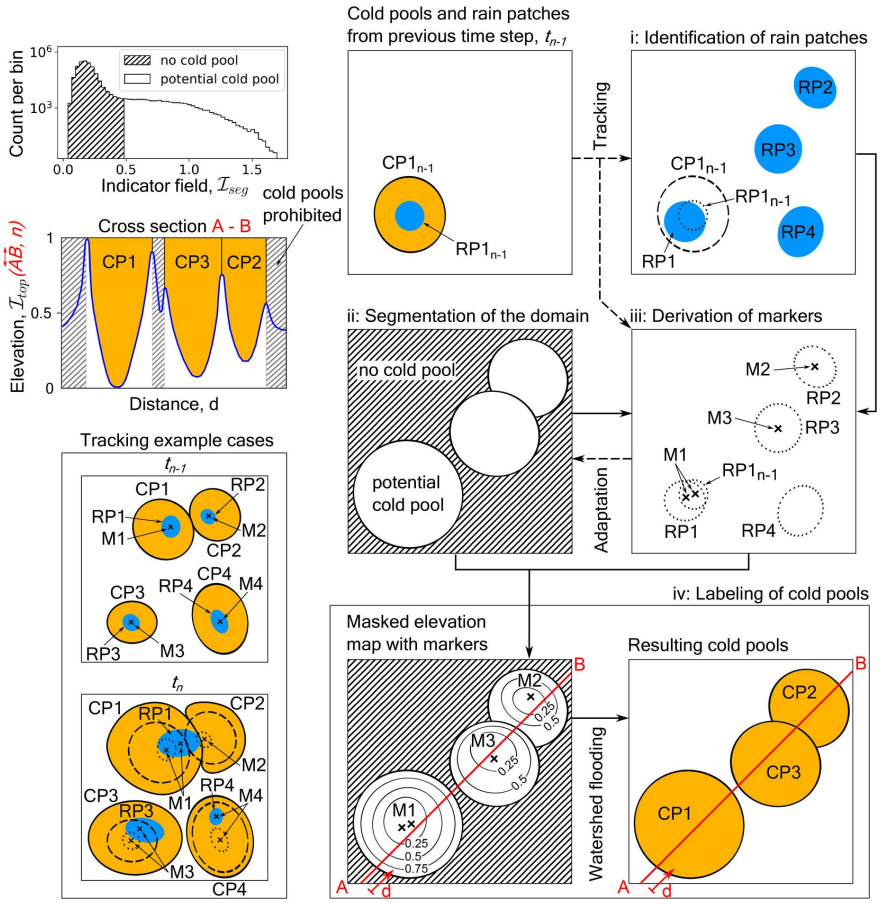

Figure 1. *Proposed cold pool (CP) detection and tracking algorithm.* (a) Histogram of the indicator field, $\mathcal{I}_{seg}(i,j,n)$ (Equation 6), for diu4K at t_{471}. "no cold pool (CP)" and "potential CP" grid cells, as determined by the k-means algorithm, are shown as hatched and striped curve fillings. (b) Main algorithm steps: Rain patches (RPs) and CPs are shown as blue and orange areas, respectively. Markers (Ms) are denoted as "x"-symbols; Dashed and dotted lines indicate CP and RP contours, respectively. The steps are repeated for every simulation output time step Δt. (c) Elevation map values (blue curve), $\mathcal{I}_{top}\left(\overleftrightarrow{AB}, n\right)$, of grid cells on line $\overleftrightarrow{AB}$ defined in (b), step (iv) for time step t_n. Hatched areas are locations classified as "no CP" by the segmentation, and thus not flooded by the watershed algorithm. The elevation of these "no CP" regions can be thought of as infinite. Orange areas represent labeled CPs which result from flooding the elevation map from the markers M1, M2 and M3. (d) Example cases for the tracking of RPs and CPs. In time step t_n (labeled above panels), RP1, RP3 and RP4 are tracked from t_{n-1}. Each marker represents an RP center of mass and acts as starting point for the watershed flooding.

and analogously for C_y^m. $\left(C_x^m, C_y^m\right)$ maps onto a 2D index $\left(i_{mar}^m, j_{mar}^m\right)$ by determining the nearest integer pixel indices. We collect these marker indices into a field $p_{mar}(i, j, n)$, where $p_{mar}\left(i_{mar}^m, j_{mar}^m, n\right) = m$ and which is zero for all locations without markers.

When the rain associated with a CP labeled m from the previous time step t_{n-1} stops, the CP will have no active RP p_r^m in $p_r(i, j, n)$ anymore, that is, $\sum_{i,j=1}^{N} \delta\left(p_r(i,j,n), m\right) = 0$. However, cold pools may still spread and trigger new convection. Therefore, we in this case introduce their latest rain marker to $p_{mar}(i, j, n)$ instead.

19422466, 2024, 1, Downloaded from https://agupubs.onlinelibrary.wiley.com/doi/10.1029/2023MS003682 by Cochrane Germany, Wiley Online Library on [28/02/2024]. See the Terms and Conditions (https://onlinelibrary.wiley.com/terms-and-conditions) on Wiley Online Library for rules of use; OA articles are governed by the applicable Creative Commons License

Apart from the *rain* marker in the center of the active or latest RP, cold pools which were present in the previous time step t_{n-1} obtain an *origin* marker. An origin marker represents the first rain marker which initially generated the CP, that is, the center of its initial RP. Analogous to the rain markers, origin markers are introduced to $p_{mar}(i, j, n)$. The combination of origin and rain markers increases the robustness of the final CP labeling, which will be illustrated in step (iv).

(iv) *Labeling cold pools*. For a time step t_n, the final field with labeled cold pools, $p_{cp}(i, j, n)$, is—analogous to the RP field $p_r(i, j, n)$ (compare Equation 5)—a horizontal $N \times N$ integer ID field where $p_{cp}(i, j, n)$ specifies the ID of a CP or $p_{cp}(i, j, n) = 0$, if no CP is present at (i, j) and time index n. The CP field is obtained using a watershed algorithm (van der Walt et al., 2014), which can be thought of as placing different water sources in a topographical map and flooding it up to the highest elevation (see Figure 1c), such that the water table is equal in all basins. The resulting watersheds represent the boundaries between the different water sources and the corresponding basins represent regional minima.

In order to derive the labeled CP field, we provide the watershed algorithm with three ingredients: the locations of the water sources, that is, the marker locations $p_{mar}(i, j, n)$ computed in step (iii), an elevation map $\mathcal{I}_{top}$, and a mask, which acts like a stencil preventing certain regions from being flooded. The elevation map is computed as

$$\mathcal{I}_{top}(i,j) = \hat{T}(i,j) + \hat{q}^2(i,j) + \hat{w}(i,j). \tag{11}$$

Cold pool regions are characterized by cold (low $\hat{T}(i,j)$) and often dry air (low $\hat{q}(i,j)$) which forms basins with regional minima in the elevation map, whereas horizontal convergence with associated vertical updrafts towers up walls at CP boundaries (large $\hat{w}(i,j)$), thus separating the CP basins from each other. The mask, as a final ingredient to the watershed algorithm, is provided by the binary segmentation $p_{bin}(i, j, n)$ from step (ii). Whereas CP1 and CP3 in Figure 1c are separated by the mask's "no CP" region between them, CP2 and CP3 are in contact with each other. The contact location, that is, the point where the two cold pools collide (in 2D, it is a line), depends on the elevation map $\mathcal{I}_{top}$. Since water from different sources, representing different cold pools, does not mix, the contact location remains constant for the rest of the flooding.

Since only its gust front should separate a CP from its environment, we do not allow holes, that is, enclosed grid cells with different ID values, within individual cold pools. Thus, we close potential holes within individual cold pools by assigning each grid cell of the hole the ID of the surrounding CP. By this procedure, we thus merge cold pools if the grid cells of the hole carry the ID of other cold pools.

In later stages, a CP basin in the elevation map can consist of multiple local minima, caused by newly formed RPs within the CP area or an advected initial RP. By providing both rain and origin markers to cold pools which were present in the previous time step t_{n-1}, we make sure that cold pools in later stages of their life cycle are not accidently flooded by neighboring cold pools.

Figure 1b summarizes the main steps of CoolDeTA. Note that both tracking and the interactions between steps (ii) and (iii) will be described separately in the following Sections 2.3 and 2.6, respectively.

2.3. Cold Pool Tracking

Provided that RPs, $p_r(i, j, n-1)$, and/or cold pools, $p_{cp}(i, j, n-1)$, from the previous time step t_{n-1} are available, we track cold pools already during the identification of RPs in step (i). Since a RP, labeled m in $p_r(i, j, n)$, obtains a corresponding marker $p_{mar}\left(i^m_{mar}, j^m_{mar}, n\right) = m$, an associated CP which might be identified based on the watershed algorithm in step (iv) would be labeled m in $p_{cp}(i, j, n)$, as well. The label m thus represents the ID of a RP in $p_r(i, j, n)$ and the ID of an associated CP in $p_{cp}(i, j, n)$. Accordingly, cold pools can be tracked by adjusting the label of tracked RPs in step (i). For this purpose, we evaluate the spatial overlap of patches from consecutive time steps. A RP labeled m' at time step t_n is tracked if the overlap with a RP labeled m from time step t_{n-1}, $O_r(m,m',n-1,n) \geq f_r \times A\left(p_r^{m'}\right)$ with $f_r = 0.01$ and

$$O_r(m,m',n-1,n) \equiv \sum_{i=1,j=1}^{N,N} \mathbf{1}((i,j) \in S_1), \tag{12}$$

19422466, 2024, 1, Downloaded from https://agupubs.onlinelibrary.wiley.com/doi/10.1029/2023MS003682 by Cochrane Germany, Wiley Online Library on [28/02/2024]. See the Terms and Conditions (https://onlinelibrary.wiley.com/terms-and-conditions) on Wiley Online Library for rules of use; OA articles are governed by the applicable Creative Commons License

where **1** is the indicator function and the set $S_1 \equiv \{(i,j) \in [1,N] \times [1,N], p_r(i,j,n-1) = m \wedge p_r(i,j,n) = m'\}$, or if the overlap with a CP labeled m from time step t_{n-1}, $O_{cp}(m,m',n-1,n) = f_{cp} \times A\left(p_r^{m'}\right)$ with $f_{cp} = 1$ and

$$O_{cp}(m,m',n-1,n) \equiv \sum_{i=1,j=1}^{N,N} \mathbf{1}((i,j) \in S_2), \tag{13}$$

where the set $S_2 \equiv \{(i,j) \in [1,N] \times [1,N], p_{cp}(i,j,n-1) = m \wedge p_r(i,j,n) = m'\}$. Figure 1d visualizes both cases: On the one hand, RP3 is tracked in time step t_n since the corresponding RP overlaps RP3 from the previous time step t_{n-1}. On the other hand, RP4 is tracked in time step t_n since the corresponding RP fully overlaps CP4 from time step t_{n-1}.

If a RP labeled m' is overlapped sufficiently by a previous RP labeled m_1 and a previous CP labeled m_2, that is, $O_r(m_1,m',n-1,n) \geq f_r \times A\left(p_r^{m'}\right) \wedge O_{cp}(m_2,m',n-1,n) = f_{cp} \times A\left(p_r^{m'}\right)$, the previous CP provides its label, that is, the label of RP m' is replaced with the label m_2. In case RP m' is overlapped by multiple RPs from the previous time step with deviating labels, the RP with the largest overlap, $O_r^{\max}$, provides its label. For this reason, the new RP in time step t_n of Figure 1d which overlaps RP1 and RP2 from the previous time step t_{n-1} is tracked as RP1.

Apart from the rain markers derived from RPs, all cold pools in $p_{cp}(i,j,n-1)$, which existed in the previous time step, receive origin markers and—if they do not have an active RP anymore—also their latest rain marker (see step (iv)). Accordingly, CP1, CP3 and CP4 in Figure 1d each receive two markers in time step t_n, representing the COM of the current RP and that of the initial RP from the previous time step t_{n-1}, respectively, whereas CP2 only receives its latest rain marker from time step t_n. However, due to its origin marker CP2 is still present at time step t_n although it does not possess an active RP anymore.

2.4. Cold Pool Relationships

The association of RPs and cold pools allows the method to consistently label cold pools. Beyond this, through the spatial dependencies, we are also able to capture relationships between individual cold pools. By tracing which CP (gust front) triggered which RP and thus also a potential CP resulting from it, CoolDeTA reveals CP networks and their associated causal chains.

In order to describe the relationships between cold pools, we introduce the roles of "parent" and "child." A RP labeled m' at time step t_n which was not present in time step t_{n-1}, is a child of a CP, labeled m, from time step t_{n-1}, if the overlap $0 < O_{cp}(m,m',n-1,n) < f_{cp} \times A\left(p_r^{m'}\right)$, that is, if the RP intersects the boundary of the CP, but is not fully located within its area. Conversely, CP m becomes a parent of RP m'. If RP m' is a child of CP m and generates a new CP m', the new CP adopts CP m as a parent and becomes its child, as well. Since cold pools can trigger new rain events, they can become parents—both of RPs and the resulting cold pools—as well as children, whereas RPs can only be children.

In case a RP labeled m' at time step t_n which was not present in time step t_{n-1} overlaps multiple cold pools from time step t_{n-1}, any CP m with an overlap $0 < O_{cp}(m,m',n-1,n) < f_{cp} \times A\left(p_r^{m'}\right)$ becomes a parent of RP m' and thus also of potential cold pools resulting from it.

2.5. Cold Pool Dissipation

When the rain associated with a CP stops and thus no longer feeds the density current anymore, the surface boundary layer recovers until the CP is eventually dissipated. However, providing origin markers to cold pools from the previous time step t_{n-1} in time step t_n, cold pools could potentially exist forever, even after their rain has stopped. To rule out infinite lifetime, we implemented a dissipation mechanism within step (iii) of CoolDeTA. To this end, we differentiate between "dissipating" cold pools that are still in the process of dissipating and "dissipated" cold pools that have completely dissipated. We define a CP, labeled m, as dissipating at time step t_n if it has no active rain anymore, that is, $\sum_{i=1,j=1}^{N,N} \mathbf{1}\left((i,j) \in \left\{(i,j) \in [1,N] \times [1,N], p_r(i,j,n) = m\right)\right\} = 0$, and if parts of its latest RP p_r^m from time step t_n^{last} are classified as "no CP" in $p_{bin}(i,j,n)$, that is, $O_{seg}\left(m,1,n^{last},n\right) < 1.0 \times A\left(p_r^m\right)$ with

$$O_{seg}\left(m,1,n^{last},n\right) \equiv \sum_{i=1,j=1}^{N,N} \mathbf{1}((i,j) \in S_3), \tag{14}$$

where the set $S_3 \equiv \{(i,j) \in [1,N] \times [1,N], p_r(i,j,n^{last}) = m \wedge p_{bin}(i,j,n) = 1\}$. For each CP we count the number of time steps in which it is dissipating, n_{dis}. We consider a CP, labeled m, as dissipated if $n_{dis}^m \geq 3$ and $O_{seg}(m, 1, n^{last}, n) = 0$, that is, if it is dissipating for ≥3 time steps (=30 min) and if its latest RP p_r^m is completely classified as "no CP" in $p_{bin}(i,j,n)$. A CP which is dissipated at time step t_n does not obtain markers anymore in $p_{mar}(i,j,n)$ and will thus not exist in the labeled CP field $p_{cp}(i,j,n)$.

2.6. Additional Algorithm Rules

The evolution of the populated fields of both cold pools, p_{cp}, and RPs, p_r, is highly complex. On the one hand, relatively cool air associated with remnants of dissipated cold pools might lead to the misclassification of grid cells as "potential CP" in the segmentation, p_{bin}, in time steps with very weak or suppressed convection and thus only weak down and updrafts. On the other hand, processes such as the merging of RPs or cold pools, as well as the formation of new RPs at CP gust fronts, complicate the tracking. In the following, we introduce several rules implemented in CoolDeTA to increase its robustness with respect to these and other cases.

2.6.1. Divergence Criterion

Cold pools are driven by atmospheric density gradients resulting from the evaporation of rain. Evaporative cooling causes the affected air to sink toward the ground and spread outwards, creating wind gusts. Consequently, cold pools are associated with a horizontally divergent flow in their center and a horizontally converging flow at their gust front. Thus, we only keep a "potential CP" region, labeled m in $p_{seg}(i,j,n)$ at time step t_n, in the segmentation, $p_{bin}(i,j,n)$, if the mean divergence of the horizontal wind field, $\overline{\nabla \cdot \mathbf{u}(i,j,n)} \geq 0$ for grid cells (i,j) in its patch interior $\mathrm{int}\, p_{seg}^m$ and if $\overline{\nabla \cdot \mathbf{u}(i,j,n)} \leq 0$ for grid cells in its patch boundary ∂p_{seg}^m. The divergence is approximated using a central difference scheme. We define a grid cell (i,j) as part of the interior $\mathrm{int}\, p_{seg}^m$ of patch m if all contiguous grid cells are contained in p_{seg}^m. A grid cell (i,j) is part of the boundary ∂p_{seg}^m of patch m if it encompasses at least one contiguous grid cell contained in p_{seg}^m and one contiguous grid cell not contained in p_{seg}^m. Since the "potential CP" region m in $p_{seg}(i,j,n)$ can contain multiple CP instances and thus colliding gust fronts, we exclude a grid cell (i,j) from $\mathrm{int}\, p_{seg}^m$ if $\nabla \cdot \mathbf{u}(i,j,n) < \overline{\nabla \cdot \mathbf{u}(n)} - z_{95th}\, \sigma_d(n)$ where σ_d represents the standard deviation of the horizontal wind field divergence and $z_{95\mathrm{th}} = 1.645$.

Furthermore, new rain cells might be triggered at the boundary of the "potential CP" region m compensating its convergent flow. Analogous to $\mathrm{int}\, p_{seg}^m$ we thus exclude a grid cell (i,j) from ∂p_{seg}^m if $\nabla \cdot \mathbf{u}(i,j,n) > \overline{\nabla \cdot \mathbf{u}(n)} + z_{75th}\, \sigma_d(n) \vee I(i,j,n) \geq 1$ mm/h with $z_{75\mathrm{th}} = 0.675$. We chose deviating factors $z_{95\mathrm{th}}$ and $z_{75\mathrm{th}}$ for the exclusion of grid cells from CP interior and boundary, as colliding CP gust fronts will be associated with relatively strong convergence in the patch interior, whereas new rain cells triggered at the boundary will be associated with relatively weak divergence compared to the domain mean. The values of both $z_{95\mathrm{th}}$ and $z_{75\mathrm{th}}$ were determined by experiment. The exclusion of potentially misleading grid cells, as well as the weak conditions in terms of $\mathrm{int}\, p_{seg}^m$ not being convergent and ∂p_{seg}^m not being divergent ensure that no correctly classified "potential CP" region is dropped.

Due to CP interactions such as collisions and the formation of new cold pools at gust fronts, a CP can loose its occupied area to another CP. To not supersede this process artificially, a CP, labeled m, at the previous time step, t_{n-1}, only obtains an origin marker $p_{mar}^m\left(i_{mar}^m, j_{mar}^m, n\right) = m$ if it still occupied the marker location $\left(i_{mar}^m, j_{mar}^m\right)$ at t_{n-1}, that is, if $p_{cp}\left(i_{mar}^m, j_{mar}^m, n-1\right) = m$.

Apart from CP interactions, where a CP gust front can be pushed toward the CP center, CP gust fronts spread outwards only, due to the horizontally diverging flow in the CP interior. As long as a CP, labeled m, is not dissipated and receives at least one marker at time step t_n, we thus adapt the segmentation $p_{bin}(i,j,n)$ in step (iii) so that all grid cells occupied by the CP at the previous time step t_{n-1}, $p_{cp}(i,j,n-1) = m$, are labeled as "potential CP" in $p_{bin}(i,j,n)$. Whether CP m looses parts of its occupied area to an intersecting CP in time step n depends on the topography of the elevation map, $I_{top}(i,j,n)$, and is determined during the watershed flooding in step (iv).

19422466, 2024, 1, Downloaded from https://agupubs.onlinelibrary.wiley.com/doi/10.1029/2023MS003682 by Cochrane Germany, Wiley Online Library on [28/02/2024]. See the Terms and Conditions (https://onlinelibrary.wiley.com/terms-and-conditions) on Wiley Online Library for rules of use; OA articles are governed by the applicable Creative Commons License

19422466, 2024, 1, Downloaded from https://agupubs.onlinelibrary.wiley.com/doi/10.1029/2023MS003682 by Cochrane Germany, Wiley Online Library on [28/02/2024]. See the Terms and Conditions (https://onlinelibrary.wiley.com/terms-and-conditions) on Wiley Online Library for rules of use; OA articles are governed by the applicable Creative Commons License

Table 1
Parameters and Conditions in the Proposed Algorithm

Parameter	Value/condition used	Description
I_0	2 mm hr^{-1}	Surface rainfall intensity threshold
A_0	2 km^2	Potential CP and RP area threshold
f_r	0.01	Tracking factor for RPs overlapping RPs
f_{cp}	1	Tracking factor for RPs overlapping CPs
	$0 < O_{cp} < 1.0 \times A(p_r)$	Overlap condition for a new RP to become a child of a CP
n_{dis}	3 time steps (30 min)	Dissipation threshold
	$\overline{\nabla \cdot \mathbf{u}} \geq 0$	Divergence criterion for potential CP interior
	$\overline{\nabla \cdot \mathbf{u}} \leq 0$	Divergence criterion for potential CP boundary
f_s	0.75	RP-potential CP overlap factor
	$1 \leq A(p_{cp})/A(p_r) \leq 3$	New CP-RP area ratio

Note. Parameters handling rain intensity threshold, minimal potential cold pool (CP) and rain patch (RP) areas, overlap conditions, and CP dissipation. Parameters and conditions below the horizontal line represent additional algorithm rules.

2.6.2. Additional Overlap Criteria

When new cold pools start to form, grid cells with strong negative temperature perturbations inside the downdraft region might already be classified as "potential CP" in p_{bin}. In order to detect fully developed cold pools only, a new RP, labeled m, detected at time step n, obtains a rain marker at time step n only if $O_{seg}(m,1,n,n) \geq f_s \times A\left(p_r^m\right)$ with $f_s = 0.75$.

The final check is applied to the labeled CP field p_{cp} derived based on the watershed flooding in step (iv). By comparing the area, A_{cp}, of newly formed cold pools with the area, A_r, of their RPs, we get an indication of erroneous labeling. Erroneous labeling can result from cool air remnants being classified as "potential CP" during time steps with very weak or suppressed convection. In this case, markers of isolated rain events could flood areas $A_{cp} \gg A_r$. Another potential source of erroneous labeling is new RPs, triggered at CP gust fronts: Since not each of these RPs generates an independent child CP which is separated from its parent CP by their colliding gust fronts, child cold pools may flood into the area of their parent cold pools and vice versa. Thus, an independent and fully developed CP should, on the one hand, at least feature the size of its RP. On the other, a new CP cannot occupy an area substantially larger than its RP, given the time step of $\Delta t = 10$ min. To intervene only in erroneous cases, we keep a new CP, labeled m, if $1 \leq A\left(p_{cp}^m\right)/A\left(p_r^m\right) \leq 3$. Otherwise, we either drop it, that is, $p_{cp}^m = 0$, if it has no other CP in its neighborhood, or we assign the label of another CP, labeled m', that is, $p_{cp}^m = m'$, otherwise. In the latter case, the CP label m' is determined based on its number of parents, k_p: if $k_p = 0$, it is either the label of the CP which overlaps the largest area of RP m (if $A\left(p_{cp}^m\right)/A\left(p_r^m\right) < 1$), or the label of the CP which lost the largest area with respect to the previous time step t_{n-1} to CP m (if $A\left(p_{cp}^m\right)/A\left(p_r^m\right) > 3$). If $k_p = 1$, CP m is simply assigned the parent label, m_p, that is, $m' = m_p$. The final case, $k_p > 1$, is analogous to the first but based on the parents of CP m.

Table 1 summarizes the parameters and conditions used in the proposed algorithm. Recommendations for the application of CoolDeTA to other simulation setups are provided in Text S1 in Supporting Information S1.

2.7. Analysis of the Simulation Data

We consider the first 3 days (432 time steps) of the simulations as spin-up period. The spin-up period is chosen so that the total domain rainfall per time step, R, has visibly reached a steady state in both the RCE and diurnal cycle setups (Figures 2e and 2f). Further time series are visualized in Figure A1. To be able to track the full life cycle of cold pools and their causal relationships, the onset of convection is an ideal starting point for the analysis with CoolDeTA. Apart from rce0K, where R is essentially constant (Figure 2f), we identify the corresponding starting time step based on the standard deviation of the virtual temperature, σ_{Tv}, and its time derivative, $\dot{\sigma}_{Tv}$. Based on their 1 hr running average, we find $\sigma_{Tv} \geq 0.15$ K and $\dot{\sigma}_{Tv} \geq 0.02$ K s^{-1} as good indicators for the onset of

19422466, 2024, 1, Downloaded from https://agupubs.onlinelibrary.wiley.com/doi/10.1029/2023MS003682 by Cochrane Germany, Wiley Online Library on [28/02/2024]. See the Terms and Conditions (https://onlinelibrary.wiley.com/terms-and-conditions) on Wiley Online Library for rules of use; OA articles are governed by the applicable Creative Commons License

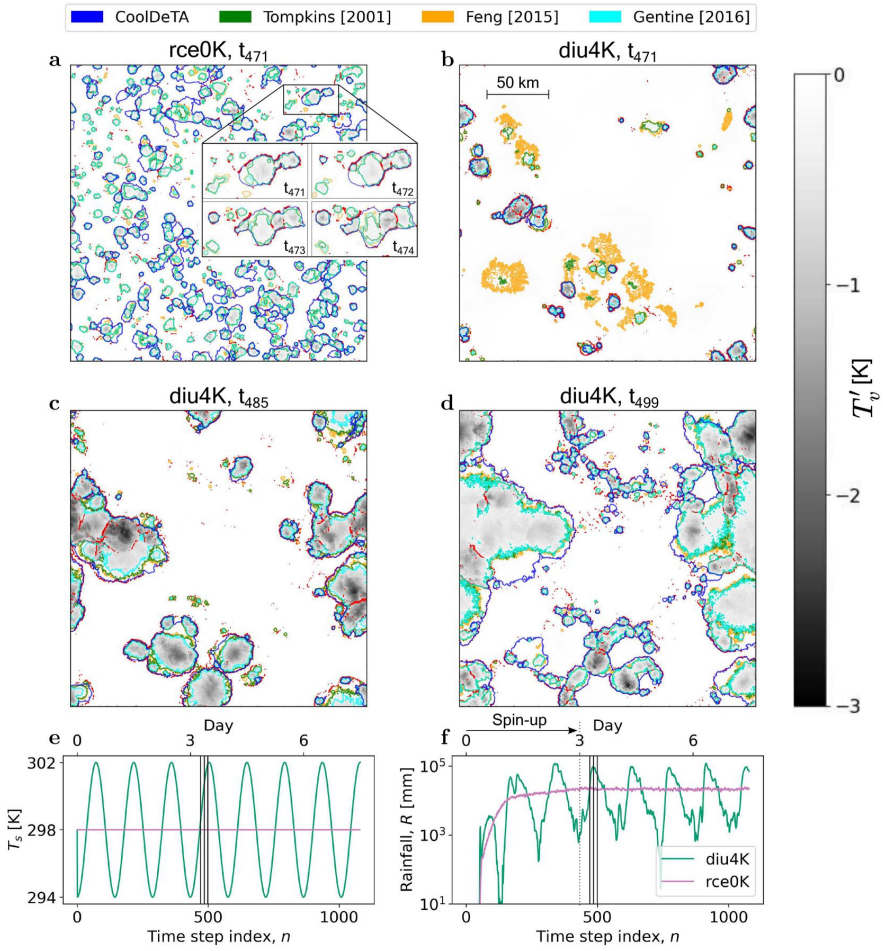

Figure 2. *Comparison of cold pool (CP) detection methods.* (a) Time step index 471 of rce0K, showing near-surface virtual temperature perturbations, T_v', with superimposed dynamical gust front, that is, $w > \overline{w} + 2\sigma_w$ (red scatter); The superimposed colors represent contours of CP patches $\geq A_0$ based on different CP detection methods. The enlarged inset shows a magnification for a subregion highlighting a sequence of four time steps. (b) Analogous to (a) but for diu4K. (c) Analogous to (b) but for time step index 485, corresponding to the peak of diurnal rainfall. (d) Analogous to (b) but for time step index 499. (e) Surface temperature, T_s, for the two simulation setups visualized in (a)–(d); Solid vertical lines within the plot denote the time steps depicted in (a)–(d). (f) Analogous to (e) but for total domain rainfall per time step, R; The chosen spin-up period of 3 days (432 time steps) is indicated by the vertical dotted line and the horizontal arrow above the panel.

convection in our simulations. In the diurnal cycle setups, as well as the rce0K setup with wind shear, we choose the starting time step on day four, t^{start}, so that the two conditions are fulfilled at least for the next hour (6 time steps). For rce0K we simply start the analysis with CoolDeTA at the first time step of day four, at t_{432}.

In the diurnal cycle setups, R oscillates nearly periodically (Figure 2f). Especially in the two diu4K simulation setups, convective activity is largely suppressed during time steps with low T_s. Since the k-means algorithm always clusters the horizontal domain into two groups, namely "potential CP" and "no CP," the segmentation cannot work properly in the absence of cold pools. In such cases, also the additional rules may be insufficient. For this purpose, we stop the CoolDeTA analysis if $R_{px} < 0.001$ mm for more than 30 min (3 time steps) or as soon as $\sigma_{Tv} < 0.15\ \mathrm{K} \wedge R_{px} < 0.0015$ mm, with $R_{px} = \frac{R}{N \times N}$. Analogous to the definition of the start time step, we apply the

19422466, 2024, 1, Downloaded from https://agupubs.onlinelibrary.wiley.com/doi/10.1029/2023MS003682 by Cochrane Germany, Wiley Online Library on [28/02/2024]. See the Terms and Conditions (https://onlinelibrary.wiley.com/terms-and-conditions) on Wiley Online Library for rules of use; OA articles are governed by the applicable Creative Commons License

conditions to the 1 hr running averages of σ_{Tv} and R_{px}. The stop conditions affect only the two diu4K setups, which we stop at the end of each day and re-start on the following day based on the defined start conditions.

3. Results

In the following, we present results of our CP detection and tracking method. We first compare our method to previous ones (Feng et al., 2015; Gentine et al., 2016; Tompkins, 2001a). We then employ our current method to discuss the effect of the simulation setup, that is, wind shear or diurnal cycles, on CP expansion. Third, we make use of our method to analyze the causal relationships between cold pools and their effect on CP rainfall. Based on our findings we then propose a simple model to capture CP spreading-triggering dynamics. We finish the chapter by visualizing the family trees of two cold pools.

3.1. Comparison to Other Methods

Several previous CP detection methods have exploited thermodynamic CP features (Feng et al., 2015; Gentine et al., 2016; Tompkins, 2001a). While Feng et al. (2015) and Tompkins (2001a) use buoyancy thresholds of $-0.005\ \mathrm{m^2\ s^{-1}}$ and $-0.003\ \mathrm{m^2\ s^{-1}}$, respectively, for the detection, Gentine et al. (2016) apply a k-means algorithm to the horizontal virtual temperature field of the first model level to distinguish cold pools from their environment. For an RCE-like setup, rce0K (Figure 2a), as well as a diurnal cycle case, diu4K (Figures 2b–2d), we compare CoolDeTA to such existing methods. The time steps shown are highlighted in the time series (Figures 2e and 2f) as thin vertical lines. Inspecting the different examples (Figures 2a–2d), it is apparent that the CP dynamics in rce0K occurs at relatively small scales $\mathcal{O}(10\,\mathrm{km})$, whereas the dynamics in diu4K ranges from scattered small scale events during the early stages of the diurnal cycle to elaborate mesoscale features $\mathcal{O}(100\,\mathrm{km})$ at the late stages of the diurnal cycle.

A primary goal of CoolDeTA is to detect both thermodynamic and dynamical features of cold pools. To obtain a reference for the latter, we highlight grid cells of pronounced positive vertical velocity in each panel, typically indicating locations of dynamical CP gust fronts (red pixels in Figures 2a–2d). Inspecting the plots, it is apparent that on several occasions, the detection results by all four methods nearly coincide, especially during early stages of CP expansion. However, important differences can also be seen, notably within the inset to panel (a), where CoolDeTA is able to capture the locations of the dynamic gust front (red pixels) reliably, whereas methods based on thermodynamics typically indicate gust fronts that are located further inward, seen for example, by comparing the lines of different colors in the inset. As is visible on the left side of the larger CP patch in t_{473} of the inset, CoolDeTA keeps dissipating CP instances as long as they feature a partly active dynamic gust front.

For the early stage of the diurnal cycle (Figure 2b) the agreement of CoolDeTA, Gentine et al. (2016) and Tompkins (2001a) is arguably good. However, as cold pools spread in the course of the day, the dynamic gust fronts tend to detach from the thermodynamic ones, leading to an increased discrepancy between the methods. It can be visually verified that CoolDeTA is still capable of identifying most regions of strong vertical velocity.

Apart from the common minimum area A_0 which we apply in Figures 2a–2d for CP patches of all methods, CoolDeTA applies the threshold A_0 also to RPs associated with individual cold pools and conducts further checks to confirm the existence of a CP (see Section 2.6). Consequently, the minimum CP area detected by CoolDeTA tends to be larger than for other methods. As a case in point, some of the smaller patches identified by the other methods either suddenly disappear or do not feature a spreading dynamic gust front (Figure 2a, enlarged area), suggesting that CoolDeTA manages to successfully detect only robust cold pools.

3.2. Effect of the Simulation Setup on Cold Pool Expansion

We now employ CoolDeTA to investigate CP temporal expansion and how it depends on the choice of simulation setup. Cold pool expansion is a basic dynamical CP feature, which we here capture as the change in CP area, A_{cp}, over time, on the one hand for cold pools without offspring during their lifetime (Figure 3a) and on the other for cold pools with offspring (Figure 3b). To not distort the results with cold pools which shrink due to CP interactions, we only consider a CP as long as its area is expanding and thus $A_{cp}(n) > A_{cp}(n-1)$.

Conditioning on cold pools without children (Figure 3a), it is noticeable that within the log-log representation, all curves start out following a modest increase of CP area with time. To make contact with previous works suggesting power law dependencies of CP radius on time (Meyer & Haerter, 2020; Rooney, 2015), we indicate a

19422466, 2024, 1, Downloaded from https://agupubs.onlinelibrary.wiley.com/doi/10.1029/2023MS003682 by Cochrane Germany, Wiley Online Library on [28/02/2024]. See the Terms and Conditions (https://onlinelibrary.wiley.com/terms-and-conditions) on Wiley Online Library for rules of use; OA articles are governed by the applicable Creative Commons License

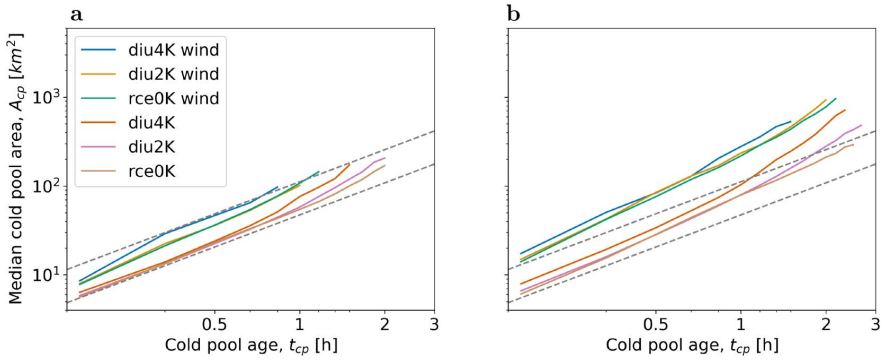

Figure 3. *Cold pool (CP) expansion for various simulation setups*. (a) Median CP area, A_{cp}, versus CP age, t_{cp} for cold pools without any children during their lifetime. Colors represent different simulation setups; Dashed gray lines indicate areas $\propto {t_{cp}}^{1.2}$; Only CP ages with ≥50 cold pools are depicted. (b) Analogous to (a) but for cold pools with children during their lifetime. Note the logarithmic vertical axis scaling.

dependency of $A_{cp} \sim t^{\alpha}$ with $\alpha = 1.2$ (dashed gray lines). After approximately 1 hr of expansion, the curves of setups without wind shear somewhat increase in exponent, thus departing from a power-law dependency. We attribute this to the higher density of cold pools for setups without wind shear, which increases the probability for cold pools to merge with others. The departure is even stronger for diu2K and diu4K where cold pools increasingly cluster within thermodynamically favorable subregions.

The curves for cold pools with children exhibit an increased power-law exponent already at earlier stages (Figure 3b). In comparison to the curves of cold pools without children, the exponent seems to be increasing more strongly, especially during the later stages of expansion. We interpret this strong increase as a consequence of enhanced triggering near CP edges for cold pools with children, whereby the original CP can merge with additional offspring excited by it—thus developing into a mesoscale CP. Apart from this, the diurnal cycle again appears to promote rapid CP expansion, especially during the later stages.

In both Figures 3a and 3b, cold pools under wind shear conditions have larger areas from the outset. A possible reason is the overlap that a RP is required to have with a "potential CP" region in order to obtain a marker and thus form an associated CP: when wind shear is present, rain might reach beyond the emerging CP and limit their overlap.

3.3. Effect of Cold Pool Relationships on Cold Pool Rainfall

Given these findings on CP dynamics we now investigate: (a) how the total accumulated rainfall corresponding to any given CP relates to its capacity to trigger offspring (Figure 4a); and (b) how this rainfall relates to the number of parents of a given CP (Figure 4b). For this purpose, we define the total accumulated rainfall of a CP labeled m as

$$R_{cp}(m) \equiv \sum_{n} \sum_{i,j=1}^{N} \Delta t \; I(i,j,n) \; \delta\big(p_r(i,j,n),m\big). \tag{15}$$

Overall, the majority of cold pools do not give rise to offspring, with approximately 50% of cold pools without detectable children (Figure 5a). However, as we inspect the probability distributions, it is found that, moving from rce0K to diu4K, the distribution function is close to an exponential for rce0K (dotted line), whereas it is well approximated by a power-law $\propto k^{-1.5}$ in the case of diu4K (dashed line). This qualitative finding is also mirrored by the wind shear cases. A power-law distribution hints at a "rich-gets-richer" feedback, where cold pools that have already grown, may be more likely to grow further.

At the same time, it is clear that for large numbers of CP children, associated RPs tend to have much greater total rainfall rates (Figure 4a). These rates range from a factor of two for rce0K to more than an order of magnitude for

19422466, 2024, 1, Downloaded from https://agupubs.onlinelibrary.wiley.com/doi/10.1029/2023MS003682 by Cochrane Germany, Wiley Online Library on [28/02/2024]. See the Terms and Conditions (https://onlinelibrary.wiley.com/terms-and-conditions) on Wiley Online Library for rules of use; OA articles are governed by the applicable Creative Commons License

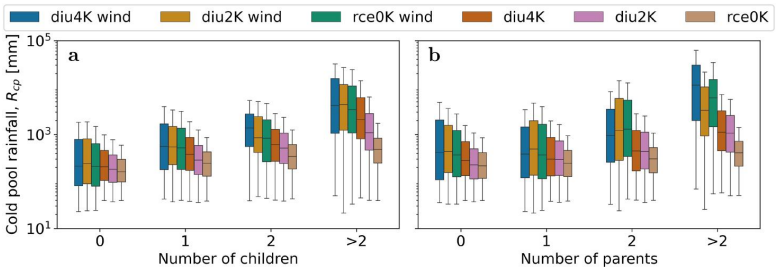

Figure 4. *Total cold pool (CP) rainfall.* (a) Total accumulated rainfall associated with cold pools, R_{cp}, depending on their number of children for different simulation setups. Colored bars represent the interquartile ranges $IQR = Q3 - Q1$ of the simulation setups, with the first quartile $Q1$ and the third quartile $Q3$, along with the corresponding median (horizontal dash). Whiskers range from $Q1 - 1.5 \times IQR$ (minimum) to $Q3 + 1.5 \times IQR$ (maximum); Outliers w.r.t. this range are not visualized. (b) Analogous to (a) but for the number of parents. Note the logarithmic vertical axis scaling.

diu4K. Notable differences also exist between the different setups: diurnal T_s-forcing and wind shear seem to promote larger numbers of children and generally come with greater parent rainfall.

Apart from cold pools with one parent, the relation between parental rainfall and the number of children is almost perfectly mirrored by the number of parents (Figure 4b): larger total rainfall typically implies a larger number of parents. Also, for setups with T_s-diurnal cycles or wind shear, the role of parent cold pools contributing to rain cell formation increases. Yet, the rainfall rates of cold pools with one parent hardly differ from those of cold pools without a parent. We attribute this to the higher risk that a single-parent CP has of getting merged into the parent CP: whereas multiple parents are associated with CP collisions, which interrupt the expansion of the parents, single-parents might still spread and thus merge with excited offspring.

3.4. Simple Cold Pool Offspring Model

To capture CP spreading-triggering dynamics, we suggest a simple model (Figure 5b) where cold pools primarily grow by peripheral spawning of new rain cells, thus child cold pools, that then help the CP expand further. The model is hence different from those in the recent literature (Böing, 2016; Haerter, 2019; Haerter et al., 2019; Nissen & Haerter, 2021) in that the dynamics described previously was inward-directed, such that existing cold pools could excite new convection by collisions among two or three gust fronts. As a result, a given population of cold pools could topologically only cause new convection within the interior of an ensemble of spreading cold pools. In the current model we describe an outward-directed dynamics, where a given evolving mesoscale convective system, embedded in an unstable environment, can give rise to cascading additional convective activity at its periphery—thus leading to an outward expansion of the population of convective cells.

In our model each CP is initialized with an area a of $a = a_0 \equiv 6\ \mathrm{km}^2$ representing the median area of all cold pools from Figure 3 at $t_{cp} = 10$ min, and circumference $l = 2(\pi a_0)^{1/2} \approx 8.7$ km. This circumference is subdivided into segments, each of length $l_0 \equiv 1.6$ km, taken to represent the approximate diameter of a new rain cell of area A_0. Within each segment and time interval $\Delta\tau \sim 20$ min, chosen to represent the timescale of a convective rain cell, the model allows for a new rain cell to be spawned with a small probability $0 < p \ll 1$. The constant $l_0 \ll l$ is thereby assumed to be substantially less than the total circumference l, such that even small cold pools can have several segments. Any new rain cell will add an area increment a_0 to the existing CP area a. In addition, as the CP area increases, its total number of segments $n_s = l/l_0$ will also increase due to the larger circumference. Thus, larger cold pools will typically have a larger number of successful spawning events.

As mentioned, the dynamics proceeds in discrete time steps $\Delta\tau$, during which each segment will be able to experience spawning at probability p. If none of the segments give rise to spawning during the time step, the CP is considered terminated and no further expansion is possible. If a number $m_s > 0$ of segments give rise to spawning, the CP area is incremented by $\Delta a \equiv m_s a_0$ and the expansion proceeds iteratively (tree diagram in Figure 5b). At each fork of the tree diagram, at probability $1 - P(a_i)$ the CP expansion is terminated. $1 - P(a_i)$ represents the probability that none of the segments spawn a new rain cell, that is, for $n_s = l/l_0$ segments and spawning probability p,

19422466, 2024, 1, Downloaded from https://agupubs.onlinelibrary.wiley.com/doi/10.1029/2023MS003682 by Cochrane Germany, Wiley Online Library on [28/02/2024]. See the Terms and Conditions (https://onlinelibrary.wiley.com/terms-and-conditions) on Wiley Online Library for rules of use; OA articles are governed by the applicable Creative Commons License

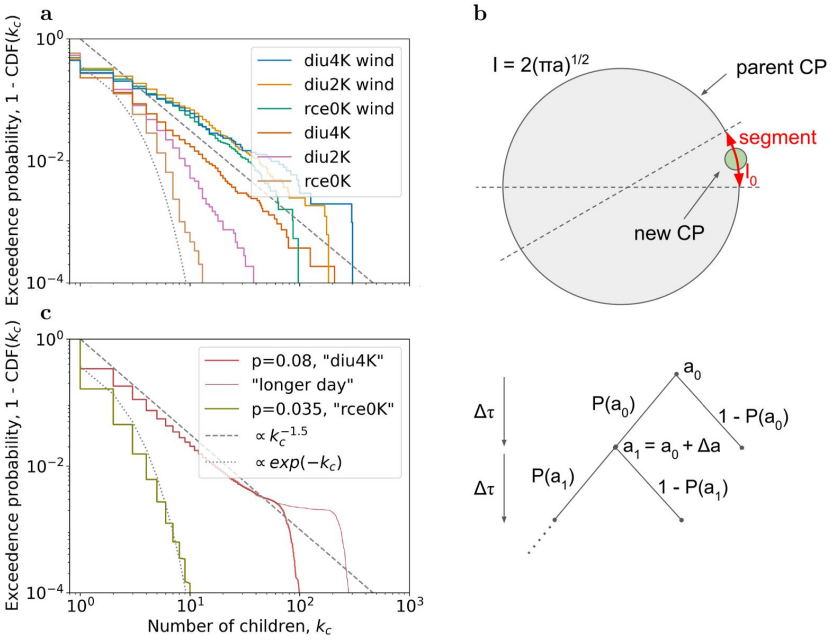

Figure 5. *Children probability distribution*. (a) Exceedance probability for a cold pool (CP) to have a certain number of children; Colors indicate different simulation setups. (b) Simple model for CP expansion and spawning of new rain cells. (c) Analogous to (a) but for our simple model.

$$1 - P(a_i) = (1 - p)^{n_s}. \tag{16}$$

Conversely, the probability for continued CP expansion is

$$P(a_i) = 1 - (1 - p)^{n_s}. \tag{17}$$

As cold pools expand, n_s continues to increase and $P(a_i) \to 1$—thus allowing larger cold pools to experience a larger probability of further expansion.

Simulating the model using a total of 30 time steps $\Delta\tau$ and 10^5 CP realizations allows us to mimic the statistics found for the cloud-resolving simulations (Figure 5c): whereas small values of spawning probability, for example, $p = 0.035$, yield a nearly exponential distribution of the number of children, a larger value of $p = 0.08$ gives rise to approximate power-law decay. Notably, as cold pools grow to large areas, spawning will be essentially guaranteed at subsequent time steps—thus giving rise to run-away expansion. This is verified by allowing for a greater number of 60 time steps (thin brown curve), where a fraction of "successful" cold pools accumulates ever larger numbers of children. Using this model, our interpretation of the CP dynamics is twofold: spawning probability p may be determined by the convective instability surrounding a given parent CP, and different p can yield very different offspring distributions.

For the RCE case, p may be overall modest, as the atmosphere tends to be in a marginally stable state close to the moist adiabat. For the diu cases the situation is quite different, where activity is invigorated by the destabilizing effect of the increased diurnal surface heating—thus allowing for larger values of p, yielding potentially long-tailed offspring distributions. A complete run-away effect is likely prevented by the finite duration of the diurnal heating. It may thus be interesting to revisit the statistics (Figure 5a) for an artificially lengthened diurnal cycle, say, corresponding to a 48 hr-day.

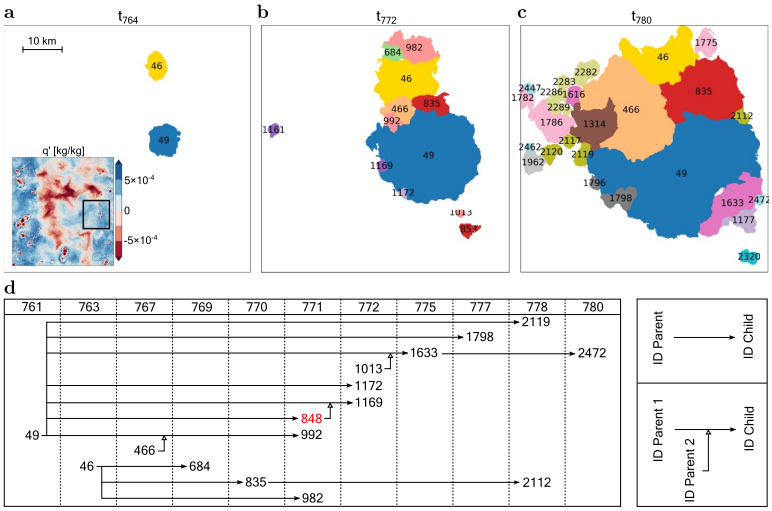

Figure 6. *Cascades of tracked cold pools*. (a) Labeled cold pools for a subsection of the full simulation domain at time step index 764 of diu4K. The inset plot depicts full domain specific humidity anomalies at the same time step; The black square indicates the subsection of interest. (b) Analogous to (a) but without inset plot and for time step index 772. (c) Analogous to (b) but for time step index 780. (d) Family tree for CP "46" and CP "49." The tree features the IDs of all related cold pools which are present in (a)–(c); Columns represent the time steps indices of CP formation; Filled arrows point from the IDs of CP parents to the IDs of CP offspring; Empty arrows denote additional parents; Red text indicates the IDs of cold pools that are not present in the depicted time steps of (a)–(c), but which contributed to the related cold pools.

3.5. Cold Pool Family Trees

Based on a subsection of the full simulation domain we now visualize an example of the temporal evolution of a labeled CP field from diu4K (Figures 6a–6c), along with the corresponding family trees of the two initial cold pools (Figure 6d). The subsection of interest is indicated as black square in the inset which shows the specific humidity anomalies, q', for the full simulation domain at t_{764}. Like most of the other regions in which cold pools start forming (dark red blobs with large gradients), the subsection of interest features a moisture-rich surface layer. Here, the two initial cold pools depicted in Figure 6a, CP46 (yellow patch) and CP49 (blue patch), formed at t_{763} and t_{761}, respectively (Figure 6d).

In Figure 6b, 80 min later, the two cold pools have expanded and several offspring have been generated. However, CP848 (red ID in Figure 6d), one of the first children of CP49 which was triggered at the freely expanding gust front, could only exist for one time step until it was merged by its parent. Although CP848 contributed to the formation of the new CP CP1169 (see Figure 6d), it is thus not present anymore at t_{772}. Comparing Figures 6b and 6c, it is apparent that also the other cold pools which were triggered at freely expanding gust fronts, namely CP684, CP982, CP1169 and CP1172, shared the same fate. Only the two cold pools CP466 and CP835 in the collision zone of CP46 and CP49 are still present at t_{780} and managed to expand over the former area of CP46 and CP49. Since it is not evident from Figure 6b we note that CP466 and CP835 formed before the collision of CP46 and CP49, otherwise both CP46 and CP49 would be their parents.

4. Discussion

Cold pools have been implicated in a large range of cloud field properties, including the formation of MCS (Haerter et al., 2020; Houze Jr, 2004; Jensen et al., 2021; Kain & Fritsch, 1992; Schumacher & Rasmussen, 2020), the evolution of squall lines (M. D. Parker, 2008; D. J. Parker & Diop-Kane, 2017; Rotunno et al., 1988; Weisman et al., 1988), the organization of trade-wind cumuli (Dauhut et al., 2022; Seifert & Heus, 2013; Vogel et al., 2021; Zuidema et al., 2012) and stratocumuli (Glassmeier & Feingold, 2017), and idealized studies on convective self-aggregation (Haerter, 2019; Haerter et al., 2019; Jeevanjee & Romps, 2013; Muller & Bony, 2015; Nissen &

19422466, 2024, 1, Downloaded from https://agupubs.onlinelibrary.wiley.com/doi/10.1029/2023MS003682 by Cochrane Germany, Wiley Online Library on [28/02/2024]. See the Terms and Conditions (https://onlinelibrary.wiley.com/terms-and-conditions) on Wiley Online Library for rules of use; OA articles are governed by the applicable Creative Commons License

19422466, 2024, 1, Downloaded from https://agupubs.onlinelibrary.wiley.com/doi/10.1029/2023MS003682 by Cochrane Germany, Wiley Online Library on [28/02/2024]. See the Terms and Conditions (https://onlinelibrary.wiley.com/terms-and-conditions) on Wiley Online Library for rules of use; OA articles are governed by the applicable Creative Commons License

Haerter, 2021) and the convective diurnal cycle (Böing, 2016; Böing et al., 2012; Haerter et al., 2019; Haerter & Schlemmer, 2018; Schlemmer & Hohenegger, 2016). In all of these systems, the exact role of cold pools in giving structure to the cloud and precipitation fields is still not well-understood. Yet, it is becoming more and more obvious, especially as higher model grid resolutions are approached, that cold pools do play a potentially crucial role in providing an interaction mechanism between rain cells in space and time.

A number of CP detection methods exist, which often make use of a buoyancy threshold (Feng et al., 2015; Gentine et al., 2016; Tompkins, 2001a) or a detection of the gust front through a criterion on the dynamics (Fournier & Haerter, 2019; Henneberg et al., 2020). We have presented a method, CoolDeTA, that combines thermodynamic and dynamic CP signatures. CoolDeTA detects and tracks cold pools as well as the location of their dynamical gust front. On this basis, CoolDeTA is able to identify relationships between cold pools and subsequent rain cells and thus CP "offspring." CoolDeTA therefore can be used to analyze interactions between one or more cold pools and the ones emerging in the surroundings.

Like most other methods (Drager & van den Heever, 2017; Feng et al., 2015; Fournier & Haerter, 2019; Gentine et al., 2016; Henneberg et al., 2020), CoolDeTA cannot fully refrain from setting some threshold values. In the present work we apply a surface rainfall intensity threshold, $I_0 = 2$ mm hr^{-1}, to delineate spatially contiguous RPs, and a corresponding area threshold, $A_0 = 2$ km^2, for RPs and potential CP regions. Thresholds are generally case dependent and thus limit a method's scope of application. Although particularly the CP labeling of RCE frameworks would occasionally benefit from an even smaller A_0, we however claim that both of our thresholds serve only as a preselection of robust rain and CP patches and do not impact the final CP contours: Since we provide each new RP above A_0 one marker in its downdraft COM, all of these RPs have the same chance of forming a CP. The CP contour, and whether a RP forms a CP at all, depends on the result of the k-means algorithm. A sufficiently large RP and an associated marker are accordingly necessary, rather than sufficient, conditions with respect to the formation of a CP. Also the additional conditions summarized in Table 1 serve solely the purpose of optimizing the preselection in order to increase the robustness of the CP labeling. To verify this, we deactivated the dissipation threshold, n_{dis}, as well as all additional conditions and reproduced Figures 2 and 6 based on this parameter setup in Figures S1 and S2 in Supporting Information S1, respectively: whereas the deactivation causes essentially no change in the diu4K plots (Figures S1b–S1d in Supporting Information S1), several of the smaller patches in the rce0K plot which were identified as cold pools by other methods but not by CoolDeTA before, get classified as cold pools without the additional conditions (Figure S1a in Supporting Information S1). The same applies to the CP relationships (Figure S2 in Supporting Information S1), which are identical under deactivated conditions, except for a few additional CPs that disappear shortly after being detected. With respect to dissipating cold pools, the omission of n_{dis} can even positively affect the results in the rce0K plot since some of the weak cold pools dissipate in less than 30 min.

We see the benefit of CoolDeTA in allowing for a systematic disentanglement of the processes leading up to organized convective cloud and rainfall fields in the systems mentioned above. We have shown that the method can build "cold pool family trees" in RCE and diurnal cycle frameworks, with and without wind shear. These family trees lay the groundwork for a more elaborate analysis of the evolution of convective organization throughout longer simulated periods. Moreover, as CoolDeTA considers dynamic CP signatures, the identified CP boundaries align with the cloud patterns associated with cold pools in satellite images or corresponding simulation output. CoolDeTA thus offers a systematic and objective ground truth labeling for artificial intelligence methods that detect cold pools from simulated cloud fields and that potentially pave the way for future satellite-based CP observations (Hoeller et al., 2024).

As an extension of the current method, it could be interesting to devise a moisture tracking for simulated convective cloud fields. Especially for hysteretic phenomena, such as convective self-aggregation, the long-term memory of mesoscale moisture anomalies could play a critical role in maintaining a persistent atmospheric circulation (Bretherton et al., 2005; Jensen et al., 2021; Muller & Bony, 2015). In RCE, horizontal moisture variations were suggested to give rise to imbalances in thermal radiative emission, which would then drive a persistent circulation and resultant upstream moisture transport—reinforcing the initial moisture imbalance (Emanuel et al., 2014). Recent numerical work extends this notion to diurnal cycle simulations, where MCS emerge and cause abrupt transitions to such a moisture segregated state (Jensen et al., 2021). Importantly, the mesoscale convective system dynamics was found to occur only at sufficiently high horizontal model grid

19422466, 2024, 1, Downloaded from https://agupubs.onlinelibrary.wiley.com/doi/10.1029/2023MS003682 by Cochrane Germany, Wiley Online Library on [28/02/2024]. See the Terms and Conditions (https://onlinelibrary.wiley.com/terms-and-conditions) on Wiley Online Library for rules of use; OA articles are governed by the applicable Creative Commons License

resolution, where CP interactions could be resolved sufficiently. Deciphering the complex moisture and precipitation dynamics requires a tool, such as CoolDeTA, where causal relations can be objectively mapped.

5. Conclusion

We have devised a CP detection and tracking method, CoolDeTA, which uses a combination of thermodynamic and dynamical variables to track cold pools from their initial forcing by rainfall evaporation until their dissipation stage. The method is shown to function well in a range of contexts, involving RCE and diurnal cycle experiments, as well as simulations with or without wind shear. In comparison to existing buoyancy-focused CP detection methods, CoolDeTA offers the additional benefit of determining the actual dynamical gust front, which is often displaced several kilometers from the thermodynamic boundary. In this way, the method is particularly well suited for the tracking of CP families, where the entire causal cascade of cold pools and their "offspring" can be identified. Such offspring tracking and attribution to parent cold pools would be hampered if only the thermodynamic gust front were available—many new rain cells are triggered at the dynamic gust front.

Appendix A: Supplementary Data

The following appendix presents a figure with supplementary data for the assessment of the spin-up periods in the conducted simulations (Figure A1).

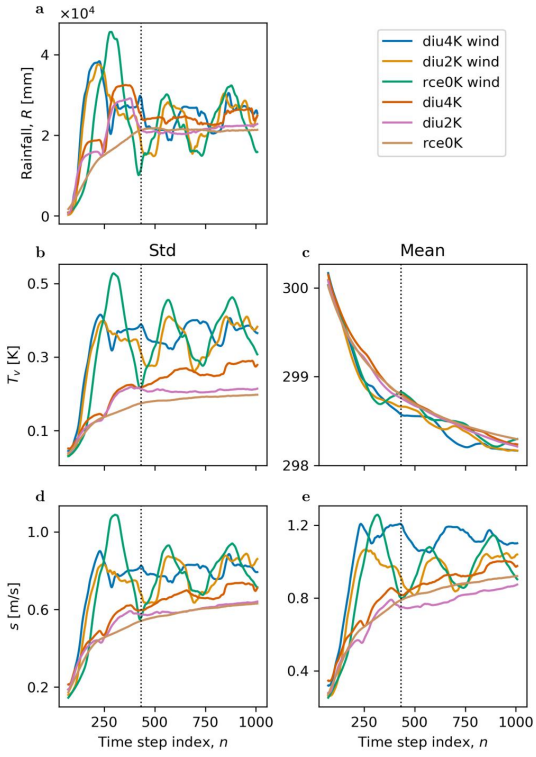

Figure A1. *Definition of spin-up time steps*. (a) Total domain rainfall per time step as running average of 1 day (144 time steps) for different simulation setups; The dotted black line indicates the chosen spin-up period of 3 days (432 time steps). (b) Analogous to (a) but for domain-standard deviation of virtual temperature, T_v. (c) Analogous to (b) but for domain-mean. (d) Analogous to (b) but for horizontal wind speed, s. (e) Analogous to (d) but for domain-mean.

19422466, 2024, 1, Downloaded from https://agupubs.onlinelibrary.wiley.com/doi/10.1029/2023MS003682 by Cochrane Germany, Wiley Online Library on [28/02/2024]. See the Terms and Conditions (https://onlinelibrary.wiley.com/terms-and-conditions) on Wiley Online Library for rules of use; OA articles are governed by the applicable Creative Commons License

Data Availability Statement

Figures were made with Matplotlib version 3.5.2 (Caswell et al., 2022; Hunter, 2007) and seaborn version 0.12.2 (Waskom, 2021). The code for the simple CP offspring model is licensed under MIT and published on GitHub https://github.com/Shakiro7/coldPool-detection-and-tracking. The CP detection and tracking algorithm (CoolDeTA) was used in version 1.0 and is licensed under Creative Commons Attribution 4.0 International (Hoeller, 2023). CoolDeTA makes use of a watershed algorithm (van der Walt et al., 2014) and a k-means algorithm (Pedregosa et al., 2011). The simulations are run with the cloud-resolving three-dimensional atmosphere simulator System for Atmospheric Modeling (SAM) (Khairoutdinov & Randall, 2003), version 6.11.

Acknowledgments
The authors gratefully acknowledge funding by a grant from the VILLUM Foundation (Grant 13168) and the European Research Council (ERC) under the European Union's Horizon 2020 research and innovation program (Grant 771859) and the Novo Nordisk Foundation Interdisciplinary Synergy Program (Grant NNF19OC0057374). This work used resources of the Deutsches Klimarechenzentrum (DKRZ), granted by its Scientific Steering Committee (WLA) under project ID bb1166. The authors would also like to express their sincere gratitude to the anonymous reviewers for their valuable feedback and constructive comments, which have contributed to improving the quality of this publication. Open Access funding enabled and organized by Projekt DEAL.

References

Barnes, G. M., & Garstang, M. (1982). Subcloud layer energetics of precipitating convection. *Monthly Weather Review*, *110*(2), 102–117. https://doi.org/10.1175/1520-0493(1982)110<0102:sleopc>2.0.co;2

Böing, S. J. (2016). An object-based model for convective cold pool dynamics. *Mathematics of Climate and Weather Forecasting*, *2*(1), 43–60. https://doi.org/10.1515/mcwf-2016-0003

Böing, S. J., Jonker, H. J., Siebesma, A. P., & Grabowski, W. W. (2012). Influence of the subcloud layer on the development of a deep convective ensemble. *Journal of the Atmospheric Sciences*, *69*(9), 2682–2698. https://doi.org/10.1175/JAS-D-11-0317.1

Bretherton, C. S., Blossey, P. N., & Khairoutdinov, M. (2005). An energy-balance analysis of deep convective self-aggregation above uniform SST. *Journal of the Atmospheric Sciences*, *62*(12), 4273–4292. https://doi.org/10.1175/jas3614.1

Bryan, G. H., Wyngaard, J. C., & Fritsch, J. M. (2003). Resolution requirements for the simulation of deep moist convection. *Monthly Weather Review*, *131*(10), 2394–2416. https://doi.org/10.1175/1520-0493(2003)131<2394:rrftso>2.0.co;2

Caswell, T. A., Droettboom, M., Lee, A., de Andrade, E. S., Hoffmann, T., Klymak, J., et al. (2022). matplotlib/matplotlib: Release (version 3.5.2) [Software]. Zenodo. https://doi.org/10.5281/zenodo.6513224

Chandra, A. S., Zuidema, P., Krueger, S., Kochanski, A., de Szoeke, S. P., & Zhang, J. (2018). Moisture distributions in tropical cold pools from equatorial Indian Ocean observations and cloud-resolving simulations. *Journal of Geophysical Research: Atmospheres*, *123*(20), 11–445. https://doi.org/10.1029/2018jd028634

Collins, W. D., Rasch, P. J., Boville, B. A., Hack, J. J., McCaa, J. R., Williamson, D. L., et al. (2006). The formulation and atmospheric simulation of the Community Atmosphere Model version 3 (CAM3). *Journal of Climate*, *19*(11), 2144–2161. https://doi.org/10.1175/JCLI3760.1

Dauhut, T., Couvreux, F., Bouniol, D., Beucher, F., Volkmer, L., Pörtge, V., et al. (2022). Flower trade-wind clouds are shallow mesoscale convective systems. *Quarterly Journal of the Royal Meteorological Society*, *149*(750), 325–347. https://doi.org/10.1002/qj.4409

de Szoeke, S. P., Skyllingstad, E. D., Zuidema, P., & Chandra, A. S. (2017). Cold pools and their influence on the tropical marine boundary layer. *Journal of the Atmospheric Sciences*, *74*(4), 1149–1168. https://doi.org/10.1175/jas-d-16-0264.1

Drager, A. J., Grant, L. D., & van den Heever, S. C. (2020). Cold pool responses to changes in soil moisture. *Journal of Advances in Modeling Earth Systems*, *12*(8), e2019MS001922. https://doi.org/10.1029/2019ms001922

Drager, A. J., & van den Heever, S. C. (2017). Characterizing convective cold pools. *Journal of Advances in Modeling Earth Systems*, *9*(2), 1091–1115. https://doi.org/10.1002/2016ms000788

Droegemeier, K., & Wilhelmson, R. (1985). Three-dimensional numerical modeling of convection produced by interacting thunderstorm outflows. Part I: Control simulation and low-level moisture variations. *Journal of the Atmospheric Sciences*, *42*(22), 2381–2403. https://doi.org/10.1175/1520-0469(1985)042⟨2381:TDNMOC⟩2.0.CO;2

Emanuel, K., Wing, A. A., & Vincent, E. M. (2014). Radiative-convective instability. *Journal of Advances in Modeling Earth Systems*, *6*(1), 75–90. https://doi.org/10.1002/2013ms000270

Engerer, N. A., Stensrud, D. J., & Coniglio, M. C. (2008). Surface characteristics of observed cold pools. *Monthly Weather Review*, *136*(12), 4839–4849. https://doi.org/10.1175/2008mwr2528.1

Feng, Z., Hagos, S., Rowe, A. K., Burleyson, C. D., Martini, M. N., & de Szoeke, S. P. (2015). Mechanisms of convective cloud organization by cold pools over tropical warm ocean during the AMIE/DYNAMO field campaign. *Journal of Advances in Modeling Earth Systems*, *7*(2), 357–381. https://doi.org/10.1002/2014MS000384

Fiévet, R., Meyer, B., & Haerter, J. O. (2023). On the sensitivity of convective cold pools to mesh resolution. *Journal of Advances in Modeling Earth Systems*, *15*(8), e2022MS003382. https://doi.org/10.1029/2022ms003382

Fournier, M. B., & Haerter, J. O. (2019). Tracking the gust fronts of convective cold pools. *Journal of Geophysical Research: Atmospheres*, *124*(21), 11103–11117. https://doi.org/10.1029/2019jd030980

Gentine, P., Garelli, A., Park, S.-B., Nie, J., Torri, G., & Kuang, Z. (2016). Role of surface heat fluxes underneath cold pools. *Geophysical Research Letters*, *43*(2), 874–883. https://doi.org/10.1002/2015gl067262

Glassmeier, F., & Feingold, G. (2017). Network approach to patterns in stratocumulus clouds. *Proceedings of the National Academy of Sciences*, *114*, 201706495.

Grandpeix, J.-Y., & Lafore, J.-P. (2010). A density current parameterization coupled with Emanuel's convection scheme. Part I: The models. *Journal of the Atmospheric Sciences*, *67*(4), 881–897. https://doi.org/10.1175/2009jas3044.1

Haerter, J. O. (2019). Convective self-aggregation as a cold pool-driven critical phenomenon. *Geophysical Research Letters*, *46*(7), 4017–4028. https://doi.org/10.1029/2018GL081817

Haerter, J. O., Böing, S. J., Henneberg, O., & Nissen, S. B. (2019). Circling in on convective organization. *Geophysical Research Letters*, *46*(12), 7024–7034. https://doi.org/10.1029/2019GL082092

Haerter, J. O., Meyer, B., & Nissen, S. B. (2020). Diurnal self-aggregation. *npj Climate and Atmospheric Science*, *3*(1), 30. https://doi.org/10.1038/s41612-020-00132-z

Haerter, J. O., & Schlemmer, L. (2018). Intensified cold pool dynamics under stronger surface heating. *Geophysical Research Letters*, *45*(12), 6299–6310. https://doi.org/10.1029/2017GL076874

Härtel, C., Carlsson, F., & Thunblom, M. (2000). Analysis and direct numerical simulation of the flow at a gravity-current head. Part 2. The lobe-and-cleft instability. *Journal of Fluid Mechanics*, *418*, 213–229. https://doi.org/10.1017/S0022112000001270

Henneberg, O., Meyer, B., & Haerter, J. O. (2020). Particle-based tracking of cold pool gust fronts. *Journal of Advances in Modeling Earth Systems*, *12*(5), e2019MS001910. https://doi.org/10.1029/2019ms001910

Hirt, M., Craig, G. C., Schäfer, S. A., Savre, J., & Heinze, R. (2020). Cold-pool-driven convective initiation: Using causal graph analysis to determine what convection-permitting models are missing. *Quarterly Journal of the Royal Meteorological Society*, *146*(730), 2205–2227. https://doi.org/10.1002/qj.3788

Hoeller, J. (2023). CoolDeTa: Detection and tracking of convective cold pools and their causal chains in cloud-resolving simulation data release (version 1.0) [Software & Dataset]. Zenodo. https://doi.org/10.5281/zenodo.10115957

Hoeller, J., Fiévet, R., Engelbrecht, E., & Haerter, J. O. (2024). U-net segmentation for the detection of convective cold pools from cloud and rainfall fields. *Journal of Geophysical Research: Atmospheres*, *129*, e2023JD040126. https://doi.org/10.1029/2023JD040126

Hohenegger, C., Ament, F., Beyrich, F., Löhnert, U., Rust, H., Bange, J., et al. (2023). Fesstval: The field experiment on submesoscale spatio-temporal variability in lindenberg. *Bulletin of the American Meteorological Society*, *104*(10), E1875–E1892. https://doi.org/10.1175/bams-d-21-0330.1

Houze, R. A., Jr. (2004). Mesoscale convective systems. *Reviews of Geophysics*, *42*, RG4003. https://doi.org/10.1029/2004RG000150

Hunter, J. D. (2007). Matplotlib: A 2D graphics environment [Software]. Computing in Science & Engineering, *9*(3), 90–95. https://doi.org/10.1109/MCSE.2007.55

Jeevanjee, N., & Romps, D. M. (2013). Convective self-aggregation, cold pools, and domain size. *Geophysical Research Letters*, *40*(5), 994–998. https://doi.org/10.1002/grl.50204

Jensen, G. G., Fiévet, R., & Haerter, J. O. (2021). The diurnal path to persistent convective self-aggregation. arXiv preprint arXiv:2104.01132.

Kain, J., & Fritsch, J. (1992). The role of the convective "trigger function" in numerical forecasts of mesoscale convective systems. *Meteorology and Atmospheric Physics*, *49*(1–4), 93–106. https://doi.org/10.1007/bf01025402

Khairoutdinov, M. F., & Randall, D. (2006). High-resolution simulation of shallow-to-deep convection transition over land. *Journal of the Atmospheric Sciences*, *63*(12), 3421–3436. https://doi.org/10.1175/jas3810.1

Khairoutdinov, M. F., & Randall, D. A. (2003). Cloud resolving modeling of the arm summer 1997 IOP: Model formulation, results, uncertainties, and sensitivities [Software]. Journal of the Atmospheric Sciences, *60*(4), 607–625. https://doi.org/10.1175/1520-0469(2003)060<0607:crmota>2.0.co;2

Kruse, I. L., Haerter, J. O., & Meyer, B. (2022). Cold pools over The Netherlands: A statistical study from tower and radar observations. *Quarterly Journal of the Royal Meteorological Society*, *148*(743), 711–726. https://doi.org/10.1002/qj.4223

Kurowski, M. J., Suselj, K., Grabowski, W. W., & Teixeira, J. (2018). Shallow-to-deep transition of continental moist convection: Cold pools, surface fluxes, and mesoscale organization. *Journal of the Atmospheric Sciences*, *75*(12), 4071–4090. https://doi.org/10.1175/jas-d-18-0031.1

Markowski, P., & Richardson, Y. (2010). *Mesoscale meteorology in midlatitudes*. John Wiley and Sons. https://doi.org/10.1002/9780470682104

Meyer, B., & Haerter, J. O. (2020). Mechanical forcing of convection by cold pools: Collisions and energy scaling. *Journal of Advances in Modeling Earth Systems*, *12*(11), e2020MS002281. https://doi.org/10.1029/2020ms002281

Moncrieff, M. W., & Liu, C. (1999). Convection initiation by density currents: Role of convergence, shear, and dynamical organization. *Monthly Weather Review*, *127*(10), 2455–2464. https://doi.org/10.1175/1520-0493(1999)127<2455:cibdcr>2.0.co;2

Moseley, C., Hohenegger, C., Berg, P., & Haerter, J. O. (2016). Intensification of convective extremes driven by cloud–cloud interaction. *Nature Geoscience*, *9*(10), 748–752. https://doi.org/10.1038/ngeo2789

Muller, C., & Bony, S. (2015). What favors convective aggregation and why? *Geophysical Research Letters*, *42*(13), 5626–5634. https://doi.org/10.1002/2015GL064260

Muller, C., Yang, D., Craig, G., Cronin, T., Fildier, B., Haerter, J. O., et al. (2022). Spontaneous aggregation of convective storms. *Annual Review of Fluid Mechanics*, *54*(1), 133–157. https://doi.org/10.1146/annurev-fluid-022421-011319

Niehues, J., Jensen, G. G., & Haerter, J. O. (2021). Self-organized quantization and oscillations on continuous fixed-energy sandpiles. arXiv preprint arXiv:2111.04470.

Nissen, S. B., & Haerter, J. O. (2021). Circling in on convective self-aggregation. *Journal of Geophysical Research: Atmospheres*, *126*(20), e2021JD035331. https://doi.org/10.1029/2021jd035331

Parker, D. J., & Diop-Kane, M. (2017). *Meteorology of tropical West Africa: The forecasters' handbook*. John Wiley & Sons.

Parker, M. D. (2008). Response of simulated squall lines to low-level cooling. *Journal of the Atmospheric Sciences*, *65*(4), 1323–1341. https://doi.org/10.1175/2007jas2507.1

Pedregosa, F., Varoquaux, G., Gramfort, A., Michel, V., Thirion, B., Grisel, O., et al. (2011). Scikit-learn: Machine learning in Python [Software]. *Journal of Machine Learning Research*, *12*, 2825–2830. Retrieved from https://www.jmlr.org/papers/volume12/pedregosa11a/pedregosa11a.pdf

Pei, S., Shinoda, T., Soloviev, A., & Lien, R.-C. (2018). Upper ocean response to the atmospheric cold pools associated with the Madden-Julian Oscillation. *Geophysical Research Letters*, *45*(10), 5020–5029. https://doi.org/10.1029/2018gl077825

Rio, C., Hourdin, F., Grandpeix, J.-Y., & Lafore, J.-P. (2009). Shifting the diurnal cycle of parameterized deep convection over land. *Geophysical Research Letters*, *36*, L07809. https://doi.org/10.1029/2008gl036779

Rochetin, N., Hohenegger, C., Touzé-Peiffer, L., & Villefranque, N. (2021). A physically based definition of convectively generated density currents: Detection and characterization in convection-permitting simulations. *Journal of Advances in Modeling Earth Systems*, *13*(7), e2020MS002402. https://doi.org/10.1029/2020ms002402

Romps, D. M., & Jeevanjee, N. (2016). On the sizes and lifetimes of cold pools. *Quarterly Journal of the Royal Meteorological Society*, *142*(696), 1517–1527. https://doi.org/10.1002/qj.2754

Rooney, G. G. (2015). Descent and spread of negatively buoyant thermals. *Journal of Fluid Mechanics*, *780*, 457–479. https://doi.org/10.1017/jfm.2015.484

Rooney, G. G., Stirling, A. J., Stratton, R. A., & Whitall, M. (2021). C-Pool: A scheme for modelling convective cold pools in the Met Office unified model. *Quarterly Journal of the Royal Meteorological Society*, *148*(743), 962–980.

Rotunno, R., Klemp, J. B., & Weisman, M. L. (1988). A theory for strong, long-lived squall lines. *Journal of the Atmospheric Sciences*, *45*(3), 463–485. https://doi.org/10.1175/1520-0469(1988)045<0463:atfsll>2.0.co;2

Schlemmer, L., & Hohenegger, C. (2016). Modifications of the atmospheric moisture field as a result of cold-pool dynamics. *Quarterly Journal of the Royal Meteorological Society*, *142*(694), 30–42. https://doi.org/10.1002/qj.2625

Schumacher, R. S., & Rasmussen, K. L. (2020). The formation, character and changing nature of mesoscale convective systems. *Nature Reviews Earth & Environment*, *1*(6), 300–314. https://doi.org/10.1038/s43017-020-0057-7

Seifert, A., & Heus, T. (2013). Large-eddy simulation of organized precipitating trade wind cumulus clouds. *Atmospheric Chemistry and Physics*, *13*(11), 5631–5645. https://doi.org/10.5194/acp-13-5631-2013

Simpson, J. E. (1972). Effects of the lower boundary on the head of a gravity current. *Journal of Fluid Mechanics*, *53*(4), 759–768. https://doi.org/10.1017/S0022112072000461

19422466, 2024, 1, Downloaded from https://agupubs.onlinelibrary.wiley.com/doi/10.1029/2023MS003682 by Cochrane Germany, Wiley Online Library on [28/02/2024]. See the Terms and Conditions (https://onlinelibrary.wiley.com/terms-and-conditions) on Wiley Online Library for rules of use; OA articles are governed by the applicable Creative Commons License

Simpson, J. E. (1980). Downdrafts as linkages in dynamic cumulus seeding effects. *Journal of Applied Meteorology*, *19*(4), 477–487. https://doi.org/10.1175/1520-0450(1980)019<0477:dalidc>2.0.co;2

Smagorinsky, J. (1963). General circulation experiments with the primitive equations: I. The basic experiment. *Monthly Weather Review*, *91*(3), 99–164. https://doi.org/10.1175/1520-0493(1963)091<0099:gcewtp>2.3.co;2

Straka, J. M., Wilhelmson, R. B., Wicker, L. J., Anderson, J. R., & Droegemeier, K. K. (1993). Numerical solutions of a non-linear density current: A benchmark solution and comparisons. *International Journal for Numerical Methods in Fluids*, *17*(1), 1–22. https://doi.org/10.1002/fld.1650170103

Tompkins, A. M. (2001a). Organization of tropical convection in low vertical wind shears: The role of cold pools. *Journal of the Atmospheric Sciences*, *58*(13), 1650–1672. https://doi.org/10.1175/1520-0469(2001)058<1650:ootcil>2.0.co;2

Tompkins, A. M. (2001b). Organization of tropical convection in low vertical wind shears: The role of water vapor. *Journal of the Atmospheric Sciences*, *58*(6), 529–545. https://doi.org/10.1175/1520-0469(2001)058<0529:ootcil>2.0.co;2

Torri, G., & Kuang, Z. (2016). Rain evaporation and moist patches in tropical boundary layers. *Geophysical Research Letters*, *43*(18), 9895–9902. https://doi.org/10.1002/2016gl070893

Torri, G., & Kuang, Z. (2019). On cold pool collisions in tropical boundary layers Giuseppe. *Geophysical Research Letters*, *46*(1), 399–407. https://doi.org/10.1029/2018GL080501

van der Walt, S., Schönberger, J. L., Nunez-Iglesias, J., Boulogne, F., Warner, J. D., Yager, N., et al. (2014). scikit-image: Image processing in Python [Software]. PeerJ, *2*, e453. https://doi.org/10.7717/peerj.453

Vogel, R., Konow, H., Schulz, H., & Zuidema, P. (2021). A climatology of trade-wind cumulus cold pools and their link to mesoscale cloud organization. *Atmospheric Chemistry and Physics*, *21*(21), 16609–16630. https://doi.org/10.5194/acp-21-16609-2021

Wakimoto, R. (2001). Convectively driven high wind events (pp. 255–298). https://doi.org/10.1007/978-1-935704-06-5_7

Waskom, M. L. (2021). Seaborn: Statistical data visualization [Software]. Journal of Open Source Software, *6*(60), 3021. https://doi.org/10.21105/joss.03021

Weisman, M. L., Klemp, J. B., & Rotunno, R. (1988). Structure and evolution of numerically simulated squall lines. *Journal of the Atmospheric Sciences*, *45*(14), 1990–2013. https://doi.org/10.1175/1520-0469(1988)045<1990:saeons>2.0.co;2

Zuidema, P., Li, Z., Hill, R. J., Bariteau, L., Rilling, B., Fairall, C., et al. (2012). On trade wind cumulus cold pools. *Journal of the Atmospheric Sciences*, *69*(1), 258–280. https://doi.org/10.1175/jas-d-11-0143.1

Zuidema, P., Torri, G., Muller, C., & Chandra, A. (2017). A survey of precipitation-induced atmospheric cold pools over oceans and their interactions with the larger-scale environment. *Surveys in Geophysics*, *38*(6), 1–23. https://doi.org/10.1007/s10712-017-9447-x

19422466, 2024, 1, Downloaded from https://agupubs.onlinelibrary.wiley.com/doi/10.1029/2023MS003682 by Cochrane Germany, Wiley Online Library on [28/02/2024]. See the Terms and Conditions (https://onlinelibrary.wiley.com/terms-and-conditions) on Wiley Online Library for rules of use; OA articles are governed by the applicable Creative Commons License

Supporting Information for "Detecting Cold Pool Family Trees in Convection Resolving Simulations"

Jannik Hoeller[1,2], Romain Fiévet[2], Jan O. Haerter[1,2,3,4]

[1]Integrated Modeling, Leibniz Centre for Tropical Marine Research, Fahrenheitstr. 6, 28359 Bremen, Germany

[2]Niels Bohr Institute, Copenhagen University, Blegdamsvej 17, 2100 Copenhagen, Denmark

[3]Physics and Earth Sciences, Constructor University Bremen, Campus Ring 1, 28759 Bremen, Germany

[4]Department of Physics and Astronomy, University of Potsdam, Karl-Liebknecht-Straße 32, 14476 Potsdam, Germany

Contents of this file

Introduction

Text S1 provides recommendations for the application of the proposed cold pool detection and tracking algorithm (CoolDeTA) to other simulation setups. Fig. S1 shows cold pools detected using CoolDeTA with deactivated additional rules and compares them to cold pools detected based on other methods. Fig. S2 illustrates the cascades of cold pools tracked by CoolDeTA with deactivated additional rules.

Text S1.

The proposed cold pool (CP) detection and tracking algorithm (CoolDetA) is designed for idealized simulations that resolve cold pool dynamics. In our study, we utilized simulation setups with a horizontal resolution of 200 m. While CoolDeTA can be applied to simulation data with coarser resolutions of 1–2 km, we recommend using resolutions equal to or less than 400 m for effective tracking of cold pool relationships. When applying CoolDeTA to simulation data with different horizontal resolutions, it is important to adapt the potential CP and rain patch (RP) area threshold, A_0, which is defined based on pixel count rather than patch area. For area thresholds with small pixel counts, it might be considered to deactivate the divergence criteria by setting the "patchCheck" variable in the main.py file to "False" and to relax the RP-potential CP overlap factor, f_s, as well as the new CP-RP area ratio.

In terms of the temporal resolution of simulation data, we suggest using a minimum output interval of 10 min when applying CoolDeTA. For simulation setups with longer CP life times, an interval of 20 min may be sufficient. However, in such cases, it is important to relax both f_s and the new CP-RP area ratio. Otherwise, CPs that form immediately after the previous output time step may not meet the criteria for new CPs in the subsequent time step and could be rejected by the algorithm. While smaller output intervals than 10 min are possible, they generally do not lead to significant improvements in results.

The applicability of CoolDeTA to simulation data based on realistic setups is limited and depends on the specific setup employed: CoolDeTA is not applicable if the CP associated virtual temperature anomalies are weak compared to the gradients of the horizontal virtual

temperature field at the lowest model level. Similarly, CoolDeTA is not applicable if the CP associated wind anomalies are weak compared to other wind anomalies in the domain. For instance, in simulation setups with both ocean and land surfaces, CoolDeTA may mistakenly identify sea breezes as CPs. In cases where there are large near-surface temperature differences between land and ocean surfaces, even the entire region of the colder surface may be classified as a CP, when sufficiently strong rainfall is present. While strong winds generally do not pose a problem, caution should be exercised if wind shear reduces the overlap between RPs and CPs significantly. In such situations, we recommend decreasing the value of f_s or even setting it to zero.

We also note that CoolDeTA may not accurately detect CPs with very moist specific humidity anomalies due to the influence of moisture on the computation of the indicator field, $\mathcal{I}_{seg}$, and the elevation map, $\mathcal{I}_{top}$.

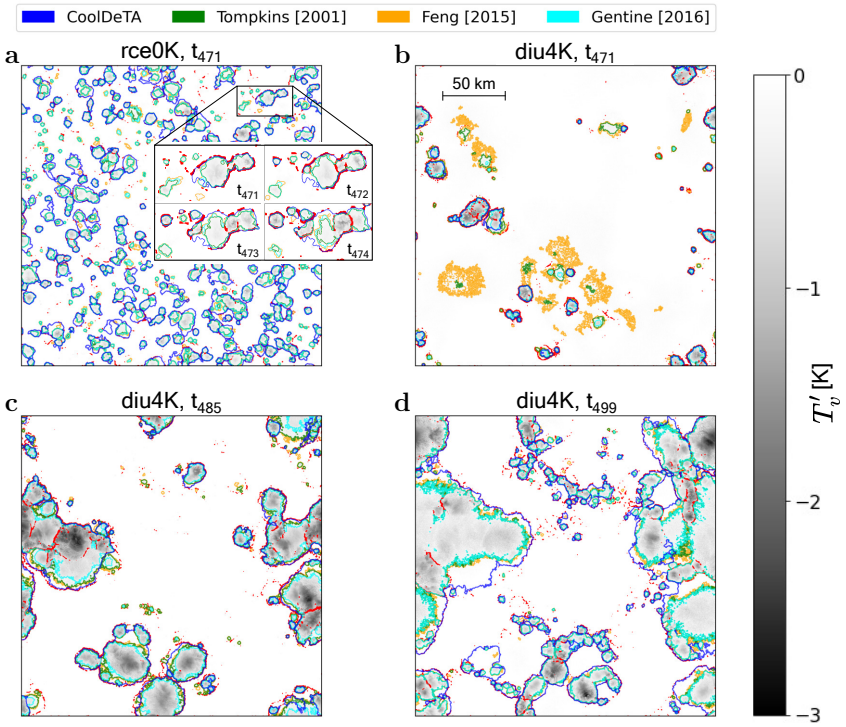

Figure S1. Comparison of cold pool detection methods. Analogous to Fig. 2a—d but with CoolDeTA contours based on a setup with $n_{dis} = 0$, i.e., without minimum dissipation time for cold pools, and without the additional rules listed in Table 1. Omitted rules comprise the checks of interior and boundary of "potential cold pool" regions with respect to their mean divergence, the required overlap between rain patches and "potential cold pool" regions to obtain a marker, and the required ratio between a newly formed cold pool and its rain patch.

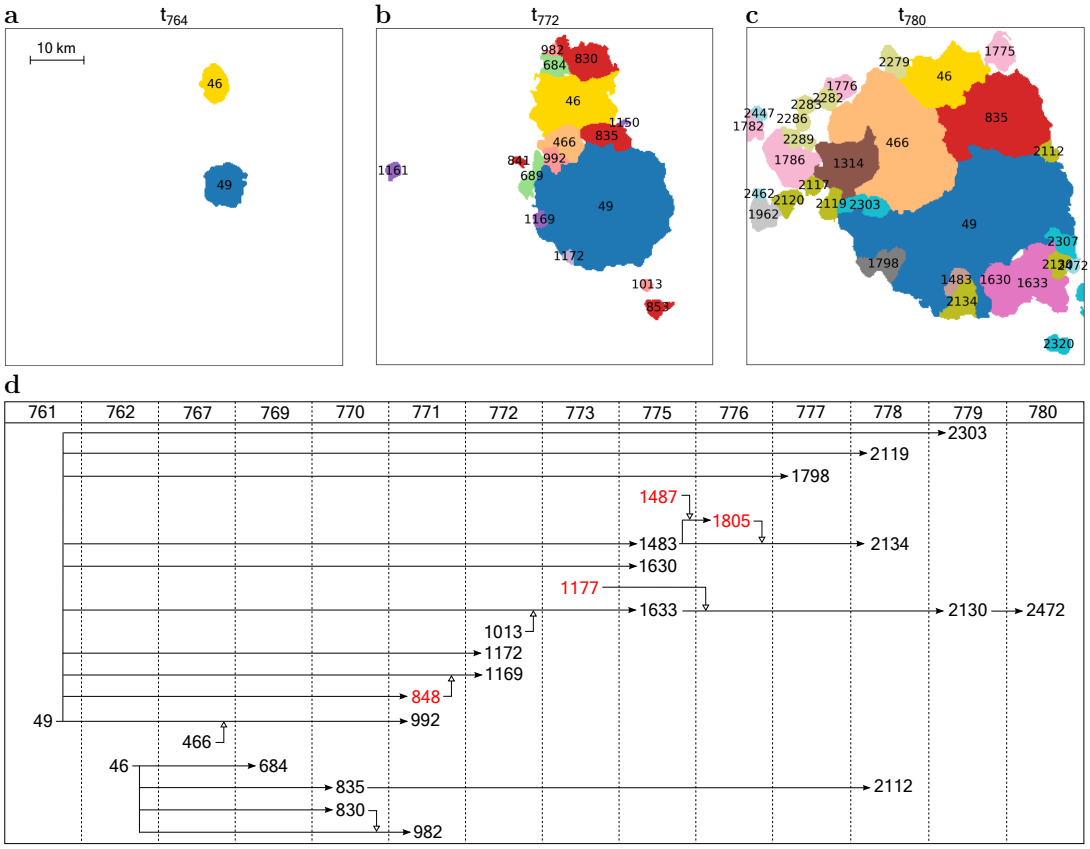

Figure S2. Cascades of tracked cold pools. Analogous to Fig. 6a—d but with CoolDeTA contours based on a setup with $n_{dis} = 0$, i.e., without minimum dissipation time for cold pools, and without the additional rules listed in Table 1. Omitted rules analogous to Fig. S1.

5.3 U-Net Segmentation for the Detection of Convective Cold Pools From Cloud and Rainfall Fields

The main goal of the following manuscript is to present a novel method for segmenting CPs in satellite-observable data and validate its effectiveness. Given the limited availability of alternative observational data sources and the prevalence of CPs, this study concentrates on CPs over tropical land areas. Based on the findings of manuscript I and other studies, potential CP signatures in corresponding satellite data encompass (i) spatial patterns such as deep convective clouds with pronounced brightness temperature gradients at their boundaries and the emergence or deepening of clouds at the CP gust front, as well as (ii) temporal patterns linked to the evolution of the parent convection and the propagation of the CP gust front. To leverage these signatures and potentially benefit from additional patterns hidden so far, the devised CP segmentation method relies on neural networks with a U-Net architecture. Since CP masks for real satellite observations are rarely accessible and time-intensive to create, we trained and tested our neural networks using simulated cloud and rainfall fields. This approach enabled the generation of corresponding ground truth images using the cold pool detection and tracking algorithm outlined in manuscript II (Section 5.2).

Check for updates

JGR Atmospheres

RESEARCH ARTICLE
10.1029/2023JD040126

U-Net Segmentation for the Detection of Convective Cold Pools From Cloud and Rainfall Fields

Jannik Hoeller[1,2], Romain Fiévet[2], Edward Engelbrecht[1,3], and Jan O. Haerter[1,2,3,4]

[1]Integrated Modeling, Leibniz Centre for Tropical Marine Research, Bremen, Germany, [2]Niels Bohr Institute, Copenhagen University, Copenhagen, Denmark, [3]Physics and Earth Sciences, Constructor University Bremen, Bremen, Germany, [4]Department of Physics and Astronomy, University of Potsdam, Potsdam, Germany

Key Points:

- A neural network is trained to detect cold pools from cloud top temperature and precipitation
- The method works reliably and a pseudo-3D approach, which includes dynamic cold pool evolution, performs best
- The method offers new perspectives for the cold pool detection from geostationary satellite observations over tropical land

Correspondence to:
J. Hoeller,
jannik.hoeller@leibniz-zmt.de

Citation:
Hoeller, J., Fiévet, R., Engelbrecht, E., & Haerter, J. O. (2024). U-Net segmentation for the detection of convective cold pools from cloud and rainfall fields. *Journal of Geophysical Research: Atmospheres*, *129*, e2023JD040126. https://doi.org/10.1029/2023JD040126

Received 3 OCT 2023
Accepted 8 DEC 2023

Abstract Convective cold pools (CPs) mediate interactions between convective rain cells and help organize thunderstorm clusters, in particular mesoscale convective systems and extreme rainfall events. Unfortunately, the observational detection of CPs on a large scale has been hampered by the lack of relevant near-surface data. Unlike numerical studies, where fields, such as virtual temperature or wind, are available at high resolution and frequently used to detect CPs, observational studies mainly identify CPs based on surface time series, for example, from weather stations or research vessels—thus limiting studies to a regional scope. To expand to a global scope, we here develop and evaluate a methodology for CP detection that relies exclusively on data with (a) global availability and (b) high spatiotemporal resolution. We trained convolutional neural networks to segment CPs in high-resolution cloud-resolving simulation output by deliberately restricting ourselves to only cloud top temperature and rainfall fields. Apart from simulations, such data are readily available from geostationary satellites that fulfill both (a) and (b). The networks employ a U-Net architecture, popular with image segmentation, where spatial correlations at various scales must be learned. Despite the restriction imposed, the trained networks systematically identify CP pixels. Looking ahead, our methodology aims to reliably detect CPs over tropical land from space-borne sensors on a global scale. As it also provides information on the spatial extent and the relative positioning of CPs over time, our method may unveil the role of CPs in convective organization.

Plain Language Summary Cold pools come about when rain evaporates underneath thunderstorm rain cells. Such cold pools are colder and thus denser than the surrounding air, which makes them flow over the surface. The associated gust fronts can often be felt when observing thunderstorm clouds in nature, as strong, but relatively short-lasting, winds occurring near the thunderstorm downpour. Such cold pools can bring about clumps of thunderstorms, which can deliver large quantities of rainfall within areas of approximately 100 km across. Thus, detecting cold pools on these and larger scales is important, but so far difficult due to the challenge of observing the air currents underneath clouds from satellite. We here present a method that may be able to do just that, namely detecting cold pools from above, by identifying signatures left behind in cloud patterns, for example, arc-like shapes along the gust front. We demonstrate the algorithms capabilities using high-resolution simulation data, where we are able to "know" the true result. We use an artificial intelligence framework to carry out this statistical task. We suggest that our method should be applicable to satellite data and thus give new insight into cloud organization at large scales.

1. Introduction

Cold pools (CPs) are volumes of atmospheric air that are cooled by evaporation of precipitation. The resultant denser air experiences negative buoyancy (Markowski & Richardson, 2011), resulting from convective downdrafts, or microbursts (Lundgren et al., 1992). At Earth's surface, CPs spread horizontally as density currents (Drager & van den Heever, 2017; Droegemeier & Wilhelmson, 1985; Zuidema et al., 2017). While expanding radially along the surface, CPs can be characterized as consisting of (a) a head, which can measure hundreds to several thousand meters vertically and (b) a shallower interior, which is separated from the head by a wake region (Benjamin, 1968; Cafaro & Rooney, 2018; Droegemeier & Wilhelmson, 1987; Fiévet et al., 2023; Kneller et al., 1999; Kruse et al., 2022; Markowski & Richardson, 2011; Meyer & Haerter, 2020; Simpson, 1980).

Substantial mechanistic significance has been attributed to the thin surface of horizontal convergence between the CP head and the ambient atmosphere, often referred to as CP gust front. On the one hand, this CP gust front

© 2023. The Authors.
This is an open access article under the terms of the Creative Commons Attribution License, which permits use, distribution and reproduction in any medium, provided the original work is properly cited.

21698996, 2024, 1, Downloaded from https://agupubs.onlinelibrary.wiley.com/doi/10.1029/2023JD040126 by Cochrane Germany, Wiley Online Library on [28/02/2024]. See the Terms and Conditions (https://onlinelibrary.wiley.com/terms-and-conditions) on Wiley Online Library for rules of use; OA articles are governed by the applicable Creative Commons License

features pronounced vertical wind speed. On the other, the initial negative-buoyancy anomaly near the CP's gust front is gradually reduced as the CP spreads, a possible consequence of enhanced surface latent and sensible heat fluxes (Drager et al., 2020; Tompkins, 2001; Torri & Kuang, 2016). Thus, in the course of the lateral expansion, buoyant ambient air can be lifted (Drager & van den Heever, 2017), resulting in further condensation and convection. "Communication" between cells (Simpson, 1980) can thus be encoded by such mechanical and thermodynamic effects.

Although the relative contributions of the thermodynamic versus the dynamic effect are still under debate (Fuglestvedt & Haerter, 2020; Romps & Jeevanjee, 2016; Torri et al., 2015) and can depend on the environmental and boundary conditions (Feng et al., 2015), there is substantial consensus that CPs can trigger new clouds in their vicinity and modify the subcloud moisture distribution (Böing et al., 2012; Drager & van den Heever, 2017; Haerter et al., 2020; Jensen et al., 2022; Schlemmer & Hohenegger, 2016).

Due to their ability to influence the organization (Böing, 2016; Haerter et al., 2019; Schlemmer & Hohenegger, 2016), the maintenance of squall line structures (Rotunno et al., 1988; Schumacher & Rasmussen, 2020), and potential intensification of thunderstorms (Houze & Betts, 1981; Zipser et al., 1981), CP characteristics have been investigated in past decades, often within numerical studies: virtual temperature (T_v) anomalies have been used to track CPs in cloud-resolving simulations by patch detection (Schlemmer & Hohenegger, 2016) or by unsupervised image segmentation (Gentine et al., 2016). Drager and van den Heever (2017) compared the utility of different variables for CP identification in simulations. Torri and Kuang (2019) used a Lagrangian tracking to investigate CP collisions. Focusing on the dynamical gust front, Fournier and Haerter (2019) and Henneberg et al. (2020) introduced tracking algorithms targeting the thin (dynamic) convergence rings surrounding each CP.

Over continental regions in the tropical climate and during midlatitude summer, CP dynamics has been implicated in the evolution of so-called mesoscale convective systems (MCS; Jensen et al., 2022), which are extended clusters, $\mathcal{O}$(100 km), of thunderstorms cells (Houze, 2004; Schumacher & Johnson, 2008; Schumacher & Rasmussen, 2020) and have been found to contribute to the majority of tropical rainfall and dominate potential increases in extremes (Tan et al., 2015). Despite their climatic relevance, tropical MCS are still nearly impossible to forecast by simulations (Fritsch & Carbone, 2004; Sukovich et al., 2014).

At smaller spatiotemporal scales, idealized simulations allow for detailed analysis of specific mechanisms as they provide near-continuous output data for many variables—making CP detection and tracking feasible. Yet, numerical studies still depend on the model and resolution chosen, so that findings do not immediately carry over to the real world. Since traditional general circulation models are too coarse to resolve CP processes (Feng et al., 2015; Fiévet et al., 2022), CP mechanisms are mostly studied in high-resolution simulations within limited domain sizes or, less commonly, by including specific parameterizations (Grandpeix & Lafore, 2010; Rio et al., 2009). In both cases, the validity of the outcome is limited by the underlying modeling assumptions.

Observational CP studies are usually hampered by the lack of spatially resolved near-surface data. Using point-like near-surface station observations at subhourly temporal resolution, the spread of a given CP can however be detected as a rapid temperature drop in the time series (de Szoeke et al., 2017; Kirsch et al., 2021; Kruse et al., 2022; Vogel et al., 2021; Zuidema et al., 2017). At times, perhaps as a result of strong surface sensible heat fluxes (Knippertz et al., 2007), a dew point temperature increase, rather than a temperature drop, is found to be a robust characteristic of CP gust fronts, for example, in arid regions (Emmel et al., 2010; Redl et al., 2015). Also combinations with dynamic features, such as changes in wind speed have been employed (Emmel et al., 2010; Redl et al., 2015). While Emmel et al. (2010) ultimately validated each event subjectively with infrared satellite imagery, Redl et al. (2015) implemented a criterion based on satellite microwave data. Making use of the dust signature in brightness temperature differences, Caton Harrison et al. (2021) devised an algorithm to automatically identify and track Saharan CP outflows based on gradients of the corresponding brightness temperature difference fields. In a validation based on 35 manually identified CP outflows, the approach achieved a detection rate of 74.2% (26/35). Also "thin line" echoes associated with the CP leading edge in radar imagery have been used in manual CP detections (Borque et al., 2020; Brandes, 1977; Engerer et al., 2008; Wakimoto, 1982).

CP detection over the ocean has occasionally benefited from the imprint that CPs leave on the sea surface (Atlas, 1994). During the Variability of American Monsoon Systems (VAMOS) Ocean–Cloud–Atmosphere–Land Survey Regional Experiment (VOCALS-REx) in the Southeast Pacific, Wilbanks et al. (2015) applied an air density increase criterion to detect stratocumulus-topped boundary layer CPs from in situ ship measurements.

21698996, 2024, 1, Downloaded from https://agupubs.onlinelibrary.wiley.com/doi/10.1029/2023JD040126 by Cochrane Germany, Wiley Online Library on [28/02/2024]. See the Terms and Conditions (https://onlinelibrary.wiley.com/terms-and-conditions) on Wiley Online Library for rules of use; OA articles are governed by the applicable Creative Commons License

Garg et al. (2020) introduced a method based on wind gradients from space-borne scatterometers to detect CP regions over tropical oceans. To validate their method, they employed in situ air temperature measurements from buoys and a simulation. As part of the Elucidating the Role of Cloud–Circulation Coupling in Climate (EUREC4A) field campaign (Stevens et al., 2021), Touzé-Peiffer et al. (2022) developed a method for detecting CPs over tropical oceans based on the mixed-layer height in atmospheric soundings.

Detecting CPs over continents at a spatially extended scale can be more cumbersome. Reaching real-world CP detection results for the continental areas is however the only realistic benchmark for CP representation in numerical models, and thus the proper dynamics of MCS. To approach automatized and global-scale CP detection over land surfaces, we developed an algorithm using convolutional neural networks (CNNs) which relies only on quantities that are observable from geostationary satellite imagery. The algorithm was trained and tested using data from idealized cloud-resolving simulations, where all field variables are available over the entire domain. The chosen configurations correspond to an atmosphere over tropical land surfaces. To our knowledge, this is the first approach for detecting CPs over land on a global scale based on satellite data. Our algorithm may allow for new insight into the role of CPs in convective organization and the formation of weather extremes.

2. Methods

CNNs, which gradually coarsen a field of input data through filtering operations, are widely used for classification and segmentation problems. Upon each filtering step, spatial correlations at larger and larger scales are distinguished. Whereas CNNs for classification problems group the entire input data field into a set of classifiers, CNNs for segmentation problems return to the resolution of the input to mark each pixel as being of one of several categories. For the problem at hand, we wish to mark each pixel in the 2D plane as either belonging to a CP or not—thus the segmentation technique is appropriate.

2.1. Simulation Data

In order to simplify the generation of labeled data sets, the network training and testing is conducted using data from numerical simulations. To this end, the cloud-resolving three-dimensional atmosphere simulator System for Atmospheric Modeling (SAM; Khairoutdinov & Randall, 2003), version 6.11, is used. It resolves the Euler equations in the anelastic approximation on a staggered mesh. Convective fluxes are evaluated using a fifth-order finite difference scheme from Yamaguchi et al. (2011) and turbulent dissipation is modeled by an eddy-viscosity-based closure. Moist thermodynamics is resolved by transporting liquid and ice water static energy, total precipitating and nonprecipitating water mass fractions, and uses a bulk single-moment microphysics closure scheme.

The configuration chosen for this study corresponds to an atmosphere over an idealized moist tropical land surface. It is similar to the configuration studied by Jensen et al. (2022) which exhibited strong and complex CP activity and is therefore suited to design and test our detection method. Parts of the underlying simulation output were used in Hoeller, Fiévet, and Haerter (2023) to devise a detection and tracking method for CPs in cloud-resolving simulation data. The computational domain has a size of $L_x = L_y = 240$ km in the horizontal directions and extends vertically to a maximum altitude of $L_z = 26$ km. It is discretized by an orthogonal mesh of horizontal resolution $\Delta x = \Delta y = 200$ m and vertical resolution Δz increasing from $\Delta z(z = 25\text{ m}) = 50$ m to $\Delta z(z = 25\text{ km}) = 1{,}000$ m over 100 levels. In the following, we use $n_x, n_y \in [0, N]$, as integers labeling the indices of the horizontal model grid, with $N = 1{,}200$ the total number of grid points in either horizontal dimension. The lateral boundary conditions are set to be periodic. Relevant two-dimensional simulated fields are sampled instantaneously every $\Delta t = 10$ min. We often denote the discrete time $t = t_n \equiv n\Delta t$, measured from the beginning of the simulation, by the integer time step n.

Surface heat fluxes are evaluated using Monin-Obukhov similarity theory with a saturated humidity (moist surface) condition and a prescribed diurnally varying temperature T, with an average of $T_0 = 298$ K. The temperature amplitude ΔT, defined as half the diurnal temperature range between maximum and minimum, is chosen to represent plausible ranges measured for tropical land (Sharifnezhadazizi et al., 2019). The effect of the surface forcing is to trigger idealized diurnally varying convective activity typical of tropical land surfaces: moist convection tends to develop and self-organize during the afternoon hours—giving rise to a complex organizational pattern. The nocturnal cooling reduces convective activity and precipitation rates typically reach a domain-wide minimum during the early morning hours of the subsequent model day. In order to work with a diverse set of

21698996, 2024, 1, Downloaded from https://agupubs.onlinelibrary.wiley.com/doi/10.1029/2023JD040126 by Cochrane Germany, Wiley Online Library on [28/02/2024]. See the Terms and Conditions (https://onlinelibrary.wiley.com/terms-and-conditions) on Wiley Online Library for rules of use; OA articles are governed by the applicable Creative Commons License

atmospheric conditions, four different configurations are considered, where $\Delta T \in \{2, 4\}$ K and wind shear is either switched off or set to a temporally and spatially averaged vertical profile over tropical Africa (LAT: 5.5°–16°N, LON: −20°–10°E) obtained from ERA5 reanalysis data for July 2016. The vertical profile consists in a piecewise linear profile with zero velocity below $z = 1$ km, linearly increasing speeds from 0 to 16 m s^{-1} up to 19 km altitude and 16 m s^{-1} beyond. Depending on their ΔT, we term the configurations either "diu2K" or "diu4K." Configurations with wind shear further obtain the addition "wind," that is, "diu2K wind" denotes the setup with $\Delta T = 2$ K and wind shear.

2.1.1. Ground Truth Labeling

Labeled data sets are derived from simulation output based on a CP detection and tracking algorithm (CoolDeTA) devised by Hoeller, Fiévet, and Haerter (2023). CoolDeTA applies a *k*-means algorithm to the sum of the normalized lowest domain level fields of virtual temperature and horizontal wind speed to classify each pixel in the two-dimensional field as either "potential CP" or "no CP" without defining a fixed threshold. We note that, in the following, only such potential CP areas can contain actual CPs. Individual CP instances are differentiated and labeled based on a watershed algorithm. The starting points for the flooding of the watershed algorithm are the downdraft centers within spatially contiguous rain patches with a surface rain intensity, r_{int}, exceeding a threshold of $r_{\text{int}} \geq r_0$. Like Hoeller, Fiévet, and Haerter (2023), we apply $r_0 = 2$ mm h^{-1}. Additionally, the flooding starts in the centers of tracked CP instances from the previous time step, if there are any. To detect only robust CP instances, we keep rain patches and potential CP areas only when their area $A \geq A_0$ with $A_0 = 3$ km^2, as opposed to the 2 km^2 threshold used by Hoeller, Fiévet, and Haerter (2023). Valid rain patches with a downdraft center, which is located in an area classified as "no CP" by the *k*-means algorithm, will not be labeled as CPs. The same is true for potential CP areas which do not coincide with the center of a downdraft or a tracked CP instance from the previous time step.

Providing the fields of virtual temperature, T_v, and both horizontal and vertical wind speed in the lowest domain level, as well as r_{int}, CoolDeTA can identify, label, and track each CP instance individually while storing additional information. To use the simplest possible case in the present study, we here keep the labels derived based on CoolDeTA binary, comprising the two classes "CP" and "no CP."

2.1.2. Input Variables

Regarding the potential input for the neural network, SAM outputs several variables which are accessible from space-borne data. The present study focuses on the cloud top temperature, T_{CT}, and r_{int}. For T_{CT}, we employ the standard output of SAM where T_{CT} equals the cloud top temperature for cloudy domain columns and the surface temperature otherwise. T_{CT} and r_{int} are readily available from infrared emissions and an increasing number of precipitation products. Depending on the region of interest and problem-specific requirements in terms of spatial and temporal resolution, as well as accuracy, these precipitation products can be multisatellite products with global coverage such as IMERG (Huffman et al., 2015) or even products based on ground-based weather radars.

2.1.3. Training and Test Sets

For each of the four simulation setups, output is available for 7.5 simulation days in total. The first 3 days are considered as spin-up phase (Hoeller, Fiévet, & Haerter, 2023). After these spin-up days, we employ the simulation output of day 4 for network training and validation. While we train networks based on the training set, the validation set is used to monitor the progress of the training on separate data which has not been trained on. As is common in supervised learning, we randomly split the data by assigning each instance with a probability of 75% to the training set and with 25% to the validation set. Throughout the entire training, including different network trainings, we keep the obtained allocation fixed to facilitate the comparison between networks. Yet, the order of the training data is randomly shuffled every training epoch, that is, every time the training set is passed through a neural network.

When all network trainings are completed, the final performance is evaluated based on a test set (Willemink et al., 2020) consisting of simulation output of day 6, that is, the test set is not considered at any earlier stage. Although the observed CPs, and the complex pattern formed by their interaction, are unique for each simulation day, the offset of 1 day between the test set and the training and validation set guarantees fully independent sets w.r.t. the distribution of relevant quantities such as humidity.

To ensure sufficient variation between consecutive time steps of the data sets, we consider only every second time step of the corresponding simulation output for the training and validation set, and every fourth time step

21698996, 2024, 1, Downloaded from https://agupubs.onlinelibrary.wiley.com/doi/10.1029/2023JD040126 by Cochrane Germany, Wiley Online Library on [28/02/2024]. See the Terms and Conditions (https://onlinelibrary.wiley.com/terms-and-conditions) on Wiley Online Library for rules of use; OA articles are governed by the applicable Creative Commons License

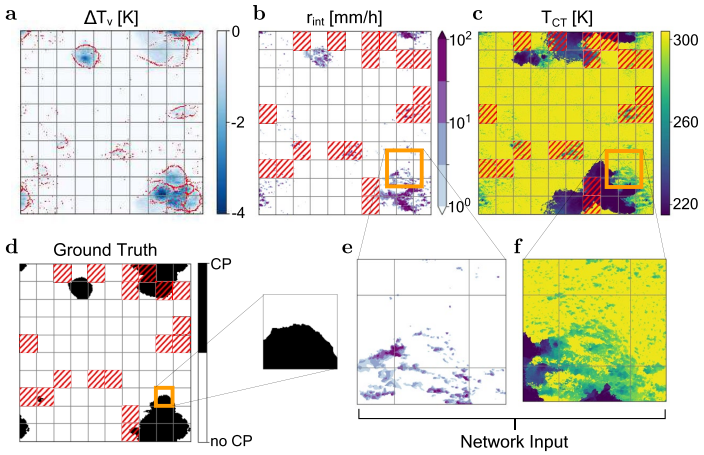

Figure 1. Defining patches for neural network input and ground truth. (a) Time step 497, that is, 80 min before T_{max} on simulation day 4, of "diu4K wind," showing near-surface virtual temperature anomaly, ΔT_v, with superimposed dynamical gust front, that is, $w > \overline{w} + 2\sigma_w$ (red scatter). The superimposed grid represents the individual $n_p \times n_p$ pixel patches, processed by the neural network. (b) Analogous to (a) but for surface rain intensity, r_{int}. Patches that were omitted from the data set are hatched. (c) Analogous to (a) but for cloud top temperature, T_{CT}. (d) Ground truth labeling showing cold pool (CP) areas as black regions; a single patch is enlarged for clarity. (e) Highlighted patch, including padding, for r_{int}. (f) Analogous to (e) but for T_{CT}.

for the test set. This is particularly important for the test set to prevent any distortion of the final results due to correlated data.

In order to reduce the computational cost and accelerate network training, we subdivided every $N \times N$ pixel output field, termed "image," into 100 subregions, which we refer to as "patches," of $n_p \times n_p$ pixels each. As our downsampling requires the integer n_p to be a power of 2 (see Section 2.2) and to compromise between computational effort and prediction skill, we chose $n_p = 128$ as the linear dimension of each two-dimensional patch. To accomplish this, each original output image is padded from $n_x = 1{,}200$ to $n_{x,pad} \equiv 1{,}280$ in compliance with the periodic lateral boundary conditions.

Eventually, each network prediction requires an input and a corresponding ground truth to optimize and/or evaluate the network performance. While the ground truth corresponds to an $n_p \times n_p$ pixel patch of the output images with derived labels, the input consists of stacked patches corresponding to T_{CT} and r_{int}. To compensate for lacking context information at patch boundaries, the input patch is $n_p/2$ pixels larger than the underlying ground truth patch on either side, resulting in an input patch size of $2n_p \times 2n_p$ pixels (Figure 1). Although the additional $n_p/2$ pixels on each side are thus ranging into the adjacent ground truth patch, this overlap does not distort the results as the final network prediction only comprises the underlying central $n_p \times n_p$ pixel patch.

To ensure a robust training process and reliable results, we manually checked the ground truth labeling of every patch in the data set. We omitted patches if they (a) contained at least 1, but less than 25 pixels (i.e., 1 km^2) of class "CP," (b) were in the center of a larger convective system with a gust front significantly beyond the boundaries of the input patch, (c) were poorly labeled by the CP detection algorithm, or (d) featured ambiguous scenes where an unequivocal verification of the labeling is not possible. For the evaluation of both (c) and (d), the dynamical gust front, that is, $w > \overline{w} + 2\sigma_w$ served as main indicator: clear offsets between gust front and boundaries of ground truth CPs were interpreted as poor labeling, discontinuous, and thus dissipating gust fronts as ambiguous cases. Omitted patches were excluded from the data set. We did not modify the individual pixels which belong to a certain CP instance. Only if a certain CP instance in an otherwise accurately labeled patch was a complete artifact, we set all pixels of that CP instance in the patch to "no CP" and kept the corrected patch in the data set.

As simulation setups affect the cloud and rainfall patterns associated with CPs, we considered patches from simulations with different environmental conditions. Yet, both simulations with imposed wind profiles feature

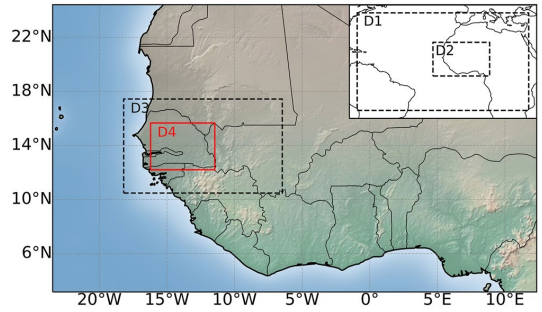

Figure 2. Weather Research and Forecasting (WRF)-nested domains for Senegal case study. Map of Africa showing the regional/outer domain (dashed), denoted as D1 at 9 km horizontal resolution. D2, D3, and D4 denote the nested domain boundaries at horizontal resolutions 3, 1, and 0.333 km, respectively. The red domain is the primary region used in this case study.

prevailing easterly winds. To allow the network to capture underlying patterns independent of the wind direction, we rotate each patch of the two simulations with wind by 90°, 180°, and 270° and add the resulting patches to the data sets. Extending data sets with slightly modified copies of the data based on operations such as rotations or translations is a common approach to increase the amount and diversity of data and is called data augmentation (Chlap et al., 2021; Shorten & Khoshgoftaar, 2019).

Data imbalances due to the underrepresentation of classes or features in the training set are a common issue of learning algorithms (He & Garcia, 2009). Taking the reduced convective activity due to nocturnal cooling into account, the majority of patches does not contain any CP pixels in the ground truth data and features only the class "no CP." We compensated for this by randomly removing a certain number of these patches (Shi et al., 2021). By experiment, we selected the number of patches with only class "no CP" to be 4% of the training and validation set. The other extreme are patches with class "CP" only. Surface temperature oscillations promote the sudden organization of CPs into convective systems (Haerter et al., 2020; Jensen et al., 2022). Since the surface areas of these convective systems often exceed the patch size, a great number of patches have class "CP" only. However, omitting patches in the center of larger convective systems according to (b) already lowered the number of patches with class "CP" only to ≈5.5% resulting in a sufficiently balanced training and validation set distribution (Figure 3a) with mean class "CP" fractions of 0.26 (diu2K), 0.31 (diu2K wind), 0.38 (diu4K), and 0.52 (diu4K wind). We chose not to balance the distribution of the test set in order to not affect the results in any way.

The resulting data set for training and validation comprises 4,208 patches with 984 different CP instances. Each CP instance represents a certain CP event as labeled by CoolDeTA. Depending on both their lifetime and their spatial extent, individual CP instances can be present in multiple patches in the data set. Thus, the number of CP instances is higher for diu2K (420) and diu4K (389) compared to the two setups with wind shear, diu2K wind (107) and diu4K wind (68), which feature less, but often larger and more persistent CP events. The number of CP instances provides an indication of the CP variety within the data set. It should be noted though that CPs and their patterns are often affected by complex interaction processes. Although a specific CP event might undergo significant changes during its lifetime and even merge with other CP events, it would still be counted as one CP instance by CoolDeTA. Accordingly, we consider the provided numbers of CP instances a rather conservative estimate of the CP variety in the data set. The test set comprises 7,226 patches with 183 CP instances. With 44 CP instances in diu2K, 31 in diu2K wind, 77 in diu4K, and 31 in diu4K wind, they are more uniformly distributed among the different simulations. We attribute this also to the fact that we considered only every fourth time step for the test set, thus excluding some short-lived CP instances. Since the test set was not balanced, 6,684 of the 7,226 patches contain only class "no CP."

2.1.4. Senegal Case Study

In addition to the network training and testing, we also conducted a numerical simulation over West Africa to validate the method under more realistic conditions. For this case study, we used the nonhydrostatic Advanced Research Weather Research and Forecasting (WRF) model version 4.3 (Skamarock et al., 2021) for a 24-hr numerical simulation on 4 August 2022 over Senegal in West Africa (Figure 2). The date was chosen primarily for the high frequency of convective systems during this period, as well as the occurrence of smaller-scale convection in other parts of the study domain. To obtain numerical simulation data at a relatively high grid resolution, in this case 333 m, a nesting approach was necessary. We therefore created four domains with grid spacing of 9, 3, 1, and 0.333 km with a one-way nesting strategy. Only data from the 0.333 km domain simulation are used in this study.

National Oceanic and Atmospheric Administration/National Centers for Environmental Prediction Global Forecasting Model (GFS) forecasts, with a 0.25° horizontal grid spacing, were employed for the initial and boundary conditions in the 9 km outer domain, provided at 3 hourly intervals. Fifty-five vertical levels were chosen, such that their vertical spacing decreases closer to the surface. To represent surface fluxes, we used the Noah Land Surface Model scheme with soil temperature and moisture at four layers. The 3–0.333 km domains were run with explicit convection. In the 9 km domain, we used the Kain-Fritsch convection scheme with a mass-flux approach.

21698996, 2024, 1, Downloaded from https://agupubs.onlinelibrary.wiley.com/doi/10.1029/2023JD040126 by Cochrane Germany, Wiley Online Library on [28/02/2024]. See the Terms and Conditions (https://onlinelibrary.wiley.com/terms-and-conditions) on Wiley Online Library for rules of use; OA articles are governed by the applicable Creative Commons License

21698996, 2024, 1, Downloaded from https://agupubs.onlinelibrary.wiley.com/doi/10.1029/2023JD040126 by Cochrane Germany, Wiley Online Library on [28/02/2024]. See the Terms and Conditions (https://onlinelibrary.wiley.com/terms-and-conditions) on Wiley Online Library for rules of use; OA articles are governed by the applicable Creative Commons License

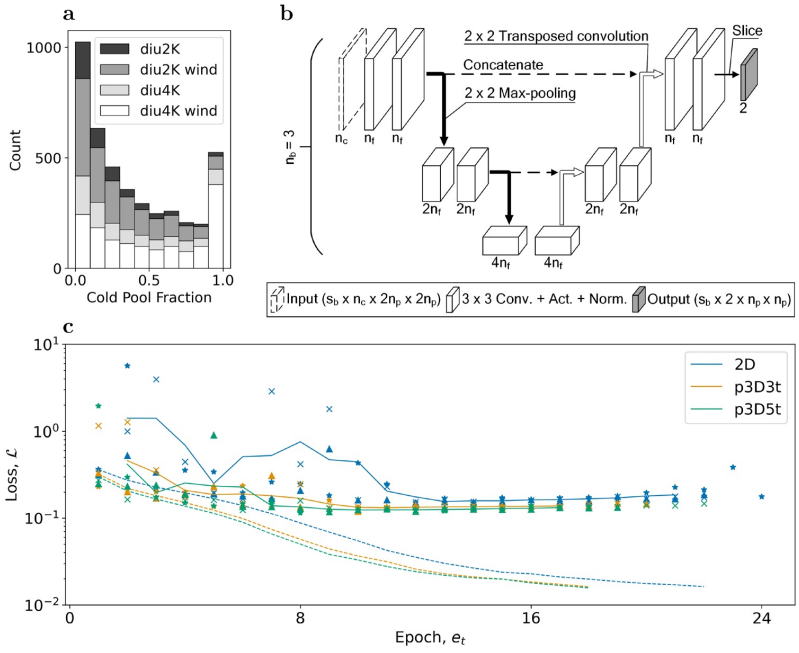

Figure 3. Training statistics and U-Net architecture. (a) Distribution of the data set used for network training and validation w.r.t. the fraction of class "CP" in each patch. (b) U-Net architecture for cold pool segmentation, here for the case with three filtering blocks ($n_b = 3$). The number of input channels n_c represents the number of different variables provided to the network as input. In the case of pseudo-3D models, the number of input channels, n_c = number of variables × number of utilized time steps, n_t. The number of output channels comprises the two classes "CP" and "no CP." (c) Loss, $\mathcal{L}$, as a function of the epoch, e_t, for the 2D, p3D3t, and p3D5t neural networks. Dashed lines represent running averages of training loss for all training runs of a respective neural network type. Thin colored are running averages of validation loss for all training runs of a respective neural network type additionally averaged over a centered window of three e_t; different symbols correspond to the validation loss of the different training runs. Note: As the mean variance of the training loss for the three neural network types is only between 2.5×10^{-6} (2D) and 6.1×10^{-6} (p3D3t), markers for the training loss of different training runs are not visualized.

Finally, we applied the large-eddy simulation approach to represent the planetary boundary layer (PBL) in the 333 m domain, while the Yonsei University PBL scheme was employed for the other domains.

2.2. Network Architecture

As mentioned, instead of predicting one specific label per provided input image (classification), the detection of CPs requires an output, such as "CP" or "no CP," for every pixel of the image (segmentation). A common architecture used for segmentation is the U-Net (Ronneberger et al., 2015), a CNN that consists of an encoder path and a decoder path. In the encoder path, input images are downsampled after every block, allowing the network to learn features at larger scales. A common downsampling method, where the output is generated from the input by considering only the maximum value of a moving window of size $s \times s$ and which we also apply in the present study with $s = 2$, is max pooling. By reducing the resolution of the image in each downsampling step, typically by a factor of 2 as we do here, the network can learn features at different scales. To be able to capture the underlying correlations, the number of filter layers is doubled with every downsampling step. In the decoder path, on the other hand, the images are upsampled again via transposed convolution or interpolation to finally enable pixel-wise predictions. After each upsampling step, concatenated filter layers of the same depth encoder block provide additional information. The employed U-Net architecture for the simplified case with three vertical blocks ($n_b = 3$) is depicted in Figure 3b.

21698996, 2024, 1, Downloaded from https://agupubs.onlinelibrary.wiley.com/doi/10.1029/2023JD040126 by Cochrane Germany, Wiley Online Library on [28/02/2024]. See the Terms and Conditions (https://onlinelibrary.wiley.com/terms-and-conditions) on Wiley Online Library for rules of use; OA articles are governed by the applicable Creative Commons License

Apart from n_b and the starting number of filter layers n_f, neural networks and U-Nets in particular offer a variety of modeling choices, termed hyperparameters, to tune. After an exploration phase, in which we identified hyperparameters significant for our network along with promising orders of magnitude based on training and validation performances, we investigated the following seven hyperparameters in more detail: n_b, ultimately chosen as $n_b = 6$; n_f, ultimately chosen as $n_f = 64$; the activation function, ultimately chosen as LeakyReLU; the normalization strategy, ultimately chosen as batch normalization; the loss function, ultimately chosen as combination of cross entropy loss and dice loss; the learning rate l_r, ultimately chosen as exponentially decaying function $l_r = 10^{-5} \times \gamma^{e_t}$ with e_t as the training epoch and $\gamma = 0.9$; and the batch size s_b, ultimately chosen as $s_b = 8$. Activation functions are nonlinear functions and a fundamental part of CNNs. Following convolutional layers in the convolution block (cf., Figure 3b), activation functions enable the network to capture complex patterns. Typically, convolution blocks are completed by normalization steps, which can support an efficient learning process (Ioffe & Szegedy, 2015). While the loss function is the function to be minimized during training, l_r controls the corresponding optimization step size. The number of instances considered per optimization step is the batch size. Typically, training batch sizes are greater one to reduce the risk of getting stuck in local minima.

In order to determine the most promising network configuration w.r.t. the seven hyperparameters, we conducted a number of experiments based on the training and validation set. Instead of analyzing all possible combinations of configurations, we limited the number of experiments by structuring them in two stages. Starting from a first guess reference configuration for which all seven hyperparameters were defined pragmatically, the first stage consists of multiple levels, each containing experiments for a group of hyperparameters with all their combinations. After each level, the reference configuration is updated based on the best candidates of those hyperparameters. Due to their close relation, we grouped l_r with s_b (Group 1), activation function with normalization strategy and loss function (Group 2), and n_b with n_f (Group 3). Whereas the hyperparameters in Group 1 are essential for robust learning and thus investigated first, the hyperparameters in Group 3 are examined last as larger numbers of n_b and n_f, which were expected to be advantageous, would slow down the remaining experiments significantly.

Since some hyperparameters could have candidates with similarly good performance so that the best candidate might thus change for other configurations, we performed a second stage of experiments with all combinations of these candidates plus some fine-tuned ones.

Depending on the convolution kernel, CNNs can be categorized into 2D and 3D CNNs. Conventional end-to-end 2D CNNs receive 2D input, which may consist of multiple channels, for example, 2D fields of different variables, apply 2D convolutions, that is, convolutions with 2D kernel matrix, and generate a corresponding 2D output, whereas 3D CNNs analogously process 3D data. At the expense of significantly higher computational cost, 3D CNNs are thus able to learn correlations in a third dimension based on the 3D convolution kernel. As we are interested in 2D segmentations and the simplest model possible, we selected the 2D version. However, since CPs are density currents and exhibit gust fronts typically emanating radially from a precipitation cell center, expansion over time constitutes one of the main CP features (Benjamin, 1968). In order to include this time-dependent component and potentially enable the network to learn the correlations between consecutive time steps, we also implement the so-called pseudo-3D approach. The term "pseudo-3D," as introduced by Vu et al. (2020), represents a model class that is intermediate between conventional 2D CNNs and 3D CNNs. In pseudo-3D models, the information of the third dimension (here time) is inserted as additional input channels to the network, therefore without modifying the network's 2D architecture. As a consequence, the total number of input channels of pseudo-3D models depends not only on the number of input variables provided, but on the product of the numbers of input variables and utilized time steps. Thus, pseudo-3D models might potentially benefit from time-dependent information without being as computationally expensive as end-to-end 3D models (Vu et al., 2020). In the present study, we investigate the pseudo-3D model with three (p3D3t) and five time steps (p3D5t). Time steps are thereby centered about the time step for which a prediction is to be made.

2.3. Loss and Evaluation Metrics

The selection of an appropriate loss function depends on the specific problem at hand. All loss functions use the pixel-wise network prediction $U = [U^{(0)}, U^{(1)}]$, consisting of the two output channels $U^{(0)}, U^{(1)} \in \mathbb{R}^{n_P \times n_P}$, where indexes "0" and "1" indicate the "no CP" and "CP" channels, respectively, and compare U with the corresponding ground truth derived by CoolDeTA, denoted $V \in \mathbb{N}^{n_P \times n_P}$, where $V_{kl} \in \{0, 1\}$, indicating "no CP" and "CP," respectively.

21698996, 2024, 1, Downloaded from https://agupubs.onlinelibrary.wiley.com/doi/10.1029/2023JD040126 by Cochrane Germany, Wiley Online Library on [28/02/2024]. See the Terms and Conditions (https://onlinelibrary.wiley.com/terms-and-conditions) on Wiley Online Library for rules of use; OA articles are governed by the applicable Creative Commons License

We examined several loss functions during the experiments. For this purpose, we rescaled each pixel $U_{kl}^{(j)}$ in U to the range [0,1] so that the "probabilities" of both the "no CP" and "CP" channel sum up to one. We term the result of this so-called "softmax" function u. The corresponding function is written as

$$u_{kl}^{(j)} \equiv \frac{e^{U_{kl}^{(j)}}}{e^{U_{kl}^{(0)}} + e^{U_{kl}^{(1)}}}, \text{for } j \in \{0, 1\}. \tag{1}$$

In order to compare u to the ground truth, we split V analogously to the prediction via one-hot encoding into two slices of binary data $v = [v^{(0)}, v^{(1)}]$, that is, $v_{kl}^{(0)} = 1 - V_{kl}$ and $v_{kl}^{(1)} = V_{kl}$. As loss functions, we employed a cross entropy loss which is often used as default in image segmentation and defined as

$$\mathcal{L}_{\mathrm{CE}}(u, v) = \sum_{j,k,l} \frac{-v_{kl}^{(j)} \log\left(u_{kl}^{(j)}\right)}{\sum_{m,n,q} v_{nq}^{(m)}}, \tag{2}$$

a soft Dice coefficient loss, defined as

$$\mathcal{L}_{\mathrm{Dice}}(u, v) = 1 - \frac{2 \sum_{j,k,l} u_{kl}^{(j)} v_{kl}^{(j)} + \epsilon}{\sum_{j,k,l} u_{kl}^{(j)} + \sum_{j,k,l} v_{kl}^{(j)} + \epsilon}, \tag{3}$$

where $\epsilon = 1$ is a constant preventing divisions by zero (Jadon, 2020), and a combination of both

$$\mathcal{L}(u, v) = \alpha \mathcal{L}_{\mathrm{Dice}}(u, v) + (1 - \alpha)\mathcal{L}_{\mathrm{CE}}(u, v), \tag{4}$$

with $\alpha = 0.5$. Whereas $\mathcal{L}_{\mathrm{Dice}}$ can deal with imbalanced data sets (Milletari et al., 2016) and focuses on how good the predicted CPs overlap the ground truth CPs, $\mathcal{L}_{\mathrm{CE}}$ evaluates the difference between the probability distributions of u and v. For our problem, we chose $\mathcal{L}$ as loss function as it combines the strengths of both $\mathcal{L}_{\mathrm{Dice}}$ and $\mathcal{L}_{\mathrm{CE}}$ and outperformed both these functions during the experiments.

For the evaluation of the trained networks, we distinguish between patches containing only one of the two classes for the corresponding ground truth data and patches with at least one pixel of both classes. In the former case, the only evaluation metric will be pixel accuracy, PA, which evaluates the fraction of predictions that are correct, defined as

$$\mathrm{PA} = \frac{\mathrm{TP} + \mathrm{TN}}{\mathrm{TP} + \mathrm{TN} + \mathrm{FP} + \mathrm{FN}}. \tag{5}$$

In Equation 5, TP and TN indicate true positive and true negative predictions, respectively, whereas FP and FN denote false positive and false negative predictions, respectively.

In case the ground truth patch contains at least one pixel of both classes, we additionally calculate the intersection over union, IOU,

$$\mathrm{IOU} = \frac{\mathrm{TP}}{\mathrm{TP} + \mathrm{FP} + \mathrm{FN}}. \tag{6}$$

The IOU score is a measure of how well the specific objects of prediction and ground truth overlap one another, ranging from zero, where no overlap is found, to unity, for perfect overlap. Furthermore, we consider Precision and Recall, defined as

$$\mathrm{Precision} = \frac{\mathrm{TP}}{\mathrm{TP} + \mathrm{FP}}, \tag{7}$$

and

$$\mathrm{Recall} = \frac{\mathrm{TP}}{\mathrm{TP} + \mathrm{FN}}. \tag{8}$$

As IOU both Precision and Recall range from zero, where no "CP" pixel was correctly identified, to unity, for a perfect prediction. However, shedding light on different components of the prediction, they help to understand potential sources of good and bad performances.

21698996, 2024, 1, Downloaded from https://agupubs.onlinelibrary.wiley.com/doi/10.1029/2023JD040126 by Cochrane Germany, Wiley Online Library on [28/02/2024]. See the Terms and Conditions (https://onlinelibrary.wiley.com/terms-and-conditions) on Wiley Online Library for rules of use; OA articles are governed by the applicable Creative Commons License

Table 1
Mean Test Performances of Different Models

Patches	Model	PA (%)	IOU	Precision	Recall
Both classes	2D	93.8	0.71	0.84	0.83
	p3D3t	94.8	0.75	0.83	0.88
	p3D5t	94.5	0.74	0.84	0.87
Only no CP	2D	99.8			
	p3D3t	99.9			
	p3D5t	99.9			
Only CP	2D	92.0			
	p3D3t	94.1			
	p3D5t	85.9			

Note. Presented are mean performances for pixel accuracy (PA), intersection over union (IOU) score, Precision, and Recall for patches with at least one pixel of both classes "CP" and "no CP" in the ground truth (both classes) and PA for patches with only pixel of class "no CP" (only no CP) or "CP" (only CP) in the ground truth.

To enable a more application-oriented perspective on the performance of the three models, we define cold pool objects (CPOs) as spatially four-connected regions of ≥25 "CP" pixels (≥1 km^2) and evaluate both the probability of detection, POD, and the false alarm ratio, FAR, defined as

$$\mathrm{POD} = \frac{D}{D+M}, \tag{9}$$

and

$$\mathrm{FAR} = \frac{\mathrm{FA}}{\mathrm{FA}+D}, \tag{10}$$

with the numbers of successfully detected CPOs, D, missed CPOs, M, and false alarm, FA. The minimum CPO size of 25 "CP" pixels ensures that only robust predictions are considered. Ground truth CPOs are considered detected if (a) predicted CPOs overlap at least 50% of their area and (b) at least 50% of the area of the predicted CPOs falls inside ground truth CPOs. Condition (b) makes sure that only skilled predictions with CPO areas in the correct order of magnitude are considered successful detections. As the smallest ground truth CPO in the test set comprises 59 pixels, the defined minimum size does not affect the CPO detection. Undetected ground truth CPOs are considered missed CPOs. Predicted CPOs which do not coincide with any "CP" pixel of the ground truth are considered false alarms.

2.4. Network Validation

We plot the training and validation losses for the 2D and both pseudo-3D models as a function of the epoch, e_t (Figure 3c). e_t describes how many times the entire training set has been passed through the neural network. The loss measures the quality of the prediction, where a value of zero means perfect prediction. Instead of defining a fixed e_t, we stop the training if the validation loss has not improved for 10 consecutive e_t. Taking into account the stochasticity involved in the training process, we conducted three runs for each model. As might be expected, the *training loss* decreases monotonically with the data employed for learning, that is, e_t, and reaches a value close to zero for our maximum e_t of 22–24. Notably, for intermediate e_t, both pseudo-3D neural networks perform better than the 2D counterpart, whereas for the final e_t, the three are essentially indistinguishable.

However, a good value of training loss does not necessarily imply optimal *validation loss*, a measure of prediction quality for a previously unseen data set. Indeed, we find that intermediate e_t (≈10) yield lowest validation loss for all three cases, such that a global minimum occurs. This type of optimum at intermediate e_t is typical of neural networks and is often interpreted as large e_t constituting a form of overfitting w.r.t. the training data—yielding less than optimal behavior for the unknown validation data. Yet, the minimum is characterized by an asymmetric increase of validation loss, where somewhat larger e_t lead to only small increases in validation loss. Further, we again find quantitative improvements in validation loss for the pseudo-3D cases, which systematically reach lower values of loss than 2D.

3. Results

For the final evaluation of the trained neural networks, we now employ the test set, that is, the data for day 6 of each simulation. We ensure that the results obtained are on the conservative side, by considering only the worst run with the greatest final validation loss for each model. We conclude this chapter with a case study, where we shed light on potential sources of misclassifications through realistic examples from a simulation over Senegal.

3.1. Test Set Performance

We quantify the utility of our segmentation method by applying typical performance metrics (Table 1). A key measure is pixel accuracy (PA), which is generally high (mean PA $\gtrsim$ 94%) for all models, with the pseudo-3D models performing slightly better than the 2D model. The intersection over union (IOU) score denotes the fidelity

21698996, 2024, 1, Downloaded from https://agupubs.onlinelibrary.wiley.com/doi/10.1029/2023JD040126 by Cochrane Germany, Wiley Online Library on [28/02/2024]. See the Terms and Conditions (https://onlinelibrary.wiley.com/terms-and-conditions) on Wiley Online Library for rules of use; OA articles are governed by the applicable Creative Commons License

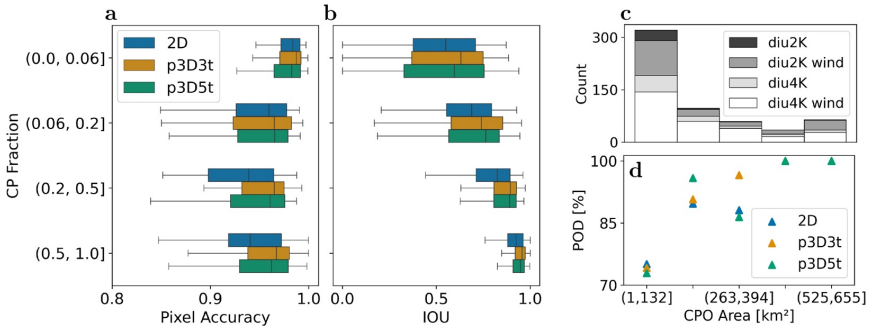

Figure 4. Selected test performances of different models. (a) Distributions of pixel accuracy for each neural network, grouped into quartiles of cold pool (CP) fraction with ranges, as indicated along the vertical axis. Colored bars represent the interquartile range IQR = $Q3 - Q1$ of the three tested models, with the first quartile $Q1$ and the third quartile $Q3$, along with the corresponding median (vertical dash). Whiskers range from $Q1 - 1.5 \times$ IQR (minimum) to $Q3 + 1.5 \times$ IQR (maximum). Outliers w.r.t. this range are not visualized. (b) Analogous to (a) but for the intersection over union (IOU) score. Note that for both metrics a value of unity reflects a perfect prediction. (c) Distribution of spatially contiguous test set cold pool objects (CPOs) w.r.t. their CPO area. (d) Percentage of successfully detected CPOs from (c), POD, for varying CPO area. Note the shared horizontal axis between (c, d) and the overlapping markers for the largest two CPO area intervals in (d).

of spatial overlap of ground truth CPs and neural network-predicted CPs and is thereby sensitive to the underlying CP areas, yielding lower values than PA for all models. Again the pseudo-3D models achieve higher mean IOU scores of 0.75 (p3D3t) and 0.74 (p3D5t) compared with 0.71 for the 2D model. As mean Precision is almost equally high for all models (Table 1), the difference in IOU is mainly driven by the higher mean Recall of the pseudo-3D models, that is, they miss less "CP" pixels than the 2D model.

In order to investigate the sensitivity of the network performances w.r.t. the CP fraction in the patch, we group PA and IOU score into quartiles of CP fraction. For all these quartiles, PA is high (PA $\gtrsim 0.95$) for all models (Figure 4a). Yet, systematic differences exist: Generally, PA is greatest for small CP fraction and somewhat decreases for intermediate fractions, where it then seems to saturate. This behavior is expected, since (a) the majority of the training and validation set patches contained only small fractions of class "CP," slightly biasing the neural networks toward "no CP" predictions and (b) regions without "CP" pixels often feature neither precipitation, nor clouds, simplifying the network prediction. Overall, PA is somewhat greater for the pseudo-3D models, however, this benefit is nearly lost for small CP fractions, a finding we attribute to the potential noise at the early stages of CP expansion: in p3D3t and p3D5t, where additional time steps are included, data taken before the onset of the CP might contribute to the training—thus obscuring the signal of actual CP expansion.

The IOU score (Figure 4b) can be substantially lower for the smallest CP fraction quartile, with some improvement for the pseudo-3D models. This loss for small CP fraction is however not surprising to us, as for small CP fraction there will often be only few pixels in a patch which actually qualify as CP pixels and small spatial displacements of these pixels in the predicted data can already lead to a drastic reduction of the IOU. Refined measures could be designed that still assign a score to a minimally displaced CP pixel. However, physically relevant CPs, for example, in terms of collision effects (Fiévet et al., 2023; Meyer & Haerter, 2020) and intense precipitation (Jensen et al., 2022) tend to cover larger patch fractions and the IOU score is systematically high—again with best performances for the pseudo-3D models.

We now turn to test patches which contain only "no CP" or "CP" pixels in the ground truth. For the former case, PA yields near-perfect accuracy (Table 1). Thus, the models show high fidelity in capturing cases where CPs are not present, most likely due to the absence of precipitating clouds in a majority of the patches. PA is however substantially reduced in the latter case (Table 1). The reduction in PA is especially pronounced for p3D5t, thus the model where five time steps were used. We attribute this loss of accuracy to the temporal mixing of patches with and without CP pixels, whereby the lack of CP pixels at earlier stages may skew the results.

In Figures 4c and 4d, we evaluate the percentage of successfully detected CPOs, POD (see Section 2.3), as a function of CPO area. The results are quite clear: larger CPOs are detected at quite high fidelity ($\gtrsim$90%), whereas the fidelity

21698996, 2024, 1, Downloaded from https://agupubs.onlinelibrary.wiley.com/doi/10.1029/2023JD040126 by Cochrane Germany, Wiley Online Library on [28/02/2024]. See the Terms and Conditions (https://onlinelibrary.wiley.com/terms-and-conditions) on Wiley Online Library for rules of use; OA articles are governed by the applicable Creative Commons License

Table 2
Detection Performance on the Test Set for the Different Simulations

Simulation	Total CPOs	2D		p3D3t		p3D5t	
		POD	FAR	POD	FAR	POD	FAR
diu2K	35	0.71	0.24	0.71	0.32	0.83	0.29
diu2K wind	180	0.88	0.15	0.86	0.22	0.87	0.23
diu4K	83	0.90	0.04	0.92	0.04	0.93	0.09
diu4K wind	292	0.80	0.21	0.83	0.23	0.78	0.30
All	590	0.84	0.17	0.84	0.21	0.83	0.25

Note. For each neural network, the probability of detection, POD, and the false alarm ratio, FAR, are shown. The test set patches and thus also the contained cold pool objects (CPOs) to be detected are identical for all networks. Note that only patches with at least one CPO in the ground truth were evaluated here.

for the smallest area class is lower (Figure 4d). Again, a clear improvement in detection cannot be achieved for either of the three models, even though a slight improvement is seen for pseudo-3D models for the intermediate area classes.

Table 2 shows both POD and the false alarm ratio (FAR) for each simulation. Whereas POD is similarly good for all models, the pseudo-3D networks feature higher and thus worse FAR of 0.21 (p3D3t) and 0.25 (p3D5t), compared to 0.17 of the 2D network. In case of the p3D5t model, this means on average one spuriously predicted CPO for every three successfully detected CPOs. However, as the mean validation losses of the p3D5t training runs are lowest in comparison to the other models (Figure 3c), this should not be a problematic characteristic for p3D5t, but is most likely caused by an unfavorable epoch to stop the training run. Apart from lower detection rates for CPOs from "diu2K," which are mainly attributed to a high proportion of CPOs in the smallest area class, the performance of the networks seems to be relatively independent w.r.t. the simulation setup.

As the morphology of patterns is so diverse and quantification of spatial pattern overlap always requires to make choices as to the metrics used, we also provide a qualitative discussion on typical cases now. We visualize several predictions based on the test set and present 2D fields of rainfall intensity (r_{int}), cloud top temperature (T_{CT}), and virtual temperature anomaly (ΔT_{v}) as well as the ground truth segmentation and predictions of the three neural network models side by side (Figure 5). The cases selected represent a range of circumstances: in some cases, cloud patterns are rather obvious and yield reasonable segmentation for all models (Figure 5a). Only in a few cases, some models miss CPOs completely (Figure 5b). As in the presented example, these CPOs are generally rather small and weak, and often associated with cloud-free gust fronts. Where different aspects overlap temporally, such as cirrus from previous convection obscuring the present scene (Figure 5c), all models may struggle with proper segmentation. In fact, cirrus clouds are a major source of false positives, as all models associate very cold T_{CT} with CPs. However, whether cirrus clouds eventually lead to false positives depends also on their pattern. For the pseudo-3D models, simultaneous advection seems to increase the probability of false positives. Although cases with advection pose additional challenges, all models perform well for large CPs with large cloud-free areas, for example, Figure 5d. Yet, for cases in which the parent convection partly dissipated (Figure 5e) or dissipates (Figure 5f) pseudo-3D models give results which are physically more accurate w.r.t. the plausibility of the gust front. The same seems to be true for scenes with advected parent convection (Figure 5g)—likely due to the fact that parts of the gust front are obscured when only using single patches, but revealed when taking a sequence of time steps into account. As a general outcome, all models perform reasonably well on the test cases described, yet, the distinction between 2D and pseudo-3D quality metrics is not as clear cut and should be assessed dependent on the scientific questions in focus.

3.2. Case Study: Detecting Cold Pools Over Senegal

As we trained the neural networks solely with data from idealized simulations, they are not intended for direct application to observational data. However, to gain a better understanding of potential challenges associated with transitioning to more realistic data, we now apply the neural networks to segment CPs in the case study data from Senegal (see Section 2.1). Due to its location in the transition zone from tropical savannah to arid steppe, sea breezes from the Atlantic Ocean, and orographic effects of the Northern Guinea Highlands, the region of the case study features complex cloud and rainfall patterns and is thus well-suited for a realistic trial. Contrary to the evaluation of the test set predictions, we here refrain from analyzing any quantitative metrics based on ground truth images. This way, we avoid omitting any patches and can thus test the network performance over the entire simulation domain, including patches with ambiguous scenes.

To obtain the predictions for the entire domain, we subdivided the simulation domain into patches of $n_{\mathrm{p}} \times n_{\mathrm{p}}$ pixels, which the networks can process, and recombined the network-generated segmentations. Unlike in the network test, we use the neural networks of all three training runs for the prediction of each model: Only if all three networks of a certain model segment a pixel as "CP," it is predicted as "CP." Otherwise, it is predicted as "no CP." Hereby, we can identify consistent features w.r.t. false negatives and positives, which were learned by a certain model during all training runs.

21698996, 2024, 1, Downloaded from https://agupubs.onlinelibrary.wiley.com/doi/10.1029/2023JD040126 by Cochrane Germany, Wiley Online Library on [28/02/2024]. See the Terms and Conditions (https://onlinelibrary.wiley.com/terms-and-conditions) on Wiley Online Library for rules of use; OA articles are governed by the applicable Creative Commons License

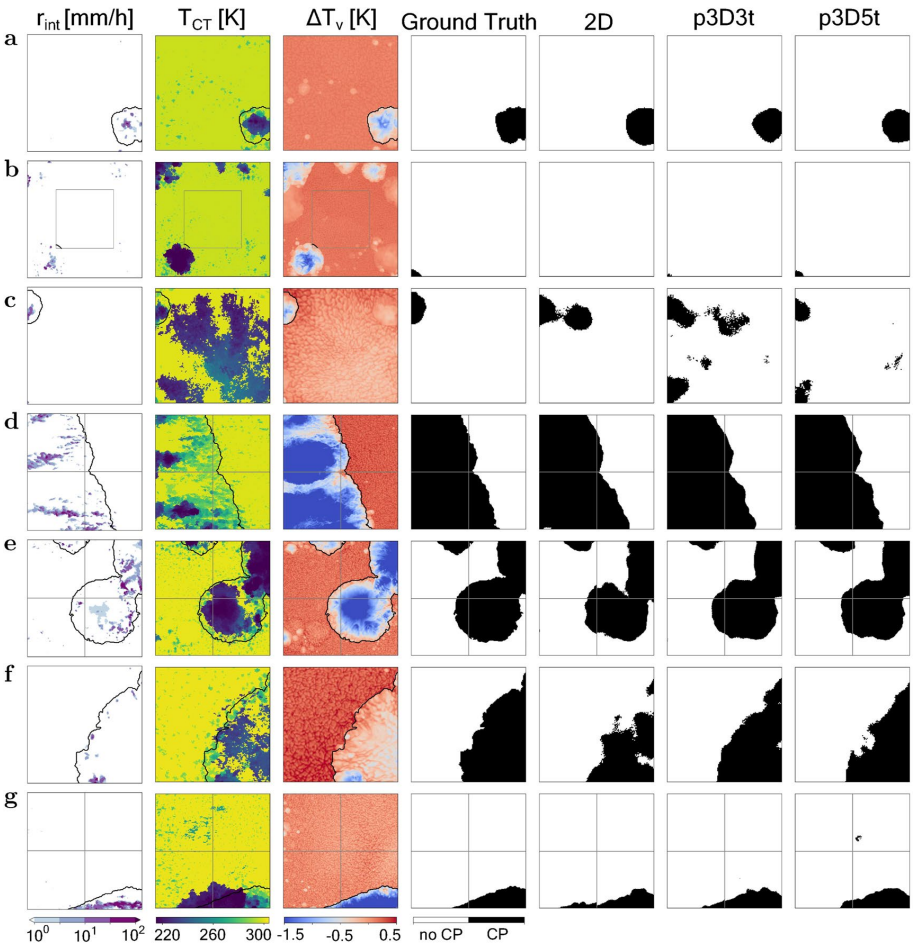

Figure 5. Examples of cold pool predictions based on the test set. Two-dimensional fields of surface rain intensity, r_{int}, cloud top temperature, T_{CT}, and near-surface virtual temperature anomaly, ΔT_v, for various examples, along with ground truth segmentations based on CoolDeTA, as well as predictions of the 2D and pseudo-3D neural networks. For comparison, black contours in r_{int}, T_{CT}, and ΔT_v indicate the boundary of the corresponding ground truth. (a) Morning cold pool (CP; time step 740) from "diu2K." (b) Analogous to (a) but for time step 744. For clarity, r_{int}, T_{CT}, and ΔT_v are plotted with their additional overlap while ground truth and predictions are only shown for the $n_p \times n_p$ pixel patch indicated by the gray frame. (c) CP from "diu2K" which developed during the afternoon (time step 780) at the boundary of a recently dissipated convective system, represented by high-altitude cirrus remnants. (d) Parts of an eastward propagating gust front of a convective system from "diu2K wind" (time step 772) with large cloud-free areas ($\gtrsim$300 km^2) and new emerging rain cells. (e) Afternoon scene (time step 772) from "diu4K" with parts of an early stage CP in the north of the upper left patch and parts of a convective system which consists of CPs at different stages. (f) Gust front of a convective system from "diu4K" (time step 780) with dissipating parent convection. (g) Northern part of a CP from "diu4K wind" (time step 780) where westward advected parent convection masks parts of its CP gust front. Note that superimposed grids represent the individual $n_p \times n_p$ pixel patches, processed by the neural networks.

In Figure 6, we present examples of the network predictions for the entire domain along with the corresponding 2D fields of r_{int}, T_{CT}, and ΔT_v. The patches processed by the networks are indicated by the superimposed grid. The selected cases represent CPs in different stages of their life cycle at different times of the day. In most of these cases, all neural networks detect the CPs and their gust fronts reasonably well. When the CP is small enough so that the networks can track its gust front (Figures 6a and 6e), the networks are even able to identify most of the associated CP region correctly, although parts of the gust front are obscured by deeper clouds (Figures 6a and 6e) or rain-free (Figure 6e). In later stages of the life cycle, when the CP is large compared to the patch size, the networks may struggle to properly detect CP regions where the gust front is already too far beyond the patch

21698996, 2024, 1, Downloaded from https://agupubs.onlinelibrary.wiley.com/doi/10.1029/2023JD040126 by Cochrane Germany, Wiley Online Library on [28/02/2024]. See the Terms and Conditions (https://onlinelibrary.wiley.com/terms-and-conditions) on Wiley Online Library for rules of use; OA articles are governed by the applicable Creative Commons License

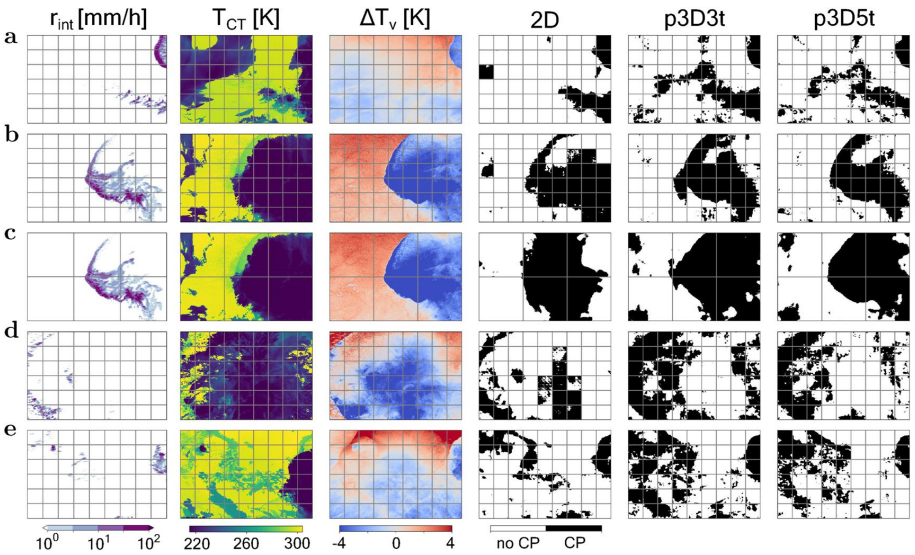

Figure 6. Examples of cold pool predictions for the case study. Two-dimensional fields of surface rain intensity, r_{int}, cloud top temperature, T_{CT}, and near-surface virtual temperature anomaly, ΔT_v, for various examples, along with predictions of the 2D and pseudo-3D neural networks. (a) Early stage cold pool (CP) entering the northeastern part of the domain at 07:40 UTC. (b) The CP from (a) but in a mature stage at 11:10 UTC. (c) Analogous to (b) but with the resolution lowered by a factor of 3 by computing the mean values. (d) The CP from (a) but in a dissipating stage at 14:40 UTC. (e) Late evening scene (22:10 UTC) with two CPs entering the domain from the east and the south, a sea breeze coming from the west and the dissipating CP from (a–c) in the center. Note that superimposed grids represent the individual $n_p \times n_p$ pixel patches, processed by the neural networks.

boundaries (Figures 6b and 6d). Yet, enlarging the networks' field of view by lowering the resolution compensates for this effect for all networks (Figure 6c).

However, the example cases also reveal challenges: The segmentations of (dissipating) CPs in later stages can be somewhat noisy (Figures 6d and 6e). This applies to both large convective systems (Figure 6d) and smaller systems (southeast in Figure 6e). For large systems, the limited field of view of the neural networks can again play a role when the gust front is located too far outside the patch boundaries. In this regard, particularly the 2D networks tend to uniformly segment patches as only CP when the (cold) cloud cover is much larger than the patch (Figures 6a, 6b, and 6d), possibly due to less contextual information compared to the pseudo-3D networks with multiple input time steps. Concerning false positive classifications, organized low-level clouds seem to constitute a potential source (Figures 6a and 6e), especially when associated with rain. As a result, particularly the pseudo-3D networks struggle to distinguish the sea breeze coming from the west in Figure 6e from CPs.

4. Conclusion and Outlook

CPs likely play a key role in organizing the atmospheric convective cloud and precipitation field (Böing, 2016; Böing et al., 2012; Haerter, 2019; Haerter et al., 2019, 2020; Muller et al., 2022; Nissen & Haerter, 2021; Schlemmer & Hohenegger, 2016). Robust detection of CP processes leading to the formation of thunderstorm clusters could enable better understanding of how convective systems organize through the interaction of CPs, such as lifting and collision processes, and how heavy precipitation events associated with MCS emerge.

The present study demonstrates that CPs can be detected in simulation data via an artificial neural network by employing variables readily available from geostationary satellite observations, namely cloud top temperature and precipitation. Using these two variables only, our networks were able to detect CPs in data from cloud-resolving simulations with an overall mean accuracy between 93.8% (2D) and 94.8% (p3D3t) for patches with at least one pixel of both classes, ≥99.8% for patches without any pixel of class "CP," and between 85.9% (p3D5t) and 94.1% (p3D3t) for patches with pixel of class "CP" only.

21698996, 2024, 1, Downloaded from https://agupubs.onlinelibrary.wiley.com/doi/10.1029/2023JD040126 by Cochrane Germany, Wiley Online Library on [28/02/2024]. See the Terms and Conditions (https://onlinelibrary.wiley.com/terms-and-conditions) on Wiley Online Library for rules of use; OA articles are governed by the applicable Creative Commons License

We conducted several experiments to identify the most promising architecture for our network. The computationally most expensive architecture, using 6 blocks and 64 starting filters, performed best, as might be expected—given the physical insight that CPs over tropical land are often linked to organized convective systems with spatial and temporal correlations at different scales. Whereas already the two-dimensional input fields gave satisfactory results, we find that taking into account three to five time steps does improve the performance further, comparable to the improvements found in Vu et al. (2020) for some of their data sets. Including several time steps within the input channels is a computationally inexpensive means of mimicking a three-dimensional input data set.

The training and test data sets contain data from different simulation setups, which correspond to an atmosphere over an idealized moist tropical land surface. The comparison between the two diurnal forcings is important as results show qualitatively different cloud organization, such as the formation of pronounced convective systems for a larger diurnal range but more scattered, smaller CPs for a smaller range. Assessing large-scale wind effects is important, as it compares the prominent model idealization of no wind shear (Bretherton et al., 2005; Manabe et al., 1965; Tompkins & Craig, 1998) with the more realistic sheared case. In the Senegal case study, we additionally applied the trained neural networks to simulation output from a realistic simulation setup. Our overall finding is that the detection works well for all these cases.

While the trained neural networks reliably detected gust fronts obscured by higher clouds in most situations, we identified several potential sources of misclassification. Concerning false positives or spuriously predicted CPs, the most common sources are (cirrus) clouds with very cold T_{CT} and organized low-level clouds, particularly in scenes with simultaneous advection and/or rain. When transitioning to actual satellite data, the former could be addressed by replacing the cloud top temperature input with satellite channels or products that also respond to cloud opacity. Focusing on false negatives, that is, missed CPs or CP pixels, one of the main sources are patches in the center of larger convective systems where the CP gust front is too far beyond the patch boundaries and thus out of the networks' sight. Yet, we showed that enlarging the networks' field of view by lowering the image resolution can compensate for this effect to some extent. Another source of false negatives are CP gust fronts without any signal in the cloud or rainfall field, that is, cloud-free gust fronts without any rain. However, unlike in our idealized simulations, CPs in more realistic simulations without a fixed surface temperature or even in satellite data would be noticeable in such situations based on their colder air compared to their environment. When transitioning to such data, this characteristic could be learned by the neural networks and used for the detection of CPs in cases with clear sky gust fronts.

Looking ahead, the obvious next step is to apply the method to actual satellite data. To make full use of the available satellite channels and address the identified sources of misclassification, this step will most likely involve new network training based on real observations. Likely, several new challenges will need to be addressed, such as the lower spatial resolution of the available data. The lower resolution may require us to focus on CPs that have already evolved into larger-scale structures, thus increasing the minimum detectable CP size. Yet, by training the neural networks with some of the multiple available satellite channels instead of the cloud top temperature input used so far, the neural network performance may benefit from additional information about the atmosphere, such as water vapor content, cloud phase, and cloud particle size and make use of potential patterns hidden so far.

To avoid inconsistencies between the neural network inputs w.r.t. their spatial and temporal resolutions, the selected satellite channels could be combined with a precipitation product based on calibrated infrared images. Such precipitation products are derived by calibrating infrared images from geostationary satellites with rain rates from low Earth orbiting passive microwave satellite sensors. While not applicable for low rain rates, a precipitation product based on calibrated infrared images might provide a sufficient estimate to detect CPs, particularly over tropical land. Considering the case-dependent accuracy of these products as well as potential errors associated with spatial and temporal interpolations when using IMERG data, it might be worth testing the neural networks without precipitation input in future studies based on satellite data.

Ultimately, being able to extract self-organization effects from observational data will enable us to improve cloud-resolving models that still struggle to capture organizational effects with high fidelity. For this purpose, the network training should additionally focus on minimizing the number of spuriously predicted CPs, for example, by adding more examples of organized and/or precipitating clouds to the training set that do not produce any CPs. By enlarging the variety of CPs in the data set, also the applicability of the method could be extended. One way forward could be to advance CP interaction parameterizations in coarser-scale models.

21698996, 2024, 1, Downloaded from https://agupubs.onlinelibrary.wiley.com/doi/10.1029/2023JD040126 by Cochrane Germany, Wiley Online Library on [28/02/2024]. See the Terms and Conditions (https://onlinelibrary.wiley.com/terms-and-conditions) on Wiley Online Library for rules of use; OA articles are governed by the applicable Creative Commons License

Conflict of Interest

The authors declare no conflicts of interest relevant to this study.

Data Availability Statement

Figures were made with Matplotlib version 3.5.2 (Caswell et al., 2022; Hunter, 2007) and seaborn version 0.12.2 (Waskom, 2021). The neural network was implemented using PyTorch version 1.11.0 (Paszke et al., 2019). Both the code and the data sets for the training and testing of the neural networks were used in version 1.0 and are licensed under Creative Commons Attribution 4.0 International (Hoeller, Fiévet, Engelbrecht, & Haerter, 2023). The idealized simulations used for training and testing are run with the cloud-resolving three-dimensional atmosphere simulator System for Atmospheric Modeling (SAM; Khairoutdinov & Randall, 2003), version 6.11. For the Senegal case study simulation, we used the nonhydrostatic Advanced Research Weather Research and Forecasting (WRF) model version 4.3 (Skamarock et al., 2021). Ground truth labels were derived from this simulation output based on the cold pool detection and tracking algorithm by Hoeller, Fiévet, and Haerter (2023).

Acknowledgments
The authors gratefully acknowledge funding by a grant from the VILLUM Foundation (Grant 13168) and the European Research Council (ERC) under the European Union' Horizon 2020 research and innovation program (Grant 771859), and the Novo Nordisk Foundation Interdisciplinary Synergy Program (Grant NNF19OC0057374). This work used resources of the Deutsches Klimarechenzentrum (DKRZ), granted by its Scientific Steering Committee (WLA) under project ID bb1166. Open Access funding enabled and organized by Projekt DEAL.

References

Atlas, D. (1994). Footprints of storms on the sea: A view from spaceborne synthetic aperture radar. *Journal of Geophysical Research*, *99*(C4), 7961–7969. https://doi.org/10.1029/94JC00250

Benjamin, T. B. (1968). Gravity currents and related phenomena. *Journal of Fluid Mechanics*, *31*(2), 209–248. https://doi.org/10.1017/s0022112068000133

Böing, S. J. (2016). An object-based model for convective cold pool dynamics. *Mathematics of Climate and Weather Forecasting*, *2*(1), 43–60. https://doi.org/10.1515/mcwf-2016-0003

Böing, S. J., Jonker, H. J., Siebesma, A. P., & Grabowski, W. W. (2012). Influence of the subcloud layer on the development of a deep convective ensemble. *Journal of the Atmospheric Sciences*, *69*(9), 2682–2698. https://doi.org/10.1175/JAS-D-11-0317.1

Borque, P., Nesbitt, S. W., Trapp, R. J., Lasher-Trapp, S., & Oue, M. (2020). Observational study of the thermodynamics and morphological characteristics of a midlatitude continental cold pool event. *Monthly Weather Review*, *148*(2), 719–737. https://doi.org/10.1175/mwr-d-19-0068.1

Brandes, E. A. (1977). Gust front evolution and tornado genesis as viewed by Doppler radar. *Journal of Applied Meteorology*, *16*(4), 333–338. https://doi.org/10.1175/1520-0450(1977)016<0333:GFEATG>2.0.CO;2

Bretherton, C. S., Blossey, P. N., & Khairoutdinov, M. (2005). An energy-balance analysis of deep convective self-aggregation above uniform SST. *Journal of the Atmospheric Sciences*, *62*(12), 4273–4292. https://doi.org/10.1175/jas3614.1

Cafaro, C., & Rooney, G. G. (2018). Characteristics of colliding density currents: A numerical and theoretical study. *Quarterly Journal of the Royal Meteorological Society*, *144*(715), 1761–1771. https://doi.org/10.1002/qj.3337

Caswell, T. A., Droettboom, M., Lee, A., de Andrade, E. S., Hoffmann, T., Klymak, J., et al. (2022). matplotlib/matplotlib: Release (version 3.5.2) [Software]. Zenodo. https://doi.org/10.5281/zenodo.6513224

Caton Harrison, T., Washington, R., & Engelstaedter, S. (2021). Satellite-derived characteristics of Saharan cold pool outflows during boreal summer. *Journal of Geophysical Research: Atmospheres*, *126*, e2020JD033387. https://doi.org/10.1029/2020JD033387

Chlap, P., Min, H., Vandenberg, N., Dowling, J., Holloway, L., & Haworth, A. (2021). A review of medical image data augmentation techniques for deep learning applications. *Journal of Medical Imaging and Radiation Oncology*, *65*(5), 545–563. https://doi.org/10.1111/1754-9485.13261

de Szoeke, S. P., Skyllingstad, E. D., Zuidema, P., & Chandra, A. S. (2017). Cold pools and their influence on the tropical marine boundary layer. *Journal of the Atmospheric Sciences*, *74*(4), 1149–1168. https://doi.org/10.1175/jas-d-16-0264.1

Drager, A. J., Grant, L. D., & van den Heever, S. C. (2020). Cold pool responses to changes in soil moisture. *Journal of Advances in Modeling Earth Systems*, *12*, e2019MS001922. https://doi.org/10.1029/2019MS001922

Drager, A. J., & van den Heever, S. C. (2017). Characterizing convective cold pools. *Journal of Advances in Modeling Earth Systems*, *9*, 1091–1115. https://doi.org/10.1002/2016MS000788

Droegemeier, K. K., & Wilhelmson, R. B. (1985). Three-dimensional numerical modeling of convection produced by interacting thunderstorm outflows. Part I: Control simulation and low-level moisture variations. *Journal of the Atmospheric Sciences*, *42*(22), 2381–2403. https://doi.org/10.1175/1520-0469(1985)042<2381:TDNMOC>2.0.CO;2

Droegemeier, K. K., & Wilhelmson, R. B. (1987). Numerical simulation of thunderstorm outflow dynamics. Part I: Outflow sensitivity experiments and turbulence dynamics. *Journal of the Atmospheric Sciences*, *44*(8), 1180–1210. https://doi.org/10.1175/1520-0469(1987)044<1180:NSOTOD>2.0.CO;2

Emmel, C., Knippertz, P., & Schulz, O. (2010). Climatology of convective density currents in the southern foothills of the Atlas Mountains. *Journal of Geophysical Research*, *115*, D11115. https://doi.org/10.1029/2009JD012863

Engerer, N. A., Stensrud, D. J., & Coniglio, M. C. (2008). Surface characteristics of observed cold pools. *Monthly Weather Review*, *136*(12), 4839–4849. https://doi.org/10.1175/2008mwr2528.1

Feng, Z., Hagos, S., Rowe, A. K., Burleyson, C. D., Martini, M. N., & Szoeke, S. P. (2015). Mechanisms of convective cloud organization by cold pools over tropical warm ocean during the AMIE/DYNAMO field campaign. *Journal of Advances in Modeling Earth Systems*, *7*, 357–381. https://doi.org/10.1002/2014MS000384

Fiévet, R., Meyer, B., & Haerter, J. O. (2022). On the sensitivity of convective cold pools to mesh resolution. *Earth and Space Science Open Archive*, *24*. https://doi.org/10.1002/essoar.10512297.1

Fiévet, R., Meyer, B., & Haerter, J. O. (2023). On the sensitivity of convective cold pools to mesh resolution. *Journal of Advances in Modeling Earth Systems*, *15*, e2022MS003382. https://doi.org/10.1029/2022MS003382

Fournier, M. B., & Haerter, J. O. (2019). Tracking the gust fronts of convective cold pools. *Journal of Geophysical Research: Atmospheres*, *124*, 11103–11117. https://doi.org/10.1029/2019JD030980

Fritsch, J. M., & Carbone, R. (2004). Improving quantitative precipitation forecasts in the warm season: A USWRP research and development strategy. *Bulletin of the American Meteorological Society*, *85*(7), 955–966. https://doi.org/10.1175/bams-85-7-955

Fuglestvedt, H. F., & Haerter, J. O. (2020). Cold pools as conveyor belts of moisture. *Geophysical Research Letters*, *47*, e2020GL087319. https://doi.org/10.1029/2020GL087319

Garg, P., Nesbitt, S. W., Lang, T. J., Priftis, G., Chronis, T., Thayer, J. D., & Hence, D. A. (2020). Identifying and characterizing tropical oceanic mesoscale cold pools using spaceborne scatterometer winds. *Journal of Geophysical Research: Atmospheres*, *125*, e2019JD031812. https://doi.org/10.1029/2019JD031812

Gentine, P., Garelli, A., Park, S., Nie, J., Torri, G., & Kuang, Z. (2016). Role of surface heat fluxes underneath cold pools. *Geophysical Research Letters*, *43*, 874–883. https://doi.org/10.1002/2015GL067262

Grandpeix, J.-Y., & Lafore, J.-P. (2010). A density current parameterization coupled with Emanuel's convection scheme. Part I: The models. *Journal of the Atmospheric Sciences*, *67*(4), 881–897. https://doi.org/10.1175/2009jas3044.1

Haerter, J. O. (2019). Convective self-aggregation as a cold pool-driven critical phenomenon. *Geophysical Research Letters*, *46*, 4017–4028. https://doi.org/10.1029/2018GL081817

Haerter, J. O., Böing, S. J., Henneberg, O., & Nissen, S. B. (2019). Circling in on convective organization. *Geophysical Research Letters*, *46*, 7024–7034. https://doi.org/10.1029/2019GL082092

Haerter, J. O., Meyer, B., & Nissen, S. B. (2020). Diurnal self-aggregation. *npj Climate and Atmospheric Science*, *3*(1), 30. https://doi.org/10.1038/s41612-020-00132-z

He, H., & Garcia, E. A. (2009). Learning from imbalanced data. *IEEE Transactions on Knowledge and Data Engineering*, *21*(9), 1263–1284. https://doi.org/10.1109/tkde.2008.239

Henneberg, O., Meyer, B., & Haerter, J. O. (2020). Particle-based tracking of cold pool gust fronts. *Journal of Advances in Modeling Earth Systems*, *12*, e2019MS001910. https://doi.org/10.1029/2019MS001910

Hoeller, J., Fiévet, R., Engelbrecht, E., & Haerter, J. (2023). Cold pool detection U-Net release (version 1.0) [Software and Dataset]. Zenodo. https://doi.org/10.5281/zenodo.8376599

Hoeller, J., Fiévet, R., & Haerter, J. O. (2023). Detecting cold pool family trees in convection resolving simulations [Software]. *Authorea Preprints*. https://doi.org/10.22541/essoar.167768111.14938799/v1

Houze, R. A. Jr. (2004). Mesoscale convective systems. *Reviews of Geophysics*, *42*, RG4003. https://doi.org/10.1029/2004RG000150

Houze, R. A. Jr., & Betts, A. K. (1981). Convection in gate. *Reviews of Geophysics*, *19*(4), 541–576. https://doi.org/10.1029/RG019i004p00541

Huffman, G. J., Bolvin, D. T., Braithwaite, D., Hsu, K., Joyce, R., Xie, P., & Yoo, S.-H. (2015). NASA Global Precipitation Measurement (GPM) Integrated Multi-satellitE Retrievals for GPM (IMERG). *Algorithm Theoretical Basis Document (ATBD) Version*, *4*(26).

Hunter, J. D. (2007). Matplotlib: A 2D graphics environment. *Computing in Science & Engineering*, *9*(3), 90–95. https://doi.org/10.1109/MCSE.2007.55

Ioffe, S., & Szegedy, C. (2015). Batch normalization: Accelerating deep network training by reducing internal covariate shift. In *International Conference on Machine Learning* (pp. 448–456).

Jadon, S. (2020). A survey of loss functions for semantic segmentation. In *2020 IEEE Conference on Computational Intelligence in Bioinformatics and Computational Biology (CIBCB)* (pp. 1–7).

Jensen, G. G., Fiévet, R., & Haerter, J. O. (2022). The diurnal path to persistent convective self-aggregation. *Journal of Advances in Modeling Earth Systems*, *14*, e2021MS002923. https://doi.org/10.1029/2021MS002923

Khairoutdinov, M. F., & Randall, D. A. (2003). Cloud resolving modeling of the ARM summer 1997 IOP: Model formulation, results, uncertainties, and sensitivities. *Journal of the Atmospheric Sciences*, *60*(4), 607–625. https://doi.org/10.1175/1520-0469(2003)060<0607:CRMOTA>2.0.CO;2

Kirsch, B., Ament, F., & Hohenegger, C. (2021). Convective cold pools in long-term boundary layer mast observations. *Monthly Weather Review*, *149*(3), 811–820. https://doi.org/10.1175/mwr-d-20-0197.1

Kneller, B. C., Bennett, S. J., & McCaffrey, W. D. (1999). Velocity structure, turbulence and fluid stresses in experimental gravity currents. *Journal of Geophysical Research*, *104*(C3), 5381–5391. https://doi.org/10.1029/1998JC900077

Knippertz, P., Deutscher, C., Kandler, K., Müller, T., Schulz, O., & Schütz, L. (2007). Dust mobilization due to density currents in the Atlas region: Observations from the Saharan Mineral Dust Experiment 2006 field campaign. *Journal of Geophysical Research*, *112*, D21109. https://doi.org/10.1029/2007JD008774

Kruse, I. L., Haerter, J. O., & Meyer, B. (2022). Cold pools over the Netherlands: A statistical study from tower and radar observations. *Quarterly Journal of the Royal Meteorological Society*, *148*(743), 711–726. https://doi.org/10.1002/qj.4223

Lundgren, T., Yao, J., & Mansour, N. (1992). Microburst modelling and scaling. *Journal of Fluid Mechanics*, *239*, 461–488. https://doi.org/10.1017/s002211209200449x

Manabe, S., Smagorinsky, J., & Strickler, R. F. (1965). Simulated climatology of a general circulation model with a hydrologic cycle. *Monthly Weather Review*, *93*(12), 769–798. https://doi.org/10.1175/1520-0493(1965)093<0769:SCOAGC>2.3.CO;2

Markowski, P., & Richardson, Y. (2011). *Mesoscale meteorology in midlatitudes* (Vol. 2). John Wiley & Sons.

Meyer, B., & Haerter, J. O. (2020). Mechanical forcing of convection by cold pools: Collisions and energy scaling. *Journal of Advances in Modeling Earth Systems*, *12*, e2020MS002281. https://doi.org/10.1029/2020MS002281

Milletari, F., Navab, N., & Ahmadi, S.-A. (2016). V-Net: Fully convolutional neural networks for volumetric medical image segmentation. In *2016 Fourth International Conference on 3D Vision (3DV)* (pp. 565–571).

Muller, C., Yang, D., Craig, G., Cronin, T., Fildier, B., Haerter, J. O., et al. (2022). Spontaneous aggregation of convective storms. *Annual Review of Fluid Mechanics*, *54*(1), 133–157. https://doi.org/10.1146/annurev-fluid-022421-011319

Nissen, S. B., & Haerter, J. O. (2021). Circling in on convective self-aggregation. *Journal of Geophysical Research: Atmospheres*, *126*, e2021JD035331. https://doi.org/10.1029/2021JD035331

Paszke, A., Gross, S., Massa, F., Lerer, A., Bradbury, J., Chanan, G., et al. (2019). Pytorch: An imperative style, high-performance deep learning library. In *Advances in Neural Information Processing Systems* (Vol. 32, pp. 8024–8035). Curran Associates, Inc. Retrieved from http://papers.neurips.cc/paper/9015-pytorch-an-imperative-style-high-performance-deep-learning-library.pdf

Redl, R., Fink, A. H., & Knippertz, P. (2015). An objective detection method for convective cold pool events and its application to northern Africa. *Monthly Weather Review*, *143*(12), 5055–5072. https://doi.org/10.1175/mwr-d-15-0223.1

Rio, C., Hourdin, F., Grandpeix, J.-Y., & Lafore, J.-P. (2009). Shifting the diurnal cycle of parameterized deep convection over land. *Geophysical Research Letters*, *36*, L07809. https://doi.org/10.1029/2008GL036779

Romps, D. M., & Jeevanjee, N. (2016). On the sizes and lifetimes of cold pools. *Quarterly Journal of the Royal Meteorological Society*, *142*(696), 1517–1527. https://doi.org/10.1002/qj.2754

Ronneberger, O., Fischer, P., & Brox, T. (2015). U-Net: Convolutional networks for biomedical image segmentation. In *Medical Image Computing and Computer-Assisted Intervention (MICCAI)* (Vol. 9351, pp. 234–241). Springer. https://doi.org/10.1007/978-3-319-24574-4_28

21698996, 2024, 1, Downloaded from https://agupubs.onlinelibrary.wiley.com/doi/10.1029/2023JD040126 by Cochrane Germany, Wiley Online Library on [28/02/2024]. See the Terms and Conditions (https://onlinelibrary.wiley.com/terms-and-conditions) on Wiley Online Library for rules of use; OA articles are governed by the applicable Creative Commons License

Rotunno, R., Klemp, J. B., & Weisman, M. L. (1988). A theory for strong, long-lived squall lines. *Journal of the Atmospheric Sciences*, *45*(3), 463–485. https://doi.org/10.1175/1520-0469(1988)045<0463:ATFSLL>2.0.CO;2
Schlemmer, L., & Hohenegger, C. (2016). Modifications of the atmospheric moisture field as a result of cold-pool dynamics. *Quarterly Journal of the Royal Meteorological Society*, *142*(694), 30–42. https://doi.org/10.1002/qj.2625
Schumacher, R. S., & Johnson, R. H. (2008). Mesoscale processes contributing to extreme rainfall in a midlatitude warm-season flash flood. *Monthly Weather Review*, *136*(10), 3964–3986. https://doi.org/10.1175/2008mwr2471.1
Schumacher, R. S., & Rasmussen, K. L. (2020). The formation, character and changing nature of mesoscale convective systems. *Nature Reviews Earth & Environment*, *1*(6), 300–314. https://doi.org/10.1038/s43017-020-0057-7
Sharifnezhadazizi, Z., Norouzi, H., Prakash, S., Beale, C., & Khanbilvardi, R. (2019). A global analysis of land surface temperature diurnal cycle using MODIS observations. *Journal of Applied Meteorology and Climatology*, *58*(6), 1279–1291. https://doi.org/10.1175/jamc-d-18-0256.1
Shi, J., Dang, J., Cui, M., Zuo, R., Shimizu, K., Tsunoda, A., & Suzuki, Y. (2021). Improvement of damage segmentation based on pixel-level data balance using VGG-Unet. *Applied Sciences*, *11*(2), 518. https://doi.org/10.3390/app11020518
Shorten, C., & Khoshgoftaar, T. M. (2019). A survey on image data augmentation for deep learning. *Journal of Big Data*, *6*(1), 60. https://doi.org/10.1186/s40537-019-0197-0
Simpson, J. (1980). Downdrafts as linkages in dynamic cumulus seeding effects. *Journal of Applied Meteorology*, *19*(4), 477–487. https://doi.org/10.1175/1520-0450(1980)019<0477:DALIDC>2.0.CO;2
Skamarock, W. C., Klemp, J. B., Dudhia, J., Gill, D. O., Liu, Z., Berner, J., et al. (2021). A description of the advanced research WRF model release (version 4.3) (No. NCAR/TN-556+STR). https://doi.org/10.5065/1dfh-6p97
Stevens, B., Bony, S., Farrell, D., Ament, F., Blyth, A., Fairall, C., et al. (2021). EUREC^{4}A. *Earth System Science Data Discussions*, *2021*, 1–78.
Sukovich, E. M., Ralph, F. M., Barthold, F. E., Reynolds, D. W., & Novak, D. R. (2014). Extreme quantitative precipitation forecast performance at the weather prediction center from 2001 to 2011. *Weather and Forecasting*, *29*(4), 894–911. https://doi.org/10.1175/waf-d-13-00061.1
Tan, J., Jakob, C., Rossow, W. B., & Tselioudis, G. (2015). Increases in tropical rainfall driven by changes in frequency of organized deep convection. *Nature*, *519*(7544), 451–454. https://doi.org/10.1038/nature14339
Tompkins, A. M. (2001). Organization of tropical convection in low vertical wind shears: The role of cold pools. *Journal of the Atmospheric Sciences*, *58*(13), 1650–1672. https://doi.org/10.1175/1520-0469(2001)058⟨1650:OOTCIL⟩2.0.CO;2
Tompkins, A. M., & Craig, G. C. (1998). Radiative–convective equilibrium in a three-dimensional cloud-ensemble model. *Quarterly Journal of the Royal Meteorological Society*, *124*(550), 2073–2097. https://doi.org/10.1002/qj.49712455013
Torri, G., & Kuang, Z. (2016). Rain evaporation and moist patches in tropical boundary layers. *Geophysical Research Letters*, *43*, 9895–9902. https://doi.org/10.1002/2016GL070893
Torri, G., & Kuang, Z. (2019). On cold pool collisions in tropical boundary layers. *Geophysical Research Letters*, *46*, 399–407. https://doi.org/10.1029/2018GL080501
Torri, G., Kuang, Z., & Tian, Y. (2015). Mechanisms for convection triggering by cold pools. *Geophysical Research Letters*, *42*, 1943–1950. https://doi.org/10.1002/2015GL063227
Touzé-Peiffer, L., Vogel, R., & Rochetin, N. (2022). Cold pools observed during EUREC^{4}A: Detection and characterization from atmospheric soundings. *Journal of Applied Meteorology and Climatology*, *61*(5), 593–610. https://doi.org/10.1175/jamc-d-21-0048.1
Vogel, R., Konow, H., Schulz, H., & Zuidema, P. (2021). A climatology of trade-wind cumulus cold pools and their link to mesoscale cloud organization. *Atmospheric Chemistry and Physics*, *21*(21), 16609–16630. https://doi.org/10.5194/acp-21-16609-2021
Vu, M. H., Grimbergen, G., Nyholm, T., & Löfstedt, T. (2020). Evaluation of multislice inputs to convolutional neural networks for medical image segmentation. *Medical Physics*, *47*(12), 6216–6231. https://doi.org/10.1002/mp.14391
Wakimoto, R. M. (1982). The life cycle of thunderstorm gust fronts as viewed with Doppler radar and rawinsonde data. *Monthly Weather Review*, *110*(8), 1060–1082. https://doi.org/10.1175/1520-0493(1982)110<1060:TLCOTG>2.0.CO;2
Waskom, M. L. (2021). Seaborn: Statistical data visualization. *Journal of Open Source Software*, *6*(60), 3021. https://doi.org/10.21105/joss.03021
Wilbanks, M. C., Yuter, S. E., De Szoeke, S. P., Brewer, W. A., Miller, M. A., Hall, A. M., & Burleyson, C. D. (2015). Near-surface density currents observed in the southeast pacific stratocumulus-topped marine boundary layer. *Monthly Weather Review*, *143*(9), 3532–3555. https://doi.org/10.1175/mwr-d-14-00359.1
Willemink, M. J., Koszek, W. A., Hardell, C., Wu, J., Fleischmann, D., Harvey, H., et al. (2020). Preparing medical imaging data for machine learning. *Radiology*, *295*(1), 4–15. https://doi.org/10.1148/radiol.2020192224
Yamaguchi, T., Randall, D. A., & Khairoutdinov, M. F. (2011). Cloud modeling tests of the ultimate–macho scalar advection scheme. *Monthly Weather Review*, *139*(10), 3248–3264. https://doi.org/10.1175/mwr-d-10-05044.1
Zipser, E. J., Meitín, R. J., & LeMone, M. A. (1981). Mesoscale motion fields associated with a slowly moving gate convective band. *Journal of the Atmospheric Sciences*, *38*(8), 1725–1750. https://doi.org/10.1175/1520-0469(1981)038<1725:MMFAWA>2.0.CO;2
Zuidema, P., Torri, G., Muller, C., & Chandra, A. (2017). A survey of precipitation-induced atmospheric cold pools over oceans and their interactions with the larger-scale environment. *Surveys in Geophysics*, *38*(6), 1283–1305. https://doi.org/10.1007/s10712-017-9447-x

21698996, 2024, 1, Downloaded from https://agupubs.onlinelibrary.wiley.com/doi/10.1029/2023JD040126 by Cochrane Germany, Wiley Online Library on [28/02/2024]. See the Terms and Conditions (https://onlinelibrary.wiley.com/terms-and-conditions) on Wiley Online Library for rules of use; OA articles are governed by the applicable Creative Commons License

Chapter 6

Conclusions

6.1 Key Results and Discussion

The primary objectives of this thesis were to (i) investigate detectable signatures of convective cold pools (CPs) in geostationary satellite data and (ii) develop a corresponding segmentation approach with a focus on CPs over tropical continents. In these regions, CPs are ubiquitous and play a crucial role in extreme weather events. However, due to the lack of other observational data sources such as high-resolution dense station networks and ground-based radars, which are commonly used for CP detection, there remains a substantial gap in CP observations over tropical continents.

To address objective (i), 4218 CPs were identified in 5-minute near-surface time series recorded by twelve automatic weather stations across equatorial Africa. For this purpose, almost 43 years of data spanning from 2019 to 2023 were scanned using an algorithm based on temperature and wind criteria. The analysis of satellite-derived brightness temperature time series associated with the identified CPs showed that gust front passages typically coincide with rapid drops in brightness temperature, indicating either a deepening of existing clouds or, if no clouds were present before the CP arrival, an initiation of new clouds. These findings statistically confirm the prevalence of corresponding cloud patterns such as low-level cloud arcs, often observed in conjunction with CPs.

While the analysis primarily focused on one-dimensional time series data for direct comparison with the "ground truth" observations from the weather stations, it is crucial to acknowledge that the associated satellite-observed cloud patterns are inherently three-dimensional, comprising two spatial dimensions along with time as the third dimension. Neural networks prove effective in detecting such intricate patterns, but necessitate substantial annotated data for training and testing. To circumvent the laborious manual creation of pixel-wise annotations for actual satellite images, objective (ii) was thus pursued by training neural networks using simulated cloud and rainfall

fields observable from satellites.

To automatically generate precise ground truth data for the simulated scenes, we developed a novel CP detection and tracking algorithm called CoolDeTA. CoolDeTA integrates both thermodynamic and dynamic variables for CP detection, ensuring that the resulting CP boundaries align accurately with satellite-observable CP gust front signatures, including triggered convection. In manuscript II, this capability of CoolDeTA was utilized to analyze the interrelationships among CPs by tracking not only individual CPs but also the rain patches they initiated, as well as potential CPs resulting from these rain patches. By reconstructing the family trees of CPs, CoolDeTA enabled us to explore the causal chains of CPs and their responses to different environmental conditions.

In manuscript III, CoolDeTA was employed to prepare CP masks as ground truth data for the training and testing of the neural networks for the segmentation of CPs in simulated cloud and rainfall fields. The neural networks utilize a U-Net architecture, a widely adopted encoder-decoder architecture renowned for its ability to learn features across various scales. Beyond a configuration where a single snapshot of both the cloud and rainfall field serves as input (2D), we explored two additional configurations receiving temporal sequences of three and five snapshots, respectively (pseudo-3D). Demonstrating mean pixel accuracies ranging from 93.8% to 94.8% and CP detection rates between 83% and 84% against unknown test images containing CP and environmental pixels, all networks exhibited promising CP detection capabilities. Notably, the pseudo-3D networks achieved higher intersection over union (IOU) scores of 0.74 and 0.75 compared to the 2D network's 0.71, likely attributed to the additional temporal patterns they leveraged, aligning with the three-dimensional nature of CP signatures.

To assess potential challenges associated with transferring the developed method to real satellite data, we applied the trained neural networks to complex scenes generated from a simulation with realistic forcing, based on a day of significant convective activity in Senegal. While the networks successfully detected most CPs, we identified several sources of misclassification. The primary cause of false negatives, or missed CPs, was the presence of CP gust fronts devoid of clouds or rainfall. In such cases, the networks need to delineate the CP boundary based on the subtle brightness temperature drop caused by the cooler CP air compared to its surroundings. However, as the networks were trained on idealized simulations with fixed surface temperatures, they could not effectively leverage this signature, even though it was evident in the Senegal simulation data. False positives, or spuriously detected CPs, were primarily triggered by (cirrus) clouds with relatively cold top temperatures and organized low-level convection. The latter issue was particularly pronounced in scenes featuring simultaneous rain or advection due to the background wind field.

6.2 Perspectives for Future Research

Despite the potential sources of misclassification discussed in the previous section, the developed neural networks successfully learned typical satellite-observable patterns associated with CPs, yielding promising segmentation performances across various environmental conditions. Up to this point, the method has solely been evaluated using simulated cloud and rainfall fields. Nevertheless, the encouraging outcomes suggest that this approach could serve as a foundation for a new generation of satellite-based CP detection algorithms, potentially applicable on a global scale.

To achieve this, the data set utilized for network training must be expanded to include real satellite scenes. A potential improvement to minimize the number of spuriously detected CPs involves replacing the cloud top temperature and rainfall inputs with combinations of relevant infrared channels. This adjustment would provide the networks with additional information regarding cloud properties such as phase and particle size.

Two strategies appear particularly promising regarding the data sets used for network training and testing: a hybrid data set comprising both simulated and observed scenes, and a data set based solely on real satellite images. The hybrid set would facilitate the development of a CP detection method capable of segmenting CPs in both simulated and observational data consistently. Additionally, CP masks for simulated scenes could be automatically generated using CoolDeTA or similar CP detection algorithms, thereby accelerating the annotation process. However, this approach necessitates realistic simulations based on diverse environmental conditions, as well as the capability to output synthetic satellite data corresponding to individual satellite channels. Conversely, the satellite image-only data set may offer greater flexibility in selecting relevant satellite products as input data for the network.

When employing a U-Net architecture, augmenting the training data volume using strategies such as translations is advisable to facilitate efficient generalization by the network. Additionally, incorporating observations from stations or radars could assist in manually generating ground truth CP masks for real satellite scenes, thereby enhancing the quality of annotations. However, findings from Rasp et al. (2020) indicate that U-Nets can effectively learn pertinent patterns even from imprecise and noisy ground truth data.

Applying this method to segment CPs in satellite imagery on a global scale would enable the exploration of various questions concerning mesoscale CP dynamics and their impact on convective organization. This includes examining the influence of CPs on thunderstorm clustering and the amount and intensity of the associated rainfall. To investigate the latter, satellite-derived rainfall products could be studied along with the derived CP masks. By utilizing both the rainfall data and the CP masks, CoolDeTA could be adapted for the detection and tracking of individual CP instances in observational data. This adaptation would involve replacing the surface rain intensity fields with

the satellite-derived rainfall estimates, the k-means segmentations with the derived CP masks, and approximating associated fields such as the elevation map based on the available satellite data. Similar to the study presented in manuscript II, this algorithm could be employed to analyze the causal chains of CP events in observational data.

Another potential application for the developed method is the nowcasting of areas affected by extreme weather events, particularly heavy rainfall. In regions like the Sahel zone, heavy rainfall events often lead to severe floods, endangering lives and infrastructure. Establishing a nowcasting system for such events could assist local weather services in providing accurate early warnings. Research by Han et al. (2021) demonstrated the suitability of the U-Net architecture for nowcasting precipitation using radar data. Given the correlation between convective rainfall and satellite-derived brightness temperatures, it is plausible that a similar approach could be effective based on infrared data from geostationary satellites.

Bibliography

Ackerman, S. A., Strabala, K. I., Menzel, W. P., Frey, R. A., Moeller, C. C., & Gumley, L. E. (1998). Discriminating clear sky from clouds with modis. *Journal of Geophysical Research: Atmospheres*, *103*(D24), 32141–32157. https://doi.org/10.1029/1998JD200032.

Addis, R., Garstang, M., & Emmitt, G. (1984). Downdrafts from tropical oceanic cumuli. *Boundary-Layer Meteorology*, *28*, 23–49. https://doi.org/10.1007/BF00119455.

Albawi, S., Mohammed, T. A., & Al-Zawi, S. (2017). Understanding of a convolutional neural network. *International Conference on Engineering and Technology (ICET)*, 1–6. https://doi.org/10.1109/ICEngTechnol.2017.8308186.

Ameur, Z., Ameur, S., Adane, A., Sauvageot, H., & Bara, K. (2004). Cloud classification using the textural features of meteosat images. *International Journal of Remote Sensing*, *25*(21), 4491–4503. https://doi.org/10.1080/01431160410001735120.

Aminou, D. (2002). Msg's seviri instrument. *ESA Bulletin(0376-4265)*, (111), 15–17. https://www-cdn.eumetsat.int/files/2020-04/pdf_msg_seviri.pdf

Arnold, N. P., & Randall, D. A. (2015). Global-scale convective aggregation: Implications for the madden-julian oscillation. *Journal of Advances in Modeling Earth Systems*, *7*(4), 1499–1518. https://doi.org/10.1002/2015MS000498.

Asokan, A., & Anitha, J. (2019). Machine learning based image processing techniques for satellite image analysis-a survey. *International Conference on Machine Learning, Big Data, Cloud and Parallel Computing (COMITCon)*, 119–124. https://doi.org/10.1109/COMITCon.2019.8862452.

Atiah, W. A., Amekudzi, L. K., & Danuor, S. K. (2023). Mesoscale convective systems and contributions to flood cases in southern west africa (swa): A systematic review. *Weather and Climate Extremes*, *39*, 100551. https://doi.org/10.1016/j.wace.2023.100551.

Badrinarayanan, V., Kendall, A., & Cipolla, R. (2017). Segnet: A deep convolutional encoder-decoder architecture for image segmentation. *IEEE*

Transactions on Pattern Analysis and Machine Intelligence, *39*(12), 2481–2495. https://doi.org/10.1109/TPAMI.2016.2644615.

Baranwal, M., & Salapaka, S. M. (2018). Weighted kernel deterministic annealing: A maximum-entropy principle approach for shape clustering. *Indian Control Conference (ICC)*, 1–6. https://doi.org/10.1109/INDIANCC.2018.8307944.

Baydin, A. G., Pearlmutter, B. A., Radul, A. A., & Siskind, J. M. (2018). Automatic differentiation in machine learning: A survey. *Journal of Machine Learning Research*, *18*, 1–43. https://www.jmlr.org/papers/volume18/17-468/17-468.pdf

Belgiu, M., & Drăguţ, L. (2016). Random forest in remote sensing: A review of applications and future directions. *ISPRS Journal of Photogrammetry and Remote Sensing*, *114*, 24–31. https://doi.org/10.1016/j.isprsjprs.2016.01.011.

Biagioli, G., & Tompkins, A. M. (2023). Measuring convective organization. *Journal of the Atmospheric Sciences*, *80*(12), 2769–2789. https://doi.org/10.1175/JAS-D-23-0103.1.

Bieniek, A., & Moga, A. (2000). An efficient watershed algorithm based on connected components. *Pattern Recognition*, *33*(6), 907–916. https://doi.org/10.1016/S0031-3203(99)00154-5.

Bishop, C. M. (2006). *Pattern recognition and machine learning*. Springer New York, NY.

Böing, S. J. (2016). An object-based model for convective cold pool dynamics. *Mathematics of Climate and Weather Forecasting*, *2*(1), 43–60. https://doi.org/10.1515/mcwf-2016-0003.

Böing, S. J., Jonker, H. J., Siebesma, A. P., & Grabowski, W. W. (2012). Influence of the subcloud layer on the development of a deep convective ensemble. *Journal of the Atmospheric Sciences*, *69*(9), 2682–2698. https://doi.org/10.1175/JAS-D-11-0317.1.

Borque, P., Nesbitt, S. W., Trapp, R. J., Lasher-Trapp, S., & Oue, M. (2020). Observational study of the thermodynamics and morphological characteristics of a midlatitude continental cold pool event. *Monthly Weather Review*, *148*(2), 719–737. https://doi.org/10.1175/mwr-d-19-0068.1.

Bragagnolo, L., da Silva, R. V., & Grzybowski, J. M. V. (2021). Amazon forest cover change mapping based on semantic segmentation by u-nets. *Ecological Informatics*, *62*, 101279. https://doi.org/10.1016/j.ecoinf.2021.101279.

Brandes, E. A. (1977). Gust front evolution and tornado genesis as viewed by doppler radar. *Journal of Applied Meteorology (1962-1982)*, *16*(4), 333–338. http://www.jstor.org/stable/26178121

Breiman, L. (2001). Random forests. *Machine Learning*, *45*, 5–32. https://doi.org/10.1023/A:1010933404324.

Bretherton, C. S., Blossey, P. N., & Khairoutdinov, M. (2005). An energy-balance analysis of deep convective self-aggregation above uniform sst.

Journal of the Atmospheric Sciences, *62*(12), 4273–4292. https://doi.org/10.1175/jas3614.1.

Byers, H. R., & Braham, R. R. (1949). *The thunderstorm: Report of the thunderstorm project*. US Government Printing Office.

Capacci, D., & Conway, B. (2005). Delineation of precipitation areas from modis visible and infrared imagery with artificial neural networks. *Meteorological Applications*, *12*(4), 291–305. https://doi.org/10.1017/S1350482705001787.

Caton Harrison, T., Washington, R., & Engelstaedter, S. (2021). Satellite-derived characteristics of saharan cold pool outflows during boreal summer. *Journal of Geophysical Research: Atmospheres*, *126*(3), e2020JD033387. https://doi.org/10.1029/2020JD033387.

Chandra, A. S., Zuidema, P., Krueger, S., Kochanski, A., de Szoeke, S. P., & Zhang, J. (2018). Moisture distributions in tropical cold pools from equatorial indian ocean observations and cloud-resolving simulations. *Journal of Geophysical Research: Atmospheres*, *123*(20), 11–445. https://doi.org/10.1029/2018jd028634.

Charba, J. (1974). Application of gravity current model to analysis of squall-line gust front. *Monthly Weather Review*, *102*(2), 140–156. https://doi.org/10.1175/1520-0493(1974)102⟨0140:AOGCMT⟩2.0.CO;2.

Chen, H., Chandrasekar, V., Tan, H., & Cifelli, R. (2019). Rainfall estimation from ground radar and trmm precipitation radar using hybrid deep neural networks. *Geophysical Research Letters*, *46*(17–18), 10669–10678. https://doi.org/10.1029/2019GL084771.

Christensen, K., & Moloney, N. R. (2005). *Complexity and criticality* (Vol. 1). World Scientific Publishing Company.

Cintineo, J. L., Pavolonis, M. J., Sieglaff, J. M., Wimmers, A., Brunner, J., & Bellon, W. (2020). A deep-learning model for automated detection of intense midlatitude convection using geostationary satellite images. *Weather and Forecasting*, *35*(6), 2567–2588. https://doi.org/10.1175/WAF-D-20-0028.1.

Cortes, C., & Vapnik, V. (1995). Support-vector networks. *Machine Learning*, *20*(3), 273–297. https://doi.org/10.1007/BF00994018.

De Paola, F., Giugni, M., Topa, M. E., & Bucchignani, E. (2014). Intensity-duration-frequency (idf) rainfall curves, for data series and climate projection in african cities. *SpringerPlus*, *3*, 133. https://doi.org/10.1186/2193-1801-3-133.

de Szoeke, S. P., Skyllingstad, E. D., Zuidema, P., & Chandra, A. S. (2017). Cold pools and their influence on the tropical marine boundary layer. *Journal of the Atmospheric Sciences*, *74*(4), 1149–1168. https://doi.org/10.1175/JAS-D-16-0264.1.

Diakogiannis, F. I., Waldner, F., Caccetta, P., & Wu, C. (2020). Resunet-a: A deep learning framework for semantic segmentation of remotely

sensed data. *ISPRS Journal of Photogrammetry and Remote Sensing*, *162*, 94–114. https://doi.org/10.1016/j.isprsjprs.2020.01.013.

Digabel, H., & Lantuéjoul, C. (1978). Iterative algorithms. *Actes du Second Symposium Europeen d'Analyse Quantitative des Microstructures en Sciences des Materiaux, Biologie et Medecine*, 85–99. https://people.cmm.minesparis.psl.eu/users/marcoteg/cv/publi_pdf/MM_refs/Lantuejoul/1977_lantu_iterativeAlgorithms.pdf

Drager, A. J., & van den Heever, S. C. (2017). Characterizing convective cold pools. *Journal of Advances in Modeling Earth Systems*, *9*(2), 1091–1115. https://doi.org/10.1002/2016ms000788.

Droegemeier, K. K., & Wilhelmson, R. B. (1985). Three-dimensional numerical modeling of convection produced by interacting thunderstorm outflows. part i: Control simulation and low-level moisture variations. *Journal of the Atmospheric Sciences*, *42*(22), 2381–2403. https://doi.org/10.1175/1520-0469(1985)042⟨2381:TDNMOC⟩2.0.CO;2.

Drönner, J., Korfhage, N., Egli, S., Mühling, M., Thies, B., Bendix, J., Freisleben, B., & Seeger, B. (2018). Fast cloud segmentation using convolutional neural networks. *Remote Sensing*, *10*(11), 1782. https://doi.org/10.3390/rs10111782.

Dumoulin, V., & Visin, F. (2016). A guide to convolution arithmetic for deep learning. *arXiv preprint arXiv:1603.07285*. https://doi.org/10.48550/arXiv.1603.07285.

Emmel, C., Knippertz, P., & Schulz, O. (2010). Climatology of convective density currents in the southern foothills of the atlas mountains. *Journal of Geophysical Research: Atmospheres*, *115*(D11). https://doi.org/10.1029/2009JD012863.

Engerer, N. A., Stensrud, D. J., & Coniglio, M. C. (2008). Surface characteristics of observed cold pools. *Monthly Weather Review*, *136*(12), 4839–4849. https://doi.org/10.1175/2008mwr2528.1.

EUMETSAT. (2012). The conversion from effective radiances to equivalent brightness temperatures (version 1). https://www-cdn.eumetsat.int/files/2020-04/pdf_effect_rad_to_brightness.pdf

Feng, Z., Hagos, S., Rowe, A. K., Burleyson, C. D., Martini, M. N., & de Szoeke, S. P. (2015). Mechanisms of convective cloud organization by cold pools over tropical warm ocean during the amie/dynamo field campaign. *Journal of Advances in Modeling Earth Systems*, *7*(2), 357–381. https://doi.org/10.1002/2014MS000384.

Ferreira, B., Iten, M., & Silva, R. G. (2020). Monitoring sustainable development by means of earth observation data and machine learning: A review. *Environmental Sciences Europe*, *32*(1), 120. https://doi.org/10.1186/s12302-020-00397-4.

Fink, A. H., Vincent, D. G., & Ermert, V. (2006). Rainfall types in the west african sudanian zone during the summer monsoon 2002. *Monthly*

Weather Review, *134*(8), 2143–2164. https://doi.org/10.1175/MWR3182.1.

Fournier, M. B., & Haerter, J. O. (2019). Tracking the gust fronts of convective cold pools. *Journal of Geophysical Research: Atmospheres*, *124*(21), 11103–11117. https://doi.org/10.1029/2019jd030980.

Fu, K.-S., & Mui, J. (1981). A survey on image segmentation. *Pattern Recognition*, *13*(1), 3–16. https://doi.org/10.1016/0031-3203(81)90028-5.

Fuglestvedt, H. F., & Haerter, J. O. (2020). Cold pools as conveyor belts of moisture. *Geophysical Research Letters*, *47*(12), e2020GL087319. https://doi.org/10.1029/2020GL087319.

Fukushima, K. (1980). Neocognitron: A self-organizing neural network model for a mechanism of pattern recognition unaffected by shift in position. *Biological Cybernetics*, *36*(4), 193–202. https://doi.org/10.1007/BF00344251.

Galea, D., Ma, H.-Y., Wu, W.-Y., & Kobayashi, D. (2024). Deep learning image segmentation for atmospheric rivers. *Artificial Intelligence for the Earth Systems*, *3*(1), 230048. https://doi.org/10.1175/AIES-D-23-0048.1.

Gan, G., & Ng, M. K.-P. (2017). K-means clustering with outlier removal. *Pattern Recognition Letters*, *90*, 8–14. https://doi.org/10.1016/j.patrec.2017.03.008.

Garg, P., Nesbitt, S. W., Lang, T. J., Priftis, G., Chronis, T., Thayer, J. D., & Hence, D. A. (2020). Identifying and characterizing tropical oceanic mesoscale cold pools using spaceborne scatterometer winds. *Journal of Geophysical Research: Atmospheres*, *125*(5), e2019JD031812. https://doi.org/10.1029/2019JD031812.

Gentine, P., Garelli, A., Park, S.-B., Nie, J., Torri, G., & Kuang, Z. (2016). Role of surface heat fluxes underneath cold pools. *Geophysical Research Letters*, *43*(2), 874–883. https://doi.org/10.1002/2015gl067262.

Giannakos, A., & Feidas, H. (2013). Classification of convective and stratiform rain based on the spectral and textural features of meteosat second generation infrared data. *Theoretical and Applied Climatology*, *113*, 495–510. https://doi.org/10.1007/s00704-012-0802-z.

Gislason, P. O., Benediktsson, J. A., & Sveinsson, J. R. (2006). Random forests for land cover classification. *Pattern Recognition Letters*, *27*(4), 294–300. https://doi.org/10.1016/j.patrec.2005.08.011.

Goff, R. C. (1976). Vertical structure of thunderstorm outflows. *Monthly Weather Review*, *104*(11), 1429–1440. https://doi.org/10.1175/1520-0493(1976)104⟨1429:VSOTO⟩2.0.CO;2.

Grant, L. D., & van den Heever, S. C. (2016). Cold pool dissipation. *Journal of Geophysical Research: Atmospheres*, *121*(3), 1138–1155. https://doi.org/10.1002/2015JD023813.

Grimes, D., Coppola, E., Verdecchia, M., & Visconti, G. (2003). A neural network approach to real-time rainfall estimation for africa using satellite

data. *Journal of Hydrometeorology*, *4*(6), 1119–1133. https://doi.org/10.1175/1525-7541(2003)004⟨1119:ANNATR⟩2.0.CO;2.

Gu, Z., Duncan, C., Renshaw, E., Mugglestone, M., Cowan, C., & Grant, P. (1989). Comparison of techniques for measuring cloud texture in remotely sensed satellite meteorological image data. *IEE Proceedings F (Radar and Signal Processing)*, *136*(5), 236–248. https://doi.org/10.1049/ip-f-2.1989.0037.

Guo, Y., Liu, Y., Georgiou, T., & Lew, M. S. (2018). A review of semantic segmentation using deep neural networks. *International Journal of Multimedia Information Retrieval*, *7*, 87–93. https://doi.org/10.1007/s13735-017-0141-z.

Haerter, J. O., Böing, S. J., Henneberg, O., & Nissen, S. B. (2019). Circling in on convective organization. *Geophysical Research Letters*, *46*(12), 7024–7034. https://doi.org/10.1029/2019GL082092.

Haerter, J. O., Meyer, B., & Nissen, S. B. (2020). Diurnal self-aggregation. *npj Climate and Atmospheric Science*, *3*(1), 30. https://doi.org/10.1038/s41612-020-00132-z.

Han, L., Liang, H., Chen, H., Zhang, W., & Ge, Y. (2021). Convective precipitation nowcasting using u-net model. *IEEE Transactions on Geoscience and Remote Sensing*, *60*, 1–8. https://doi.org/10.1109/TGRS.2021.3100847.

Henneberg, O., Meyer, B., & Haerter, J. O. (2020). Particle-based tracking of cold pool gust fronts. *Journal of Advances in Modeling Earth Systems*, *12*(5), e2019MS001910. https://doi.org/10.1029/2019ms001910.

Hoeller, J., Haerter, J. O., & Da Silva, N. A. (2023). Characteristics of station-derived convective cold pools over equatorial africa. *Authorea Preprints*. https://essopenarchive.org/doi/full/10.22541/essoar.170067109.99041093

Holle, R. L., & Maier, M. W. (1980). Tornado formation from downdraft interaction in the face mesonetwork. *Monthly Weather Review*, *108*(7), 1010–1028. https://doi.org/10.1175/1520-0493(1980)108⟨1010:TFFDII⟩2.0.CO;2.

Hollstein, A., Segl, K., Guanter, L., Brell, M., & Enesco, M. (2016). Ready-to-use methods for the detection of clouds, cirrus, snow, shadow, water and clear sky pixels in sentinel-2 msi images. *Remote Sensing*, *8*(8), 666. https://doi.org/10.3390/rs8080666.

Hsu, K.-l., Gao, X., Sorooshian, S., & Gupta, H. V. (1997). Precipitation estimation from remotely sensed information using artificial neural networks. *Journal of Applied Meteorology and Climatology*, *36*(9), 1176–1190. https://doi.org/10.1175/1520-0450(1997)036⟨1176:PEFRSI⟩2.0.CO;2.

Jeevanjee, N., & Romps, D. M. (2015). Effective buoyancy, inertial pressure, and the mechanical generation of boundary layer mass flux by cold

pools. *Journal of the Atmospheric Sciences*, *72*(8), 3199–3213. https://doi.org/10.1175/JAS-D-14-0349.1.

John, D., & Zhang, C. (2022). An attention-based u-net for detecting deforestation within satellite sensor imagery. *International Journal of Applied Earth Observation and Geoinformation*, *107*, 102685. https://doi.org/10.1016/j.jag.2022.102685.

Kansakar, P., & Hossain, F. (2016). A review of applications of satellite earth observation data for global societal benefit and stewardship of planet earth. *Space Policy*, *36*, 46–54. https://doi.org/10.1016/j.spacepol.2016.05.005.

Kavzoglu, T., & Colkesen, I. (2009). A kernel functions analysis for support vector machines for land cover classification. *International Journal of Applied Earth Observation and Geoinformation*, *11*(5), 352–359. https://doi.org/10.1016/j.jag.2009.06.002.

Khairoutdinov, M., & Randall, D. (2006). High-resolution simulation of shallow-to-deep convection transition over land. *Journal of the Atmospheric Sciences*, *63*(12), 3421–3436. https://doi.org/10.1175/jas3810.1.

Kirsch, B., Ament, F., & Hohenegger, C. (2021). Convective cold pools in long-term boundary layer mast observations. *Monthly Weather Review*, *149*(3), 811–820. https://doi.org/10.1175/mwr-d-20-0197.1.

Kirsch, B., Hohenegger, C., & Ament, F. (2023). Morphology and growth of convective cold pools observed by a dense station network in germany. *Quarterly Journal of the Royal Meteorological Society*, 1–20. https://doi.org/10.1002/qj.4626.

Klein, C., Nkrumah, F., Taylor, C. M., & Adefisan, E. A. (2021). Seasonality and trends of drivers of mesoscale convective systems in southern west africa. *Journal of Climate*, *34*(1), 71–87. https://doi.org/10.1175/JCLI-D-20-0194.1.

Kornilov, A. S., & Safonov, I. V. (2018). An overview of watershed algorithm implementations in open source libraries. *Journal of Imaging*, *4*(10), 123. https://doi.org/10.3390/jimaging4100123.

Kruse, I. L., Haerter, J. O., & Meyer, B. (2022). Cold pools over the netherlands: A statistical study from tower and radar observations. *Quarterly Journal of the Royal Meteorological Society*, *148*(743), 711–726. https://doi.org/10.1002/qj.4223.

Kühnlein, M., Appelhans, T., Thies, B., & Nauß, T. (2014). Precipitation estimates from msg seviri daytime, nighttime, and twilight data with random forests. *Journal of Applied Meteorology and Climatology*, *53*(11), 2457–2480. https://doi.org/10.1175/JAMC-D-14-0082.1.

Kurowski, M. J., Suselj, K., Grabowski, W. W., & Teixeira, J. (2018). Shallow-to-deep transition of continental moist convection: Cold pools, surface fluxes, and mesoscale organization. *Journal of the Atmospheric Sciences*, *75*(12), 4071–4090. https://doi.org/10.1175/JAS-D-18-0031.1.

Langhans, W., & Romps, D. M. (2015). The origin of water vapor rings in tropical oceanic cold pools. *Geophysical Research Letters*, *42*(18), 7825–7834. https://doi.org/10.1002/2015GL065623.

Lantuéjoul, C. (1978). *La squelettisation et son application aux mesures topologiques des mosaiques polycristallines* [Doctoral Dissertation]. École des Mines de Paris.

Laurent, H., D'Amato, N., & Lebel, T. (1998). How important is the contribution of the mesoscale convective complexes to the sahelian rainfall? *Physics and Chemistry of the Earth*, *23*(5), 629–633. https://doi.org/10.1016/S0079-1946(98)00099-8.

Le Goff, M., Tourneret, J.-Y., Wendt, H., Ortner, M., & Spigai, M. (2017). Deep learning for cloud detection. *8th International Conference of Pattern Recognition Systems (ICPRS)*, 1–6. https://doi.org/10.1049/cp.2017.0139.

LeCun, Y., Boser, B., Denker, J. S., Henderson, D., Howard, R. E., Hubbard, W., & Jackel, L. D. (1989). Backpropagation applied to handwritten zip code recognition. *Neural Computation*, *1*(4), 541–551. https://doi.org/10.1162/neco.1989.1.4.541.

LeCun, Y., Bottou, L., Bengio, Y., & Haffner, P. (1998). Gradient-based learning applied to document recognition. *Proceedings of the IEEE*, *86*(11), 2278–2324. https://doi.org/10.1109/5.726791.

Lee, H., Calvin, K., Dasgupta, D., Krinner, G., Mukherji, A., Thorne, P., Trisos, C., Romero, J., Aldunce, P., Barret, K., et al. (2023). Ipcc, 2023: Climate change 2023: Synthesis report, summary for policymakers. contribution of working groups i, ii and iii to the sixth assessment report of the intergovernmental panel on climate change. https://doi.org/10.59327/IPCC/AR6-9789291691647.001.

Lee, Y., Wahba, G., & Ackerman, S. A. (2004). Cloud classification of satellite radiance data by multicategory support vector machines. *Journal of Atmospheric and Oceanic Technology*, *21*(2), 159–169. https://doi.org/10.1175/1520-0426(2004)021⟨0159:CCOSRD⟩2.0.CO;2.

Li, K., Wan, G., Cheng, G., Meng, L., & Han, J. (2020). Object detection in optical remote sensing images: A survey and a new benchmark. *ISPRS Journal of Photogrammetry and Remote Sensing*, *159*, 296–307. https://doi.org/10.1016/j.isprsjprs.2019.11.023.

Liu, Y., Racah, E., Correa, J., Khosrowshahi, A., Lavers, D., Kunkel, K., Wehner, M., Collins, W., et al. (2016). Application of deep convolutional neural networks for detecting extreme weather in climate datasets. *arXiv preprint arXiv:1605.01156*. https://doi.org/10.48550/arXiv.1605.01156.

Lloyd, S. (1982). Least squares quantization in pcm. *IEEE Transactions on Information Theory*, *28*(2), 129–137. https://doi.org/10.1109/TIT.1982.1056489.

Long, J., Shelhamer, E., & Darrell, T. (2015). Fully convolutional networks for semantic segmentation. *Proceedings of the IEEE Conference on Computer Vision and Pattern Recognition (CVPR)*, 3431–3440. https://doi.org/10.1109/CVPR.2015.7298965.

Maggiori, E., Tarabalka, Y., Charpiat, G., & Alliez, P. (2016). Convolutional neural networks for large-scale remote-sensing image classification. *IEEE Transactions on Geoscience and Remote Sensing*, *55*(2), 645–657. https://doi.org/10.1109/TGRS.2016.2612821.

Mahoney, W. P. (1988). Gust front characteristics and the kinematics associated with interacting thunderstorm outflows. *Monthly Weather Review*, *116*(7), 1474–1492. https://doi.org/10.1175/1520-0493(1988)116⟨1474:GFCATK⟩2.0.CO;2.

Maranan, M., Fink, A. H., & Knippertz, P. (2018). Rainfall types over southern west africa: Objective identification, climatology and synoptic environment. *Quarterly Journal of the Royal Meteorological Society*, *144*(714), 1628–1648. https://doi.org/10.1002/qj.3345.

Markowski, P. (2007). An overview of atmospheric convection. In D. B. Giaiotti, R. Steinacker, & F. Stel (Eds.), *Atmospheric convection: Research and operational forecasting aspects* (pp. 1–6). Springer Vienna. https://doi.org/10.1007/978-3-211-69291-2_1.

Markowski, P., & Richardson, Y. (2010). *Mesoscale meteorology in midlatitudes*. John Wiley & Sons. https://doi.org/10.1002/9780470682104.

Mathon, V., & Laurent, H. (2001). Life cycle of sahelian mesoscale convective cloud systems. *Quarterly Journal of the Royal Meteorological Society*, *127*(572), 377–406. https://doi.org/10.1002/qj.49712757208.

Mathon, V., Laurent, H., & Lebel, T. (2002). Mesoscale convective system rainfall in the sahel. *Journal of Applied Meteorology*, *41*(11), 1081–1092. https://doi.org/10.1175/1520-0450(2002)041⟨1081:MCSRIT⟩2.0.CO;2.

Meena, S. R., Soares, L. P., Grohmann, C. H., Van Westen, C., Bhuyan, K., Singh, R. P., Floris, M., & Catani, F. (2022). Landslide detection in the himalayas using machine learning algorithms and u-net. *Landslides*, *19*(5), 1209–1229. https://doi.org/10.1007/s10346-022-01861-3.

Meteostat. (2024). Global weather and climate data [Accessed: February 9, 2024]. https://meteostat.net/

Meyer, B., & Haerter, J. O. (2020). Mechanical forcing of convection by cold pools: Collisions and energy scaling. *Journal of Advances in Modeling Earth Systems*, *12*(11), e2020MS002281. https://doi.org/10.1029/2020ms002281.

Meyer, H., Drönner, J., & Nauss, T. (2017). Satellite-based high-resolution mapping of rainfall over southern africa. *Atmospheric Measurement Techniques*, *10*(6), 2009–2019. https://doi.org/10.5194/amt-10-2009-2017.

Meyer, H., Kühnlein, M., Appelhans, T., & Nauss, T. (2016). Comparison of four machine learning algorithms for their applicability in satellite-based optical rainfall retrievals. *Atmospheric Research*, *169*, 424–433. https://doi.org/10.1016/j.atmosres.2015.09.021.

Miller, M., & Betts, A. (1977). Traveling convective storms over venezuela. *Monthly Weather Review*, *105*(7), 833–848. https://doi.org/10.1175/1520-0493(1977)105⟨0833:TCSOV⟩2.0.CO;2.

Minaee, S., Boykov, Y., Porikli, F., Plaza, A., Kehtarnavaz, N., & Terzopoulos, D. (2021). Image segmentation using deep learning: A survey. *IEEE Transactions on Pattern Analysis and Machine Intelligence*, *44*(7), 3523–3542. https://doi.org/10.1109/TPAMI.2021.3059968.

Moncrieff, M. W., & Liu, C. (1999). Convection initiation by density currents: Role of convergence, shear, and dynamical organization. *Monthly Weather Review*, *127*(10), 2455–2464. https://doi.org/10.1175/1520-0493(1999)127⟨2455:CIBDCR⟩2.0.CO;2.

Moseley, C., Hohenegger, C., Berg, P., & Haerter, J. O. (2016). Intensification of convective extremes driven by cloud–cloud interaction. *Nature Geoscience*, *9*(10), 748–752. https://doi.org/10.1038/ngeo2789.

Mountrakis, G., Im, J., & Ogole, C. (2011). Support vector machines in remote sensing: A review. *ISPRS Journal of Photogrammetry and Remote Sensing*, *66*(3), 247–259. https://doi.org/10.1016/j.isprsjprs.2010.11.001.

Mueller, C. K., & Carbone, R. E. (1987). Dynamics of a thunderstorm outflow. *Journal of the Atmospheric sciences*, *44*(15), 1879–1898. https://doi.org/10.1175/1520-0469(1987)044⟨1879:DOATO⟩2.0.CO;2.

Muller, C. J., & Romps, D. M. (2018). Acceleration of tropical cyclogenesis by self-aggregation feedbacks. *Proceedings of the National Academy of Sciences*, *115*(12), 2930–2935. https://doi.org/10.1073/pnas.1719967115.

Nielsen, M. A. (2015). *Neural networks and deep learning* (Vol. 25). Determination Press. https://www.ise.ncsu.edu/fuzzy-neural/wp-content/uploads/sites/9/2022/08/neuralnetworksanddeeplearning.pdf

NOAA. (2024). Generate soundings from rapid refresh (rap), gfs, nam, and other model analyses and forecasts, raobs, or aircraft (restricted) [Accessed: February 10, 2024]. https://rucsoundings.noaa.gov/

Noh, H., Hong, S., & Han, B. (2015). Learning deconvolution network for semantic segmentation. *IEEE International Conference on Computer Vision (ICCV)*, 1520–1528. https://doi.org/10.1109/ICCV.2015.178.

Nolan, D. S., Rappin, E. D., & Emanuel, K. A. (2007). Tropical cyclogenesis sensitivity to environmental parameters in radiative–convective equilibrium. *Quarterly Journal of the Royal Meteorological Society*, *133*(629), 2085–2107. https://doi.org/10.1002/qj.170.

Pan, B., Hsu, K., AghaKouchak, A., & Sorooshian, S. (2019). Improving precipitation estimation using convolutional neural network. *Water*

Resources Research, *55*(3), 2301–2321. https://doi.org/10.1029/2018WR024090.

Parker, M. D. (2021). Self-organization and maintenance of simulated nocturnal convective systems from pecan. *Monthly Weather Review*, *149*(4), 999–1022. https://doi.org/10.1175/MWR-D-20-0263.1.

Parker, M. D., Borchardt, B. S., Miller, R. L., & Ziegler, C. L. (2020). Simulated evolution and severe wind production by the 25–26 june 2015 nocturnal mcs from pecan. *Monthly Weather Review*, *148*(1), 183–209. https://doi.org/10.1175/MWR-D-19-0072.1.

Paszke, A., Gross, S., Chintala, S., Chanan, G., Yang, E., DeVito, Z., Lin, Z., Desmaison, A., Antiga, L., & Lerer, A. (2017). Automatic differentiation in pytorch. *NIPS 2017 Autodiff Workshop*. https://openreview.net/pdf?id=BJJsrmfCZ

Peters, O., & Neelin, J. D. (2006). Critical phenomena in atmospheric precipitation. *Nature Physics*, *2*(6), 393–396. https://doi.org/10.1038/nphys314.

Platnick, S., King, M. D., Ackerman, S. A., Menzel, W. P., Baum, B. A., Riédi, J. C., & Frey, R. A. (2003). The modis cloud products: Algorithms and examples from terra. *IEEE Transactions on Geoscience and Remote Sensing*, *41*(2), 459–473. https://doi.org/10.1109/TGRS.2002.808301.

Prakash, N., Manconi, A., & Loew, S. (2020). Mapping landslides on eo data: Performance of deep learning models vs. traditional machine learning models. *Remote Sensing*, *12*(3), 346. https://doi.org/10.3390/rs12030346.

Provod, M., Marsham, J., Parker, D., & Birch, C. (2016). A characterization of cold pools in the west african sahel. *Monthly Weather Review*, *144*(5), 1923–1934. https://doi.org/10.1175/MWR-D-15-0023.1.

Purdom, J. F. W., & Marcus, K. (1981). Thunderstorm triggered mechanisms over the southeast united states. *Preprints: 12th Conf. on Severe Local Storms*, 487–488.

Quinlan, J. R. (1986). Induction of decision trees. *Machine Learning*, *1*, 81–106. https://doi.org/10.1007/BF00116251.

Rasp, S., Schulz, H., Bony, S., & Stevens, B. (2020). Combining crowdsourcing and deep learning to explore the mesoscale organization of shallow convection. *Bulletin of the American Meteorological Society*, *101*(11), E1980–E1995. https://doi.org/10.1175/BAMS-D-19-0324.1.

Rauber, R. M., Stevens, B., Ochs III, H. T., Knight, C., Albrecht, B., Blyth, A., Fairall, C., Jensen, J., Lasher-Trapp, S., Mayol-Bracero, O., et al. (2007). Rain in shallow cumulus over the ocean: The rico campaign. *Bulletin of the American Meteorological Society*, *88*(12), 1912–1928. https://doi.org/10.1175/BAMS-88-12-1912.

Redl, R., Fink, A. H., & Knippertz, P. (2015). An objective detection method for convective cold pool events and its application to northern africa.

Monthly Weather Review, *143*(12), 5055–5072. https://doi.org/10.1175/MWR-D-15-0223.1.

Rivolta, G., Marzano, F. S., Coppola, E., & Verdecchia, M. (2006). Artificial neural-network technique for precipitation nowcasting from satellite imagery. *Advances in Geosciences*, *7*, 97–103. https://doi.org/10.5194/adgeo-7-97-2006.

Rodriguez-Galiano, V. F., Ghimire, B., Rogan, J., Chica-Olmo, M., & Rigol-Sanchez, J. P. (2012). An assessment of the effectiveness of a random forest classifier for land-cover classification. *ISPRS Journal of Photogrammetry and Remote Sensing*, *67*, 93–104. https://doi.org/10.1016/j.isprsjprs.2011.11.002.

Romps, D. M., & Jeevanjee, N. (2016). On the sizes and lifetimes of cold pools. *Quarterly Journal of the Royal Meteorological Society*, *142*(696), 1517–1527. https://doi.org/10.1002/qj.2754.

Ronneberger, O., Fischer, P., & Brox, T. (2015). U-net: Convolutional networks for biomedical image segmentation. *Medical Image Computing and Computer-Assisted Intervention (MICCAI)*, *9351*, 234–241. https://doi.org/10.1007/978-3-319-24574-4_28.

Rooney, G. G. (2018). Similarity-based approximations for the evolution of a gravity current. *Quarterly Journal of the Royal Meteorological Society*, *144*(716), 2302–2310. https://doi.org/10.1002/qj.3371.

Rosenblatt, F. (1958). The perceptron: A probabilistic model for information storage and organization in the brain. *Psychological Review*, *65*(6), 386–408. https://doi.org/10.1037/h0042519.

Saunders, R. W., & Kriebel, K. T. (1988). An improved method for detecting clear sky and cloudy radiances from avhrr data. *International Journal of Remote Sensing*, *9*(1), 123–150. https://doi.org/10.1080/01431168808954841.

Schlemmer, L., & Hohenegger, C. (2014). The formation of wider and deeper clouds as a result of cold-pool dynamics. *Journal of the Atmospheric Sciences*, *71*(8), 2842–2858. https://doi.org/10.1175/JAS-D-13-0170.1.

Schlemmer, L., & Hohenegger, C. (2016). Modifications of the atmospheric moisture field as a result of cold-pool dynamics. *Quarterly Journal of the Royal Meteorological Society*, *142*(694), 30–42. https://doi.org/10.1002/qj.2625.

Sehad, M., Lazri, M., & Ameur, S. (2017). Novel svm-based technique to improve rainfall estimation over the mediterranean region (north of algeria) using the multispectral msg seviri imagery. *Advances in Space Research*, *59*(5), 1381–1394. https://doi.org/10.1016/j.asr.2016.11.042.

Shapiro, M., Hampel, T., Rotzoll, D., & Mosher, F. (1985). The frontal hydraulic head: A micro-α scale (1 km) triggering mechanism for mesoconvective weather systems. *Monthly Weather Review*, *113*(7), 1166–

1183. https://doi.org/10.1175/1520-0493(1985)113⟨1166:TFHHAM⟩2.0.CO;2.

Siddique, N., Paheding, S., Elkin, C. P., & Devabhaktuni, V. (2021). U-net and its variants for medical image segmentation: A review of theory and applications. *IEEE Access*, *9*, 82031–82057. https://doi.org/10.1109/ACCESS.2021.3086020.

Simpson, C. H., Brousse, O., Mohajeri, N., Davies, M., & Heaviside, C. (2023). An open-source automatic survey of green roofs in london using segmentation of aerial imagery. *Earth System Science Data*, (4), 1521–1541. https://doi.org/10.5194/essd-15-1521-2023.

Simpson, J. E. (1969). A comparison between laboratory and atmospheric density currents. *Quarterly Journal of the Royal Meteorological Society*, *95*(406), 758–765. https://doi.org/10.1002/qj.49709540609.

Stevens, B. (2005). Atmospheric moist convection. *Annual Review of Earth and Planetary Sciences*, *33*(1), 605–643. https://doi.org/10.1146/annurev.earth.33.092203.122658.

Taylor, C. M., Belušić, D., Guichard, F., Parker, D. J., Vischel, T., Bock, O., Harris, P. P., Janicot, S., Klein, C., & Panthou, G. (2017). Frequency of extreme sahelian storms tripled since 1982 in satellite observations. *Nature*, *544*(7651), 475–478. https://doi.org/10.1038/nature22069.

Taylor, C. M., Prigent, C., & Dadson, S. J. (2018). Mesoscale rainfall patterns observed around wetlands in sub-saharan africa. *Quarterly Journal of the Royal Meteorological Society*, *144*(716), 2118–2132. https://doi.org/10.1002/qj.3311.

Tompkins, A. M. (2001). Organization of tropical convection in low vertical wind shears: The role of cold pools. *Journal of the Atmospheric Sciences*, *58*(13), 1650–1672. https://doi.org/10.1175/1520-0469(2001)058⟨1650:OOTCIL⟩2.0.CO;2.

Torri, G., & Kuang, Z. (2016). Rain evaporation and moist patches in tropical boundary layers. *Geophysical Research Letters*, *43*(18), 9895–9902. https://doi.org/10.1002/2016gl070893.

Torri, G., Kuang, Z., & Tian, Y. (2015). Mechanisms for convection triggering by cold pools. *Geophysical Research Letters*, *42*(6), 1943–1950. https://doi.org/10.1002/2015GL063227.

University of Wyoming. (2024). Atmospheric soundings [Accessed: February 10, 2024]. https://weather.uwyo.edu/upperair/sounding.html

Vincent, L., & Soille, P. (1991). Watersheds in digital spaces: An efficient algorithm based on immersion simulations. *IEEE Transactions on Pattern Analysis & Machine Intelligence*, *13*(6), 583–598. https://doi.org/10.1109/34.87344.

Vogel, R., Konow, H., Schulz, H., & Zuidema, P. (2021). A climatology of trade-wind cumulus cold pools and their link to mesoscale cloud organization. *Atmospheric Chemistry and Physics*, *21*(21), 16609–16630. https://doi.org/10.5194/acp-21-16609-2021.

Wakimoto, R. M. (1982). The life cycle of thunderstorm gust fronts as viewed with doppler radar and rawinsonde data. *Monthly Weather Review*, *110*(8), 1060–1082. https://doi.org/10.1175/1520-0493(1982)110⟨1060:TLCOTG⟩2.0.CO;2.

Wang, P., Chen, P., Yuan, Y., Liu, D., Huang, Z., Hou, X., & Cottrell, G. (2018). Understanding convolution for semantic segmentation. *IEEE Winter Conference on Applications of Computer Vision (WACV)*, 1451–1460. https://doi.org/10.1109/WACV.2018.00163.

Weaver, J. F., & Nelson, S. P. (1982). Multiscale aspects of thunderstorm gust fronts and their effects on subsequent storm development. *Monthly Weather Review*, *110*(7), 707–718. https://doi.org/10.1175/1520-0493(1982)110⟨0707:MAOTGF⟩2.0.CO;2.

Weisman, M. L., Klemp, J. B., & Rotunno, R. (1988). Structure and evolution of numerically simulated squall lines. *Journal of the Atmospheric Sciences*, *45*(14), 1990–2013. https://doi.org/10.1175/1520-0469(1988)045⟨1990:SAEONS⟩2.0.CO;2.

Wills, S. M., Cronin, M. F., & Zhang, D. (2021). Cold pools observed by uncrewed surface vehicles in the central and eastern tropical pacific. *Geophysical Research Letters*, *48*(10), e2021GL093373. https://doi.org/10.1029/2021GL093373.

Wilson, J. W., & Schreiber, W. E. (1986). Initiation of convective storms at radar-observed boundary-layer convergence lines. *Monthly Weather Review*, *114*(12), 2516–2536. https://doi.org/10.1175/1520-0493(1986)114⟨2516:IOCSAR⟩2.0.CO;2.

Wood, R., & Hartmann, D. L. (2006). Spatial variability of liquid water path in marine low cloud: The importance of mesoscale cellular convection. *Journal of Climate*, *19*(9), 1748–1764. https://doi.org/10.1175/JCLI3702.1.

Yano, J.-I., Liu, C., & Moncrieff, M. W. (2012). Self-organized criticality and homeostasis in atmospheric convective organization. *Journal of the Atmospheric Sciences*, *69*(12), 3449–3462. https://doi.org/10.1175/JAS-D-12-069.1.

Yu, Y., Wang, C., Fu, Q., Kou, R., Huang, F., Yang, B., Yang, T., & Gao, M. (2023). Techniques and challenges of image segmentation: A review. *Electronics*, *12*(5), 1199. https://doi.org/10.3390/electronics12051199.

Zipser, E. J. (1977). Mesoscale and convective–scale downdrafts as distinct components of squall-line structure. *Monthly Weather Review*, *105*(12), 1568–1589. https://doi.org/10.1175/1520-0493(1977)105⟨1568:MACDAD⟩2.0.CO;2.

Zucker, S. W. (1976). Region growing: Childhood and adolescence. *Computer Graphics and Image Processing*, *5*(3), 382–399. https://doi.org/10.1016/S0146-664X(76)80014-7.

Zuidema, P., Torri, G., Muller, C., & Chandra, A. (2017). A survey of precipitation-induced atmospheric cold pools over oceans and their interactions with

the larger-scale environment. *Surveys in Geophysics*, *38*(6), 1283–1305. https://doi.org/10.1007/s10712-017-9447-x.